Computational Models for Mobile Robotics based on Reaction-Diffusion Processes

Alejandro Vázquez Otero

E.T.S de Ingeniería Informática

Universidad Nacional de Educación a Distancia

Ph.D. Dissertation

Madrid, 2015

Computational Models for Mobile Robotics based on Reaction-Diffusion Processes

Alejandro Vázquez Otero

E.T.S de Ingeniería Informática

Universidad Nacional de Educación a Distancia

Ph.D. Dissertation

Madrid, 2015

Department Informática y Automática

Faculty E.T.S. de Ingeniería Informática

Dissertation Title Computational Models for Mobile Robotics based on Reaction Diffusion Processes

Author Alejandro Vázquez Otero

Academic Degree M.Sc. Univ. Santiago de Compostela

Advisor Dr. Natividad Duro Carralero

Advisor Dr. Raquel Dormido Canto

Acknowledgements

I would like to acknowledge my debt to all people that helped me in the realization of this thesis, specially to Natividad Duro and Raquel Dormido, who have made possible this project. I would also like to thank Igal Berenstein for his continued support over the years.

Table of contents

Resumen

Es bien conocido entre la comunidad científica que una de las principales áreas de la ciencia que presenta en estos días mayor número de incógnitas está relacionada con la morfogénesis y la embriología. En otras palabras, cómo a partir de una distribución uniforme de células no diferenciadas, ni siquiera en lo que a información genética se refiere, puede aparecer una estructura constituida por reordenamientos y diferenciación celular. El por qué células aparentemente iguales experimentan procesos de diferenciación diferentes es, hoy en día, un misterio. No obstante, se está avanzando en la comprensión de estos mecanismos mediante estudios biológicos de quemotaxis, información posicional o de existencia de pre-patrones que revelan complicadas interacciones entre células.

Los modelos teóricos que predicen la formacion de algunas de estas estructuras, en concreto los modelos de Reacción diffusión, generan una dinámica no lineal extremadamente compleja. Dicha dinámica es capaz de reproducir patrones que a priori sugieren un posible tratamiento computacional. Emplear esta aparente lógica implícita que aparece durante la formación de patrones, permitiría desarrollar algoritmos computacionales donde toda la lógica de decisión sería transferida al modelo numérico. Puesto que los modelos númericos de reacción diffusión son fácilmente reproducibles en plataformas físicas especializadas, esto daría lugar a implementaciones de bajo costo.

List of figures

List of tables

Chapter 1

Introduction

When surfing the rich tapestry of patterns that arises when playing with nonlinear systems, a persistent idea comes to mind: there is a huge amount of decision-logic taking place in the background as the pattern develops [15]. By means of a simple Reaction-Diffusion (RD) system, a wide range of behaviors can be reproduced: from simple excitations waves [58] to a more complex stable pattern formation through the so called Turing instability [73].

Beyond this, different instabilities or combinations of them [75] [17] have given rise to very intriguing static and dynamic structures. And the nuances found in the resulting concentration profiles reveals a mechanism that can be summarized in a single word: *self-organization*. A local transfer of information originates self-organize complex structures in a larger scale. Computationally, these concentration profiles are identified as simple geometric information, not surprisingly early works in this topic have already emphasized this point of view [...]. RD systems can be numerically reproduced as a network of coupled cells with short-range coupling, which greatly simplifies its codification and enables a direct hardware implementation by means of standard technologies (GPU, FPGA, VLSI). Even more, combination of the intrinsic massive parallelism of the model propagation and the short-range diffusive coupling between cells results in a fault tolerance that can be interpreted as noise resistance (isolated damage cells do not influence the overall behaviour), exposing the robustness of natural phenomena. Computational models producing dynamics of RD systems have already been employed in image processing operations [32, 33, 48, 61, 62], calculation of the shortest time to reach a destination point [59] and the shortest path between two points [79]. The idea of RD-based path planning has been introduced by Adamatzky [4, 6] and Trevai et al. [71, 72] whom demonstrated experimental and strictly computational feasibility of such approaches, respectively.

That being said, it would be appealing to develop a computer algorithm based on a RD-core whose different configurations encapsulate the necessary logic to perform suitable decisions during the execution. Where some inputs deliver some outputs and where the main benefit is the ability to deal with complexity in a natural way.

In summary, although the computation using RD systems has already been explored, until now there wasn't any definitive method to design general purpose algorithms, that takes advantage of their rich spatiotemporal dynamics. Therefore an outcome in the form of an standard method to use RD systems for general purpose computation will be an interesting achievement in the use of RD systems.

1.1 Objectives

The general objective of this thesis is to investigate, design, and implement mobile robotics algorithms based on reaction-diffusion systems. The numerical study of frontwaves propagation for the FHN model is addressed. Also, due to the computational burden associated with the numerical integration of RD systems in two dimensions, the optimization of its spatial integration is also addressed.

The following specific objectives are considered in this thesis:

- Investigate the dynamics of the FHN model, particularly the propagation of wavefronts in bistable systems to derive properties that can be used in the design of algorithms.
- Perform the stability analysis of the FHN model for the ranges of interest, and analyze the associated Turing instability conditions.
- Development of numerical optimization techniques to decrease the computational burden, in order to get computation times in the average range (at least) of minutes.
- Development of mobile robotics algorithms, with a focus on exploration and planning strategies.

1.2 Outline and contributions

The organization of this thesis is as follows:

chapter 2 This chapter aims to put the self-organization research field into historical context with a focus on parts of the field related to this thesis. Therefore its origins will be briefly discuss, as well as the connection between all the terms involved in what is understood as self-organization in science, *i.e.* complexity, non-linearity, bifurcation, emergence or dissipative structures.

chapter 3 This chapter is devoted to illustrate the basic principles that govern the dynamics of RD systems, with a focus on the Fitz-Hugh Nagumo model and more particularly in the bistable configuration that is used in this thesis.

chapter 4 This chapter provides a description of the used computational framework. Therefore, a brief introduction to the FHN model, leads to the description of a new computational method in which the main decision logic is transferred to the model dynamics, that seamlessly encapsulates geometric operations. This feature will be used for general purpose computation in the next chapter.

chapter 5 This chapter illustrates all the developments achieved in this thesis. In particular, starting with a single robot exploration task, a cooperative multirobot exploration algorithm is introduced. Also a computation of the Voronoi diagram by means of the RD core, is presented. All the developed algorithms are compared with its standard counterparts.

1.3 Publications

The research done in this thesis has resulted in the following publications, included in Appendix B:

- A. Vázquez-Otero, Jan Faigl, Raquel Dormido, and Natividad Duro. Reaction diffusion voronoi diagrams: From sensors data to computing. Sensors, 15(6):12736–12764, 2015.
- A. Vázquez-Otero, J. Faigl, N. Duro, and R. Dormido. Reaction-diffusion based computational model for autonomous mobile robot exploration of unknown environments. International Journal of Unconventional Computing, 4:295–316, 2014.
- A. Vázquez-Otero, J. Faigl, N. Duro, and R. Dormido. Reaction-diffusion process based computational model for mobile robot exploration task. In Workshop Proceedings on Unconventional Approaches to Robotics, pages 16–18, Piscataway, 2013. IEEE.

Chapter 2

Nonlinear Dynamics

Abstract

The self-organization illustrated by Nature in almost all aspects of our reality exposes what are very complex behaviours. However, on the contrary, this can very often be captured by simple dynamical models. Although nowadays this constitutes a prolific area of research, throghout the last century the self-organization was struggling for acceptance among the scientific community, only in the second half, after the development of the thermodynamics-of-out-of-equilibrium it was set as a research field. This chapter thus aims to put this research field into historical context with a focus on parts of the field related to this thesis. I will therefore briefly discuss its origins and connection between all the terms involved in what is understood as self-organization in science, *i.e.* complexity, non-linearity, bifurcation, emergence, dissipative structures, spatially extended systems, *etc*.

2.1 Self-Organization

A troublesome origin

The term self-organization (self-organizing) can be traced back to a statement made by the philosopher Inmanuel Kant in his Critique of Judgment. In that work he questioned the validity of using the causality principle of classical physics to explain life. As a known scientific phenomena, it dates to early XX century, likely to 1910 when Lotka published the work *Contribution to the Theory of Periodic Reactions* (Lotka, 1910). One decade later in 1921 the chemist William Bray suggested Loctka's work as a plausible explanation of his observation of a chemical oscillationis. Nevertheless, attention to both works was conspicuous by his absence, and even 30 years later Belousov did not succeed in his attempt to publish his observation of periodic oscillations in color when oxidizing citric acid with bromate and cerium IV (the work eventually appeared in the proceedings of a conference without refereeing. During that time, the main impediment was that in the vast majority of the cases reactants do not self-organize, thus making it difficult to accept the concept of global organization in a well defined structures, although at least since the 1890s there have been reports of chemical systems that self-organize.

Regardless of the troublesome origin, throughout the century, and especially with the inclusion of chemical diffusion in the experiments, the number of systems found that show spontaneous organization was increased gradually and early in the 1950s. In these systems, the reactants interact generating periodic variations of concentration that are macroscopically interpreted as patterns. Such an outcome is the interaction between reaction and molecular diffusion.

Finally, despite the fact that the self-organization concept was around for a while (even with some experimental findings), it was not until the decades of the 1960s and 1970s that the term became used in the scientific literature. During that time, Prigogine and co-workers started the development of the thermodynamics of systems far-from-equilibrium, demonstrating that reacting systems in such conditions could lead to self-organization. Indeed, the Belouzov-Zhabotinsky reaction was presented as an experimental example of such behaviour.

The theoretical works that ends up in Prigogine (being laureate with the Nobel Prize), started in around 1940. All these works focused on the non-linear dynamics of reactive processes far-from-equilibrium, which under certain conditions may give rise to self-organization. This type of self-organizaton coming from RD systems will be the subject of the present work.

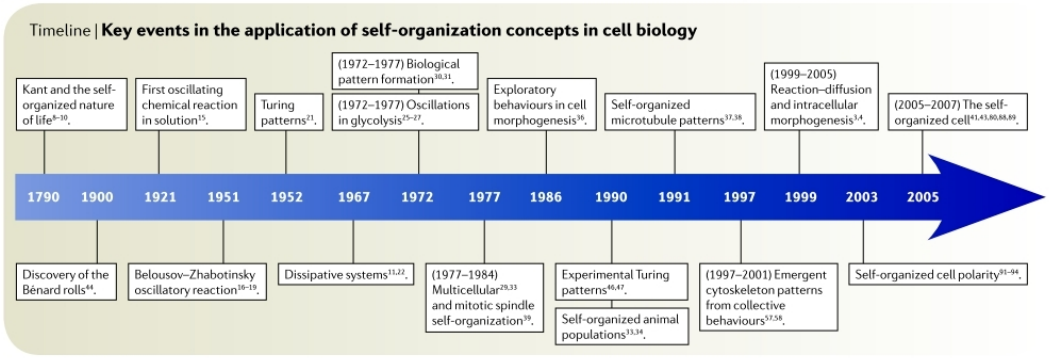

Fig. 2.1 Key events that lead to the self-organization field

The export of entrophy and the kinetic resistance

Ther term kinetic resistance, as it is used in the present context was coined in order to describe the general opposition among the scientific community against the new observed phenomena of spontaneous chemical oscillations. The well established concept of thermodynamic equilibrium for a closed system weighted like a stone, and was required the development of the afore-described *thermodynamics of out-of-equilibrium* prior to such observations were accepted.

In these open systems (far-from-equilibrium), the chemical reactions are able to generate a flux of dissipation from where the system can extract the energy, that is used for driving and mantaining the system far-from-equilibrium. That energy that flows through the system can be used to decrease its entropy, generating ordered states, and thus leading to a new type of dynamics capable of developing patterns. As expected, the consumption of the chemical species involved stops the process, and the system goes back into the standard thermodynamical equilibrium, hence the dissipative structure would disintegrate.

Although the open thermodynamical systems out-of-equilibrium have been systematically investigated, it is worth mentioning Turing's precursor statement of such sytems, in his work:

In order to maintain the wave pattern a continual supply of free energy is required. It is clear that this must be so since there is a continual degradation of energy through diffusion. This energy is supplied through the fuel substances (A, B in the last example), which are degraded into waste products.

Indeed, formalization of the self-organization processes was achieved by the Belgian chemist Ilya Prigogine, while working in the topic that he called "dissipative systems", and also by the German physicist Haken who worked on similar issues under the name of synergetics (Timeline) .

An obvious example of the so-called dissipative structures are living systems. Sunligh and nutrients constitute a source of low entropy, that in the form of waste products with high degree of entropy are exported back. During this process, the internal entropy of the living organism decreases, allowing to counteract the general tendence to reach a maximun of entropy stated in the second law of thermodynamics. Therefore a living organism is continusouly generating entropy that is transferred out of itself, and thus increasing its own order.

A good overview of the situation of that time can be found in [26], where it is noticeable that only thirty years ago the kinetic preconception was striving for acceptance among (experimental?) biologist's

Kinetic theory envisages pattern and form as being generated by movement away from equilibrium, explicable therefore only in terms of rates of chemical reactions and transport processes. Its language is necessarily that of the partial differential equation, with both position and time as variables. (...) In my experience, most physical scientists, given the problem of living self-organization and with no prior knowledge of its theories, instantly adopt the kinetic preconception, because they see nothing else in all our philosophies that seems suitable to this task. It is usually difficult to convey to them that most biologists are not envisaging explanations along kinetic lines: "But what else could do it?"

leading to an even more dramatic consideration:

General adoption or rejection of the kinetic concept in life will require a weight of evidence from many individually less definitive experiments. This will not happen until many more biologists understand the kinetic preconception and consider it promising enough to be worth following up.

In short, the kinetic theory describes the formation of patterns (*i.e.* self-organization), by means of chemical reactions and transport processes, taking place far-from-equilibrium. Partial differential equations with dependence in both, time and position are the mathematical tools required to describe such systems.

Emergent behaviours in complex systems

The export of entropy does not by itself address the problem of how or why the self-organization occurs. Prigogine noted that such self-organization typically takes place in non-linear systems, which are far from their thermodynamic equilibrium state. This is where the complex systems come into the scene, leading to the rise of self-organization in complex systems out-of-equilibrum.

A complex system can most easily be described if we begin to define the field of Complexity before. It is a paradigm that tries to study a large body of phenomena from a common perspective occurring in systems constituted by multiple small units, and the most comprehensively studied example is the Rayleigh-Benard convection. Consider a layer of fluid heated from below. As a consequence of the heat absorption the bottom layer decreases its density compared to the upper layers. At some point the temperature gradient generates a difference in density between the top and the bottom layers strong enough to overcome the liquid viscosity and the thermal diffusivity, producing a convective motion in the liquid. That convective motion can take place in two different directions of rotation (broadly speaking) in regards of a normal observer: clockwise or counterclockwise, and both of them are equally probably at the beginning of the rotation.

Therefore, the evolution of the system as a consequence of being heated from below, results in the splitting of the associated dynamics in two possible directions, both equally probably. This is what is known as a bifurcation (that leads to the acquisition of complexity), as it is shown in Figure 2.2. The name "bifurcation" was first introduced by Henri Poincaré in 1885 in the first paper in mathematics showing such a behavior, and nowadays constitute a huge field .

This prototypical example (*i.e.* Rayleigh-Benard convection) constitutes a nonlinear system exhibiting self-organization, and it shares a number of important properties with many other pattern-forming mechanisms in spatially extended systems. In particular, the majority of the concepts introduced before (patter formation, thermodynamics far from equilibrium, *etc.*) can be better understood using this example.

Nowadays complexity is a highly interdisciplinary branch of science that embodies concepts from different fields such as nonlinear dynamics, statistical physics, probability and information theories, data analysis and numerical simulation.

One of the main characteristics that these systems exhibited, is a macroscopic correlation length, understood as the maximun distance at which the local interactions between the single agents occur, leading to develop global patterns. Another interesting and related concept is the closure: albeit the system is thermodynamically open, allowing the exchange of matter and/or energy between the system and the environment, the organization is determined purely internally. Such closure in regards of the organization turns a set of interacting discrete agents into a well defined “whole”. This whole exhibits properties that cannot be reduced to the properties of its original agents. These properties that only “emerge” when considering the system as a whole are called *emergent*. This in turn is the underlying idea of approaching these complex systems, the global behaviour does no represent the simple sum of its parts. Therefore, to describe self-organization the word *emergent* is used: the mutual interaction of the elements of a system resulting in the emergence of global states that cannot be anticipated based purely on the properties of such elements. Another feature of some of these systems is that self-organization can be strongly affected at an early stage in the process by the presence

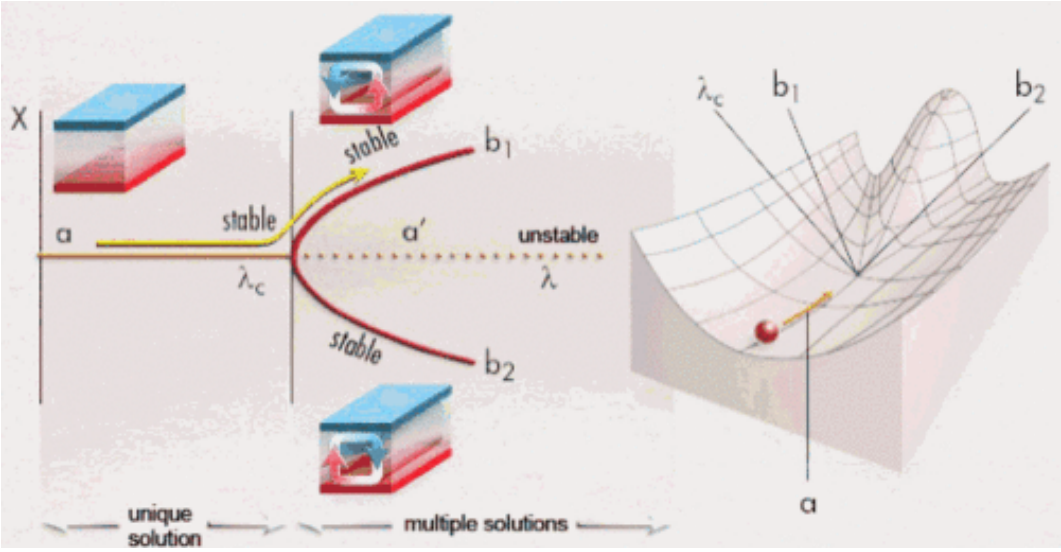

Fig. 2.2 Bifurcation...

of weak external factors that break the symmetry of the system and so modify its collective behaviour (bifurcation behaviour). Besides that, two types of modulations known as negative (damping) and positive (amplifying) feedbacks are always present in these systems.

The computational side

The main advantage of computational models that reproduce self-organization in any of its approaches, is that they do not rely on the dissipation of energy, as there is no consumption of chemical species. Hence, from a computational viewpoint one can take all the advantages of the self-organizing theory, like its inheritance of robustness -interpreted as noise tolerance- whilst dismissing the drawbacks.

The majority of the existing applications have lead to the development of computer programs such as neural networks, artificial life simulations, and genetic programming, which are indeed capable of solving complex problems. For instance, is a well known example the study of the collective behaviours of ants. The manner in which individual ants release chemicals in their attempt to show the other members of the colony the path to some source of food, generates a network of trails connecting the nest and the source. This knowledge has been succesfully applyed to the optimization of packet transport in communication networks.

Nonetheless, from an engineering point of view grasping and reproducing the behaviours that the self-organization field can exhibit through computer simulations, is only the first part of the problem. Yet an adequate application for that behaviour must be found.

Self-organization nowadays

All in all, after the aforedescribed no-less-than-troublesome origin, the term self-organization is nowadays a very complex and broad subject matter to the interests of many disciplines, often not related to each other at all. Ranging from physics and chemistry to human society, cybernetics, biology and many others.

Herein, the preferred field of application will be the classical pattern formation in systems-far-from-equilibrium, which has many potential but as of yet relatively few practical applications. Finally, in light of the previous sections, a qualitatiave description of self-organization can be set as follows:

Self-organization can be defined as process that allows the arise of overall order out of the local interacions between the components of an initally desordered system. The emergence of order relies only in those agents, and has no external agent. It is often triggered by random fluctuations that are amplified by positive feedback. Is decentralized, and thus is robust and noise resistant -understood as perturbation over the local agents-.

Our description is herein skewed according to the pattern formation field described through the Turing instability, that is the cornerstone upon which the present thesis is built. It must also be noted that both terms (emergence and self-organization) are not always necessarily conflated; there may be instances of self-organization without emergence and vice versa.

A more detailed yet qualitatiave explanation in regards of the historical background that concerns the development of the concepts involve in self-organization can be found in: [27], [68], [30], [41], [49].

Chapter 3

Reaction-Diffusion systems

Abstract

The computational framework used in this work relies in the dynamical properties of Reaction-Diffusion (RD) models, mathematically a set of coupled nonlinear partial differential equations of the parabolic type (PDEs). They are naturally applied in chemistry. However, the system can also describe dynamical processes of non-chemical nature. In spatially extended systems a RD model may develop complex behaviours, from oscillating phenomena till pattern formation by means of the Turing instability. Since there is no general rules for finding the solutions of such equations, the qualitative study of nonlinear equations, *i.e.* exploring the stability of the equations and its asymptotic behavior provides a good overview of its dynamics. Therefore, this chapter is devoted to illustrate the basic principles that govern the dynamics of RD systems, with focus on the Fitz-Hugh Nagumo model and more particularly in a bistable configuration.

3.1 The Reaction-Diffusion equations

3.1.1 Introduction

Reaction-diffusion equations are mathematical models that describes the evolution of one or more variables over a domain of interest. Originally intended to describe chemical reactions they have nowadays a wide application to describe different dynamical systems. A prototypical form can be written as follow:

$$u_t = D\Delta u + f(u). \tag{3.1}$$

Overall it describes the evolution of the state variable $u(x,t)$, and more precisely the concentration of such variable over the domain $x \in \Omega \subset \mathbb{R}$. As it can be seen, it comprises two terms with completely different associated dynamics. The so-called reactive described by $f(u) : R \to R$ that accounts for the changes in u, and the diffusive due to $D\Delta u$ -the Laplacian operator of u multiplied for a constant- that stands for the diffusion of u along Ω. Mathematically, reaction–diffusion systems constitute semi-linear parabolic partial differential equations. They can be represented in the general form of:

$$u_t = D\Delta u + f(x,u,\nabla u), \tag{3.2}$$

where $u(x,t) \in R^m$.

3.1.2 Reactions

The substration of the diffusive term transforms eq. 3.1 in a ODE (or m-D ODE in case $u(x,t) \in R^m$) as $u_t = f(u)$. A few common examples are the following. The *Logistic growth* that describes the spread of a population in space, limited by K is given by:

$$f(u) = au \cdot \left(1 - \frac{u}{K}\right) \tag{3.3}$$

The *Predator-prey*, where a population characterized by y feeds from preys defined by x is described as:

$$\begin{aligned} \dot{x} &= a_1 x \left(1 - \tfrac{x+\alpha_{12} y}{K_1}\right) \\ \dot{y} &= a_2 x \left(1 - \tfrac{x+\alpha_{21} y}{K_2}\right) \end{aligned} \tag{3.4}$$

And finally the so-called *Law of mass action* -indeed, a mathematical model, not a Law- as an example of chemical reaction. Let's define an irreversible chemical reaction as:

$$X + Y \xrightarrow{k} R, \tag{3.5}$$

being k the reaction rate. Assuming that the rate of production of R corresponds with the number of collision between molecules X and Y multiplied by the probability of reaction for each collision. Then, $\frac{\triangle c}{\triangle t} = kxy$ where x, y, r are the concentrations of X, Y, R, thus in $\triangle t \to 0$:

$$\dot{r} = kxy \tag{3.6}$$

3.1.3 Diffusion

To introduce the idea of diffusion, the conservation of mass and the Fick's law are the classical methods. For studying the variation of a variable $u(x,t) \in R^3$ that represents the concentration value of a substance inside a container, one shall study the flux $J(x,t) \in R^3$ through the surface that establish the boundaries of the container, thus:

$$\frac{d}{dt}\int_{\Omega} u(x,t)\,dV = -\int_{\Gamma} J(x,t)\,dS. \tag{3.7}$$

And from the divergence theorem:

$$\int_{\Gamma} J(x,t)\,dS = \int_{\Gamma} divJ(x,t)\,dV, \tag{3.8}$$

the previous can be reformulated as follows:

$$\left(\frac{d}{dt}u + divJ\right) = 0 \tag{3.9}$$

well known as the first law of Ficks, that connects the first time-derivative of the density and the flux when assuming conservation of mass. Finally, using Fick's second law that states that the flux has the direction of the negative gradient (of the particle distribution): $J = -D\nabla u$ (it means proportional to the concentration value) , the diffusion equation (also known as the heat equation) results:

$$u_t = D\triangle u \tag{3.10}$$

3.1.4 The Reaction-Diffusion equation

The general equation that describes the conservation of a variable c inside a volume V bounded by the surface S is:

$$\frac{\partial}{\partial t}\int_{V} \vec{c}(\vec{x},t)\,d\vec{v} = -\int_{S} \vec{J}\cdot d\vec{S} + \int_{V} \vec{f}(\vec{c},\vec{x},t)\cdot d\vec{v} \tag{3.11}$$

where the term $-\int_S \vec{J}\cdot d\vec{S}$ represents the material flux, and $\int_V \vec{f}(\vec{c},\vec{x},t)\cdot d\vec{v}$ the spontaneous creation or destruction of particles, i.e. the sources and sinks of $\vec{c}$. And finally the term

$\vec{c}(\vec{x},t)$ represents the concentration level of $\vec{c}(\vec{x},t)$ in a neighboorhod of the point $\vec{x}$ at a fixed time t.

And using the already introduced diffusion term: $u_t = D\triangle u$ the previous expression can be rewritten as:

$$\int_V \left[\frac{\partial}{\partial t}\vec{c}(\vec{x},t) + \vec{\nabla}\vec{J} - \vec{f}(\vec{c},\vec{x},t)\right] d\vec{v} = 0 \tag{3.12}$$

that yields the **general transport equation**:

$$\left(\frac{\partial}{\partial t}\vec{c}(\vec{x},t) + \vec{\nabla}\vec{J} - \vec{f}(\vec{c},\vec{x},t)\right) = 0. \tag{3.13}$$

Thus, for purely diffusive process we get the reaction-diffusion equation:

$$\frac{\partial}{\partial t}\vec{c}(\vec{x},t) = \vec{f}(\vec{c},\vec{x},t) + D\vec{\nabla}^2\vec{c} \tag{3.14}$$

which states that variations in the concentration level is due to both terms a sources and diffusive.

3.2 Reaction-Diffusion dynamics

Motivation

The main characteristic of these reaction-diffusion systems is that, under some circumstances, they exhibit spontaneous symmetry breaking phenomena and spatial self-sustained structures that were proposed as a base to explain the formation of patterns in Biochemistry and Morphogenesis [31, 55, 56]. Reaction-diffusion systems have been shown to exhibit a lot of different behaviors which will be summarized along this chapter.

The simplest way to write a reaction-diffusion equation such as the one described in 3.14 is by the set of two equations below,

$$\begin{aligned} \dot{u} &= f(u,v) + D_u\nabla^2 u \\ \dot{v} &= g(u,v) + D_v\nabla^2 u \end{aligned} \tag{3.15}$$

where u and v are the concentrations of the two relevant species identified as activator (u) and inhibitor (v). $f(u,v)$ is typically a cubic function while $g(u,v)$ is quadratic or linear.

Computationally, it describes the evolution of the states variables u and v for each point over an integration grid, being the remaining parameters constants of the model. The grid points (also called grid *cells*) are spatially coupled with its neighbours by means of the Laplacian component, which is also responsible for spreading out information along the integration domain. A standard method for analyzing the associated dynamics of Eq. 3.15 involves plotting the nullclines (sometimes called zero-growth isocline) that describe the

dynamics of a zero dimensional system or a single *cell*. Thus, the dynamics of each cell is governed by its associated nullcline configuration, plus the spatial interactions with other cells due to the diffusive coupling. The following section is a roundup of the typical systems in which RD models are split for its study. The associated nullclines configuration will help to understand qualitatively their dynamics.

3.2.1 Excitable systems: one fixed point

Let's suppose a system consisting of two chemical species RD (modeling by means of FitzHugh-Nagumo) with a set of nullclines such that the system contains only one stable fixed point, as shown in Figure 3.1. Any initial configuration far from the stable fixed point (that defines an homogeneous steady state) will decay to the stable state by means of an excitable wave. Let's study the influence in the model evolution of an initial perturbed state.

Small perturbation

If the initial state is close to the stable point, what in the phases space implies that the initial point is near the fixed stable point, the evolution of the concentration for the cell of interest is reproduced in Figure 3.1a.

Moderate Perturbation: autowaves

If the perturbation exceeds a certain threshold the linear analysis is not possible, and the overall system behavior would be completely different to that described in the previous case. In this new situation the perturbed point develop a cycle in the phases space as it is shown in Figure 3.2. This cycle can only be explained by the nonlinearity of the terms involved.

We can summarize by saying that introducing in an active RD media one perturbation higher above a certain threshold, it does not fall linearly towards the corresponding stable fixed point, but it does follow a cycle in the phases space. This leads to a wave of excitation called autowave typically consists of a wave of activation followed immediately by a wave of inhibition.

This nonlinear dynamics of the point is transferred to the neighbors because of the diffusive coupling (in a spatially extended system), forcing the original disturbance to move through the system, and thus giving rise to the phenomenon known as autowave and recognized in the form of a pulse that spreads through the system until disappear against the walls. Such behaviour is shown in Figure 3.2.

These autowaves are clearly distinct from the classical waves. The term autowave was coined by R. v. Khokhlov as an abbreviation of "autonomous waves" because once initiated does not need any external support for evolving through the media, consuming the energy

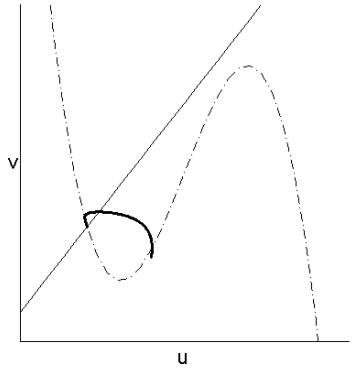

(a)

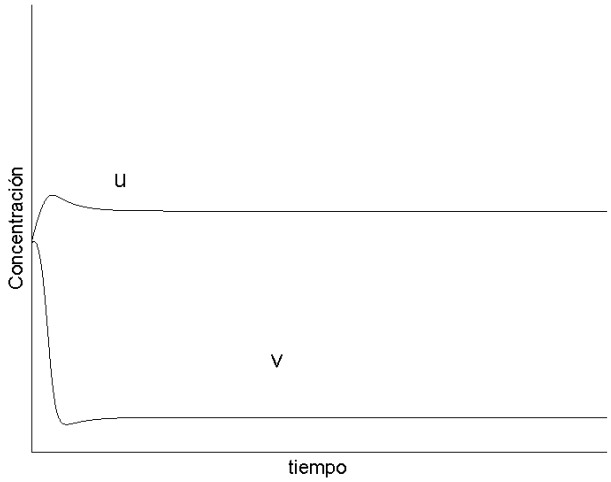

(b)

Fig. 3.1 Evolution of the concentration levels for a cell of interest after being pertubed: (**a**) phases space representation (**b**) concentration profiles of u and v over time.

stored in it till the complete consumption of the chemical species ivolved in the chemical reaction.

All the waves here presented for RD systems are commonly named autowaves. Autowaves are waves responsible for most of the processes in Nature [45]. Somehow, one can say they are the waves Nature chooses to interact. They represent a particular class of nonlinear waves that propagate through an active media at the expense of the energy stored in the medium and are manifestations of a strongly nonlinear active media [45]. These waves behave in a completely different way than those in classical mechanics [64], in fact, they conserve amplitude, shape and velocity as they propagate through a homogeneous medium, they annihilate upon collision with another wave without interfering, they do not reflect on bound-

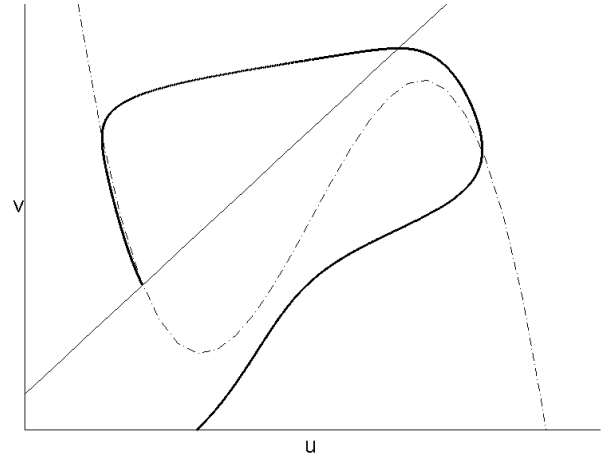

(a)

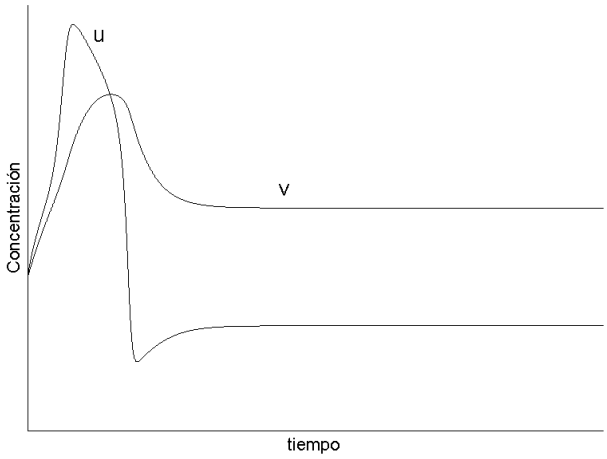

(b)

Fig. 3.2 Evolution of the concentration levels for a cell of interest after being pertubed: (**a**) phases space representation (**b**) concentration profiles of u and v over time.

aries; the only property they share with classical waves is diffraction. A list summarizing these properties is shown in Table 3.1. These are the properties that Nature takes advantage of in order to make completely different systems work. These systems range from heart muscle to pulse propagation in neurons just to name a few [23–25, 36, 37, 42, 47, 60, 63, 66]. These waves can exhibit different configurations in extended systems, a summary of them can be found in [42, 46].

Summarizing, a medium is considered as “excitable” [57] when a perturbation larger than a given threshold applied to a system does not decay immediately to its stationary value.

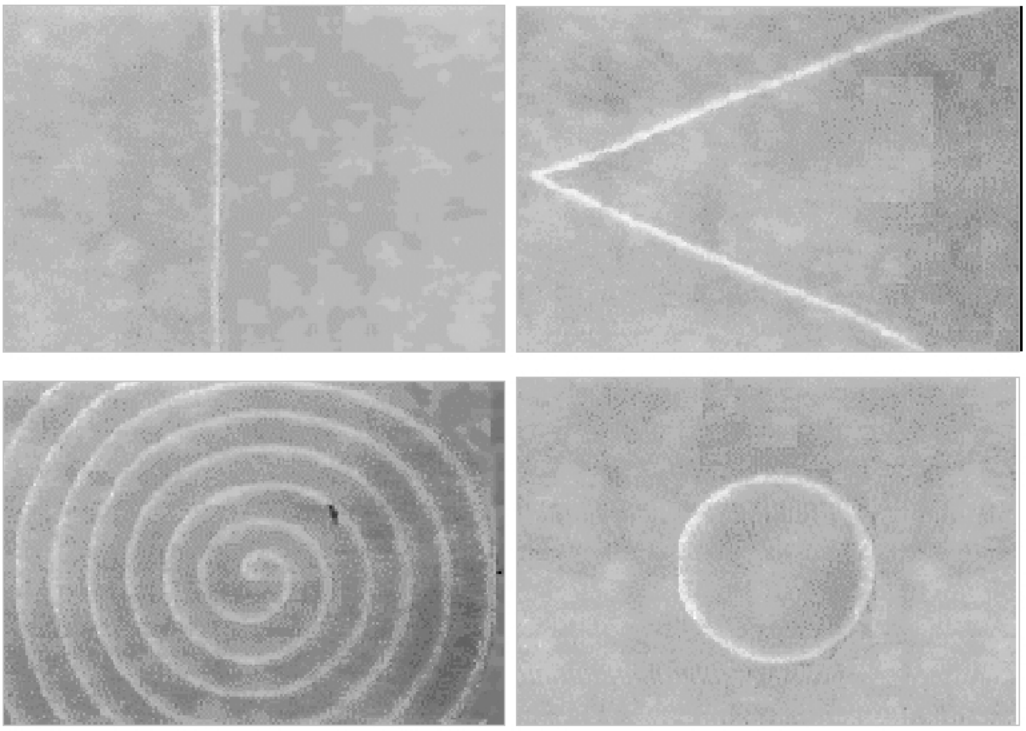

Fig. 3.3 Some examples of autowaves, propagating with different geometries in systems of two dimensions.

Table 3.1 Properties of autowaves compared with those of waves in classical mechanics.

Property	Classical waves	**Autowaves**
Conservation of Energy	+	-
Conservation of Amplitude and Waveform	-	+
Reflection	+	-
Annihilation	-	+
Interference	+	-
Diffraction	+	+

On the contrary, the perturbation grows and makes a large and non-trivial excursion in the space of variables. This cycle consists in a first part, called ”state of excitation”, where the system remains for a while. This state is able to perturb its neighboring due to diffusive process, leaving the steady state and making the same cycle, but with a delay in time. This way, a wave of excitation travels through the medium. Immediately after this wave crosses the system, it remains in a state impossible of being re-excited again (refractory state) during a certain period of time. A few examples of such waves in two dimensions are shown in Figure 3.3.

In Nature, among the most common examples of excitable systems are neurons and cardiac tissue, due to the important role that waves plays in the fibrillation mechanism and tachycardia. The propagation of electric stimuli in the heart obeys the laws of a three-dimensional excitable system, and its study has revealed new possible ways of treatment for heart dysfunctions. In the case of neurons, the excitation is due to electrical stimulus that perturbs the quiescent state. It is well known that, during neuronal diseases such as epilepsy, synchronization in state of excitability of the neurons arises [10, 13, 21].

The spatial geometry and properties of the waves excited in a medium depend on the dimensionality of the system. Traveling waves induced by diffusion are a typical solution in one-dimensional excitable media. The pulse propagates with constant velocity and profile. In two-dimensional systems the shape of the excitation wave depends on the initial perturbation: from target patterns to different kinds of spirals or chemical turbulence [53, 67].

3.2.2 Oscillatory regime

Reaction-diffusion systems may transit via a Hopf bifurcation from a steady state (excitable regime) to a periodic behavior, thus appearing a limit cycle in the system that produces periodic oscillations. This behavior is plotted in Figure 3.4 and Figure 3.5, where it can be seen that in the phases space there is on only one fixed point that is unstable. Not long ago a simple inorganic reaction oscillating periodically would have been thought to violate a natural law. Today such reactions are being systematically designed and studied as analogues of periodic behavior in living organisms. It is well known how the oscillations and the periodic changes in a natural system determines many of the main relevant aspects in its development [11, 65].

3.2.3 Bistable systems

When a system is endowed with more than one steady state (typically two stable steady states and one unstable) is called bistable [19]. Depending on the initial values of u and v, the system will evolve to either of these two stable fixed points. Figure 3.6 shows the associated nullcline configuration. Both stable states are connected via a front. The dynamics of these are well studied and understood [74]. In the biological word, a large amount of systems exhibit two steady states. For instance, bistable behavior of inhibitory neurons has been observed controlling impulse traffic through the amygdala [51]. The ultimate aim was the design, via genetic regulatory networks, of a bistable bacteria [54]. This “Toggle Switch” was implemented in E. Coli using first principles, allowing the possibility to model the gene network and predict future transitions.

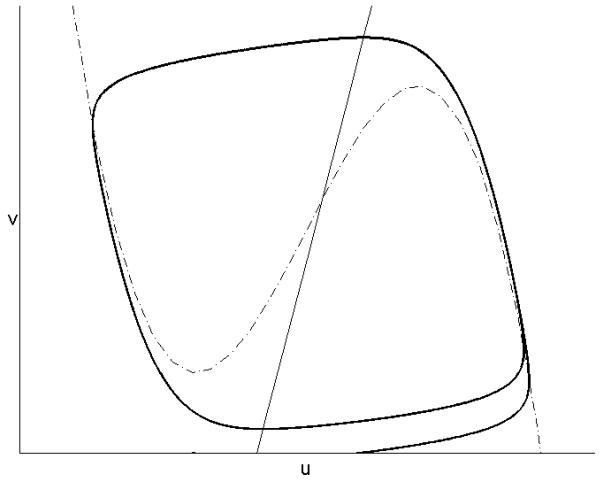

e

(a)

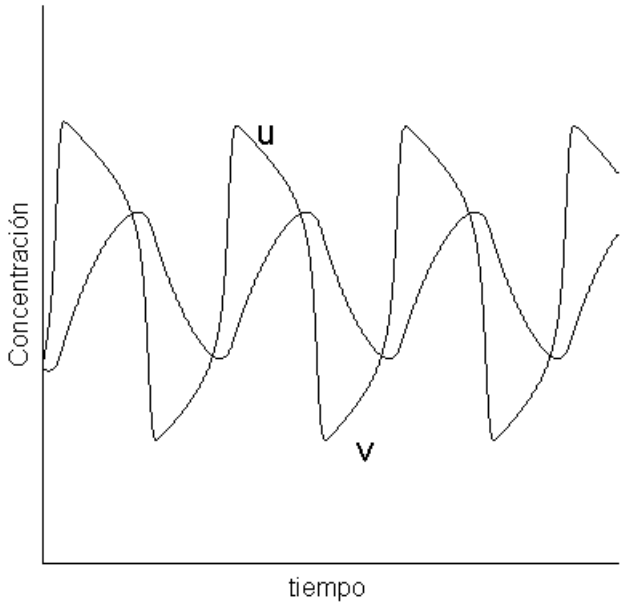

(b)

Fig. 3.4 Evolution of the concentration levels for a cell of interest after being pertubed for an oscillatory system: (**a**) phases space representation (**b**) concentration profiles of u and v over time.

3.2.4 Stationary Structures: Turing Mechanism

Reaction-diffusion systems can also exhibit different structures. Half a century ago, Alan M. Turing [38] developed a theory of Morphogenesis which had a deep impact on theoretical

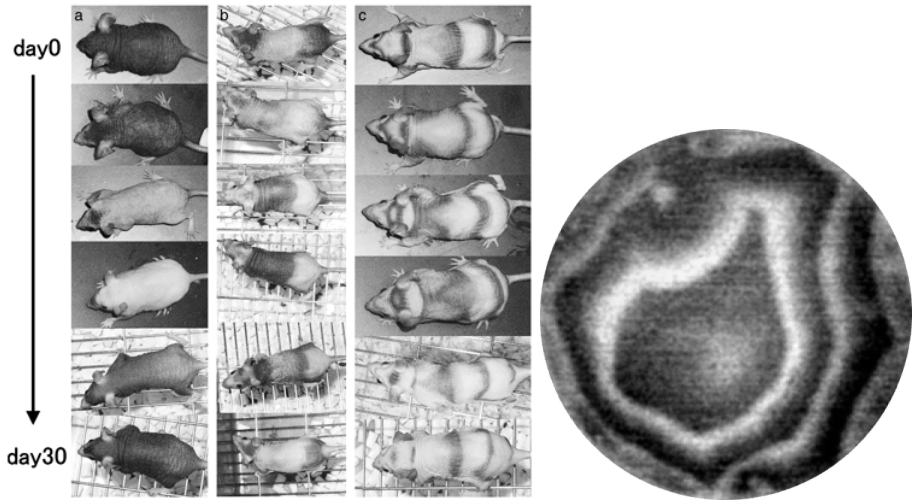

(a) (b)

Fig. 3.5 Examples of the oscilatory configuration found in 2D systems: (**a**) exotic implementation in the genes of a mouse (**b**) chemical oscillations.

developments in pattern formation and reaction-diffusion systems. Turing showed that stationary concentration patterns may spontaneously develop in an open system containing two reacting substances provided one of them diffuses much faster than the other. Nowadays, the Turing mechanism is still considered as a prototype for the formation of coherent patterns in nonequilibrium systems [29]. Turing mechanism [38] or BZ reaction [43], where proposed to explain the cell differentiation in the first days of development of early embryos [39], and the pigmentation of the skin of animals [1]. These patterns have an intrinsic wavelength which does not depend on the dimensions and geometry of the system. It is necessary that the diffusion coefficients involved are different, and that the diffusion of the inhibitor is larger than that of the activator in a proportion that depends on the nonlinearities of the system. They are non-homogeneous in space, but stationary in time. Figure 3 presents different Turing patterns obtained in chemical experiments and by numerical simulations with a reaction- diffusion set of equations.

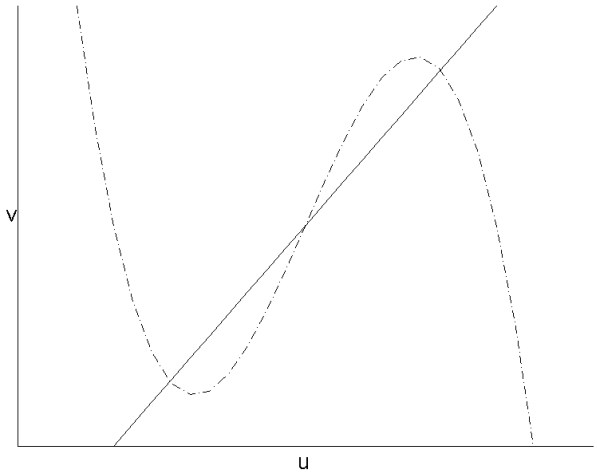

(a)

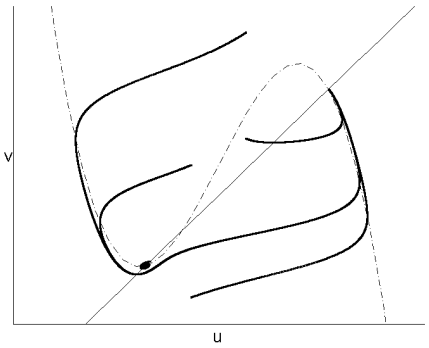

(b)

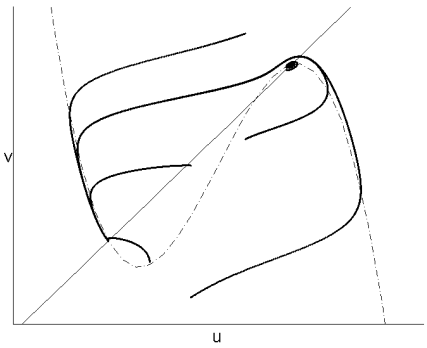

(c)

Fig. 3.6 Evolution of the concentration levels for a cell of interest after being pertubed for a bistable system: (**a**) bistable nullcline configuration where both stable states are equally stable; (**b**) the first stable stated is more stable than the second one. Reason why the majority of the trajectories in the phases space ends up in that fixed point; (**c**) conversely, the second fixed point is more stable than the first one.

3.3 Linear stability analysis for diffusion-driven instability

This section is devoted to find necessary and sufficient conditions for the diffusion-driven instability of the homogeneous steady state. We also choose zero flux boundary conditions, therefore nothing occurs due to any external input, but by *self-organisation*:

$$(n \cdot \nabla) \begin{pmatrix} u \\ v \end{pmatrix} \tag{3.16}$$

n denotes the outer normal to ∂B, the closed boundary of the considered domain B.

3.3.1 The spatially homogeneus problem

In the neighborhood of a fixed point can be found the same dynamics that in the case of a linear system, and thus the study of its dynamics can be easily performed. This, for an isolated "cell" means that any initial condition will decay to such stable point. For a nonlinear system like the following:

$$\begin{aligned} \dot{x} &= f(x,y) \\ \dot{y} &= g(x,y), \end{aligned} \tag{3.17}$$

the fixed points $(x_0, y_0)_i$ are the solutions of $0 = f(x,y)$ and $0 = g(x,y)$. And it is possible that the system has one, or more depending on the shapes of $f(x,y)$ and $g(x,y)$ that usually are quadratic, cubic or linear, and its intersections.

A brief reminder of the linearization process for this system is described in Appendix A, resulting in the eigenvalues expression A.4:

$$\lambda_{1,2} = \frac{\tau \pm \sqrt{\tau^2 - 4\Delta}}{2}, \tag{3.18}$$

where $\tau = tr(A)$. The condition that guarantees stability for this system (stable spirals, according to the standard stability analysis ref[strogad?]) is $\lambda_1, \lambda_2 \in C$ which in turn implies that $Re|\lambda| < 0$. Therefore, the conditions for obtaining a stable solution for the linearized system at the fixed point (in the absence of diffusion, as we are dealing with a single cell) are:

$$|\mathbf{A}| = f_u g_v - f_v g_u > 0 \tag{3.19}$$

$$tr\mathbf{A} = f_u + g_v < 0. \tag{3.20}$$

The above two conditions means that in a bounded area of the fixed point under consideration, it is possible to find stable solutions in the form: $\mathbf{w} \sim (\mathbf{v_1} e^{\lambda_1 t} + \mathbf{v_2} e^{\lambda_2 t})$.

3.3.2 Spatial instability or Turing conditions

The eigenvalues equation

Adding the diffusion term brings spatial dependence to the system:

$$\begin{aligned} \dot{x} &= f(x,y) + D_u \triangle x \\ \dot{y} &= g(x,y) + D_v \triangle y. \end{aligned} \tag{3.21}$$

Now each "cell" influences the behaviour of its neighbor's. The linearization described in Appendix A.3 along with the solution in the form $\mathbf{w} \sim e^{\lambda t + i\vec{k}\vec{r}}$ results in the equation A.20 for the associated eigenvalues:

$$\lambda_{1,2} = \frac{1}{2}\left(tr\mathbf{A} - tr\mathbf{D}\cdot k^2 \pm \sqrt{(tr\mathbf{D}\cdot k^2 - tr\mathbf{A})^2 - 4h}\right) \tag{3.22}$$

where $h\left(k^2\right)$ is:

$$h\left(k^2\right) = D_u D_v k^4 - k^2\left(D_v f_u^* + D_u g_v^*\right) + |\mathbf{A}|. \tag{3.23}$$

As already discussed the steady state (u_0, v_0) is (linearly) stable if $Re|\lambda| < 0$ for both eigenvalues $\lambda_{1,2}$. Remark that we wanted to have a stable steady state in case of absent spatial effects, which corresponds to $Re|\lambda(k^2 = 0)| < 0$, which again corresponds to A.14 and leads to the conditions for the trace and the determinant above (Equation 3.19). Second, we require $Re|\lambda(k \neq 0)| > 0$, *i.e.* such that the steady state is unstable if spatial disturbances (*via* diffusion term) are present. From the trace condition (for the case without diffusion) we know that $(f_u + g_v) < 0$. Besides, it's generally true that $(D_u + D_v)k^2 > 0$ for all $k \neq 0$, thus we find that the term $\left(tr\mathbf{A} - tr\mathbf{D}\cdot k^2\right)$ is always < 0. In view of this, examining Equation A.20 confirms that the only possibility to ensure that $Re|\lambda(k^2 \neq 0)| > 0$ remains in the term: $h\left(k^2 \neq 0\right) < 0$. Examination of the terms in the parable confirms that the only possibility is:

$$\left(D_v f_u^* + D_u g_v^*\right) > 0 \tag{3.24}$$

The diffusion coefficient ratio

Defining $d = \frac{D_v}{D_u}$ as the coefficient ratio between both diffusion coefficients, Equation 3.24 can be rewritten as:

$$(d f_u + g_v) > 0 \tag{3.25}$$

Since we know that $tr\mathbf{A} = f_u + g_v < 0$ (meaning they have opposite signs) this implies that at least $d \neq 1$, otherwise $(d f_u + g_v) < 0$.

Minimun of the parabola: $h\left(k^2\right)$

Still we have not yet found a sufficient condition for $Re|\lambda| > 0$ (only a necessary condition). In order to get a negative $h\left(k^2\right)$ for some k, the minimum h_{min} must be negative. Since h^2 represents a parabola, it's indeed simple to find its minimum in order to force it to be < 0:

$$\left\{0 = \frac{dh\left(k^2\right)}{dk^2} = 2D_u D_v k^2 - \left(D_v f_u + D_u g_v\right)\right\} \rightarrow k_{min}^2 = \frac{D_v f_u + D_u g_v}{2D_u D_v} \tag{3.26}$$

and substituting k^2_{min} into $h\left(k^2\right) < 0$:

$$\begin{aligned} h_{min}\left(k^2_{min}\right) &= D_u D_v \left(\tfrac{D_v f_u + D_u f_v}{2D_u D_v}\right)^2 - \tfrac{D_v f_u + D_u f_v}{2D_u D_v}\left(D_v f_u + D_u f_v\right) + |\mathbf{A}| \\ &= -\tfrac{1}{4}\tfrac{\left(D_v f_u + D_u f_v\right)^2}{D_u D_v} + |\mathbf{A}| < 0. \end{aligned} \tag{3.27}$$

Now let's investigate how the condition $h\left(k^2\right) < 0$ applies to this case. On the one hand $|\mathbf{A}| > 0$ due to the requirements for the case without diffusion (Equation 3.19). On the other,

$$-\tfrac{1}{4}\tfrac{\left(D_v f_u + D_u f_v\right)^2}{D_u D_v} + |\mathbf{A}| < 0 \tag{3.28}$$

and thus, the condition can be written as follows:

$$\left(D_v f_u + D_u g_v\right)^2 - 4 D_u D_v |\mathbf{A}| > 0, \tag{3.29}$$

or using the coefficient ratio:

$$\left(d f_u + g_v\right)^2 - 4d |\mathbf{A}| > 0. \tag{3.30}$$

Turing conditions

Finally puting together all the found requirements, the Turing conditions for getting unstable states in the presence of diffusion result in the following set of equations:

$$\begin{aligned} &f_u g_v - f_v g_u > 0 \\ &f_u + g_v < 0 \\ &\left(D_v f_u + D_u g_v\right)^2 - 4 D_u D_v \left(f_u g_v - f_v g_u\right) > 0, \end{aligned} \tag{3.31}$$

or in the more compact form:

$$\begin{aligned} |\mathbf{A}| &> 0 \\ tr\mathbf{A} &< 0 \\ \left(d f_u + g_v\right)^2 - 4d |\mathbf{A}| &> 0 \end{aligned} \tag{3.32}$$

where $\left(d f_u + g_v\right) > 0$.

Critical diffusion coefficient (d_c) and critical wavenumber (k_c)

The unstable states arise for values of $h(k^2 \neq 0) < 0$, and so the system changes its behaviour from stable to unstable at the exact point $h_{min} = 0$. For this case, from Equation 3.27 can be

extracted the equality: $|A| = \frac{(df_u+g_v)^2}{4d}$. Fixing all the kinetic parameters allows to define a critical diffusion coefficient ratio $d_c > 1$ as the appropriate root of the previous equality:

$$\left\{ (f_u g_v - f_v g_u) - \frac{(d_c f_u + g_v)^2}{4d_c} = 0 \right\} \rightarrow d_c^2 f_u^2 = 2\,(2 f_u g_v - f_u f_v)\, d_c + g_v^2 = 0 \qquad (3.33)$$

Correspondingly, we can determine the critical wavenumber k_c by:

$$\{0 = D_u D_v k^4 - k^2\,(D_v f_u + D_u g_v) + |\mathbf{A}|\} \rightarrow k_c^2 + \frac{(D_v f_u + D_u g_v)}{D_u D_v}. \qquad (3.34)$$

Unstable modes and dispersion relation

Thus, in case of $h(k^2) < 0$ when $d > d_c$, there are two zeros k_1^2 and k_2^2 of $h(k^2) = 0$, and the unstable wavenumbers are between them: $k_1^2 \leq k^2 \leq k_2^2$. Vice versa, one can plot $\lambda(k^2)$ against k^2 (the so-called dispersion relation). Examples of both, the accessible unstable modes and the dispersion relation are depicted in Figure 3.7. Of course, in the unstable range, we have $Re|\lambda(k^2)| > 0$.

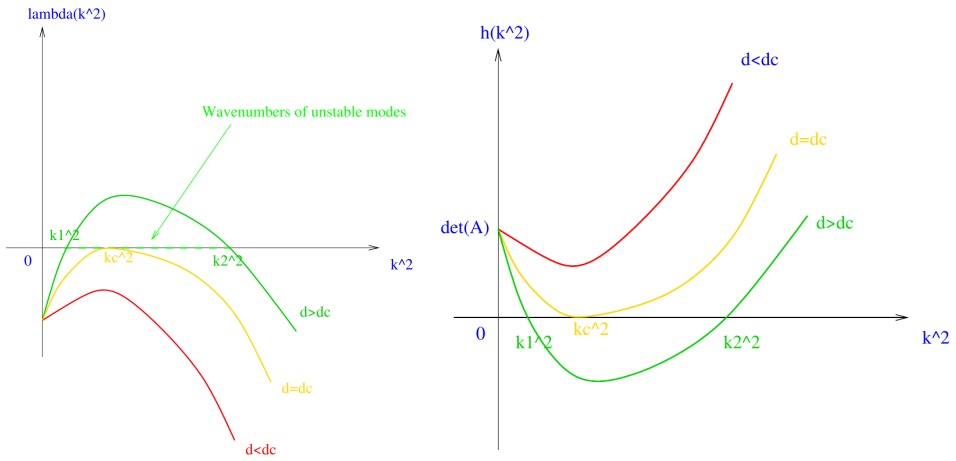

(a) (b)

Fig. 3.7 A typical representation of: (**a**) accesible wavenumbers; (**b**) dispersion relation.

The range $k_1^2 \leq k^2 \leq k_2^2$ defines the relevant nodes in the final solution (as the time increases), as all the other modes tend to zero exponentially. Therefore the final solution: $\sim \sum_{k_1}^{k_2} c_k e^{\lambda(k^2)t} W_k(\overrightarrow{r})$.

Remark: The wavenumbers are discrete when considering a finite domain, so only certain k values may be in the relevant range.

Physical interpretation

In general two types of diffusion driven instability are possible, as shown in Figure 3.8

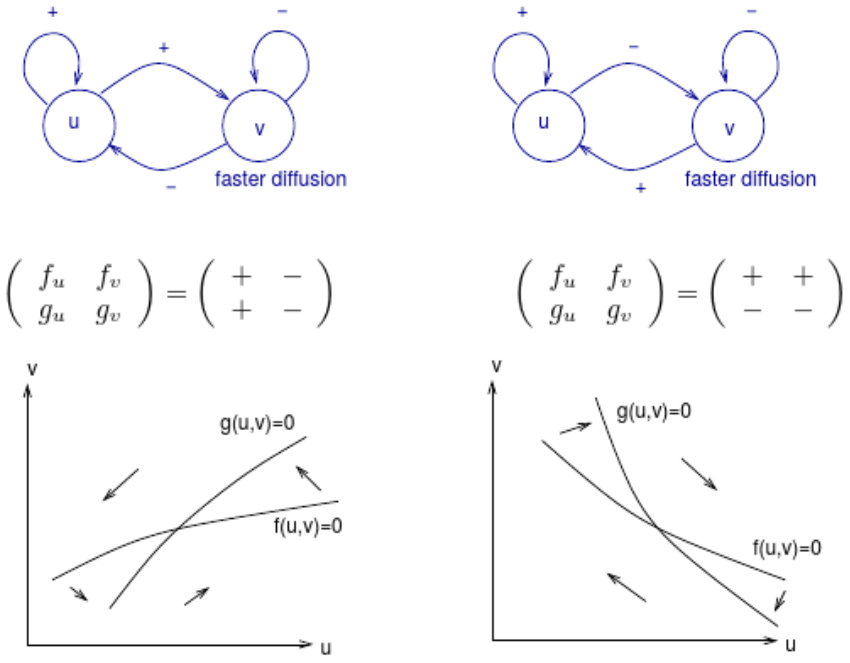

Fig. 3.8 Left case: u is the activator of v (and self-activating), v is the inhibitor (self-inhibition and inhibition of u). For the pattern formation, the inhibitor must diffuse faster than the activator. Right case: v is the activator of u (but self-inhibiting), diffuses faster. u inhibits v (but is self-activator).

3.4 The RD Model of Fitz-Hugh Nagumo (FHN)

3.4.1 The model

All the results presented so far are generic for reaction-diffusion systems (Equation 3.15). Nevertheless, for practical realizations we used the two-variable Fitz-Hugh-Nagumo model [20, 35, 52] where the nonlinearities are given by,

$$\begin{aligned} f(u,v) &= \varepsilon\left(u - u^3 - v\right) \\ g(u,v) &= \left(u - \alpha v + \beta\right) \end{aligned} \tag{3.35}$$

where ε,α, β, and ϕ are parameters characteristic of the model.

This model was based upon research of the giant squid axon by Hodgkin and Huxley, the FitzHugh-Nagumo model is one of the simpler excitable cell models available. It is a reduction of the four-variable Hodgkin-Huxley model, based upon the similarity in speed of the dynamics of the individual variables. Though primarily considered to be qualitative in nature, it is representative of the excitable phenomena of cardiac cells and has been used as a base model for testing of novel computational methods [40]. The FitzHugh-Nagumo model equations relate the cell membrane electrical potential u, and the gating variable (also called the cell's refractory potential, v). The model is able to reproduce many qualitative characteristics of electrical impulses along nerve and cardiac fibers, such as the existence of an excitation threshold, relative and absolute refractory periods, and the generation of pulse trains under the action of external currents.

3.4.2 Particularizing the RD stability analysis to the FHN model

3.4.3 Fixed points

The equations of the FHN model:

$$\begin{aligned} \dot{u} &= \varepsilon\left(u - u^3 - v\right) + D_u \triangle u \\ \dot{v} &= u - \alpha v + \beta + D_v \triangle v, \end{aligned} \tag{3.36}$$

and applying the stability analysis described in the previous section: for the fixed points in the form $f(u,v) = 0$ and $g(u,v) = 0$:

$$\left\{ \begin{array}{l} 0 = \varepsilon\left(u - u^3 - v\right) \\ 0 = u - \alpha v + \beta, \end{array} \right\} \rightarrow \begin{array}{l} u^3 + u\left(\frac{1}{\alpha} - 1\right) + \frac{\beta}{\alpha} = 0 \\ v = \frac{u+\beta}{\alpha} \end{array} \tag{3.37}$$

that represent a straight line plus a cubic equation.

Linear stable

Now applying the conditions 3.19 and 3.20, as described in previous section, for obtaining linear stability in the absence of diffusion:

$$\mathbf{A} = \begin{pmatrix} f_u & f_v \\ g_u & g_v \end{pmatrix} = \begin{pmatrix} \varepsilon\left(1-3u^2\right) & -\varepsilon \\ 1 & -\alpha \end{pmatrix} \tag{3.38}$$

that yields to:

$$\begin{aligned} \{tr\mathbf{A} < 0\} &\rightarrow \varepsilon\left(1-3u_0^2\right) - \alpha < 0 \\ \{|\mathbf{A}| > 0\} &\rightarrow \varepsilon\left(1-\alpha\left(1-3u_0^2\right)\right) > 0 \end{aligned} \tag{3.39}$$

Spatial instability

Adding the diffusion and applying the necessary and sufficient condition $\left(D_v f_u + D_u g_v\right)^2 - 4D_u D_v\left(f_u g_v - f_v g_u\right) > 0$ results in:

$$\left(D_v\varepsilon\left(1-3u^2\right) - D_u\alpha\right)^2 - 4D_u D_v\left(-\alpha\varepsilon\left(1-3u^2\right) + \varepsilon\right) > 0 \tag{3.40}$$

Or using the coefficient ratio $d = \frac{D_u}{D_v}$:

$$\begin{aligned} \left(D_v f_u + D_u g_v\right)^2 - 4D_u D_v\left(f_u g_v - f_v g_u\right) &> 0 \\ \left(df + g_v\right)^2 - 4d\left(f_u g_v - f_v g_u\right) &> 0 \\ f_u^2 d^2 - 2\left(f_u g_v - f_v g_u\right)d + g_v^2 &> 0 \end{aligned} \tag{3.41}$$

that substituing the parameters result in:

$$\left(\varepsilon\left(1-3u^2\right)\right)^2 d^2 - 2\varepsilon\left(2-\alpha\left(1-3u^2\right)\right)d + \alpha^2 > 0. \tag{3.42}$$

Finally putting together the three conditions for the diffusion-driven instability applied to the FHN model:

$$\varepsilon\left(1-3u_0^2\right) - \alpha < 0 \tag{3.43}$$

$$\varepsilon\left(1-\alpha\left(1-3u_0^2\right)\right) > 0 \tag{3.44}$$

$$\left(\varepsilon\left(1-3u^2\right)\right)^2 d^2 - 2\varepsilon\left(2-\alpha\left(1-3u^2\right)\right)d + \alpha^2 > 0 \tag{3.45}$$

$h(k^2)$

$$h\left(k^4\right) = D_u D_v k^4 - k^2\left(D_v f_u + D_u g_v\right) + |\mathbf{A}| \tag{3.46}$$

and

$$\begin{aligned} h\left(k_{min}^2\right) &= \frac{-1}{4}\frac{\left(D_v f_u + D_u f_v\right)^2}{D_u D_v} + \left(f_u g_v - f_v g_u\right) \\ &= \frac{-1}{4}\frac{\left(D_v f_u + D_u f_v\right)^2}{D_u D_v} + \left(f_u g_v - f_v g_u\right). \end{aligned} \tag{3.47}$$

Chapter 4

Computational Framework

Abstract

This chapter is devoted to provide a description of the computational framework that is used in the present work. In particular, a new method to solve computational problems using reaction diffusion systems is presented. The novelty relies on the use of model configurations that tailors its spatiotemporal dynamics to develop geometrical operations as a part of the system's natural evolution. Consequently, all the main decision logic that is usually required for performing computations in a standard algorithm is herein transferred to the model dynamics, that seamlessly encapsulates geometric operations.

4.1 The RD computational framework

4.1.1 Introduction

The idea of RD computation relies in a RD-core capable to develop all the necessary logic to perform suitable decisions during the execution. The main benefit of this approach is the ability to deal with complexity in a natural way, encapsulating all the complexity in the RD dynamics. Nevertheless, using excitable systems for developing RD-based algorithms, as it has been the norm so far, drags the problem of the volatility [Vladimir cara feliz wavefronts] of the transport of information. In this context the information is generally associated with the model evolution itself, like a traveling perturbation where the transport of information relies in the interpretation of a transient state. That's the main reason why traditional RD-based algorithms have to do a continuous checking of the system evolution, as a series of iterative processes, [Adamatzky, wave computing] in order to follow the information transport, and thus relegating their use for solving computational problems to a mere conceptual idea rather than a competitive approach with traditional algorithms. A RD-based algorithm should provide some new qualities in order to justify their use, and fulfilling this requirement entails (at least) the use of stable states to represent information rather than transient states, in order to avoid continuous checking.

Bistable systems are conceptually the best suited to meet these conditions, allowing to codify information easily distinguishable because of coexistence of both states. But such coexistence is based on the fact that both states must remain separate, without actually mixing. This feature has been achieved increasing the stability of the frontwaves separating both states. Additionally, novel properties that have been found over the course of the analysis done in the present work have allowed the implementation of different algorithms using only RD-based computation.

In short, the apparent decision-logic exhibited by the RD model can be seen as an abstraction layer for problem solving, allowing one to embed the complexity of a real problem into the model spatiotemporal evolution. This analogy confers the RD model the status of a computational framework in which geometrical operations can be performed.

4.1.2 The asymmetric bistable domain: traveling frontwave

As already discussed in Section 3.2 the fixed points of the system are the ones represented by the nullclines intersection, and basically can be classified in stable and unstable states, leading to stable steady states SS or conversely to unstable steady states US. Concentration levels of the state variables (u, v) evolve naturally toward the concentration levels determined by SS. For the purpose of this work we are concerned with the nullcline conguration depicted in Figures 3.6c and 3.6b leading to the so called bistable regime in which the model presents two SS and one US (green and red discs, respectively). It basically means that the system

(*i.e.*, the concentration levels of (u, v) for each grid-cell) tends to remain in any of these two *SS*, being feasible that some portions of the system be in one, while the remaining parts be in the other. A symmetric nullcline configuration is depicted in Figure 4.1

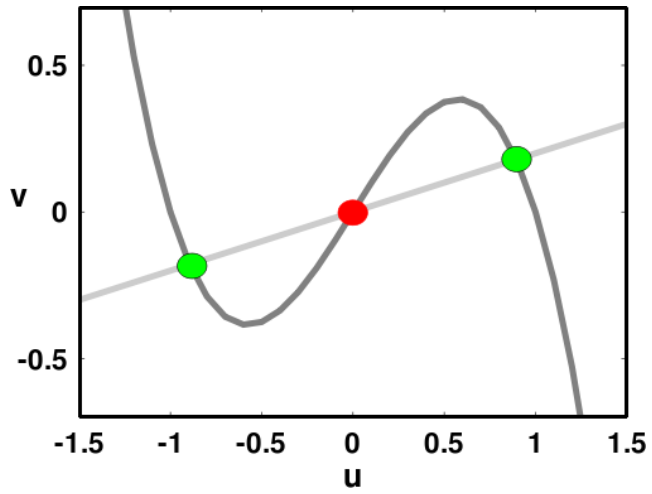

Fig. 4.1 General symmetric configuration for a bistable system. Both stable states are equally stable.

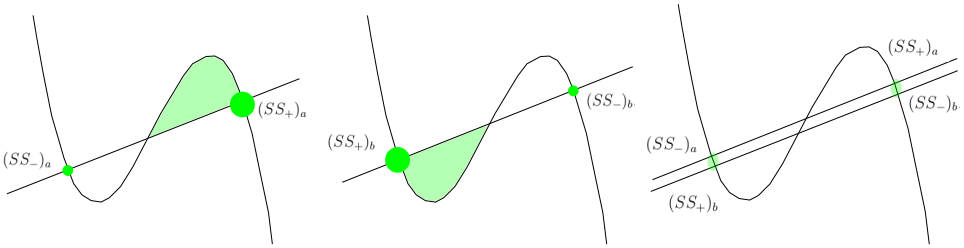

(a) (b)

Fig. 4.2 Asymmetric nullcline configurations for a bistable system. (**a**) Two possible asymmetric configurations. (**b**) Superposition of both asymmetric configurations. It can be seen how close are they fixed points.

Consequently, an interesting property of the bistable regime lies in the possibility to modulate the relative stability of both *SS*. Allowing to differentiate between SS_+ and SS_- that clearly represent the more and less *SS* respectively. Moreover, the relative stability of both *SS* can be trivially related with the area under the curve, which is reproduced in Figure 4.32g Thus, the relative stability of the system can be modulated through the nullcline conguration. Finally, as the system evolves toward the concentration level of SS_+, a default conjuration in SS_- causes the system to move to SS_+ if a small perturbation is introduced. Under these circumstances the mobile frontier that separates both *SS* and drives the shift can be considered as a traveling frontwave. Thereby, only this type of autowaves is used in this work.

4.1.3 The Switch-of-phase strategy

The nullcline configuration depicted in the left part of Fig. 4.32g characterizes a system with a tendency to evolve towards the stable point $(SS_+)_a$ while for the right diagram in the same figure the tendency is towards $(SS_+)_b$.

From a superimposion of the both figures, as it is shown in Fig. 4.32h, it is evident that the stable points are relatively close in both nullclines, *i.e.*, $(SS_-)_a \approx (SS_+)_b$ and $(SS_+)_a \approx (SS_-)_b$. The fact that their concentration levels are so close enables a smooth transition from the nullcline configuration depicted in the left part of Fig. 4.32g to the configuration depicted in the right part of the figure, and *vice versa*. Therefore, if the parameters of the model are slightly modified, after a short period conditioning in which $(SS_-)_a$ becomes $(SS_+)_b$ and $(SS_+)_a$ becomes $(SS_-)_b$, the model evolves according to the new nullcline configuration.

It is because the system dynamics can be tailored to reproduce different behaviors using diverse nullcline configurations, that geometric operations can be encapsulated in the model spatiotemporal evolution using this *switch-of-phase* mechanism.

Hence, the problem boils down to find proper nullcline configurations capable of reproducing the desired behaviors.

4.1.4 Sensory information: binary forcing

It has been shown in literature that some natural phenomena can be explained in terms of the RD systems, *e.g.*, a pattern formation where self-organization plays a key role. An intriguing characteristic of such natural processes is how its development becomes fairly robust against the unavoidable imbalances that arise in every living system. This behavior is consistently reproduced by the RD dynamics, which exhibits a strong capacity to deal with external perturbations, either overcoming it, or adapting its internal behaviour to accommodate to them. The so-called *external forcing* has been systematically studied as a mechanism for interacting with RD systems. It comprises both the spatial [**? ?**] and the spatiotemporal [**?**] domains, and it can consist in a weak influence that barely affects the dynamics, or a strong perturbation that determines its behavior. For perturbing the FHN model as it is defined in Eq. 3.36, the main technique consists in the local modification of the nullcline configuration for a few cells of interest. The effect of this modification on the dynamics is an inhibition of the frontwave propagation at these points; hence, it is equivalent to the introduction of binary information into the system, which can be used to represent obstacles in robot path planning as it was shown in [77].

An example of an environment representation created from raw sensor measurements is shown in Figure 4.3a. The showed map is created by integration of the sensors measurements into an occupancy grid, where each cell denotes a probability the cell is occupied by an obstacle. New sensor measurements, in this case a scan from a laser ranger finder,

are integrated into the occupancy grid using Bayes' rule [44]. Then, a grid map of the environment is created from the occupancy grid by thresholding the probability value of each cell into one of three states: *occupied*, *free*, and *unknown*. A wavefront evolution in a grid map is shown in Fig. 4.3b and Fig. 4.3c, where it can be noticed how the wavefront covers the available space during its evolution, while stopped at the edges of the grid map, which represent obstacles. This feature allows to integrate the external (environmental) information into the RD computational grid in a straightforward way.

(a) (b) (c)

Fig. 4.3 A visualization of sensor measurements transferred to the integration grid: (**a**) occupancy grid with integrated sensor measurements where detected obstacles are in black, identified freespace is in white, and unknown parts of the environment are in gray; (**b** and **c**) the occupancy grid that represents the map of the environment is transferred (merged) to the integration grid of the model, where a wavefront is triggered.

4.1.5 Sensory information: gradient-like forcing

In the previous section, a binary grid in the form of the grid map of the environment has been introduced as external information into the integration grid through the local modification of the nullclines of the particular point of interest (the obstacles). It means that at each point of the grid representing an obstacle the nullcline configuration is replaced by other that inhibits the wavefront propagation. This inhibition is suitable for introducing binary information into the integration grid and thus any propagating will stop at reaching any of these locations. Besides, the model allows to consider an additional constraint in the form of an extra (point dependent) term, being the final expression to be discretized:

$$\begin{aligned} \dot{u} &= \varepsilon\left(u-u^3-v+\phi\right)+F+D_u\triangle u \\ \dot{v} &= (u-\alpha v+\beta)+D_v\triangle u \end{aligned} \quad . \tag{4.1}$$

To our interest, the F term (F_{ij} for a cell at the coordinates ij in the computational grid) represents the environmental information coming from sensors, and the main difference with regards to the previous method (the local nullcline modification) is that it allows to introduce gradient-like information. In other words, the FHN dynamics is determined by a combination of the nullcline configuration plus the diffusive term, and such a behaviour is somehow *resistant* to a set of values that can be introduced through F_{ji} at each cell. For example, it can establish an effective range $F_{ji} \subset [0, max)$ which introduces a gradual delay in the wavefront propagation, reaching the complete inhibition. An intensive use of this feature is shown in [76], where the RD-model is employed for planning a path in the robotic exploration task. An example of such a behavior is depicted in Fig. 4.4, where a planar frontwave evolves according to a different values of F along the vertical axis: a maximum delay in the upper part of the front regarding the lower part where the value $F = 0$ means no forcing at all. Therefore, we can generate a profile that exhibits a gradient of velocities in the wavefront propagation along the vertical axis. This result is compatible with other RD properties used in the framework, like the annihilation upon a collision, and hence opens up a wide range of possibilities.

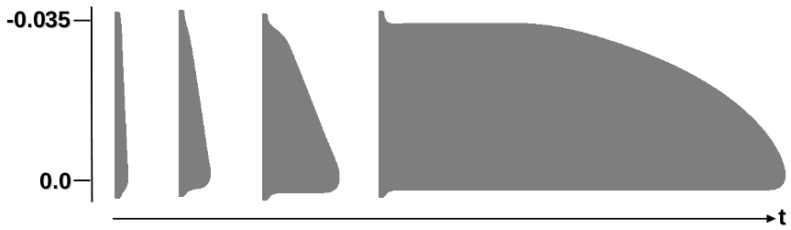

Fig. 4.4 A profile of velocities in a wavefront propagation in 2D (300×700 grid size) under the influence of the F matrix, where the abscissa represents four states of the same evolving front at different times. The forcing matrix F is introduced along the vertical axis, with values in the range $\langle 0, -0.035 \rangle$.

4.2 A computational example: path planning

4.2.1 The Path-planning approach

The afore described computational framework provides a new mechanism fully based in the dynamics of RD systems to perform geometrical computations, and thus the results include the idiosyncratic of the RD frontwaves. For instance, in [78] was introduced a path planning algorithm fully based in the RD dynamics in which the resulted path does not coincide with the geometrical shortest path as it is defined in [ref], though it has another interesting features that makes the algorithm suitable for addressing the robotic path-planning problem.

The RD algorithm is based on the following properties already discussed:

- Particular wavefront properties for reproducing different behaviours.
- Switch-of-phase mechanism for connecting different stages of the algorithm.
- Introduction of external information in the computational grid on-the-fly, through the local modification of the model nullclines for the cells of interest, as the I/O mechanism.

4.2.2 RD based Path Planning with Binary Forcing

The path planning problem is a problem of finding a shortest collision free path starting from some initial location and ending at the desired location, while a robot navigated along the path will avoid a collision with obstacles. The key point of the method introduced in [78] is a consideration of the obstacles in a form of grid map used for forcing the RD model. The concept of the RD based planning is visualized in Fig. 5.2. The planning algorithm consists of two phases: *propagation* and *contraction*. The dynamics of the *propagation* phase is ruled by the nullcline configuration depicted in Fig. 4.5a, whilst the *contraction* phase is governed by the configuration shown in Fig. 4.5b. The algorithm works as follows. First, the system is initially set in $SS-$ and a small perturbation is introduced at the robot location, which triggers a frontwave to move the system towards $SS+$, see the picture in Fig. 4.5c. When the frontwave reaches the goal area (i.e., changing the concentration values to $SS+$), which can be easily detected to constitute the termination condition for the propagation, the *contraction* phase is activated. During the contraction phase, the start and goal locations are simultaneously kept at the concentration levels of $SS-$ in opposition to the system tendency of evolving towards $SS+$.

The result of combining the changing of phase together with forcing the start and goal locations in the *contraction* phase is shown in the last series of the pictures in Fig. 4.5d. The contraction of the domain $(SS^-)_{contract}$ over itself in benefit of the more stable domain $(SS^+)_{contract}$ leads to a final single path linking the start and goal locations, which corresponds to the requested shortest path.

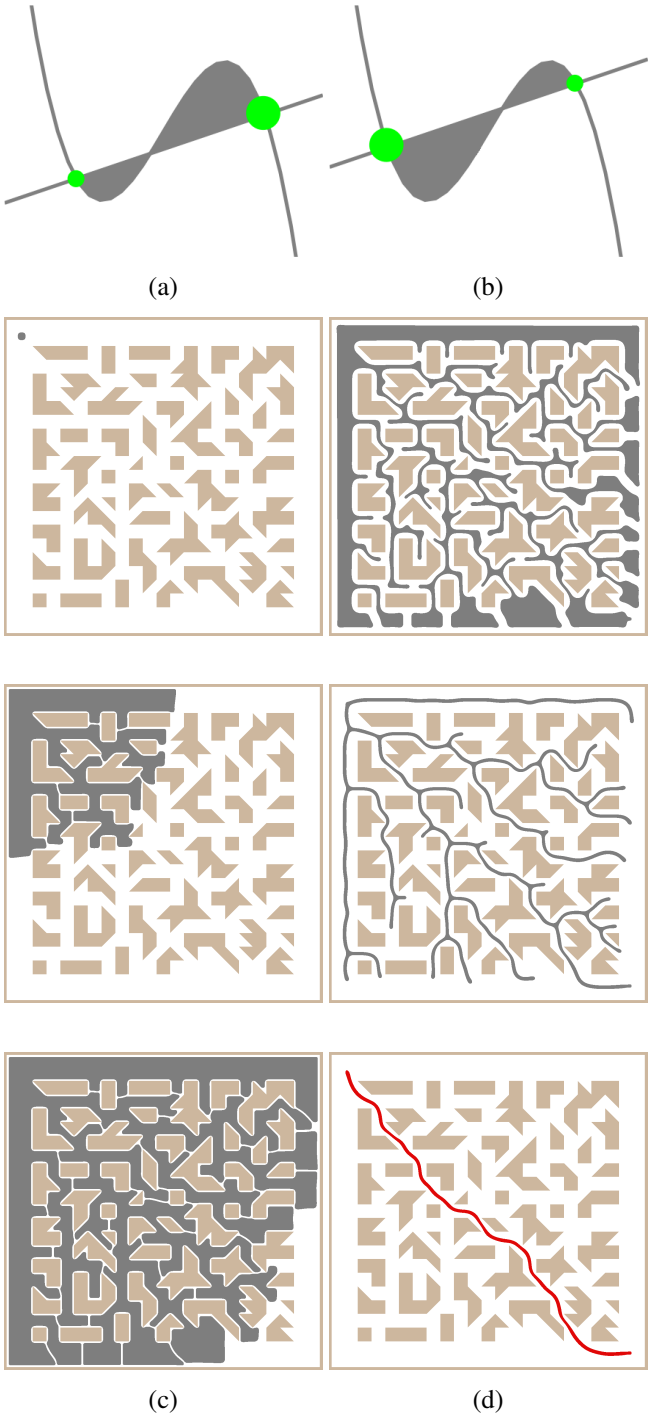

Fig. 4.5 An example of the system evolution in the path planning problem; (**a**) nullclines configuration for the expansion phase; (**b**) nullclines configuration for the contraction phase; (**c**) propagation phase; (**d**) contraction phase. The free space is in white and obstacles are in brown; values of the u state variable are in gray; the final solution is shown in red.

4.2.3 Extending the path-planning algorithm

However, the technique that has been exemplified in the path planning algorithm constitutes an approach that can be generalized in order to address different problems, rather than just calculation of the shortest path between two points. In particular, the following constitutes the key aspects in which the RD computation, for the path planning algorithm, is based:

- Natural parallelism of the model evolution.
- Natural resistance to isolated damaged cells, interpreted as noise resistance.
- The non-annihilation of frontwaves upon a collision.
- Absence of pattern formation during the frontwave evolution, therefore it spreads out like an ordinary fluid.
- Change of relative stability in a bistable configuration leading to a switch of the direction of the fronts propagation.

Each one of these properties encapsulates a different decision-logic capability. For instance, the non-annihilation provides information about frontwave collisions, where now the particular location of that collision remains as a part of the system evolution.

The aim of this work is to provide a computational framework fully based on the RD computation, and for that purpose the inclusion of additional properties will extend the scope of applicability beyond the path-planning algorithm. To that end, the next section is devoted to explore the possible behaviors that can be extracted from the general dynamics of the FHN, and suitable for being used in an algorithm that follows the technique used in the path-planning one. Such technique uses the switch-of-phase mechanism, which in turn relies in the asymmetric bistable configurations described in Section 4.1.2. According to that mechanism, there are two available configurations of the nullclines to be analyzed: depicted in Figure 4.32g, which have received the name of *expansion* and *contraction* phases. In both cases the system holds two *HSS* (namely SS_+ and SS_-) able to coexist, although the natural tendency of the system is to evolve towards the more stable one (SS_+) by means of a traveling front separating both states. All these terminology will be used in the following sections.

4.3 Stability Analysis

4.3.1 Introduction

In Figure 4.32g are depicted two nullcline configurations that have been associated in Section 4.2 with an expansion and a contraction phase respectively. Although this conforms the natural succession of stages in the path planning algorithm, the fact is that the expansion phase can also be followed by another expansion phase with a slightly different nullcline configuration. And the same applies to the contraction phase, that can be followed by another *contraction* phase, what in turn gives rise to the development of more complex algorithms. That being said, the analysis of the frontwave propagation will take place independently for both phases. Firstly, the *expansion* phase will be analyzed in order to find different behaviours that can be exploited in an algorithm design. Subsequently the *contraction* phase will undergo similar study.

4.3.2 Frontwave propagation in the expansion phase.

To analyze the properties of the frontwave propagation in the expansion phase the following experiment, exemplified in Figure 4.6 is proposed. It consists in setting up the whole system in SS_-, knowing that in the absence of any external perturbation the system will remain static indefinitely. Afterwards, a circular wavefront is initiated in the upper right corner with a concentration level very close to SS_+. The frontwave initiated at the perturbed point starts to spread through the medium moving the system to the more stable state SS_+ till a static situation is reached. The series of slits visible in the figure are introduced as binary forcing (see Section 4.1.4), and their purpose is to serve for the analysis of the wavefront behaviour when it is about to penetrate channels with different sizes.

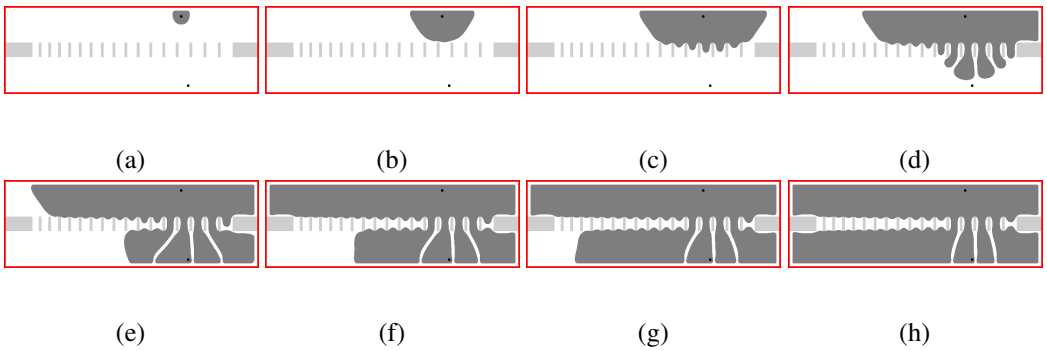

Fig. 4.6 Exemplification of the slits experiment for the expansion phase. The subfigures show different stages of the model evolution after a small perturbation is introduced in the right upper corner. Note that the slits are treated as binary forcing.

In particular, the distance between the first pair of adjacent slits in Figure 4.6 is 18 grid points. Each next pair of adjacent slits gets its distance increased by one grid point, resulting

in a series of slits with increased distance between them: $[18:1:42]$. And thus constituing a series of channels with different sizes.

4.3.3 Experimental results

The pictures are distributed in each Figure along four different columns, and the reason is a different size of the slits in each column.

Figures 4.23, 4.24, 4.25, 4.26, 4.11, 4.12 and 4.13 are composed of a grid of 4 rows and 4 columns resulting in 16 images each one. Each image is the final state of a simulation in which a wavefront has been left to evolve freely till reaches a static situation, as described in previous section. The differences in each picture are due to:

- each column has different slits width. In the first column the width of the slits is four grid points. The remaining colums have a slit width of five, six and seven grid points respectively.
- each row represents a simulation with a different α value.

Therefore, the experiment is intended to study variations in the frontwave propagation with respect to the α value, that governs the slope of the linear nullcline as it is shown in Figure 4.14.

Thus, the FHN parameters are fixed, except the variable α that varies according to the range $\alpha \subset [2:0.2:9]$, as it is shown in Table 4.1. The Slits pattern work as a set of binary

Table 4.1 FHN model values used in the *Slits* experiment.

ε	β	α	D_u	D_v
10	-0.2	[2:0.2:9]	0.1	1.5

obstacles (similarly to the path planning algorithm), that allows to study the penetration of the frontwave in openings of different widths. Thus, from the pictures in the first column, two main features can be observed in correlation with the growth of α (i.e. moving from Figure 4.23 to 4.13):

1. The background pattern that can be seen in the first row of Figure 4.23 gradually disappears as α grows, so that the frontwave clearly evolves towards a more homogeneous final state. In particular, starting with the last row in Figure 4.24, and for higher values of α, the wavefront evolution is fully homogeneous, vanishing any trace of pattern.
2. The robustness of the non-annihilation property is gradually increased with α, as for lower values (*e.g.* $\alpha \subset [2.5:0.5:4]$) some annihilations can be found upon a two fronts collision. From Figure 4.26 and thereafter the annihilation becomes a strong property.

3. In the fourth column (where the slits width is 7 grid points) the correlation between α and the ability of propagating through tunnels of different sizes (from now named as *the narrow passage problem*, as it contains further implications regarding the robotic path-planning problem) becomes clear. Revealing a mechanism for introducing information in the form of a wavefront for slits of different sizes in a simulation grid.

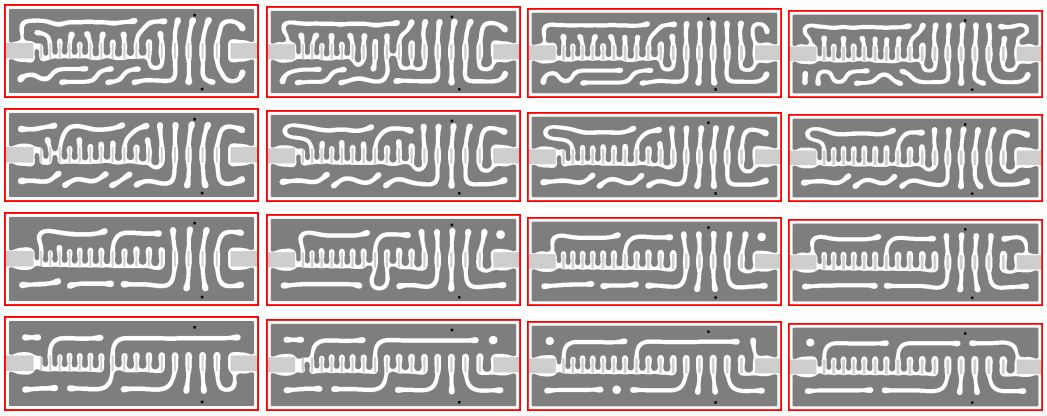

Fig. 4.7 Slits experiment

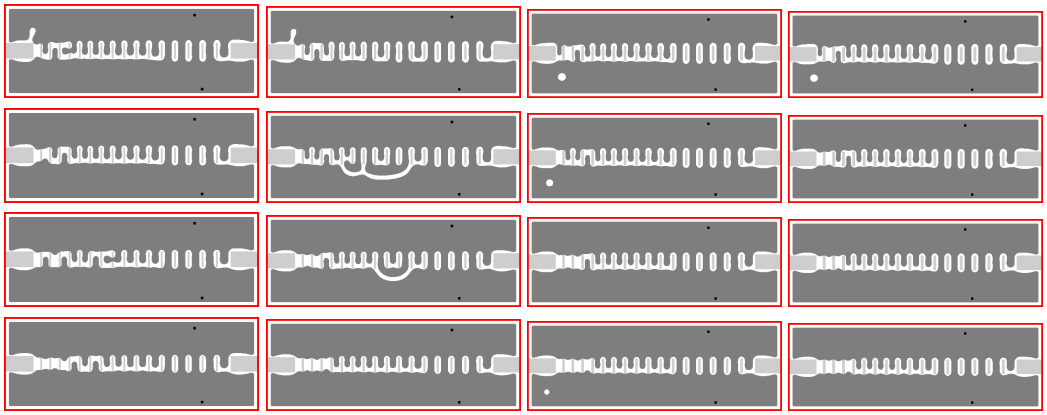

Fig. 4.8 Slits experiment

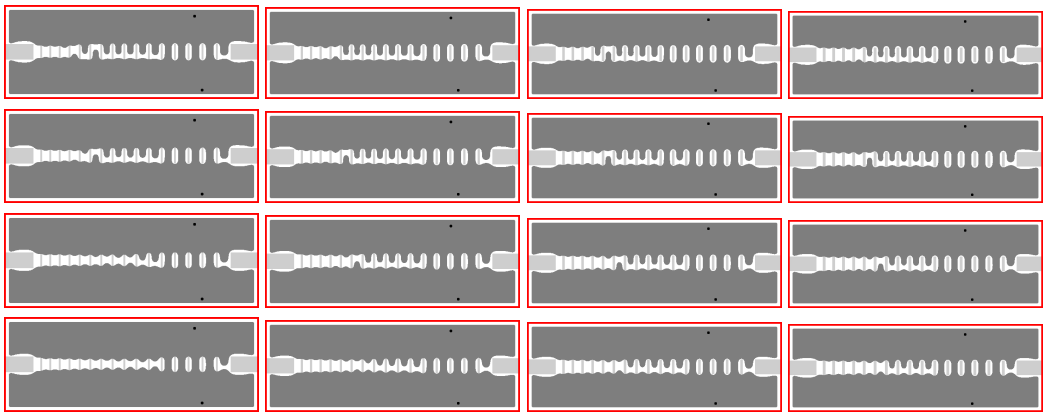

Fig. 4.9 Slits experiment

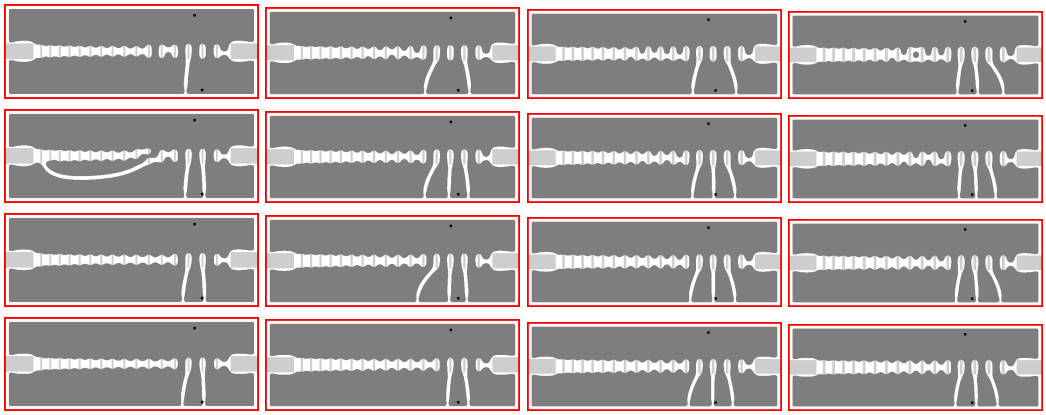

Fig. 4.10 Slits experiment

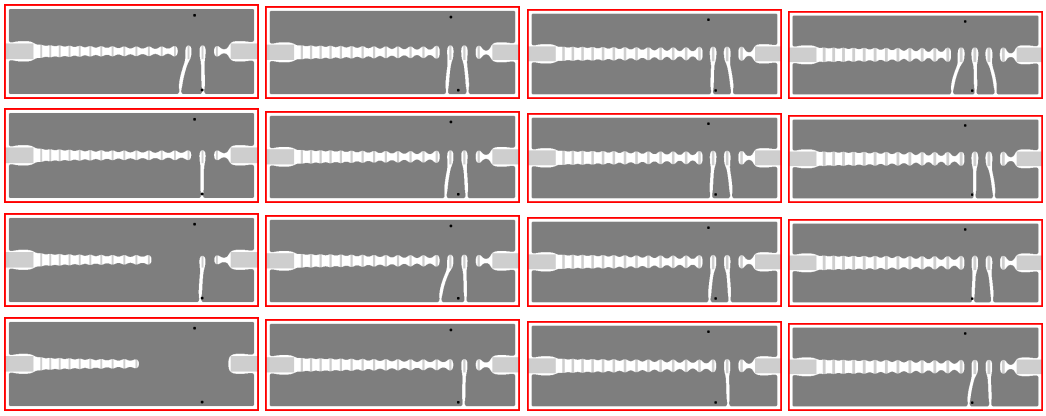

Fig. 4.11 Slits experiment

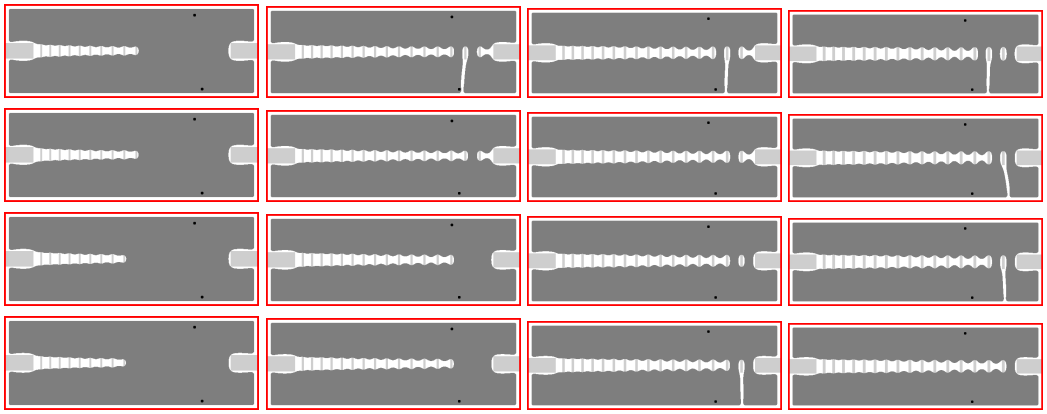

Fig. 4.12 Slits experiment

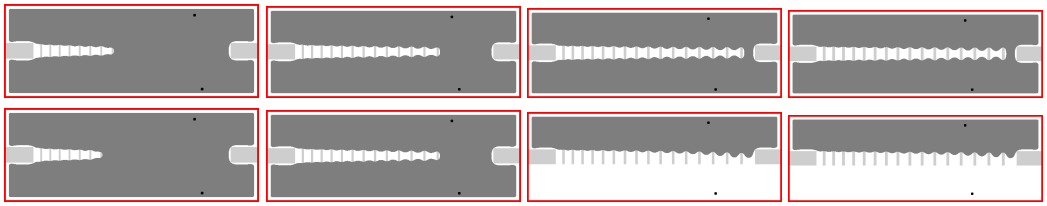

Fig. 4.13 Slits experiment

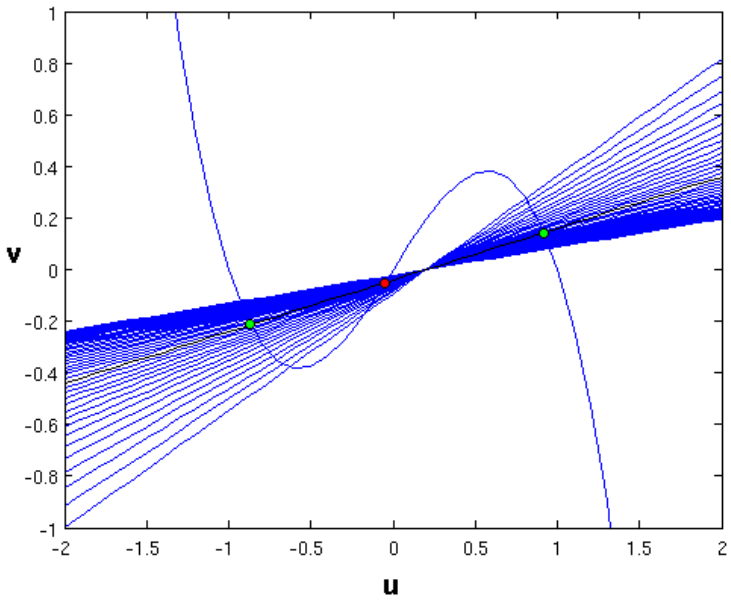

Fig. 4.14 Multiple nullclines in regard to the variation of α according with Table 4.1. The green and red disks highlight the nullcline with $\alpha = 5$ that is used in the expansion phase of the path planning algorithm.

It must be noted that the slits width used in the experiment ($[4:1:7]$) is due to the fact that lower widths are treated by the wavefront as background noise. In such case the frontwave propagation is able to overcome the slits as it is shown in the set of Figures 4.15, 4.16, 4.17, 4.18, 4.19, 4.20, **??**, where the same experiment is reproduced with slits of width $[1:1:3]$. This reveals a new feature, again according to the growth of α: the minimum slit-width that a frontwave cannot overcome in any of the studied simulations is 7 pixels, as can be observed in the third column. Therefore, it can be assumed that 7 pixels width is the maximum size from which the model switches from background noise to a binary wall: a lower limit.

Up to this point 5 empirical features associated with the frontwave propagation in our particular asymmetric bistable configuration have been found.

It should be noticed that the same experiments have been reproduced starting the wavefront in the upper left corner with similar results.

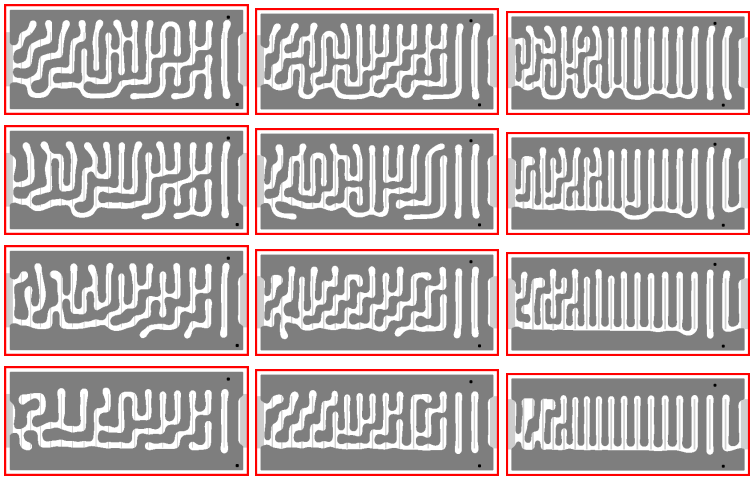

Fig. 4.15 Slits experiment

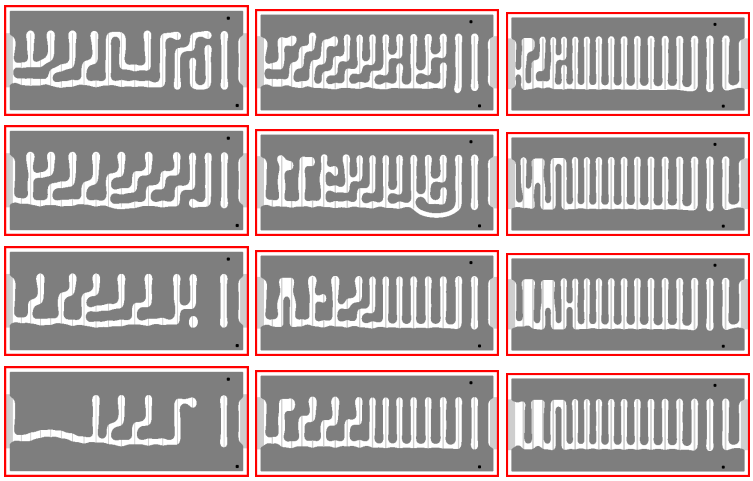

Fig. 4.16 Slits experiment

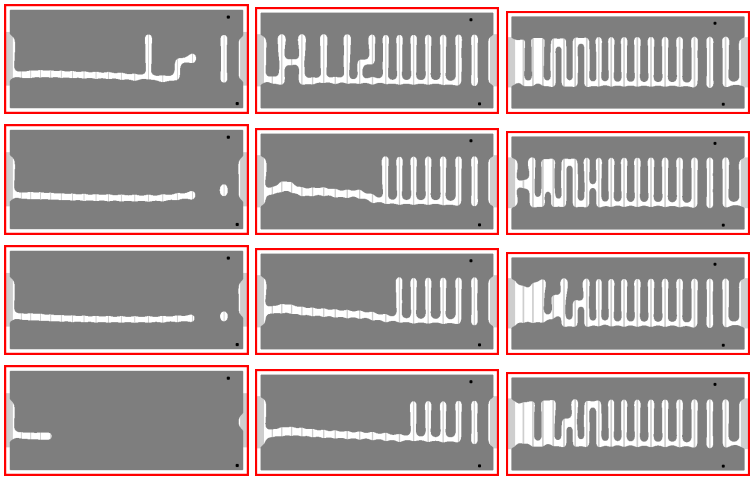

Fig. 4.17 Slits experiment

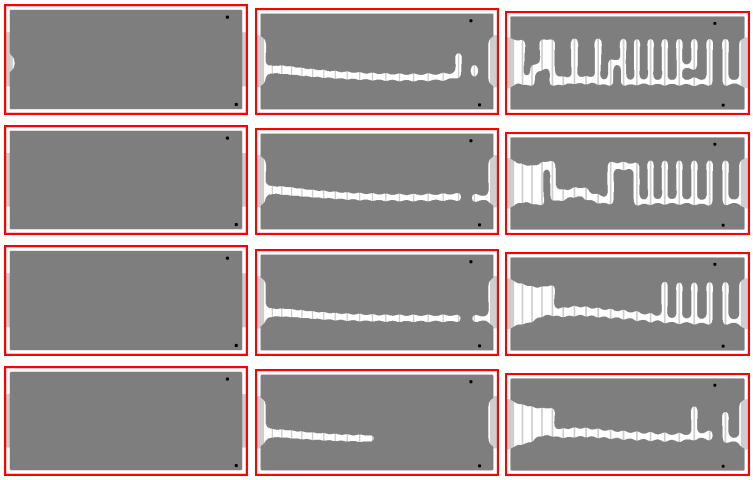

Fig. 4.18 Slits experiment

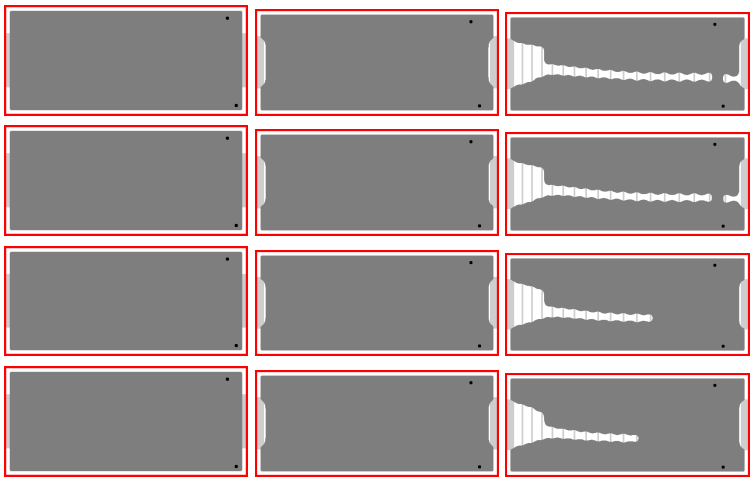

Fig. 4.19 Slits experiment

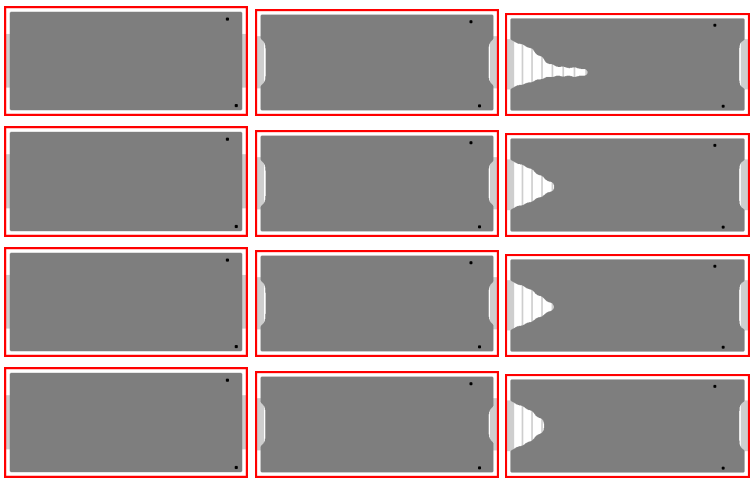

Fig. 4.20 Slits experiment

4.3.4 Frontwave propagation in the contraction phase.

For the contraction phase a slightly different experiment has to be hammer out. Taking into account the path planning algorithm, usually the second phase (contraction) is triggered after the expansion phase. For that reason a normal start for the contraction phase will be the end condition of the expansion phase. Thus, aiming to study only the contraction phase, the following experiment is proposed:

- First, lets use a flat square (*i.e.* without any obstacle) with size of $500x500$ grid points as the forcing background. Which in fact only transfers its the size to the simulation grid.
- Second, the whole system (*i.e.* u and v) is set in the concentration level of the more stable state, therefore in principle the system should remain static.
- Finally, as the forcing condition let's set a smaller square with size of $250x250$ grid points in the less stable state. This must trigger a frontwave from the more stable, with different results with regard to the model parameters. Those different results is what we are going to investigate.

An exemplification of this process is shown in the series of pictures depicted in Figure 4.21.

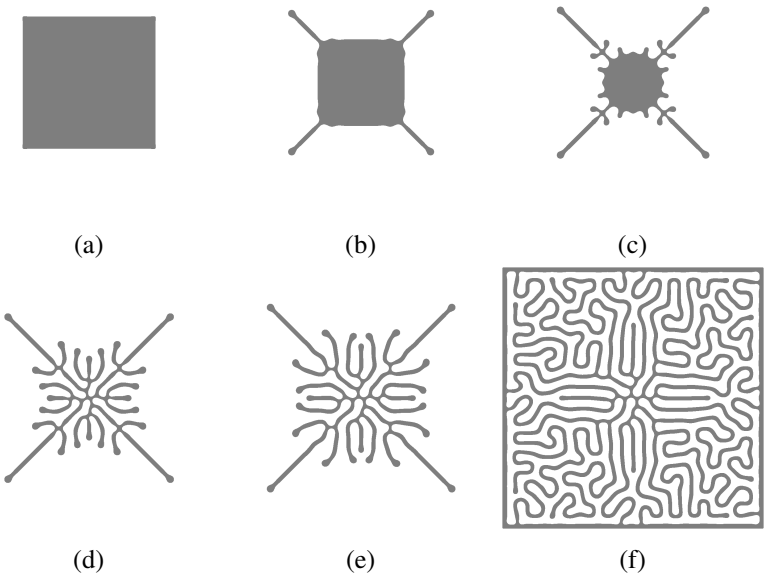

Fig. 4.21 Exemplification of the *Square* experiment for the contraction phase. The green square corresponds with the less stable state.

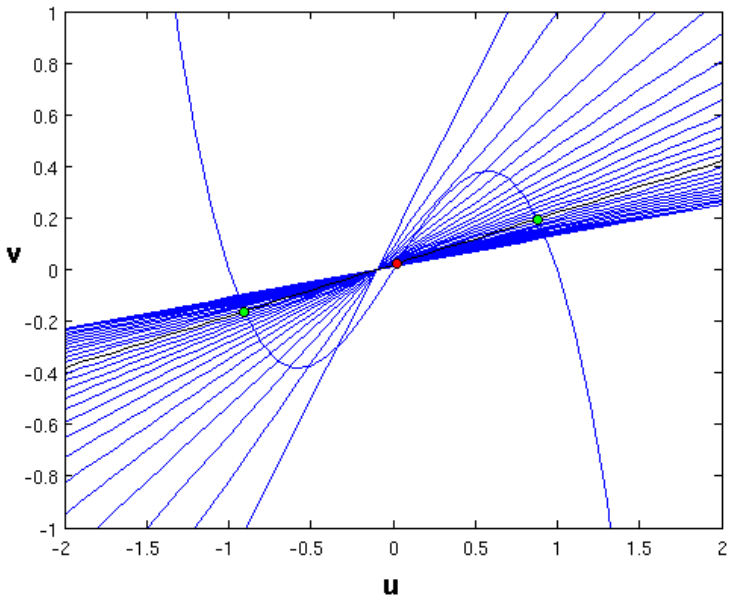

Fig. 4.22 Multiple nullclines in regard to the variation of α according with Table 4.2. The green and red disks highlight the nullcline with $\alpha = 5$ that is used in the contraction phase of the path planning algorithm.

4.3.5 Experimental results

In this experiment, the FHN parameters are fixed again except the variable α that varies according to the range $\alpha \subset [1.0 : 0.2 : 6]$, as it is shown in Table 4.1 (although all the simulations have been performed, only the more representatives are shown. For example, values bigger than 4.4 produce the same result). Also, in Figure 4.22 are depicted the corresponding nullclines for the variation of α.

Table 4.2 FHN model values used in the *Square* experiment.

ε	β	α	D_u	D_v
10	0.1	[1.0:0.2:6]	0.1	1.5

The results of the experiment are shown in Fig. **??**, from where the following features can be extracted:

- In Figure **??** the resulting pattern seems to be filling the space, but as the α gets bigger the pattern seems to be more symmetric, in the sense of a peano-like curve. Indeed, an extra set of simulations for a smaller integration grid confirm such behaviour. These resuls are shown in Figure 4.27 where the initial condition was a small circle in the center of the grid set in SS_{-}, instead a square.

- In Figures **??** the resulting pattern configures a partition of the plane that resembles a Voronoi Diagram.
- In Figure **??**, **??** and **??** the resulting patterns are circles that highlights the existance of an original wavefront. This feature is interesting since it retains the information about the existance of wavefronts during the expansion phase.
- In Figure **??** the original patch of the sytem set in SS_{-} completely dissapears in favor of SS_{+}. This is indeed the configuration used in the shortest path algorithm.

Summing up, at least four interesting behaviours for the contraction phase have been identified. These behaviours show the evolution of frontwaves in a way that they seem to bear some decision-logic rooted in their dynamics. This is, perhaps the proper way in which Reaction-Diffusion systems can be used for general purpose computation.

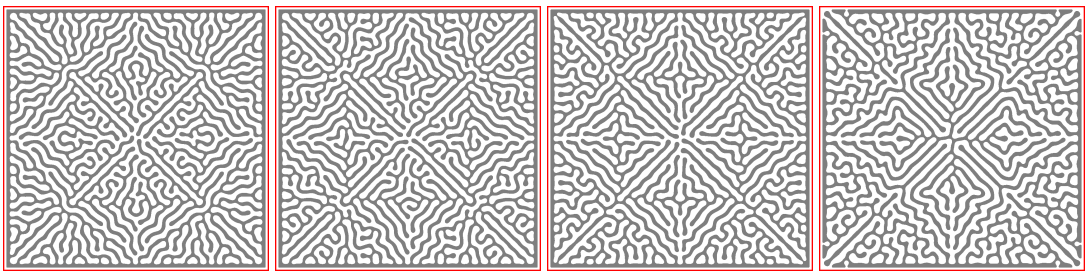

Fig. 4.23 Slits experiment

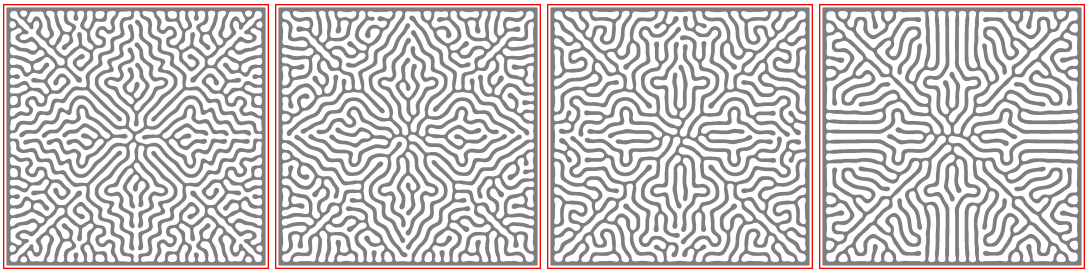

Fig. 4.24 Slits experiment

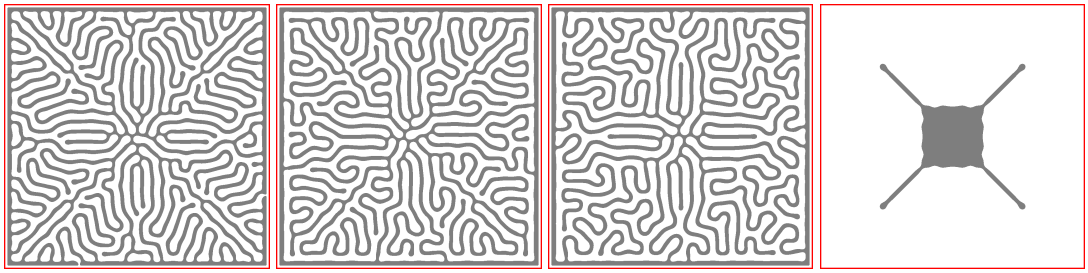

Fig. 4.25 Slits experiment

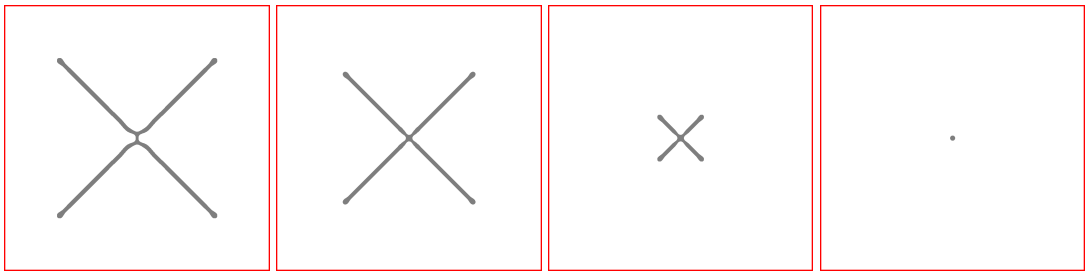

Fig. 4.26 Slits experiment

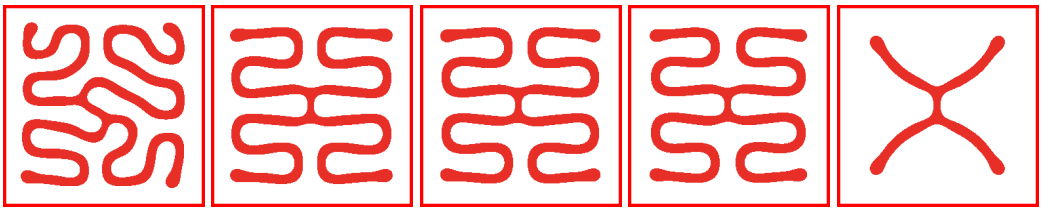

(a) (b) (c) (d) (e)

Fig. 4.27 Results for the Square experiment for the α values $[3.2, 3.4, 3.5, 3.6, 3.8]$ using a smaller matrix of size $300x300$ grid points.

4.3.6 Stability analysis

The basic stability analysis follows the steps described in Section 3.3, thus the linearization around the stable fixed points leads to the stability conditions, and later on the presence of diffusion yield to instability of the fixed points.

The first part is the stability of the fixed points. Thus, figures 4.28 and 4.30 collect the stability conditions for both phases expansion and contraction, respectively. In those figures are depicted the conditions 3.19 and 3.20 for the three fixed points of the particular nullcline configuration (*i.e.* for each α). Therefore the variation $[2 : 0.2 : 9]$ for the expansion phase and $[1 : 0.2 : 6]$ for the contraction phase are depicted. It can be confirmed with regard to the figures that each nullcline configuration posses two stable points and one unstable point.

The Turing instability conditions are designed for the stable fixed points, that in the presence of diffusion must become unstable. Therefore, conditions 3.46 have been examined

for both stable states for each nullcline configuration (*i.e.* for each α value). And again for both phases, expansion and contraction. The first fact that can observed is that all wavelengths result negative, which physically has only one possible interpretation. The associated wavelength is infinite with regard to the size of system, or in other words there is no characteristic wavelength associated with the system. And hence, both stable states are actually stable in the presence of perturbations.

Although this result is actually in agreement with the fact that frontwaves evolve without developing any actual pattern during the expansion and contraction phases of the path planning algorithm, it is not with other values of α, specially the lower ones. Nevertheless, Turing is not the only possible explanation for patter formation in bistable systems, though it is in general the most common and well study bifurcation that leads to pattern formation. There is evindence in the literature in both experimental [science] and theoretical [] side of highly irregular pattern formation in bistable systems due to frontwave interacionts. Those patterns are initated by a finite amplitude perturbation (like in the present case) rather than through spontaneous symmetry breaking.

Furthermore, in view of this result the Slits experiment developed in 4.3.2, where it was shown the ability of the frontwaves for penetrating openings with different sizes now it has to be explained not in relation with an intrinsic wavelength, but likely with regard to the frontwave curvature properties. This is an open question that should be studied in detail, but at least so far it can be asserted that conventional Turing is not the mechanism responsible of the frontwave properties used in this work.

Expansion phase

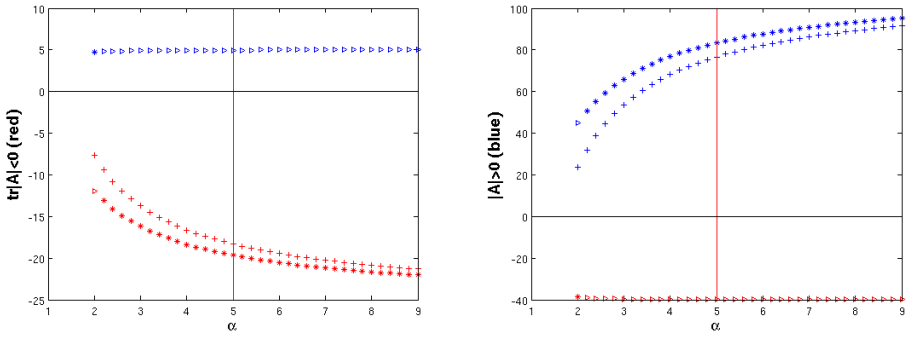

(a) (b)

Fig. 4.28 Stability conditions for the expansion phase.

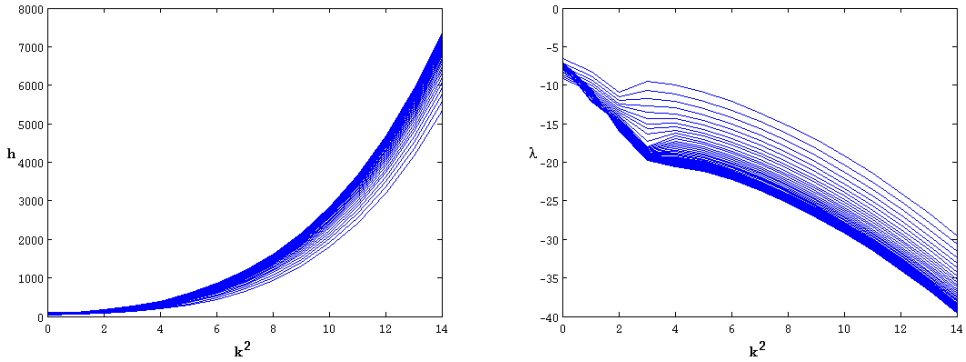

(a) (b)

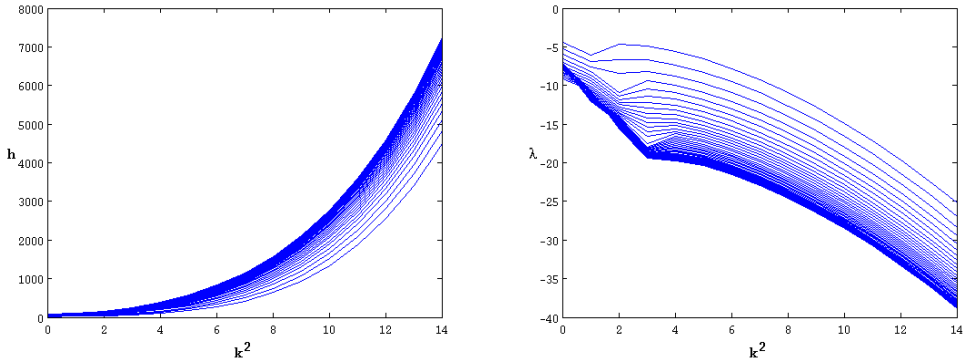

(c) (d)

Fig. 4.29 Dispersion curves for the contraction phase corresponding with the Turing analysis of both stable states: SS+ and SS-

Contraction phase

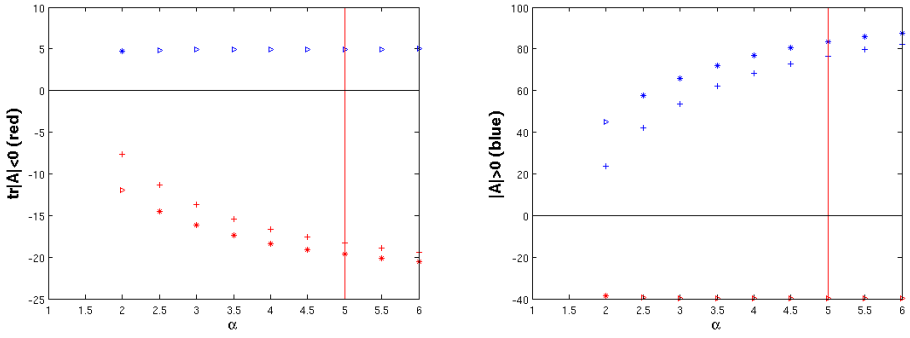

(a) (b)

Fig. 4.30 Stability conditions for the contraction phase.

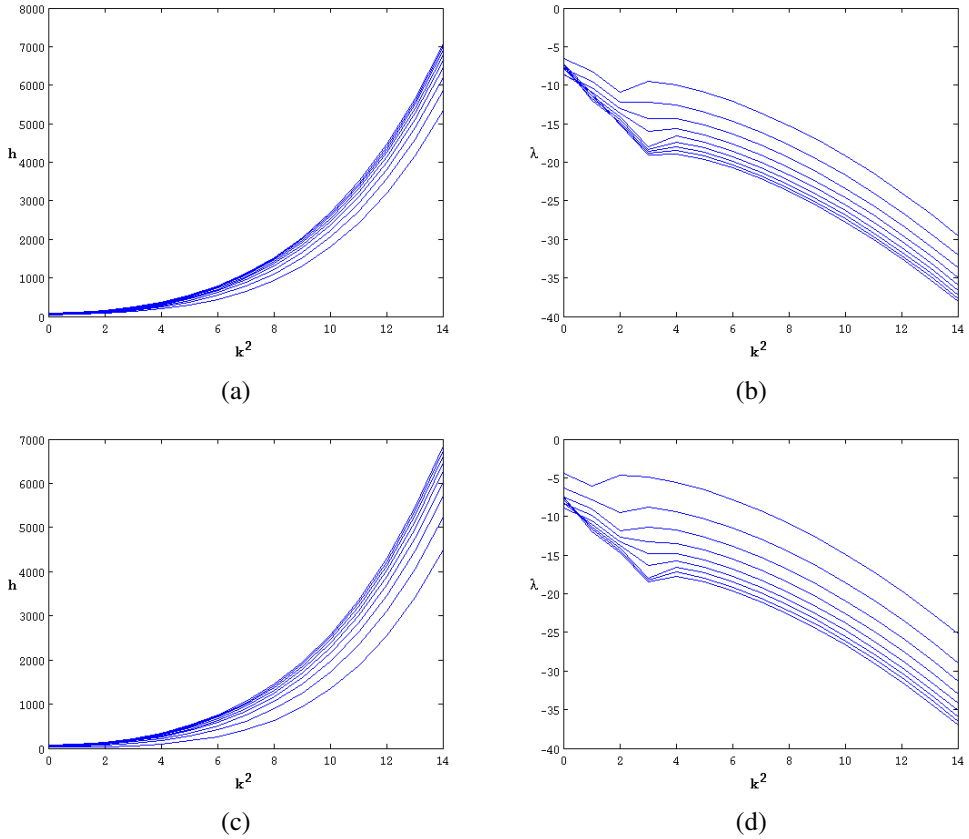

Fig. 4.31 Dispersion curves for the contraction phase corresponding with the Turing analysis of both unstable states: SS+ and SS-

4.4 Comments on Stability of the RD system and Reduction of Computational Requirements

Computational autowaves generated from the implementation of reaction-diffusion models naturally lack a good performance. The reason is the demanding computational cost of the Laplacian numerical integration, which relies on the addressing memory with an irregular pattern. Nevertheless, the computation can be significantly speed up based on observation of the system stability in the sense of Lyapunov. The wavefronts whose propagation lead to the shift from one stable state to the other define the only regions in the environment that are actually evolving. In the computational grid, this means that as the evolution of the grid-cells reaches the new stable state, these nodes remain in this state unchanged. Hence, this observation can be utilized to decrease the computational burden of the spatial integration of the model by performing computations only for these grid cells. Notice that although this approach can restrict propagation of the frontwaves in the boundaries of evolving areas, the values of u and v tend to a stable level, and therefore, the restrictions only limit the

velocity of the propagation. Moreover, the velocity of the underlying physical model is also limited and constant, and therefore, using the knowledge of the propagation behavior one can set suitable parameters without affecting the propagation. These parameters have been experimentally set for the particular developed approach.

The proposed routine can be exemplified as follows: after several computational steps, cells are examined if their value of the concentration level u has changed after the selected period T_{active}, *i.e.*, testing the value $u_{activation} = |u(k)$ - $u(k+T_{active})|$ of the computational steps k and $k+T_{active}$. Then, the cells for which the difference $u_{activation}$ is above a certain limit (e.g., $> 10^{-3}$) are denoted as active for the next batch of the computational steps. Besides, a small neighborhood of each such an active cell is also marked as an active to further support a propagation of the frontwaves. This technique is exemplified in Figure 4.32, where the active nodes in the integration grid have been highlighted as darker regions. The herein used discretization of the FHN model is a simple finite difference method on a Cartesian grid: a simple forward in time centered in space (FTCS) scheme that facilitates the manipulation of the integration loop for including the described optimization.

A basic comparison for the two environments *potholes* and *jh* is shown in Table 4.3. Using a grid resolution of 800×800 points as a baseline for the *potholes* environment and 840×960 for the *jh* environment, four additional resolutions have been computed for the propagation phase of the Voronoi problem. The results show that the proposed optimization technique scale well with the increasing grid resolution, allowing an intensive study of the possible autowave-based applications, particularly those implementations whose simulated environments are represented by large-size matrices, as for example collaborative robot exploration. Moreover, since this optimization is hardware-agnostic it can be ported to specialized platforms. Furthermore, other techniques have also been considered including the use of SSE instructions and sparse matrices. They proved to be inefficient, though.

Table 4.3 Computational time (in minutes) spend in the *expansion* phase of the Voronoi computation for the environments *potholes* and *jh*. For both variants of the RD-based algorithm: the original named *naive* and the optimized version according to Section 4.4 named *optimized*. The size of the baseline is 800×800 grid points for the *potholes*, and 840×960 grid points for the *jh*. The computational times have collected using a workstation with the Intel iCore7 3770 processor, Debian jessie (64-bit), 16 GB RAM, and C++ implementation compiled by the GCC 4.9.2 with the O3 enabled.

		Resolution factor				
		1	*1.2*	*1.5*	*1.7*	*2*
potholes	*naive*	8.49	15.3	27.4	44.4	69.3
	optimized	1.3	2.1	2.5	3.3	5.2
jh	*naive*	12.5	20.7	44.5	65.8	103.4
	optimized	1.4	2.2	4.1	5.2	7.2

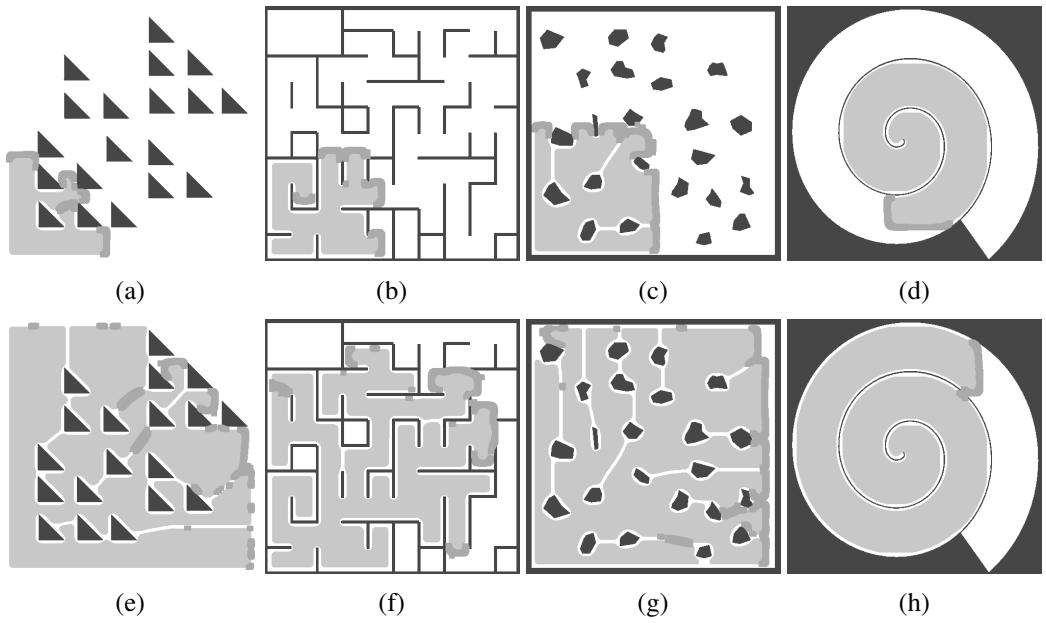

Fig. 4.32 Examples of frontwaves evolution for four different environments, *diamonds, labyrinth, potholes* and *spiral*. Darker parts of the frontwaves are the current active nodes, *i.e.* the only regions of the frontwave which are actually evolving, and hence the only nodes that undergo spatial integration.

Chapter 5

RD based algorithms and its applications to Mobile robotics

Abstract

This chapter illustrates all the developments achieved in this thesis. The properties exhibited by frontwaves in their propagation in bistable asymmetric systems, analyzed in previous chapters are herein applied to the development of computational algorithms. These algorithms have been focused on mobile robotics, and compared with state-of-the-art algorithms in their respective fields. In particular, starting with a single robot exploration task, a cooperative multi-robot exploration algorithm is introduced. Also a computation of the Voronoi diagram by means of the RD core, is presented and also compared with a standard algorithm. The RD based computation not only proves its capability to perform ordinary computations, but also provides some new qualities over the standard approaches. In view of this, the RD based computation is not a distant prospect anymore.

5.1 Introduction

The mobile robot exploration task refers to an algorithm to create a map of an unknown environment, i.e., a problem, where a mobile robot is requested to autonomously cover all reachable regions by its sensory system. Beyond the basic feature of exploring an unknown area, a desired quality of the exploration algorithms relies upon the generation of a minimal-cost path by the exploring unit. Such a property can be specified by a distribution of the possible observation points, resulting in a set of points that minimizes the path length through the environment to cover all the area. Thus, measuring the performance of the exploration task is based on the strategy for determining the next goal. Therefore, the characterization of the exploration strategy is based on the optimizations used for selection of such goals.

The basic exploration approach was introduced by Yamauchi in a seminal paper [80], along with the concept of frontier based exploration strategy. In Yamauchi's approach, the robot is navigated towards the closest location (the so-called frontier) in the limit between the known/unknown area. This approach provides a feasible solution of the exploration task and it forms a fundamental approach for more advanced exploration strategies [50], where additional improvements turn around a way how to select candidates for the next robot goal and how to evaluate the cost of navigation towards such goals. Thus, not only the distance cost is used, but also additional aspects can be considered like localization issues [70] or expected utility of the next goal [8], e.g., a combination of the distance cost with an expected information gain [22].

In this work, a new robot exploration algorithm fully based on RD processes is introduced and used for presenting a set of operations over the RD core. Although it is similar in many aspects with a regular frontier-grid-based approach, it provides a new way how the goal candidates can be generated and the next goal is determined. The approach is based on our previous work on computational autowaves applied in the path planning problem [78]. Considering the path planning method in the exploration task provides a new way how to deal with multi-criteria cost function and how a utility of the goals can be considered.

5.2 Exploration Strategy Based on Autowaves

Although the proposed exploration strategy exhibits similar behaviour as regular frontier-based approaches, it is based on different underlying principles. That is why we split the description into a formal characterization of the algorithm, features of the autowaves applied in the exploration task, and proposed concept of utility consideration in the selection of the next goal for a mobile robot. The proposed approach follows standard exploration procedure in which the main loop can be defined by the following steps:

1. Integrate new sensor measurements into a map.

2. Determine goal candidates.

3. Select the next goal.

4. Navigate the robot towards the goal.

For the first step, we consider a common approach based on the occupancy grid [16]. However, the next three steps are based on principles of autowaves. In particular, instead of explicit searching for Yamauchi's frontiers, we use propagation of the frontwave to determine the possible goal candidates. The candidates correspond to frontiers; however, we can take advantages of the RD model dynamics and consider the determination of the candidates in a completely new way, see Section 5.2.1. The next goal is then selected using the same principles of propagation the frontwave. Finally, we employ the autowaves-based path planning [78] to determine the path to the goal along which the robot is then navigated. A detailed description of these three steps is presented in Section 5.2.1. Moreover, the new concept of dealing with utility of the goal candidates is proposed in Section 5.2.2.

Prior detailed description of the proposed utilization of the frontwave propagation principles, it is necessary to consider the following assumptions to expose the particularities of the exploring units and working environment in the proposed autowaves-based exploration approach:

- The map being explored consists of a series of objects and boundaries, all treated as binary information.

- Objects and boundaries are both represented by their edges.

- Each object or boundary within the sensor range is interpreted as an object–edge. Therefore, the exploring unit shapes the environment without any awareness about the correspondence between objects or boundaries.

- Since everything is treated as binary information, the discovered area is simply split into reachable and unreachable locations.

5.2.1 Determination of the Next Goal

The goal candidates are determined as a border of the currently known space of the environment. Here, the current map of the environment is used as a medium for exhibiting the RD model dynamics. The principle of the process is visualized in Fig. 5.1. A frontwave (triggered from an excitable nullcline configuration) starts at the robot position and evolves as an ordinary fluid, covering all the available space (freespace in the integration grid) while adopting the shape of the space, and therefore, providing the boundary of the reachable area

after reaching a static situation. Then, superimposing the obstacles (unreachable positions) results in the reachable border to the robot, as depicted in the red profile shown in Fig. 5.1[1].

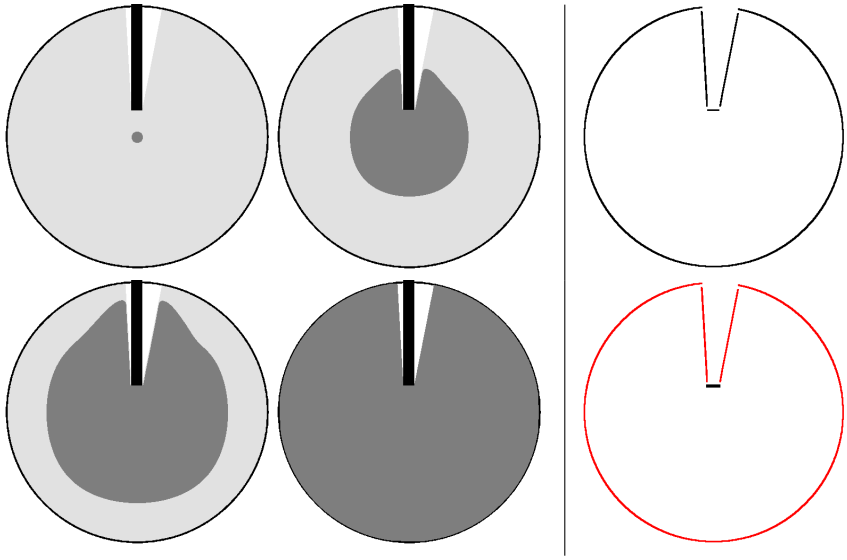

Fig. 5.1 Calculation of the frontier using autowaves. Four left pictures represent a wavefront evolution. In particular, the light gray circular area corresponds to an omnidirectional sensor data (laser scanner), whilst the black rectangle in the top is an obstacle. The gray wavefront evolves from the robot position, covering all the discovered area till it reaches a static situation. The rightmost pictures represent the complete profile of the wavefront (top), and the final border reachable to the robot depicted in red (bottom).

The determined border corresponds to the frontier; however, the main difference is that we consider only reachable and unreachable parts of the space and all the logic of getting the contour is provided by the underlying dynamics of the RD system.

Once the border is determined, the next goal can be selected. Even though any path planning algorithm can be eventually used, we rather consider autowaves-based approach [78]. The border does not distinguish the unknown cells from the obstacles. However, the frontwave propagation within the determined area given by the border takes advantage of the superimposing obstacles because autowaves preserved a distance (according to the wavelength of the frontwave) from the obstacles, see [78] for a detailed discussion. An example of determining the next robot goal together with the determination of the path using the propagation and contraction phases is depicted in Fig. 5.2. Another example of the goal determination is shown in Fig. 5.6.

It is worth to mention another interesting feature of the autowaves-based path planning that is an ability to deal with noisy data, e.g., due to an imperfect sensor measurements. The autowaves dynamics is developed over an extension of points (characterized by the

[1] Notice, the rectangular obstacle is drawn only for the visualization purpose as only its bottom edge is detected by the sensor system.

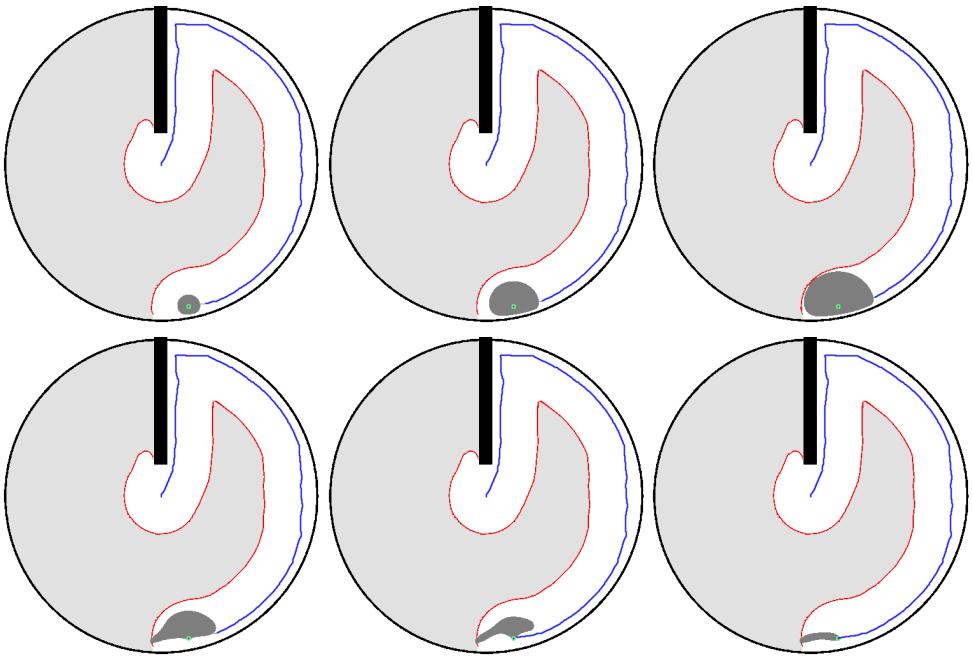

Fig. 5.2 An example of determination of the next goal and the particular path towards the goal in a circular shaped environment. The already explored area is in white while the gray denotes not yet explored areas; the black color is the shape of the environment and the obstacles are superimposed only for a visualization purpose as they are not known during the exploration.

associated wavelength) rather than isolated pixels. This feature provides the autowaves not just an ability to overcome the isolated points, but also to correctly interpret noisy data within the exploration context, i.e., to consider several isolated (but nearby points) as a part of a larger structure. In Fig. 5.3 is shown an example of this property.

5.2.2 Utility Function

The aforementioned algorithm provides a basic approach for the exploration task and can be considered as a similar to the greedy frontier-based approach. The performance of the frontier-based exploration can be improved using the so-called utility function, which aims to consider an expected benefit of the frontiers to select the most suitable frontier in order to fulfill the mission objective, e.g., to collect the map of the whole environment as quickly as possible. Such approaches usually combine the distance cost with expectations about new areas, e.g., based on entropy [8]. Contrary to these approaches, we proposed a different concept based on features of the frontwave propagation.

The dynamics of the underlying RD model allows to add an extra term representing additional information that is considered in the model evolution. This is numerically represented as a matrix term (point dependent) that can selectively introduce delays in the

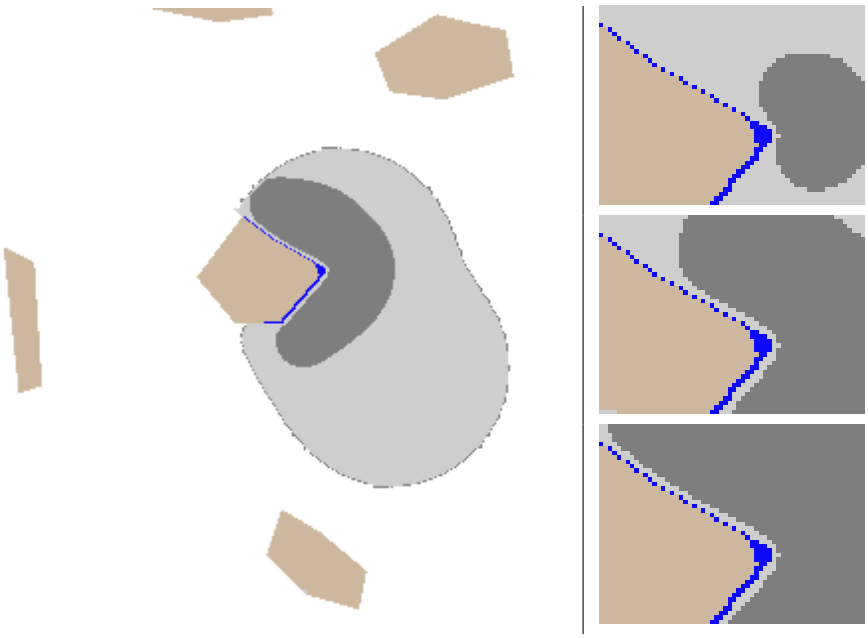

Fig. 5.3 An example how autowaves deal with noisy data. The rightmost pictures show a detailed exposition of the frontwave evolution in the vicinity of the obstacle. The final state is shown in the leftmost picture. The gray light area represents the robot sensors data as reachable locations, the brown area are obstacles, which are not part of the integration grid, but are depicted for the sake of clarity. The surrounding polygon appears as a series of blue isolated points corresponding to the mapped obstacle sides (as unreachable positions).

wavefront propagation, and therefore, it can prioritize some regions over others. This means that gradient-like information, rather than a binary map, can be used to represent the working environmenthis proposed concept has been verified in an exploration of a simple circular environment. In this deployment, the robot is equipped with an omnidirectional laser scanner with the sensing radius 5 m.

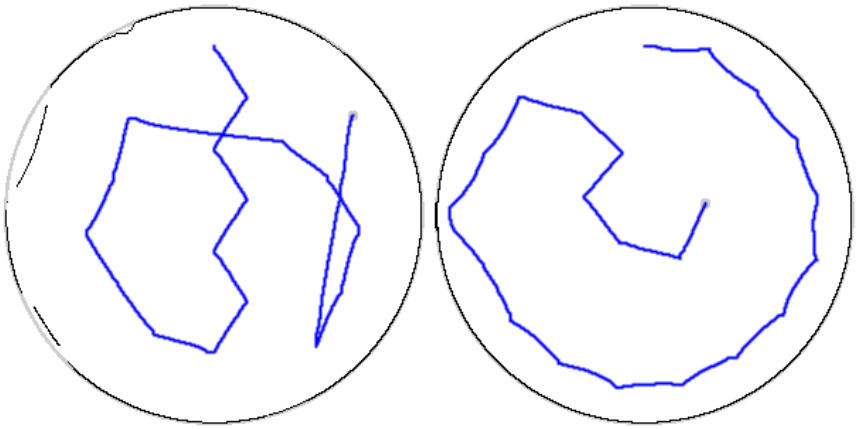

Fig. 5.4 Visualization of the exploration behaviour for two different settings of the RD based computational model using extra background for modifying velocity of the frontwave propagation. The blue curve represented the traveled path of the robot to explore the whole environment.

Two basic implementations of the utility function are visualized in Fig. 5.4, which leads to two different behaviors. In the left case, the function is designed to prefer unexplored areas, this is achieved by decreasing the extra background along regions of the frontier that do not represent obstacles, therefore these regions becomes candidates for the next goal. As a consequence, the robot prefers to explore the open-space first. Conversely, in the right sub-figure, the background is especially decreased along detected obstacles, which increases the frontwave velocity along these regions. Therefore, once the robot discovers an obstacle, the next goal is naturally selected close to the already known obstacles, which provides a wall-following behaviour.

5.2.3 Performance of the RD based Exploration and Standard Approaches

The proposed principles of the selection of the next robot goal and planning a path to the goal by means of propagation of the frontwave in the known reachable environment have been integrated into the exploration framework [18]. The integration provides an initial overview of the performance of RD based exploration strategy in comparison to standard approaches. The considered performance indicator is the path length of the robot to explore the whole environment.

The proposed RD based exploration strategy does not explicitly consider information gain, and therefore, it can be considered as a pure distance cost strategy. Therefore, we select the greedy exploration [80] and the TSP based approach [34] with the TSP distance cost for the presented comparison. However, a direct comparison of the approaches is not an easy task. It is because the proposed approach is based on a different computational model, where some properties directly accessible in regular frontier-based approaches are not straightforwardly and easily tunable. For example, a filtration of small frontier groups, which can significantly improve performance [28], and especially the planning horizon [18], i.e., a period of new goal determination. Thus, a direct comparison of the results would not be fair, and therefore, we include two variants of the greedy and TSP exploration strategies.

In the first variant, denoted by a subscript 1 (i.e., $greedy_1$ and TSP_1), the next goal is determined after the robot reaches its current goal (like in the RD based exploration), while in the second variant ($greedy_2$ and TSP_1), the next goal is determined after performing 7 navigational primitives, as it is suggested in [18]. In all these approaches, selected representative of the frontiers are considered as goal candidates using K-means algorithm, which decreases the computational burden of the TSP solution and also improves the exploration performance. A further description of this selection can be found in [34].

The RD based and greedy strategies are deterministic while the TSP based strategy is a stochastic method (due to the used approximate solution of the TSP). Despite of that, we consider a single trial for each problem in this feasibility study and thus the presented results have only an indicative importance.

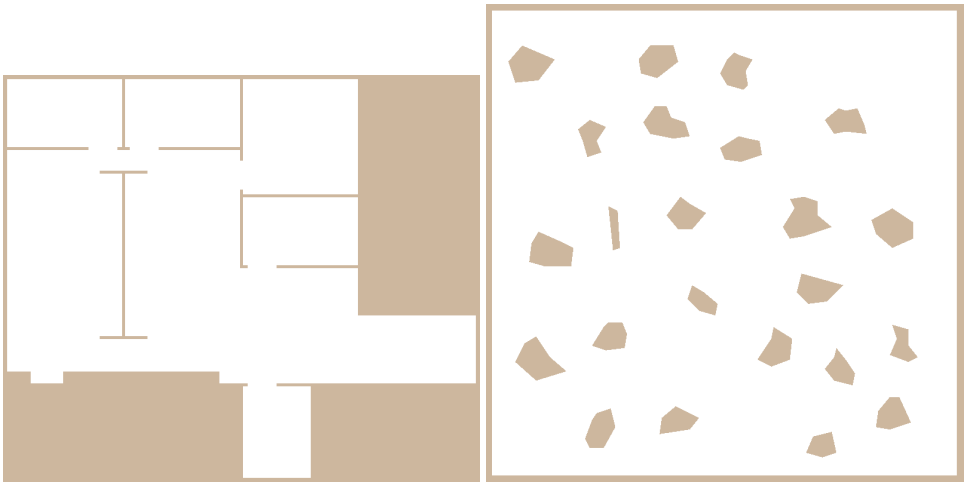

Fig. 5.5 Environments considered in the feasibility evaluation of the RD based exploration.

Two environments denoted as *autolab* and *potholes* are considered for the evaluation. The *autolab* environment represents an office like environment with dimensions 35 $\times$ 30 meters, and the *potholes* environment is a large open space (40$\times$ 40 meters) with several obstacles, see Fig. 5.5

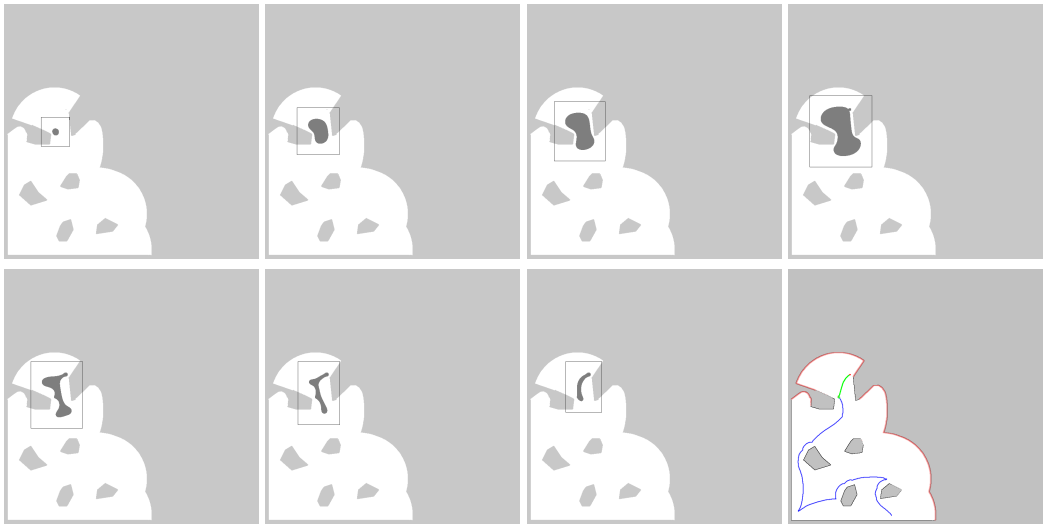

Fig. 5.6 Propagation of the frontwave towards goal candidates, selection of the next goal (**a**-**d**), an evolution of the RD model for the determination of the path to the selected goal (**e**-**g**) and the final found path is shown in green in the bottom rightmost picture; (**h**) the current travelled path is in blue.

An example of the frontwave propagation during the selection of the next robot goal and the consecutive contraction phase of the used RD based path planning [78] is shown in Fig. 5.6.

Indicative results are presented in Table 5.1, where the columns represent the length of the total traveled path (in meters) for the particular sensor range ρ. Notice, how a faster replanning period improves the exploration performance. On the other hand, for replanning after reaching the current goal, the RD based exploration provides competitive results to other approaches. Selected exploration paths for particular exploration strategies are depicted in Fig. 5.7.

Table 5.1 Length of the Exploration Path

Algorithm	*autolab*			*potholes*		
	ρ=3 m	ρ=5 m	ρ=7 m	ρ=3 m	ρ=5 m	ρ=7 m
RD based	256.1	196.4	141.1	570.7	375.7	271.1
$Greedy_1$	262.5	232.5	182.9	545.8	398.8	320.4
TSP_1	263.0	222.8	174.9	543.9	342.5	283.0
$Greedy_2$	223.6	183.7	118.2	552.6	349.0	276.8
TSP_2	219.1	159.4	107.8	466.5	345.6	243.1

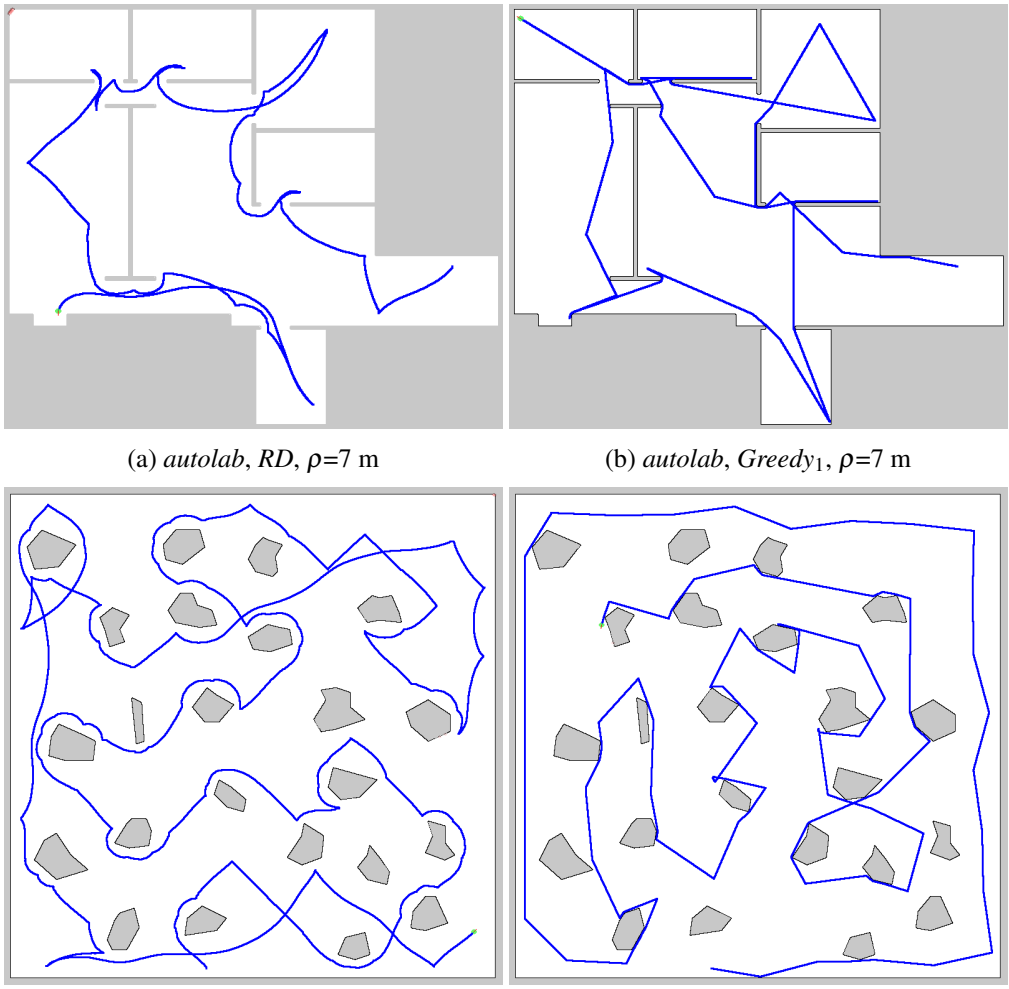

(a) *autolab*, *RD*, ρ=7 m (b) *autolab*, $Greedy_1$, ρ=7 m

(c) *potholes*, *RD*, ρ=5 m (d) *potholes*, TSP_1, ρ=5 m

Fig. 5.7 Final exploration paths, the edges of the detected obstacles are in black while the unexplored areas ("inside the obstacles") are in gray.

5.2.4 An Extension of the Proposed RD based Computational Model for Multi-Robot Exploration

The proposed computational model can be easily extended for exploration by a team of mobile robots. The extension can be considered as a semi-centralized approach, where the robots are considered independently while they shared a common map of the environment being explored. The proposed demonstration of the multi-robot exploration works as follows:

- Prior the determination of the next robot goal, each robot makes a local copy of the common map.
- The position of the other robots is introduced to the local map as a solid objects; thus, robot considers the remaining robots as simple obstacles.

- A single step of the exploration algorithm is performed and new information is gathered from the environment.
- The local maps are merged into the common map (e.g., using the notion of occupancy grid and Bayes' rule like in [69]) and the process of determination of the robot goals is repeated.

The termination condition of the exploration is the identical as in the single exploration algorithm, i.e., the exploration is terminated if all goal candidates (frontiers) have been covered. Examples of selected steps of the multi-robot exploration are visualized in Fig. 5.8.

5.2.5 Discussion

The presented results indicate the proposed RD computational model based on the underlying dynamics of the highly non-linear system can be employed in the mobile robot exploration problem and it also seems the RD based exploration provides competitive exploration paths to the standard approaches.

Regarding the computational requirements of the proposed computational model based on the evolution of the RD model, it should be noted that it can take an advantage of the implicit parallel propagation; hence, it can be computed in parallel, and therefore, pruning all the possible solutions to the most adequate ones in parallel as well. This makes us optimistic about future implementation using massive parallel computation and a practical deployment of the method in real exploration problems.

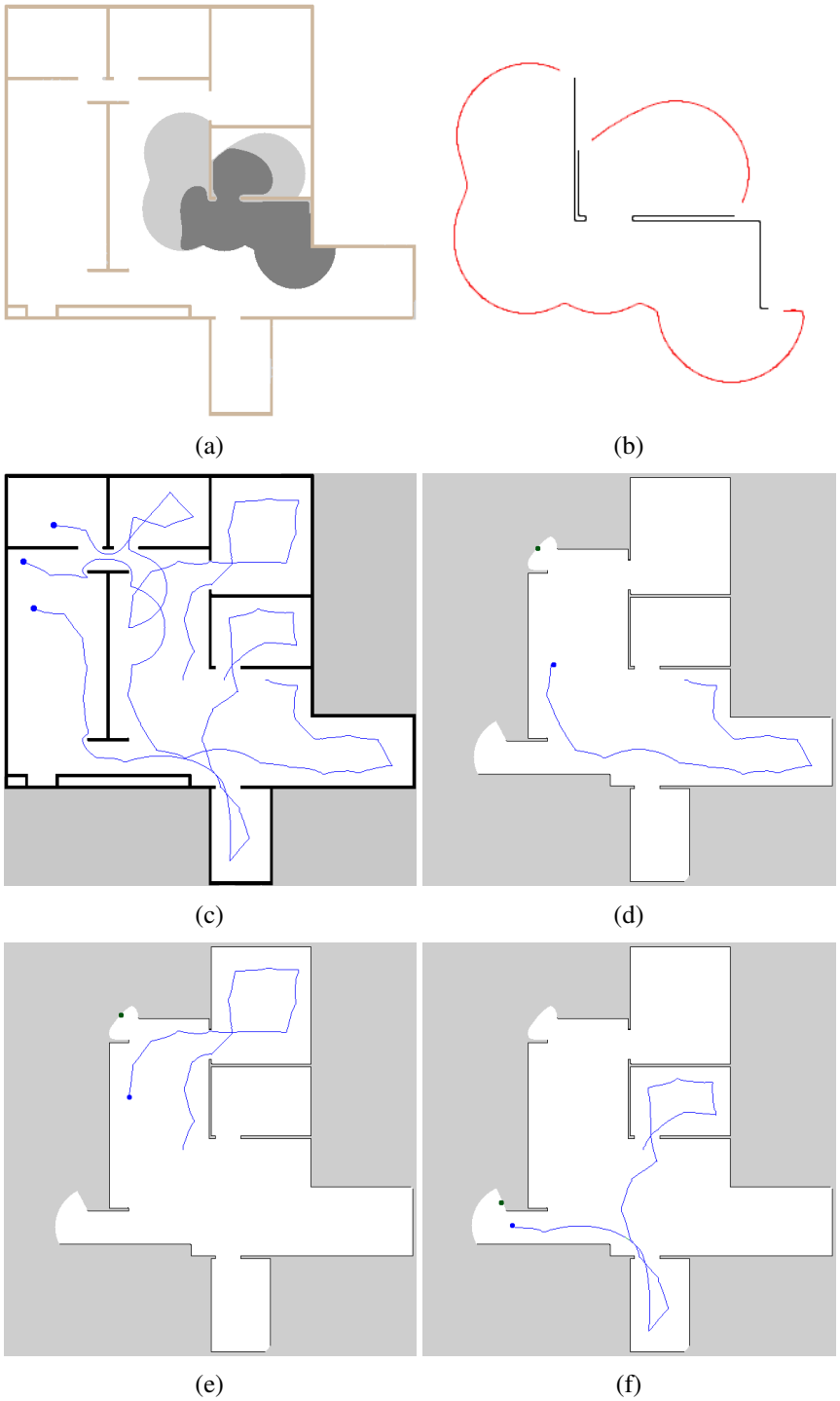

Fig. 5.8 Examples of selected steps of the multi-robot exploration: (**a**) frontwave propagation during determination of the possible goal candidates (frontiers) superimposed to the map of the environment;; (**b**) determined goal candidates (part of the map is enlarged for the sake of clarity); (**c**) final exploration paths for all robots; (d), (e), (f) same step of the exploration algorithm from the perspective of each robot (notice that all robots share the same map, corresponding to the whole discovered area in this particular step)

5.3 Voronoi diagrams

5.3.1 Conventional Computation of Voronoi diagrams

A computation of Voronoi Diagram (VD) is a basic problem studied in Computational geometry. One of the simplest cases of Voronoi diagram is a division of a plane with n points (called generating points) into a set of convex cells, where each cell contains exactly one generating point. For all points inside a cell, the distance to its generating point is smaller than to any other [**?**]. An example of this ordinary Voronoi diagram is shown in Figure 5.9a and Figure 5.9b

Many applications of the Voronoi diagram can be found. We are interested in an identification of the topology of the environment to improve the navigation of a mobile robot that is not solely based on metric information, but rather on identification of important places, *e.g.*, crossings and rooms. In our case, the environment is represented by a discrete cell lattice called a grid map. The map can be created from the occupancy grid in which new sensor measurements of the robot's surroundings taken by sonar or laser based ranger finder are integrated using Bayes rule [44]. A cell in the occupancy grid has associated probability the cell is occupied and thus a grid map is created from the occupancy grid by thresholding the value of the probability, *e.g.*, all cells with the probability of being occupied higher than 0.5 are considered as obstacles.

Regarding the navigation, a generalized Voronoi graph (GVG) has been introduced in [12] to identify topological places and also to determine paths between the places. A formal definition of the GVG can be found in [**?**] but basically the GVG is one-dimensional set of points that are equidistant to the n closest obstacles in n dimensions. For a walled environment [9], for example as visualized in Figure 5.9c and Figure 5.9d, the GVG results in a set of points equidistant from two or more obstacles.

It is known that Voronoi diagrams are sensitive to noise, which can be seen in Figure 5.10a and Figure 5.10b. That is why Beeson et al. introduced an additional pruning techniques to remove poor junction places [9].

In this paper, we consider RD-based computation of the Voronoi diagram to determine a skeleton of the grid map that represents the topology of the robot environment. The method is described in the next section.

5.3.2 RD-based Computation of Voronoi diagrams

The pioneering work at developing algorithms for computing *Planar Voronoi Diagrams* (PVD) using RD models (to the best of our knowledge) deal with the Cellular Automaton (CA) modelisations of RD systems [2, 7] in which some of the well known RD behaviors where successfully reproduced. In particular, a type of excitable waves that travel and interact with others annihilating after a collision, constituted the early pillars for developing

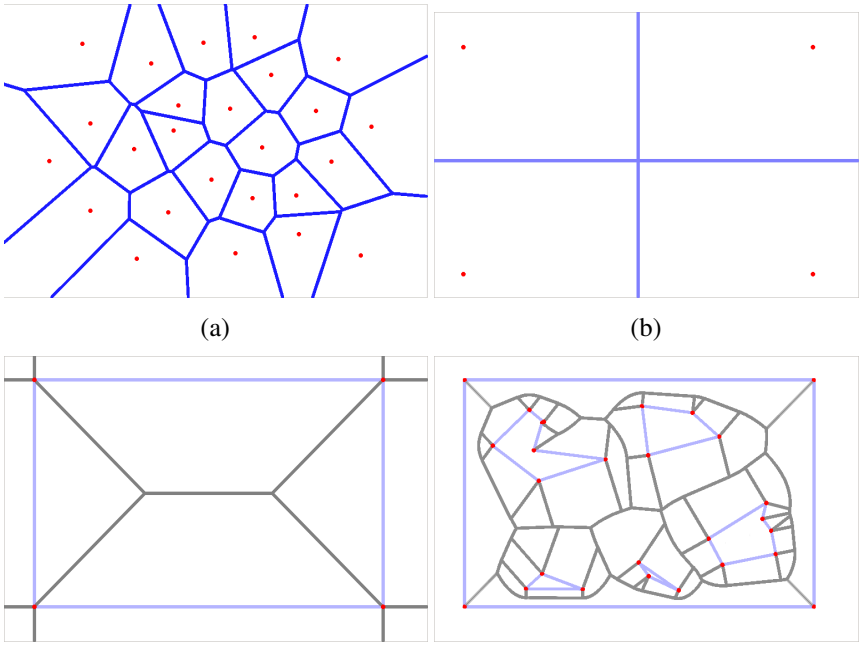

(a) (b)

(c) (d)

Fig. 5.9 Examples of the ordinary Voronoi diagram for k generating points in a plane and generalized Voronoi graph in walled environment: (**a**) random points, k=25; (**b**) four points forming a rectangle, k=4; (**c**) four walls forming a rectangular environment; (**d**) rectangular environment with fives polygonal obstacles with pruned parts of the Voronoi diagram outside the freespace of the polygonal environment.

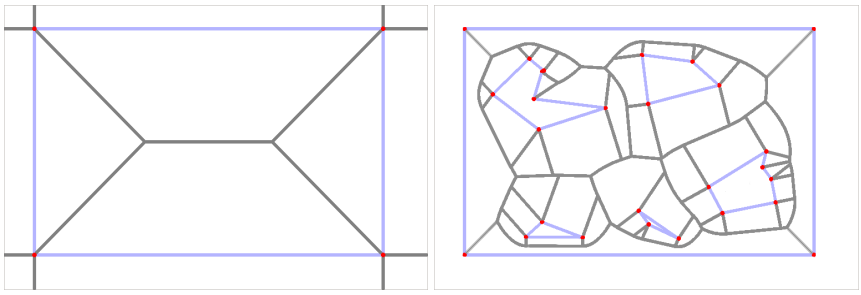

(a) (b)

Fig. 5.10 Generalized Voronoi graph in walled environment: (**a**) four walls forming a rectangular environment; (**b**) rectangular environment with fives polygonal obstacles with pruned parts of the Voronoi diagram outside the freespace of the polygonal environment.

RD-based computation. These waves in a cellular automaton lattice spreads with a constant velocity, whereby two wavefronts starting from two different sources meet at equidistant points at the same time. The result of the mutual wavefront annihilation at those points is a series of bisectors that separate the wavefront sources. Therefore, it provides a generation of the Voronoi diagram of the sources.

On the experimental side, the so-called RD computers are implemented in a spatially extended chemical media, where diffusive or excitation waves propagate and interact. In this way, the results of the computations are represented by spatial distributions of reagent concentrations. Some interesting yet computationally limited experimental realizations can be found in [3**?**]. There are based on the *palladium processor*, and on a supersaturated solution of sodium acetate, commonly called *hot ice.* Systematic studies have highlighted the drawbacks of such implementations, like the impossibility of inverting a VD using an RD chemical processor. This characteristic has been shared by all subsequent implementations of experimental RD processors. For instance, a VD irreversibility is found in [5].

Although the RD computation is the common substrate for the most of these prototypes of processors, they are better contextualized as *unconventional computing* approaches. These approaches do not only cover RD systems but they also include wider scope, like the true slime mould *Physarum polycephalum* [**?**]. A single-celled organism visible to the naked eye that in the plasmodium stage grows up to the square metre scale in size. A comprehensive description of such unconventional methods, including a gas discharge, can be found in [14].

5.3.3 FHN-based Voronoi diagrams

The technique for generating VD by means of the FHN model uses the *switch-of-phase* mechanism described in Section 4.1.3, in addition to the way of introducing information in the integration grid as described in Section **??**. Firstly, an expansion phase that uses the *fluid-like* behavior (a comprehensive description of this behaviour can be found in [76]) triggers a wavefront that evolves till it covers the whole domain. This mechanism is exemplified in the first row of pictures depicted in Figure 5.11. Then, the second stage based on a contraction phase recovers the wavefront over itself, as it is shown in the second row of pictures in Figure 5.11. The resulting concentration profile coincides with a planar Voronoi diagram. Therefore, all the logic required for a computation of the diagram is transferred to the spatiotemporal dynamics of the FHN model. The set of required values for the used FHN model, are presented in Table 5.2. Notice that the termination condition for both stages is trivially implemented by measuring the total amount of u (or v) summing over all grid points. A constant value within two different iterations means the system has reached a static situation; hence, the next phase can be triggered.

5.3.4 Experimental results

Comparison method

One of the expected advantages of the proposed RD-based computational model is that it is a less sensitivity to spatially noisy data. This is particularly interesting in the application of the Voronoi diagram to compute a skeleton of the grid map of the robot's operational

Table 5.2 Set of values for the FHN model to reproduce the desired behavior in the both phases: *expansion* and *contraction*.

		FHN Parameters				
		α	β	ε	D_u	D_v
Phase	*expansion*	4	-0.5	40	0.45	2
	contraction	3.8	0.1	10	0.1	1.5

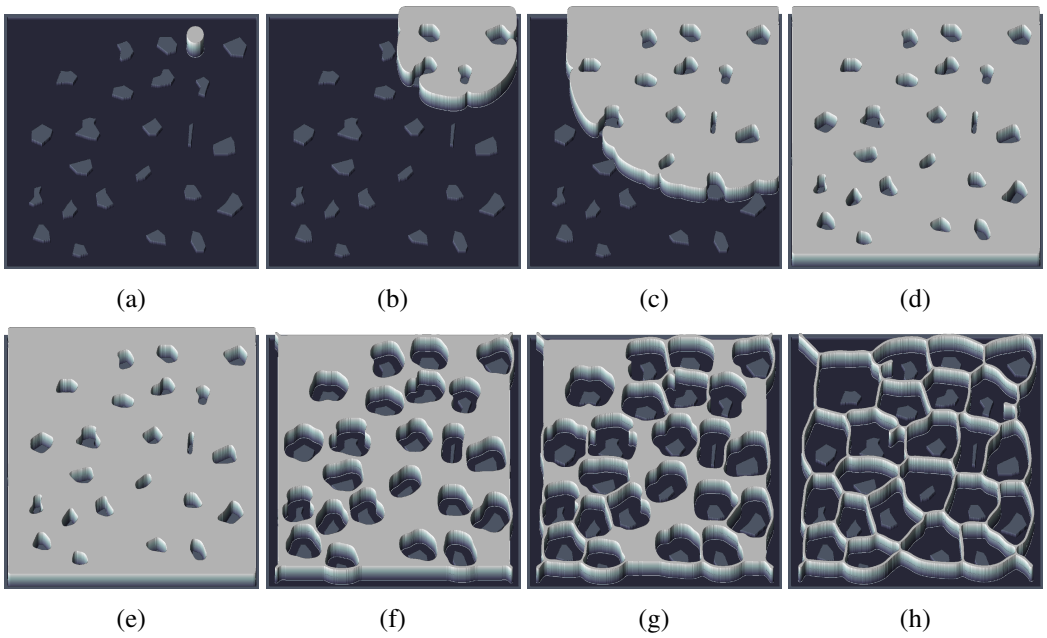

Fig. 5.11 Steps of the RD-based Voronoi algorithm applied to the *potholes* environment: (**a**, **b**, **c**, and **d**) expansion phase, a wavefront using the *fluid-like* behaviour evolves over the integration domain; (**e**, **f**, **g** and **h**) contraction phases, the resulting concentration profile of the previous stage evolves till generating a VD of the environment.

environment that can be used to create a topological representation of the environment. A map of the environment created from the sensor measurements can be noisy, *e.g.*, because of a poor localization, which can lead to a miss alignment of the range measurements and noisy grid map. Regarding the topology, the Voronoi diagram is a graph (skeleton) describing the topology of the environment, where the nodes of the graph represent topologically important places in the environment. The nodes with the degree higher than 3 are junction places that represent crossings in the environment, while the nodes with the degree 1 are the leaves of the skeleton and represent particular areas in the environment like rooms. A skeleton of a walled environment computed as the Voronoi diagram in the grid map of the environment

called *jh* is shown in Figure 5.12 together with the highlighted junction places and leaves that represent rooms.[2]

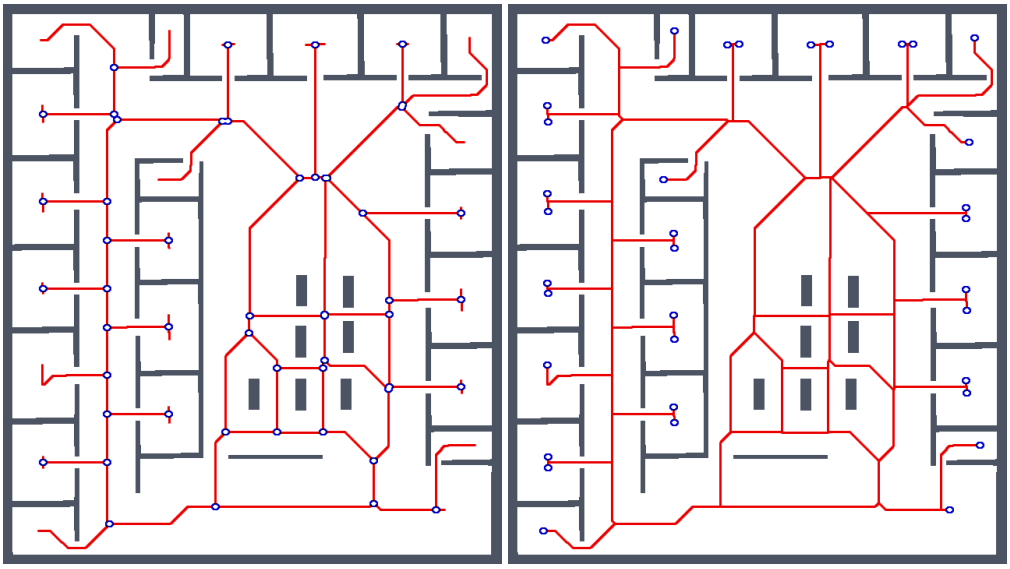

(a) (b)

Fig. 5.12 Example of the topology representation of the walled environment *jh* computed as the GVG of the grid map. The computed Voronoi diagram is transformed into a graph, where nodes with the degree (number of incident edges) higher than 2 represent junction places and nodes with the degree 1 are the leaves representing particular rooms.

If we consider a static environment, its topology is fixed and thus the number of junction places and leaves should be the same even for an imperfect reconstruction of the map using noisy sensor measurements. Based on this observation, we propose the following methodology to study sensitivity of computational model to the noisy sensor data and compare the proposed RD-based Voronoi diagram computation with the thinning algorithm for finding a skeleton of the grid map [9].

The evaluation of the sensitivity is based on adding a noise to the map, where the noise is added as small discs with the radius r at all boundary cells (*i.e.*, obstacle cells that are incident with at least one freespace cells). The radius r is drawn from a normal distribution with the zero mean and variance $\sigma_r \leq 10$. For each map we considered 10 values of σ_r and because the determination of the map skeleton (using thinning algorithm [9] as well as the proposed RD-based computational model) is deterministic we create 20 noisy maps with added noise for each original map and particular value of σ_r. Then, the studied parameters of the skeleton according to the level of noise σ_r are considered as average values and standard deviations computed from 20 trials of each algorithm runs on these 20 noisy maps. Having

[2]Notice, some rooms are represented as two leaves and a junction place, which depends on the pruning of the Voronoi diagram (skeleton). The particular figures have been obtained by the thinning algorithm [9].

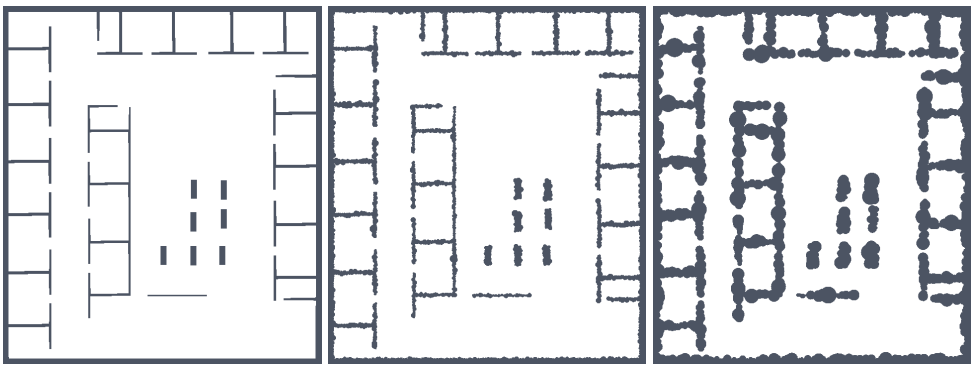

(a) (b) (c)

Fig. 5.13 Environment *jh*: (**a**) without added noise; and with added noise for (**b**) $\sigma_r = 2$; and (**c**) $\sigma_r = 5$

four environments, called *autolab*, *jh*, *cube*, and *potholes*, the number of performed trials for two algorithms in this evaluation is 1600. An example of the maps with added noise is shown in Figure 5.13. Moreover, we also performed additional evaluation for scaled maps for the *jh*, *cube*, and *potholes* environments enlarged by four different scale, which gives 4800 additional trials which gives 6400 performed trials in total.

The influence of the added noise is studied as the change of the number of detected junctions places and the number of leaves according to the reference numbers computed from the noise-less map. The change in the number of junctions places is measured as the percentage deviation from the reference value denoted as JPDM. Let J_0 be the number of junctions places detected in the noise-less map and J_σ be the number of detected junction places in the map with added noise according to σ. Then, the JPDM is computed as:

$$JPDM = \frac{\overline{J_\sigma} - J_0}{J_0} \cdot 100\%, \tag{5.1}$$

where $\overline{J_\sigma}$ is the average number of the detected junction places over all trials for the particular value σ and map. The number of leaves is computed as the average number of the detected leaves in the topology graph of the Voronoi diagram that is accompanied by the standard deviation.

The value of the JPDM around zero indicates that the particular method is not sensitive to noise. The negative value indicates that the number of junction places in the noisy map is lower than the reference value J_0. Notice, this does not necessary mean a worse result. A lower number of junction places is usually related to a lower number of leaves (*e.g.*, detected rooms) and with increasing level of noise, an entrance to a particular room can be more and more narrow. Hence, a robot cannot safely navigate to such location, and therefore, the room is unreachable, the corresponding leave is not part of the skeleton and also the number of

junction places is lower. On the other hand, if the method of the determination of the Voronoi diagram is sensitive to noise, many small branches can be part of the skeleton and thus also the number of junction places is increased.

Determine topology graph for the RD-based Voronoi Diagram

In Figure 5.11, it can be seen that the skeleton of the map determined by the proposed RD-based computational model is not a set of single pixel width paths, and therefore, there can be various ways how to determine the studied indicators.

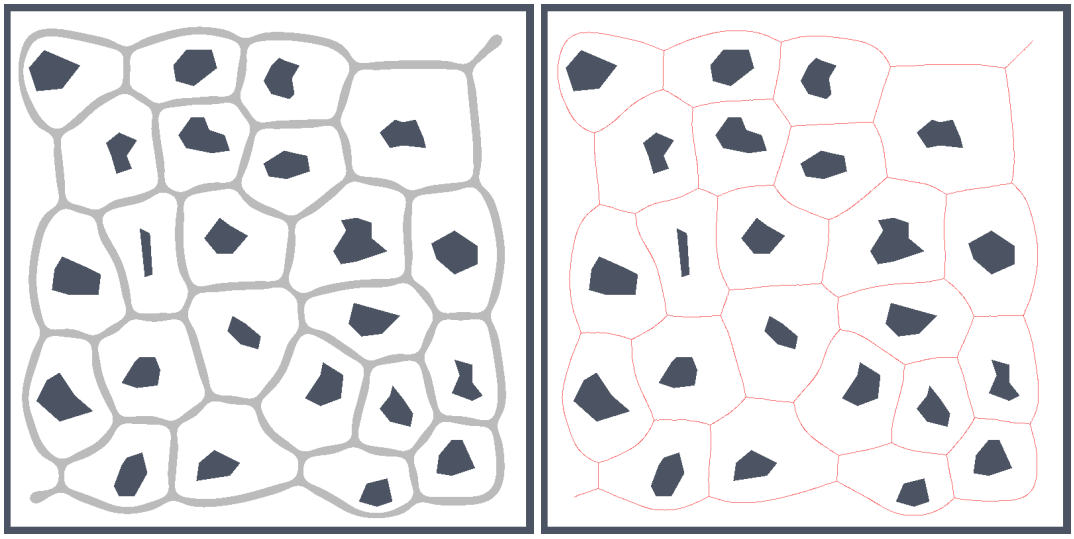

(a) (b)

Fig. 5.14 Example of found skeleton (Voronoi diagram) by the RD-based computational model for the pothole environment: (**a**) light gray structure; (**b**) and its one pixel width skeleton shown in red

For simplicity and also with regard to the used thinning algorithm [9], we considered the RD-based skeleton as a simple polygon (or a set of simple polygons) and determine single pixel width skeleton in this polygon using the thinning algorithm. This allows us to consider the identical procedure to compute the indicators for determination of the skeleton based solely on the thinning algorithm and on the RD-based computational model. Such a skeleton of the determined RD-based Voronoi diagram is shown in Figure 5.14. An example of superimposed Voronoi diagrams determined in the map with and without the added noise in the environment *autolab* is shown in Figure 5.15.

It can be noticed that the thinning algorithm prunes branches of the skeleton that would go to the corners of the particular rooms. On the other hand, this is not exactly the case of the RD-based computation of the skeleton, which splits the skeleton according to the space around the propagated frontwave. Therefore, instead of direct comparison of the RD-based

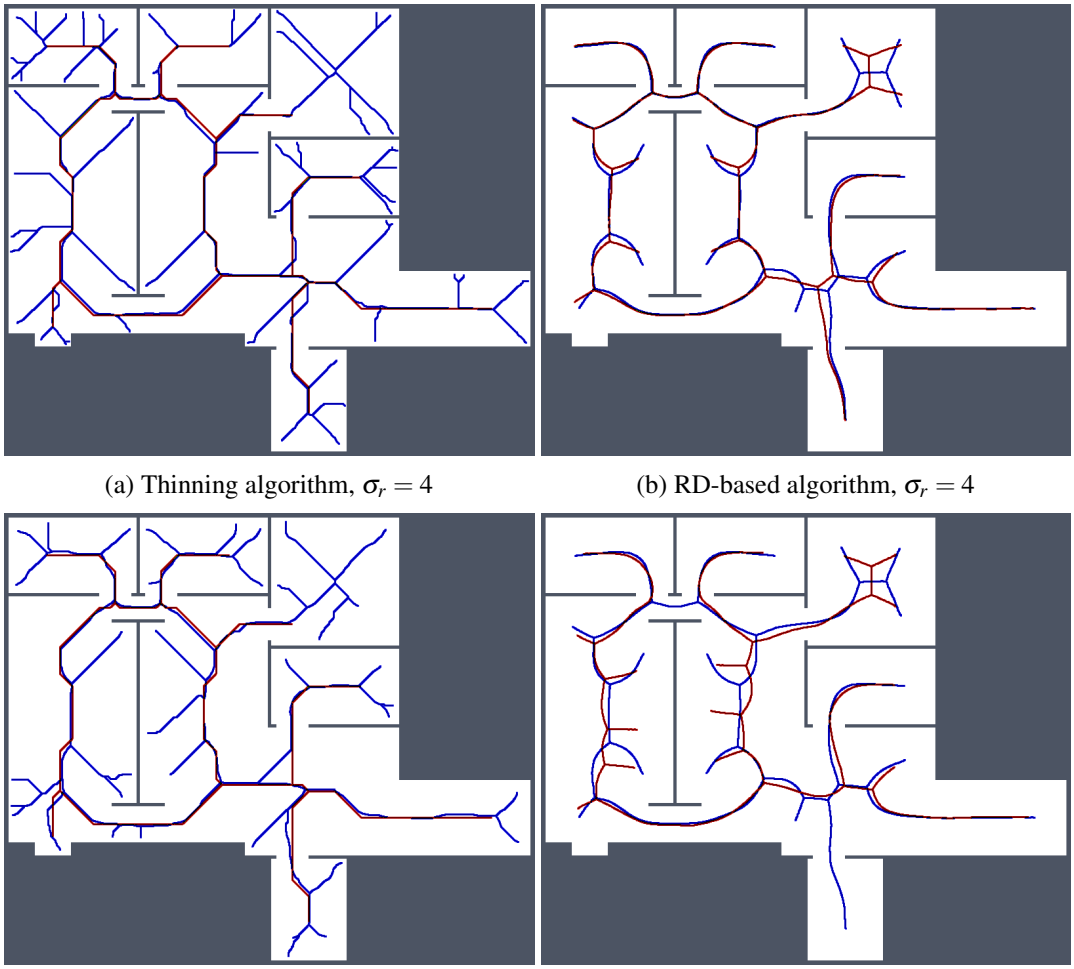

(a) Thinning algorithm, $\sigma_r = 4$ (b) RD-based algorithm, $\sigma_r = 4$

(c) Thinning algorithm, $\sigma_r = 7$ (d) RD-based algorithm, $\sigma_r = 7$

Fig. 5.15 Example of found skeleton (Voronoi diagram) by the RD-based computational model for the pothole environment: (**a**) light gray structure; (**b**) and its one pixel width skeleton shown in red; (**c**) light gray structure; (**d**) and its one pixel width skeleton shown in red.

skeleton with the thinning algorithm accompanied by advanced pruning of branches, we study how the determined skeletons differ with increasing σ_r for each particular method and thus we study the algorithms' sensitivity to the level of the noise.

Results

The proposed statistical indicators of the noise sensitivity, *i.e.*, JPDM (5.1) and the average number of the detected leaves are depicted in Figure 5.16 and Figure 5.17, respectively. The results show that the proposed RD-based computation of the Voronoi diagram is a less sensitive to the added noise as the number of junction places is usually lower than the number

of junction places for the map without the noise. The lowest value of the JPDM is -100% for the *cube* environment, where none of the junction place has been detected in the environment, see Figure 5.18 and Figure 5.19. On the other hand, the thinning algorithm is more sensitive to the noise as the number junction places is quickly increasing and for the *autolab*, *jh*, and *potholes* environments the maximal number of the junction places is for the noise level $\sigma = 4$, see example in Figure 5.21.

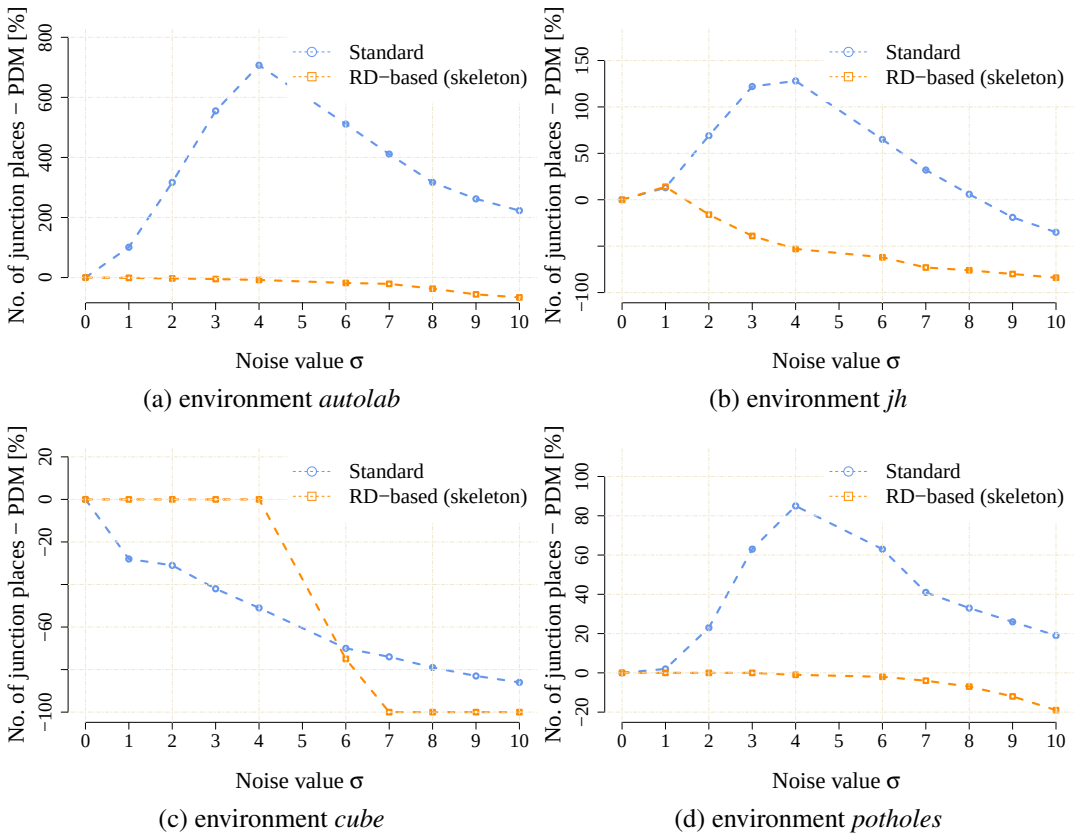

(a) environment *autolab* (b) environment *jh*

(c) environment *cube* (d) environment *potholes*

Fig. 5.16 the noise sensitivity indicator jpdm (5.1) in the noisy maps created for the particular value of the noise level σ

The number of leaves significantly changes with the noise level for the thinning algorithm, while for the proposed RD-based computation of the skeleton changes only slightly and typically decreases with a higher level of the noise σ as it can be seen in Figure 5.17. The only exception is the environment *potholes*, where the initial skeleton for $\sigma = 0$ does not contain any leaves, see Figure 5.22, while with increasing σ some parts become unreachable for the robot (frontwave propagation), which is visualized in Figure 5.23.

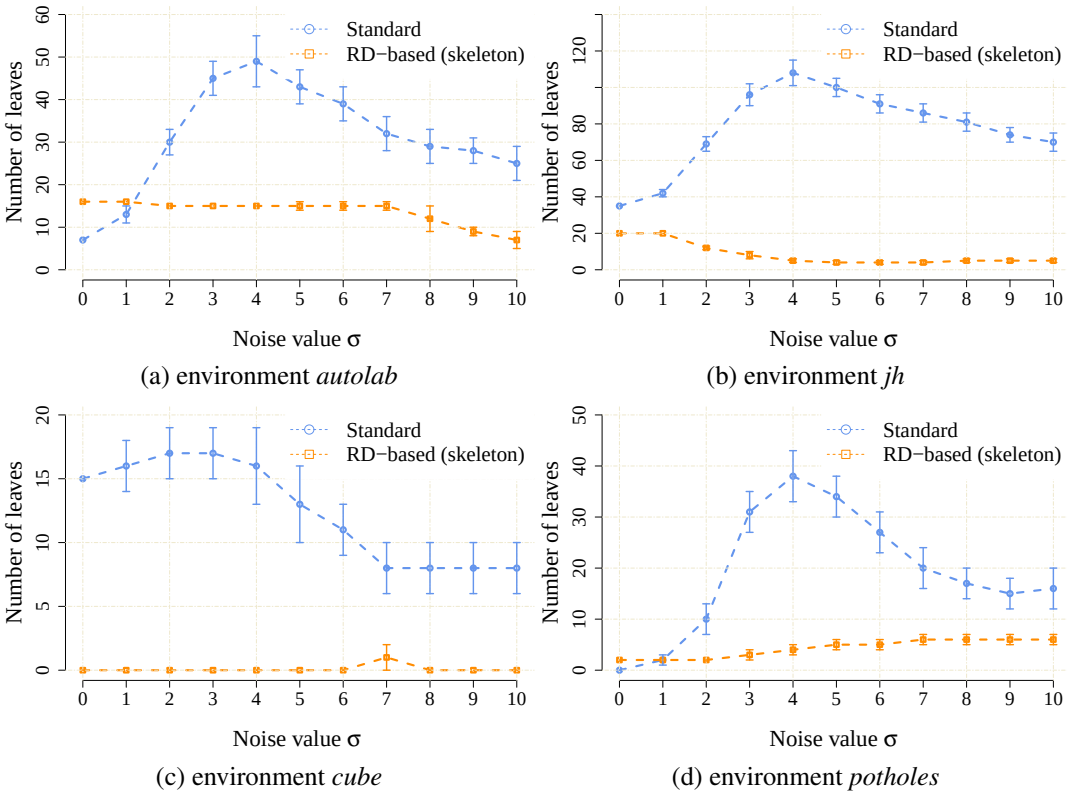

Fig. 5.17 Average numbers of the leaves detected in the noisy maps created for the particular value of the noise level σ

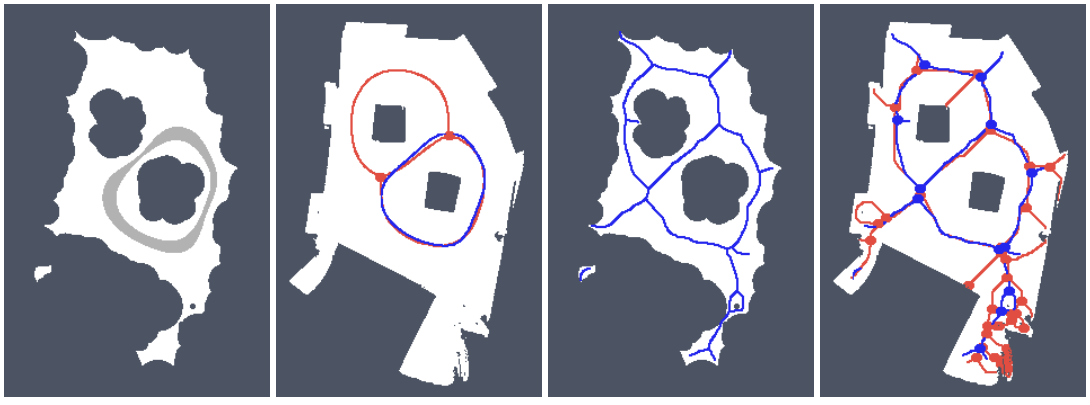

Fig. 5.18 Skeletons and the determined topological maps with highlighted junction places and leaves in the map *cube* with the noise level $\sigma = 7$: (**a**) RD-based Voronoi diagram; (**b**) and its corresponding skeleton (shown in green) that is superimposed on the skeleton determined in the noise-less map (in red); (**c**) Pruned GVG representing skeleton of the map determined by the thinning algorithm [9]; (**d**) and the corresponding skeleton superimposed on the skeleton determined in the noise-less map.

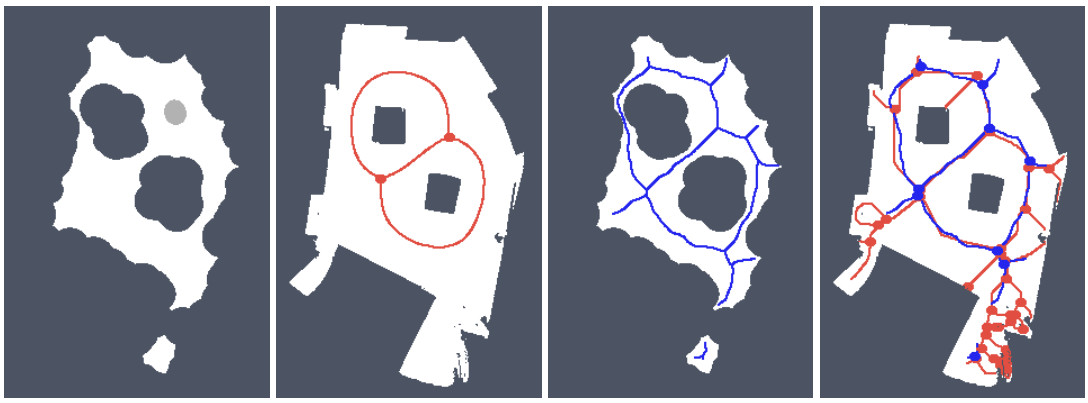

(a) (b) (c) (d)

Fig. 5.19 Determined skeletons and topological maps with highlighted junction places and leaves in the map *cube* with the noise level $\sigma = 8$: (**a**) RD-based Voronoi diagram; (**b**) and its corresponding skeleton (shown in green) that is superimposed on the skeleton determined in the noise-less map (in red); (**c**) Pruned GVG representing skeleton of the map determined by the thinning algorithm [9]; (**d**) and the corresponding skeleton superimposed on the skeleton determined in the noise-less map.

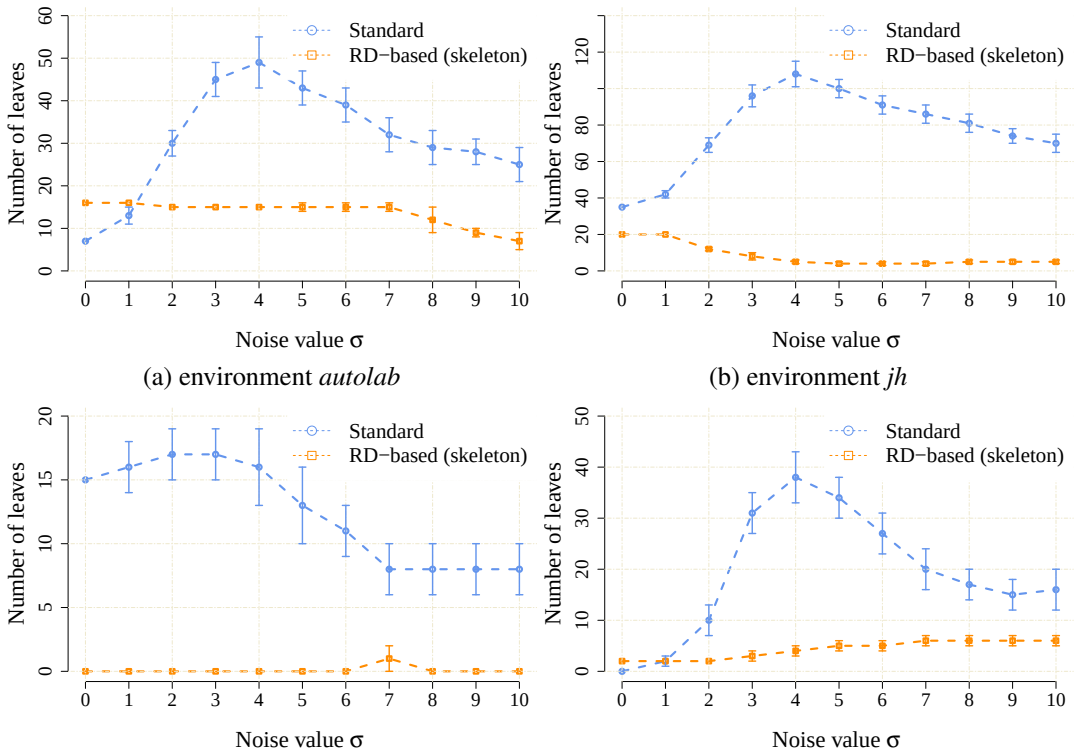

(a) environment *autolab* (b) environment *jh*

(c) environment *cube* (d) environment *potholes*

Fig. 5.20 Average numbers of the leaves detected in the noisy maps created for the particular value of the noise level σ

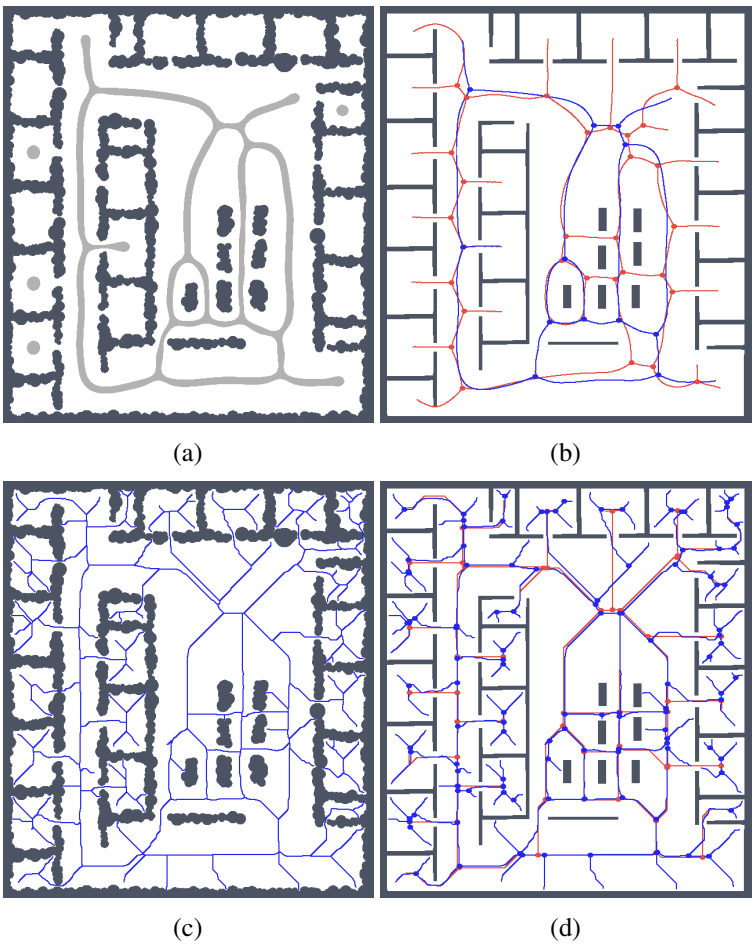

Fig. 5.21 Determined skeletons and topological maps with highlighted junction places and leaves in the map *jh* with the noise level $\sigma = 4$: (**a**) RD-based Voronoi diagram; (**b**) and its corresponding skeleton superimposed on the skeleton determined in the noise-less map (in red); (**c**) Pruned GVG representing skeleton of the map determined by the thinning algorithm [9]; (**d**) and the corresponding skeleton superimposed on the skeleton determined in the noise-less map.

Influence of the map resolution

A resolution of the grid map may influence both computational techniques to determine the Voronoi diagram, and therefore, its influence has been studied for the *potholes*, *cube*, and *jh* environments for which all the maps have been scaled 1.2, 1.5, 1.7, and 2 times. Particular results of the JPDM indicator are shown in Figure 5.25, Figure 5.26, Figure 5.27. Examples of the determined skeletons for both algorithms using different map resolutions are shown in Figure **??**, Figure **??**, Figure **??**. Although a higher resolution increases computational burden of the both techniques, it can be noticed the proposed RD-based computation is

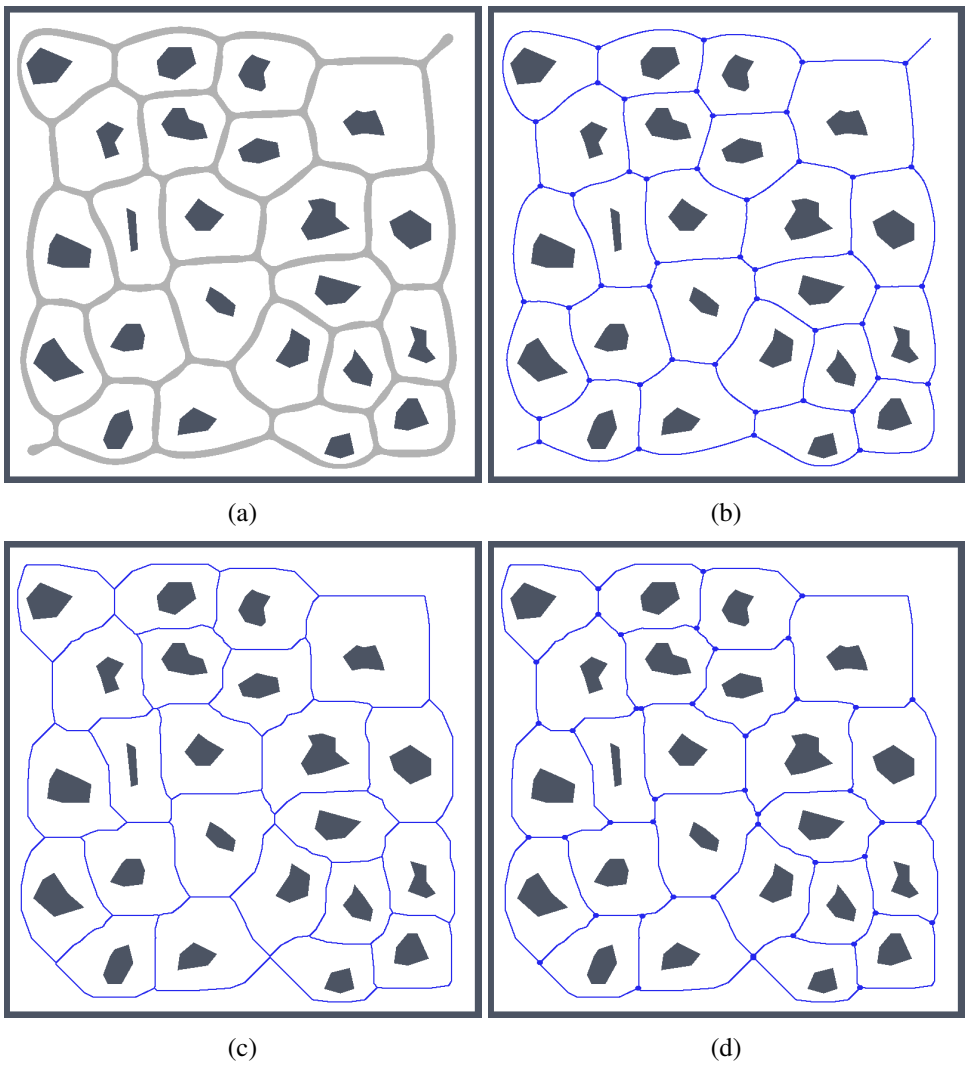

Fig. 5.22 Determined skeletons and topological maps with highlighted junction places and leaves in the map *potholes* with the noise level $\sigma = 0$: (**a**) RD-based Voronoi diagram; (**b**) and its corresponding skeleton superimposed on the skeleton determined in the noise-less map (in red); (**c**) Pruned GVG representing skeleton of the map determined by the thinning algorithm [9]; (**d**) and the corresponding skeleton superimposed on the skeleton determined in the noise-less map.

significantly less sensitive to the change of the resolution and the number of junction places and leaves remains almost the same according to the change in the thinning algorithm.

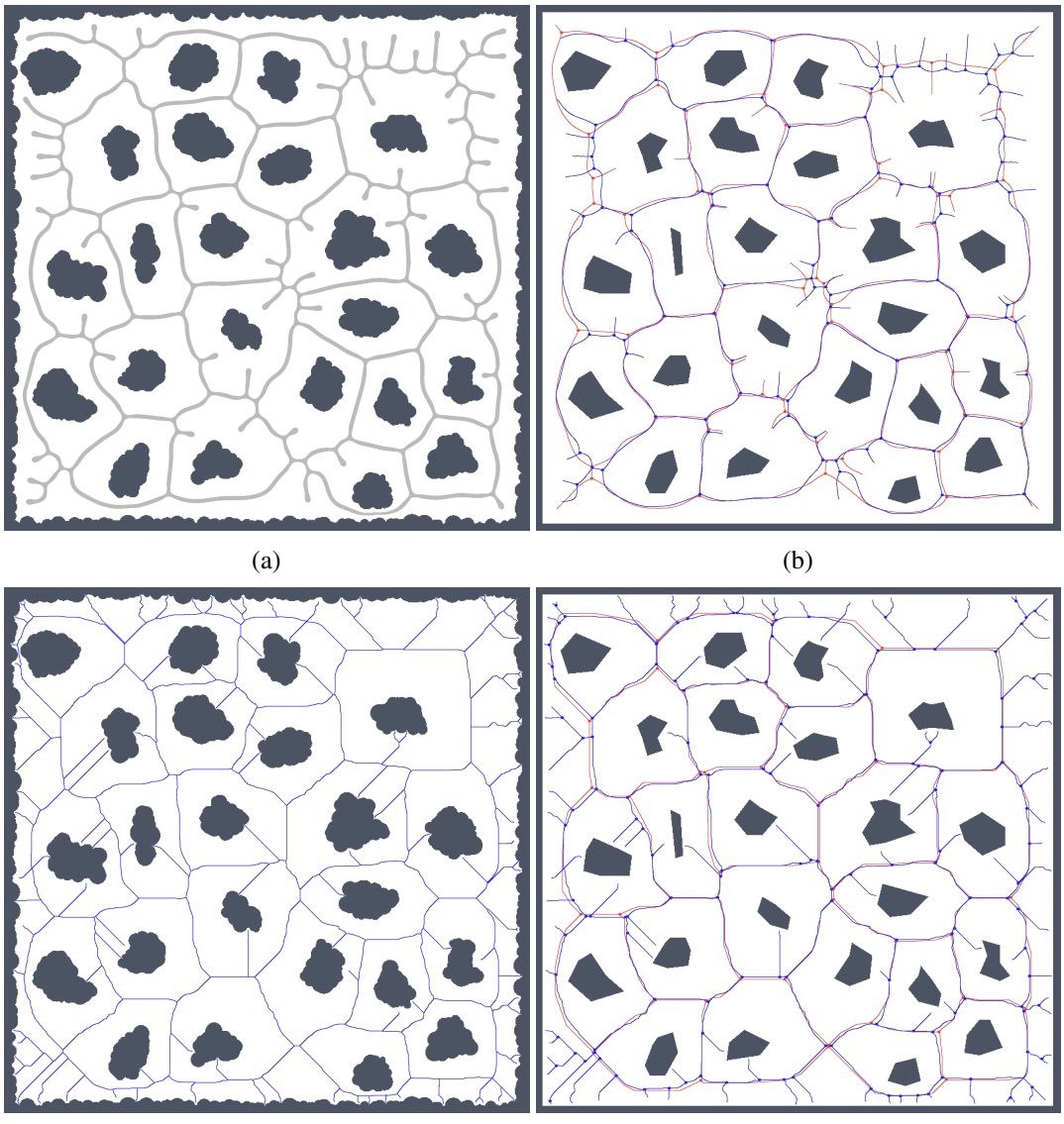

Fig. 5.23 Determined skeletons and topological maps with highlighted junction places and leaves in the map *potholes* with the noise level $\sigma = 5$ for the scaled map with 1600×1600 grid points: (**a**) RD-based Voronoi diagram; (**b**) and its corresponding skeleton superimposed on the skeleton determined in the noise-less map (in red); (**c**) Pruned GVG representing skeleton of the map determined by the thinning algorithm [9]; (**d**) and the corresponding skeleton superimposed on the skeleton determined in the noise-less map.

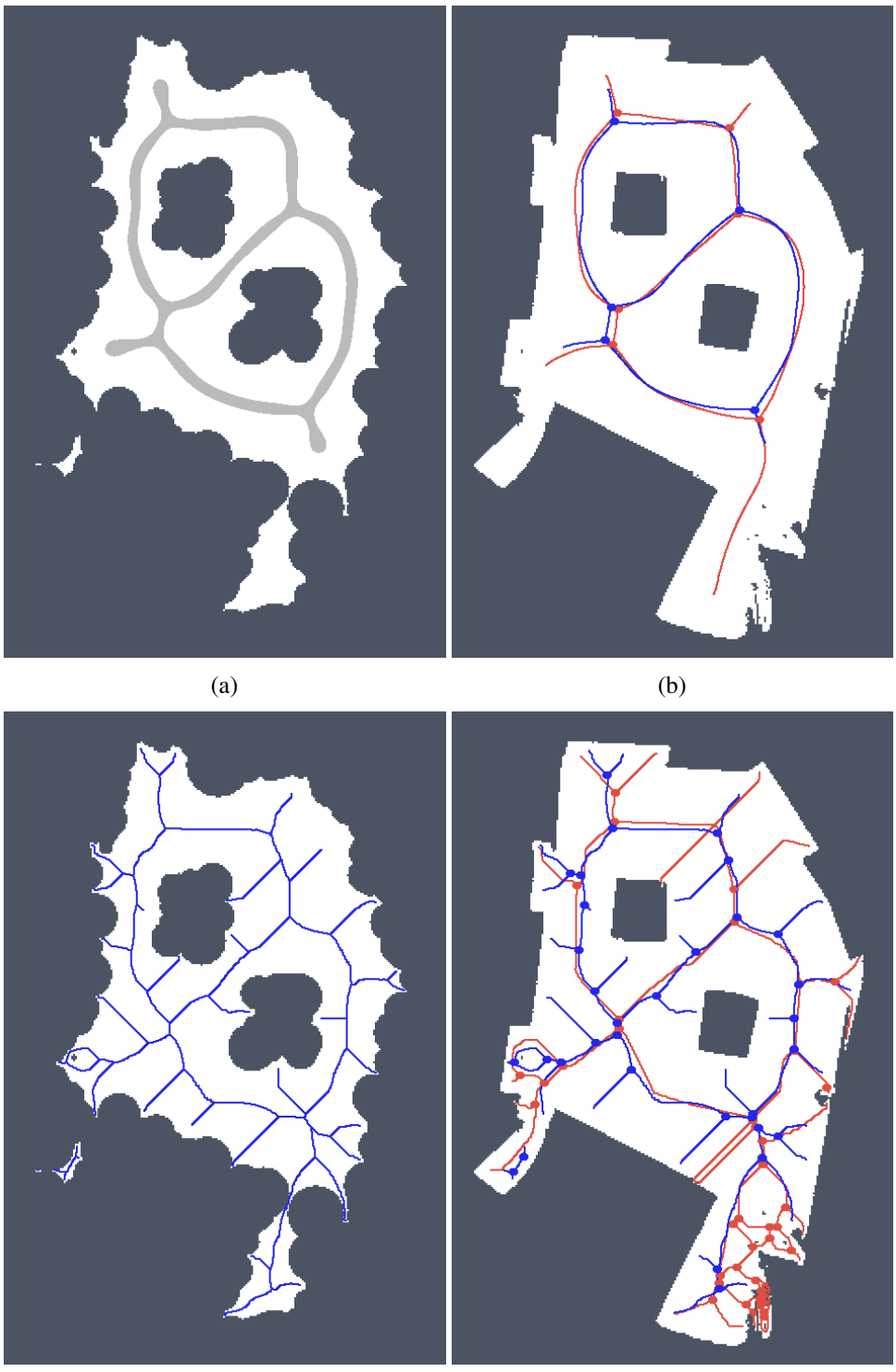

Fig. 5.24 Determined skeletons and topological maps with highlighted junction places and leaves in the map *cube* with the noise level $\sigma = 5$ for the scaled map with 478×698 grid points: (**a**) RD-based Voronoi diagram; (**b**) and its corresponding skeleton superimposed on the skeleton determined in the noise-less map (in red); (**c**) Pruned GVG representing skeleton of the map determined by the thinning algorithm [9]; (**d**) and the corresponding skeleton superimposed on the skeleton determined in the noise-less map.

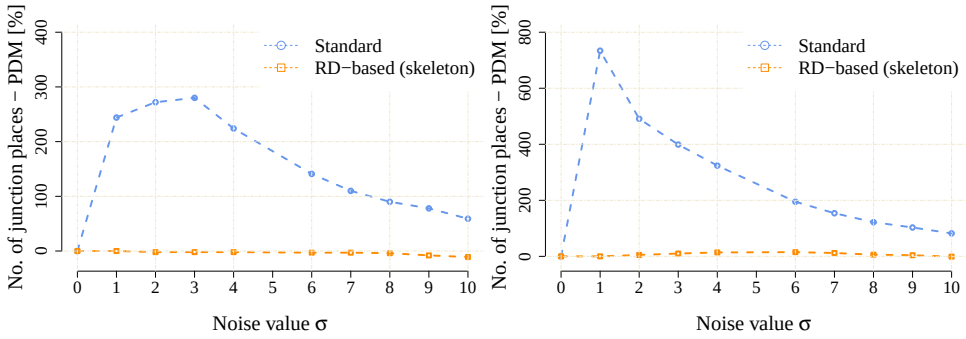

(a) *potholes*, 960 (b) *potholes*, 1200

(c) *potholes*, 1360 (d) *potholes*, 1600

Fig. 5.25 The noise sensitivity indicator JPDM (5.1) in the scaled noisy maps of the *potholes* environment

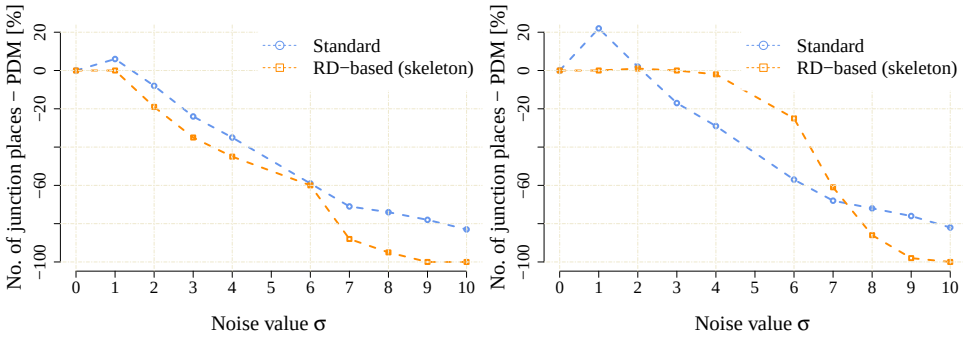

(a) *potholes*, 960

(b) *potholes*, 1200

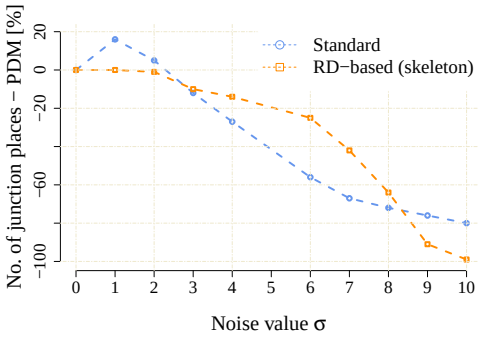

(c) *potholes*, 1360

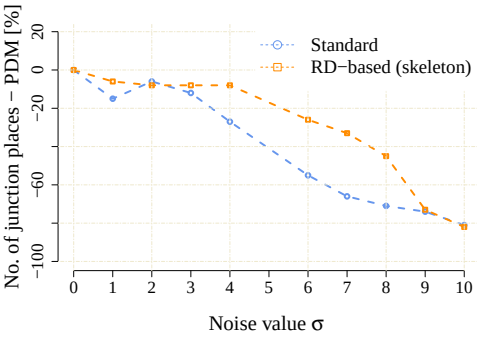

(d) *potholes*, 1600

Fig. 5.26 The noise sensitivity indicator JPDM (5.1) in the scaled noisy maps of the *cube* environment

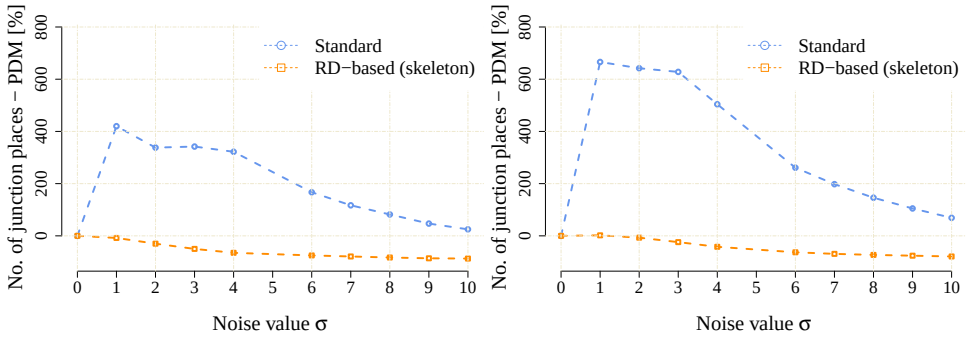

(a) *potholes*, 960

(b) *potholes*, 1200

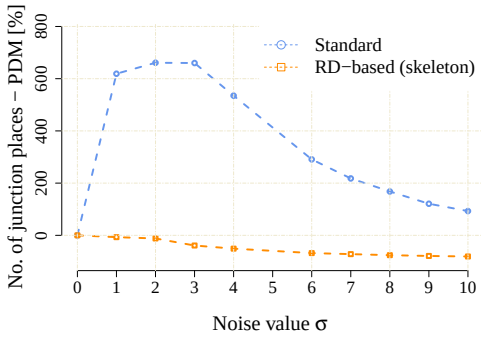

(c) *potholes*, 1360

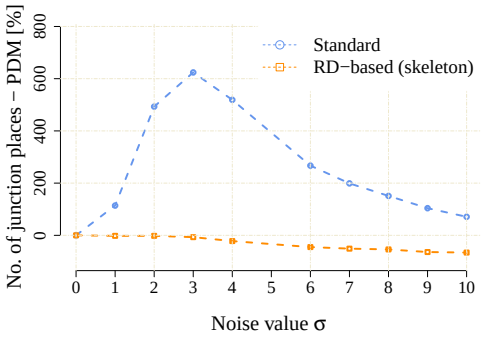

(d) *potholes*, 1600

Fig. 5.27 The noise sensitivity indicator JPDM (5.1) in the scaled noisy maps of the *cube* environment

Chapter 6

Conclusions and future work

The outcomes of the research done in this thesis can be divided into numerical and experimental results.

6.0.5 Numerical results

The numerical results are related to the study of the behaviour of RD systems. Particularly, the special properties exhibited by frontwaves in bistable asymmetric nullcline configurations have been study. All these types of waves with strong non-linear character are commonly known as autowaves, as they do not share the properties of standard waves, like the conservation of energy. Although herein the FHN model is used, without loss of generality any other RD model can be used to reproduce similar results, as the dynamics of RD systems are general.

There is no standard method for solving the RD equations in order to study analytically the behaviour of the frontwaves. Despite this, the associated nullclines determined by the particular values of the model variables, along with the standard stability analysis provide some clues about the model dynamics at the neighborhood of a fixed point. A set of simulation results illustrate the behaviour of such frontwaves when the FHN undergoes an extensive modification of its variables, though only the ones that have the highest impact in the frontwaves propagation, *i.e.* α and β, are shown in this work. Based on that, a basic algorithm that relies on the switch-of-phase mechanism in asymmetric bistable nullcline configurations has been proposed as the core algorithm for developing RD based computation. The combination of this procedure with the new properties of the frontwaves propagation found in the aforementioned simulations, lead to exhibit some behaviours of the FHN dynamics that somehow are able to mimic geometric operations, in a two-dimensional computational grid. And hence, logical operations can be encapsulated in its spatio-temporal dynamics.

Moreover, due to the computational burden associated with the spatial integration of the RD models, a new technique to speed up the computations has been developed. Taking advantage of the system stability in the sense of Lyapunov, only the grid nodes in which the frontwave that separates both stable states is actually evolving are considered for the spatial integration. This hardware-agnostic optimization dramatically decreases the computation times, specially for big matrix.

6.0.6 Experimental results

The main contribution of this thesis in the experimental area is the realization of a RD based software architecture that allows to develop algorithms capable of compete with their standard counterparts. Based on the techniques used for developing the path planning algorithm, *i.e.* the switch-of-phase mechanism in a bistable nullcline configuration, in combination with I/O operations performed by means of the so-called "external forcing", constitutes a novel strategy for the use of RD systems in general purpose computation. The results of the research have materialized into the following software components:

Robot exploration task

The mobile robot exploration refers to an algorithm where a mobile robot is requested to autonomously cover all reachable regions by its sensory system, creating a map of the unknown environment. A RD-based approach has been successfully implemented for solving the exploration task. The following properties of the exploration task define the achieved results in this field:

- *Single robot exploration task*: the proposed RD based exploration strategy does not explicitly consider information gain, and therefore, it can be considered as a pure distance cost strategy. Two standard approaches have been select for comparison purposes, the greedy exploration and the TSP based approach with the TSP distance cost for the comparison presented. Additionally, two variants of both algorithms have been used for the comparison.

- *Utility function*: the performance of the frontier-based exploration can be improved using the so-called utility function. It aims to consider an expected benefit of the frontiers to select the most suitable frontier in order to fulfill the mission objective. Two basic implementations of the utility function have been presented, leading to two different behaviors with respect to how robots cover the available space. An open-space preference *vs* a wall-following preference.

- *Multi robot exploration task*: the proposed computational model has been extended for performing the exploration mission by a team of mobile robots. The extension can be considered as a semi-centralized approach, where the robots are considered independently while they shared a common map of the environment being explored.

Although the presented results are preliminary, they indicate feasibility of the proposed RD based exploration and provide a premise for at least a competitive performance with the current state-of-the-art methods.

Voronoi diagrams

Having a set of seeds, the Voronoi diagram can be imagined as partitioning of a plane into a set of cells, where each cell is originated from a particular seed, and the cell represents the region for which the seed of the cell is the closest seed. In other words, the boundary of the regions is formed from points that are equidistant to the two closest seeds. In robotics, the generalized Voronoi graphs (GVG) are used to create a navigational roadmap and a topological representation of the environment. Herein, the equidistant property of the boundary of the Voronoi regions is utilized to find a path that maximizes the clearance from the obstacles. Moreover, the junction places, i.e., locations where the boundary of the cells are connected, represent topologically important places of the environment, like corridor intersections.

The exact problem addressed in this thesis is the determination of the junction places in a grid map of the environment by generation of the Voronoi diagram in the grid map. The proposed RD-based computational model is employed in the generation of such Voronoi diagrams from which the junction places are extracted. The approach has been compared with an state-of-the-art algorithm. The following properties of the Voronoi diagram define the achieved results in this field:

- *Final stable states*: the exploitation of the newly found behavior that leads to Voronoi-like concentration patterns as the final stable states of the model spatiotemporal evolution. This feature not only overcomes previous limitation os RD-based computation, but also allows to recover the system to its original state by means of the Voronoi diagram inversion.

- *Noise sensitivity*: from the comparison point of view, is remarkable the lack of sensitiveness to the added noise that presents the RD algorithm. It makes unnecessary any pruning technique for removing poor junction places as it is required in the case of the considered thinning algorithm for the comparison. This advantage comes from the stability, in the Lyapunov sense, of the FHN system. The dynamics of the system drive it to the stable state, so that the spatiotemporal evolution is resistant to the inclusion of external information, which in the present case is interpreted as noise.

Regarding these observations, the proposed RD-based computational model seems to be a suitable technique to process real sensor data and provides more robust solutions than purely geometrical-based approaches.

6.1 Future works

There are two main lines of further work, on the one hand on the numerical side:

- *Stability analysis*: it would be desirable to dig deeper in the stability analysis of the various nullclines configurations used in this work. Also, once the Turing wavelength is ruled out as the possible underlying reason for the studied frontwave penetration properties (in regard to the Slit experiment), as the system is not in the Turing regime, such penetration properties should be further investigated with regard to the well known frontwave curvature properties.

- *Frontwave properties*: all the developed algorithms rely in some frontwave properties that have been studied in advance by means of the Slit and Square experiments, respectively. Therefore, further studies of the possible frontwave behaviours could disclose new properties that later on would be applied in the design of new RD based algorithms.

- *Non-bistable systems*: since in the computational grid is possible to set up a specific nullcline configuration for each cell, it becomes possible to mix different model configurations in the same integration grid. This feature enables the combination of excitable systems (that traditionally have been the cornerstone of RD-based computation) with unstable systems (interpreted as biological clocks) and with bistable systems. This could led to the development of more complex algorithms.

- *CNN templates*: in a previous work the path planning algorithm has already been implemented through a CNN class 1 template. The easy of implementation of CNN templates by means of commonly available hardware for specialized computation like FPGA's, in combination with the fact that no additional memory is needed per cell in the current implementation beyond the model parameters (all the info is transferred to the model spatiotemporal dynamics), makes the CNN a suitable candidate for re-implementing all the properties used in this work. This could lead to real-time implementations for the developed algorithms.

- *Optimizations*: a hardware-agnostic optimization has already been developed to speed up the computations. The optimization is also suitable for accelerating computations in any kind of RD model, because it was designed in base of a common RD dynamical property, as it is the associated stability in the sense of Lyapunov. Although this optimization has been combined with an OpenMP parallelization, it would be desirable to explore more specific parallelization techniques (like using GPU's or Xeon Phi's) or even low level optimizations (as the use of vectorial instructions).

and, on the other hand, in the experimental results:

- *Exploration task*: to further develop the exploration algorithm in order to perform quantitative comparisons with other state-of-the-art methods. This also includes a further elaboration of the proposed concept of utility function, and to address its computational requirements in order to evaluate the performance in real tasks. In general, an in deep comparison with state of the art algorithms will shed more light on whether to continue with the development of these algorithms would be interesting for the robotics community or not.

- *3D models*: so far only two dimensional approaches have been developed. Nevertheless, the spatial integration of the model can be trivially extended to cover 3D environments. Reproducing Voronoi diagrams, or the simple path planning algorithm in a 3D environment is an interesting problem to solve that can be useful, for instance in path planning strategies for UAVs navigation.

- *RD computational core*: putting together all the developed algorithms, *i.e.* path planning, exploration (single and collaborative) and Voronoi diagrams, set the foundations of a RD-based computational framework suitable for addressing geometrical problems, up to now particularly tailored to face the challenges associated with navigational problems in robotics. This premise provides a ground for a further development towards a complete computational model for robotic tasks solely based on RD principles.

References

[1] (1988). *Scientific American*, March:743–757.

[2] Adamatzky, A. (1996). Voronoi-like partition of lattice in cellular automata. *Mathematical and Computer Modelling*, 23(4):51 – 66.

[3] Adamatzky, A. (2009). Hot ice computer. *Physics Letters A*, 374(2):264 – 271.

[4] Adamatzky, A., Arena, P., Basile, A., Carmona-Galan, R., Costello, B., Fortuna, L., Frasca, M., and Rodriguez-Vazquez, A. (2004). Reaction-diffusion navigation robot control: from chemical to vlsi analogic processors. *IEEE Transactions on Circuits and Systems I: Regular Papers*, 51(5):926–938.

[5] Adamatzky, A. and de Lacy Costello, B. (2003). On some limitations of reaction diffusion chemical computers in relation to voronoi diagram and its inversion. *Physics Letters A*, 309(5-6):397–406.

[6] Adamatzky, A., de Lacy Costello, B., Melhuish, C., and Ratcliffe, N. (2003). Experimental reaction-diffusion chemical processors for robot path planning. *Journal of Intelligent and Robotic Systems*, 37(3):233–249.

[7] Adamatzky, A. and Holland, O. (1998). Voronoi-like nondeterministic partition of a lattice by collectives of finite automata. *Math. Comput. Model.*, 28(10):73–93.

[8] Amigoni, F. and Caglioti, V. (2010). An information-based exploration strategy for environment mapping with mobile robots. *Robotics and Autonomous Systems*, 58(5):684–699.

[9] Beeson, P., Jong, N., and Kuipers, B. (2005). Towards autonomous topological place detection using the extended voronoi graph. In *IEEE International Conference on Robotics and Automation (ICRA)*, pages 4373–4379.

[10] C. Tuckwell, H. (1988). *Stochastic processes in the Neuroscience*. Capital City Press, Vermont, USA.

[11] Chance, B., Kendall Pie, E., K. Gosh, A., and Hess, B. (1973). *Biological and biochemical oscillators*. Academic Press, Berlin.

[12] Choset, H. and Nagatani, K. (2001). Topological simultaneous localization and mapping (slam): toward exact localization without explicit localization. *Robotics and Automation, IEEE Transactions on*, 17(2):125 –137.

[13] D. Traub, R. and Miles, R. (1991). *Neuronal networks of the Hippocampus*. Cambridge University Press, New York, USA.

[14] DE LACY COSTELLO, B., RATCLIFFE, N., ADAMATZKY, A., ZANIN, A. L., LIEHR, A. W., and PURWINS, H.-G. (2004). The formation of voronoi diagrams in chemical and physical systems: Experimental findings and theoretical models. *International Journal of Bifurcation and Chaos*, 14(07):2187–2210.

[15] (Editor), M. M. N. (2006). *Complexus Mundi: Emergent Patterns in Nature*. World Scientific.

[16] Elfes, A. (1987). Sonar-based real-world mapping and navigation. *IEEE Journal of Robotics and Automation*, 3(3):249–265.

[17] Epstein, I. R., Berenstein, I. B., Dolnik, M., Vanag, V. K., Yang, L., and Zhabotinsky, A. M. (2008). Coupled and forced patterns in reactiondiffusion systems. *Philosophical Transactions of the Royal Society A: Mathematical, Physical and Engineering Sciences*, 366(1864):397–408.

[18] Faigl, J., Kulich, M., and Přeučil, L. (2012). Goal assignment using distance cost in multi-robot exploration. In *IEEE/RSJ Int. Conf. Intelligent Robots and Systems (IROS)*, pages 3741–3746.

[19] FitzHugh, R. (1961a). *Biophys. J.*, 1:445–446.

[20] FitzHugh, R. (1961b). Impulses and physiological states in theoretical models of nerve membrane. *J. Biophys.*, 1:445–466.

[21] Glass, L. and C. Mackey, M. (1988). *From clocks to chaos: The rhythms of life*. Princeton University Press, Princeton, UK.

[22] Gonzalez-Banos, H. H. and Latombe, J.-C. (2002). Navigation strategies for exploring indoor environments. *The International Journal of Robotics Research*, 21(10-11):829–848.

[23] Gorelova, A. and Burescaron, J. (1983). Spiral waves of spreading depression in the isolated chicken retina. *J. of Neurobiology*, 252:353–363.

[24] Grill, S., Zykov, V. S., and Muuller, S. C. (1995). Feedback-controlled dynamics of meandering spiral waves. *Phys. Rev. Lett.*, 75(18):3368–3371.

[25] H. Rotermund, H., Engel, W., and Kordesch, M. (1990). Imaging of spatio-temporal pattern evolution during catalytic co oxidation on platinum single crystal surfaces. *Nature*, 343:355–357.

[26] Harrison, L. G. (1987). What is the status of reaction-diffusion theory thirty-four years after turing? *Journal of Theoretical Biology*, 125(4):369 – 384.

[27] Heylighen, F. (1999). The science of self-organization and adaptivity. In *in: Knowledge Management, Organizational Intelligence and Learning, and Complexity, in: The Encyclopedia of Life Support Systems, EOLSS*, pages 253–280. Publishers Co. Ltd.

[28] Holz, D., Basilico, N., Amigoni, F., and Behnke, S. (2010). Evaluating the efficiency of frontier-based exploration strategies. In *ISR/ROBOTIK*, pages 1–8.

[29] J. Koch, A. and Meinhardt, H. (1994). Biological pattern formation, from basic mechanisms to complex structures. *Rev. Mod. Phys*, 66:1481.

[30] Karsenti, E. (2008). Self-organization in cell biology: a brief history. *Nature Reviews Molecular Cell Biology*, 9(3):255–262.

[31] Kondo, S. and Asai, R. (1995). A reaction-diffusion wave on the skin of the marine angelfish pomacanthus. *Nature*, 376:31.

[32] Krinsky, V. I., Biktashev, V. N., and Efimov, I. R. (1991). Autowave principles for parallel image processing. *Phys. D*, 49(1-2):247–253.

[33] Kuhnert, L., Aglazde, K. I., and Krinsky, V. I. (1989). Image-processing using light-sensitive chemical waves. *Nature*, 337(6204):244–247.

[34] Kulich, M., Faigl, J., and Přeučil, L. (2011). On distance utility in the exploration task. In *IEEE Int. Conf. on Robotics and Automation (ICRA)*, pages 4455–4460.

[35] L. Hodgkin, A. and F. Huxley, A. (1952). A quantitative description of membrane current and its application to conduction and excitation in nerve. *J. Physiology*, 49:500–544.

[36] Lechleiter, J., Girard, S., Peralta, E., and Clapham, D. (1991). Spiral calcium wave propagation and annihilation in xenopus laevis oocytes. *Science*, 252:123–126.

[37] M. Davidenko, J., Kent, P., and Jalife, J. (1991a). Spiral waves in normal isolated ventricular muscle. *Nature*, 49:182–197.

[38] M. Davidenko, J., Kent, P., and Jalife, J. (1991b). Spiral waves in normal isolated ventricular muscle. *Phys. D*, 49(1-2):182–197.

[39] M. Davidenko, J., M. Pertsov, A., Salomontsz, R., Baxter, W., and Jalife, J. (2000). *Models for pigment pattern formation in the skin of fishes*. Springer-Verlag (P. K. Maini and H. G. Othmer, eds.), Netherlands.

[40] M. Rogers, J. and D. McCulloch, A. (1994). A collocation-galerkin finite element model of cardiac action potential propagation. *IEEE Transactions on Biomedical Engineering*, 41:743–757.

[41] Maini, P. (2012). Turing's mathematical theory of morphogenesis.

[42] Markus, M., Kloss, G., and Kusch, I. (1994). Disordered waves in a homogeneous, motionless excitable medium. *Nature*, 371:402–404.

[43] Markus, M., Nagy-Ungvarai, Z., and Hess, B. (1992). Phototaxis of Spiral Waves. *Science*, 257(5067):225–227.

[44] Moravec, H. (1988). Sensor fusion in certainty grids for mobile robots. *AI Mag.*, 9(2):61–74.

[45] Murray, J. D. (2002). *Mathematical biology, III edition*. Springer-Verlag, Berlin.

[46] P. Munuzuri, A., Perez-Munuzuri, V., Gomez-Gesteira, M., O. Chua, L., and Perez-Villar, V. (1995). Spatio temporal structures in discretely-coupled arrays of nonlinear circuits: a review. *Int. J. of Bif. and Chaos (5)*, 1:17–50.

[47] P. Munuzuri, A., Perez-Munuzuri, V., Perez-Villar, V., and O. Chua, L. (1993). Spiral waves on 2d array of nonlinear circuits. *IEEE Trans. on Circ. Systems*, 40:872.

[48] Perez-Munuzuri, V., Perez-Villar, V., and Chua, L. (1993). Autowaves for image processing on a two-dimensional cnn array of excitable nonlinear circuits: flat and wrinkled labyrinths. *Circuits and Systems I: Fundamental Theory and Applications, IEEE Transactions on*, 40(3):174 –181.

[49] Petitot, J. (2015). Complexity and self-organization in turing. *ArXiv e-prints*.

[50] Puig, D., Garcia, M., and Wu, L. (2011). A new global optimization strategy for coordinated multi-robot exploration: Development and comparative evaluation. *Robotics and Autonomous Systems*, 59(9):635–653.

[51] Royer, S., Martina, M., and Pare, D. (2000). Bistable behavior of inhibitory neurons controlling impulse traffic through the amygdala: Role of a slowly deinactivating k+ current. *J. Neuroscience*, 20:9034.

[52] S . Zykov, V. (1987). *Biological rhythms and the behavior of populations of coupled oscillators*. Manchester University Press, Manchester.

[53] S. Cohen, D., C. Neu, J., and R. Rosales, R. (1978). Rotating spiral wave solutions of reaction-diffusion equations. *SIAM J. Appl. Math.*, 35:536.

[54] S. Gardner, T., R. Cantor, C., and J. Collins, J. (2000). Construction of a genetic toggle switch in escherichia coli. *Nature*, 403:339.

[55] S. Perelson, A., K. Maini, P., D. Murray, J., M. Hyman, J., and F. Oster, G. (1986). Nonlinear pattern selection in a chemical model for morphogenesis. *J. Math. Biol.*, 25:525.

[56] S. Schnell, J. Painter, K., K. Maini, P., and G. Othmer, H. (2000). *Spatiotemporal pattern formation in early development: A review of primitive streak formation and Somitogenesis*. Volumes in Mathematics and its Applications: Mathematical Models for Biological Pattern Formation (P. K. Maini and H. G. Othmer, eds.) Springer-Verlag, Berlin/Heidelberg.

[57] Showalter, K., Noyes, R., and Turner, H. (1979a). Detailed studies of trigger waves initiation and detection. *J. Am. Chem. Soc.*, 101:7463.

[58] Showalter, K., Noyes, R. M., and Turner, H. (1979b). Detailed studies of trigger wave initiation and detection. *Journal of the American Chemical Society*, 101(25):7463–7469.

[59] Showalter, K., Noyes, R. M., and Turner, H. (1979c). Detailed studies of trigger wave initiation and detection. *Journal of the American Chemical Society*, 101(25):7463–7469.

[60] Siegert, F. and J. Weijer, C. (1992). Three-dimensional scroll waves organize dictyostelium slugs. *Proc. Natl. Acad. Sci. USA*, 89(14):6433–6437.

[61] Steinbock, O., Kettunen, P., and Showalter, K. (1996). Engineering of dynamical systems for pattern recognition and information processing. *J. Phys. Chem.*, 100:18970–18975.

[62] Steinbock, O., Showalter, K., and Kettunen, P. (1994). Navigating complex labyrinths - optimal paths from chemical waves. *Science*, 100:868–871.

[63] T . Winfree, A. (1972). Persistent tangled vortex rings in generic excitable media. *Nature*, 175:634.

[64] T . Winfree, A. (1984). Organizing centers for three-dimensional chemical waves. *Nature*, 311:611.

[65] T. Winfree, A. (1967). Biological rhythms and the behavior of populations of coupled oscillators. *J. Theor. Biol.*, 16:15.

[66] T. Winfree, A. (1972a). Spiral waves of chemical activity. *Science*, 175:634.

[67] T. Winfree, A. (1972b). Spiral waves of chemical activity. *Science*, 175:634.

[68] Taboy, J. (2006). Historical and conceptual background of self-organization by reactive processes. *Biol. Cell*, (98):589–602.

[69] Thrun, S. (1998). Learning metric-topological maps for indoor mobile robot navigation. *Artificial Intelligence*, 99(1):21–71.

[70] Tovar, B., Muñoz-Gómez, L., Murrieta-Cid, R., Alencastre-Miranda, M., Monroy, R., and Hutchinson, S. (2006). Planning exploration strategies for simultaneous localization and mapping. *Robotics and Autonomous Systems*, 54(4):314–331.

[71] Trevai, C., Fukazawa, Y., Ota, J., Yuasa, H., Arai, T., and Asama, H. (2003). Cooperative exploration of mobile robots using reaction-diffusion equation on a graph. In *Robotics and Automation, 2003. Proceedings. ICRA '03. IEEE International Conference on*, volume 2, pages 2269 – 2274 vol.2.

[72] Trevai, C., Fukazawa, Y., Yuasa, H., Ota, J., Arai, T., and Asama, H. (2002). Cooperative exploration path planning for mobile robots by reaction-diffusion equation on graph. In *Industrial Technology, 2002. IEEE ICIT '02. 2002 IEEE International Conference on*, volume 2, pages 1266 – 1271 vol.2.

[73] Turing, A. M. (1952). The chemical basis of morphogenesis. *Philosophical Transactions of the Royal Society of London. Series B, Biological Sciences*, 237(641):37–72.

[74] van Saarlos, W. (2003). Front propagation into unstable states. *Physics Reports*, 386:29.

[75] Vanag, V. K. and Epstein, I. R. (2009). Pattern formation mechanisms in reaction-diffusion systems. *nternational journal of developmental biology*, 53(5-6):673–683.

[76] Vázquez-Otero, A., Faigl, J., Duro, N., and Dormido, R. (2014). Reaction-diffusion based computational model for autonomous mobile robot exploration of unknown environments. *International Journal of Unconventional Computing*, 4:295–316.

[77] Vázquez-Otero, A., Faigl, J., and Muñuzuri, A. (2012). Path planning based on reaction-diffusion process. In *Intelligent Robots and Systems (IROS), 2012 IEEE/RSJ International Conference on*, pages 896 –901.

[78] Vázquez-Otero, A., Faigl, J., and Muñuzuri, A. P. (2012). Path planning based on reaction-diffusion process. In *IEEE/RSJ Int. Conf. Intelligent Robots and Systems (IROS)*, pages 896–901.

[79] Vazquez-Otero, A. and Muuzuri, A. (2010). Navigation algorithm for autonomous devices based on biological waves. In *Cellular Nanoscale Networks and Their Applications (CNNA), 2010 12th International Workshop on*, pages 1–5.

[80] Yamauchi, B. (1997). A frontier-based approach for autonomous exploration. In *IEEE International Symposium on Computational Intelligence in Robotics and Automation (CIRA)*, pages 146–151.

Appendix A

Stability analysisis overview

A.1 Solving a linear system

Let's suppose a linear system of differential equations in the matricial form:

$$\dot{\vec{x}} = A\vec{x} \tag{A.1}$$

the solutions we are looking for are in the form: $\vec{x}(t) = e^{\lambda t}\vec{V}$ where $\vec{V}$ are the eigenvectors of the matrix $\vec{X}$. Replacing $\vec{x}(t)$ in A.1 we get $\left(A - \lambda\vec{\mathbf{I}}\right) = 0$ and the general condition for a non trivial solution is $\det|A - \lambda\mathbf{I}| = 0$. Thus, we have the system

$$\begin{vmatrix} a-\lambda & b \\ c & d-\lambda \end{vmatrix} = 0 \tag{A.2}$$

which gives a quadratic polinomia

$$\lambda^2 - \lambda(a+d) + (ad - bc) = 0 \tag{A.3}$$

whose roots

$$\lambda_{1,2} = \frac{(a+d) \pm \sqrt{(a+d)^2 - 4(ad-bc)}}{2} = \frac{\tau \pm \sqrt{\tau^2 - 4\Delta}}{2} \tag{A.4}$$

provides the well known solution

$$\overrightarrow{x}(t) = c_1 e^{\lambda_1 t}\overrightarrow{V_1} + c_2 e^{\lambda_2 t}\overrightarrow{V_2} \tag{A.5}$$

And finally, regarding the problem of initial condition:

$$x(t=0) = x_0 = c_1 v_1 + c_2 v_2 \tag{A.6}$$

A.2 Linearization around a fixed point

We are going to linearize the system at fixed points in such case To do this, a straightforward technique will be applied. Assuming that (x_0, y_0) represent a fixed point, a small perturbation around this point can be represented by: $(x_0+u, y_0+v) << \|u, v\|$. Our interest is to study the system in the area described by this perturbation. For this we only need to linearize the system in that region and study its behaviour. Since we are interested in the evolution of the variables (u, v) which represent the surroundings of the fixed point, the following transformation will be used:

$$\begin{array}{l} u = x - x_0 \\ v = y - y_0 \end{array} \quad and \quad \begin{array}{l} \dot{u} = \dot{x} \\ \dot{v} = \dot{y}. \end{array} \tag{A.7}$$

Introducing it in 3.17 gives

$$\begin{array}{l} \dot{u} = f(x_0+u, y_0+v) \\ \dot{v} = g(x_0+u, y_0+v) \end{array}. \tag{A.8}$$

Now considering the Taylor expansion at first order

$$f(x-x_0) = \sum_{k=0}^{\infty} \frac{f^k(x_0)(x-x_0)}{k!} \approx f(x_0) + f'(x_0)(x-x_0) + o\left(x^2\right)$$

an introducing the previous transformation $x = (u+x_0)$ whilst taking into account $f(x_0) = 0$, the Taylor expansion can be rewritten as:

$$f(x-x_0) \approx f'(x_0)\, u. \tag{A.9}$$

Trivially in a two-variables system:

$$f(x-x_0, y-y_0) \approx \partial_u f_{(x_0,y_0)} u + \partial_v f_{(x_0,y_0)} v + 0\left(x^2, y^2, xy\right). \tag{A.10}$$

Finally, let's rename $\partial_i f_{(x_0,y_0)}$ as f_i^*, leading 3.17 to adopt the following expresion:

$$\begin{array}{l} \dot{u} = f_u^* u + f_v^* v \\ \dot{v} = g_u^* u + g_v^* v \end{array} \tag{A.11}$$

that in matricial form turns out to be:

$$\begin{pmatrix} \dot{u} \\ \dot{v} \end{pmatrix} = \begin{pmatrix} f_u^* & f_v^* \\ g_u^* & g_v^* \end{pmatrix} \begin{pmatrix} u \\ v \end{pmatrix}, \tag{A.12}$$

or in a more compact form:

$$\mathbf{w}_t = \mathbf{A}\mathbf{w}. \tag{A.13}$$

For solving the system A.13 the prototypical solution is $\mathbf{w}\alpha\mathbf{v}e^{\lambda t}$. Where $\mathbf{v}$ is the associated eigenvector and λ represents the growing rate of the perturbation. Our interest is concerned with values of $\lambda < 0$ (exponential decay), otherwise the perturbation grows away from the fixed point. In view of this, a solution different of nontrivial must accomplish the following condition:

$$0 = |\mathbf{A} - \lambda\mathbf{I}| = \lambda^2 - \lambda tr\mathbf{A} + |\mathbf{A}|, \tag{A.14}$$

that provides the solutions:

$$\begin{aligned} \lambda_{1,2} &= \tfrac{1}{2}\left(tr\mathbf{A} \pm \sqrt{(tr\mathbf{A})^2 - 4|\mathbf{A}|}\right) \\ &= \tfrac{1}{2}\left((f_u + g_v) \pm \sqrt{(f_u + g_v)^2 - 4(f_u g_v - f_v g_u)}\right) \end{aligned} \tag{A.15}$$

A.3 Linearization with diffusion

Adding the diffusion term brings to the the equation:

$$\begin{aligned} \dot{x} &= f(x,y) + D_u \triangle x \\ \dot{y} &= g(x,y) + D_v \triangle y \end{aligned} \tag{A.16}$$

and using the same Taylor expansion than in previous section:

$$\begin{pmatrix} \dot{u} \\ \dot{v} \end{pmatrix} = \begin{pmatrix} f_u^* & f_v^* \\ g_u^* & g_v^* \end{pmatrix} \begin{pmatrix} u \\ v \end{pmatrix} + \begin{pmatrix} D_u & 0 \\ 0 & D_v \end{pmatrix} \begin{pmatrix} u \\ v \end{pmatrix} \tag{A.17}$$

or in the compact form:

$$\mathbf{w_t} = (\mathbf{A} + \mathbf{D}\triangle)\,\mathbf{w}. \tag{A.18}$$

Now the system posses spatial dependence, hence the possible solutions must reflect this fact: $\mathbf{w} \propto e^{\lambda t + i\vec{k}\vec{r}}$ (in a spatially extended system in two dimensions $\overrightarrow{r} = x\hat{i} + y\hat{j}$). Again, for obtaining non trivial solutions:

$$\begin{aligned} 0 &= \left|\lambda \mathbf{I} - A + Dk^2\right| \\ &= \left| \begin{pmatrix} \lambda & 0 \\ 0 & \lambda \end{pmatrix} - \begin{pmatrix} f_u^* & f_v^* \\ g_u^* & g_v^* \end{pmatrix} + \begin{pmatrix} D_u & 0 \\ 0 & D_v \end{pmatrix} k^2 \right| \\ &= \begin{vmatrix} \lambda - f_u^* + D_u k^2 & f_v^* \\ g_u & \lambda - g_v^* + D_v k^2 \end{vmatrix} \\ &= \lambda^2 + \lambda\left((D_u + D_v)k^2 - (f_u^* + g_v^*)\right) + h\left(k^2\right), \end{aligned}$$

where

$$h\left(k^2\right) = D_u D_v k^4 - k^2\left(D_v f_u^* + D_u g_v^*\right) + |\mathbf{A}|. \tag{A.19}$$

Therefore, the eigenvalues can be written as function of $h(k^2)$:

$$\lambda_{1,2} = \tfrac{1}{2}\left(-\left(k^2 \cdot tr\mathbf{D} - (tr\mathbf{A})\right) \pm \sqrt{\left(k^2 \cdot tr\mathbf{D} - (tr\mathbf{A})\right)^2 - 4h(k^2)}\right). \tag{A.20}$$

Reaction-Diffusion Process Based Computational Model for Mobile Robot Exploration Task

Alejandro Vázquez-Otero[1], Jan Faigl[2], Natividad Duro[1], Raquel Dormido[1]

***Abstract*— This paper presents an exploration algorithm based on properties of reaction-diffusion models. The approach is based on our previous work on this topic, in which a novel path planning algorithm was developed providing competitive paths to standard approaches like smoothness of the found solution. In this paper, it is shown how the developed principles can be applied in exploration of unknown environment with a mobile robot. The presented approach represents a novel exploration strategy where the main decision logic is based on principles arising from the underlying dynamics of the reaction-diffusion systems.**

I. Introduction

A robotic exploration can be defined as a process of building a map of unknown working environment, where a mobile robot is requested to autonomously cover all reachable regions by its sensory system. Many approaches have been proposed since the first frontier-based approach introduced by Yamauchi [1]. A frontier represents a part of the known reachable environment that is incident with the not yet explored regions. Using an occupancy grid approach [2] to integrate new sensor measurements into a probabilistic map, frontiers can be found as freespace cells incident with an unknown cell, e.g., found using 8-neighborhoods, in a navigation grid map generated from the occupancy grid by thresholding the probability values into three classes: freespace, obstacle, and unknown.

The frontiers are suitable candidates to be a next robot goal towards which the robot can be navigated because they represent a reasonable expectation that unknown parts of the environment will be covered from them. Hence, the problem of exploration can be defined as an iterative procedure in which the next robot goal is determined (by selecting from all frontiers according to the considered optimization criterion) and then the robot is navigated to that goal while collecting new sensoric information.

Beside the greedy approach [1] that simply selects the closest frontier to the current robot's position as the next goal, more advanced exploration strategies have been proposed [3], [4], [5]. In [6], authors consider an expected information gain of goal candidates generated within a sensor range vicinity of the frontiers. Then, such candidates are selected in the next-best-view manner according to an ad-hoc defined utility function in which an expected area of the unknown environment being covered by the candidate is taken into account. On the other hand, authors of [7] consider an explicit on-line segmentation of the map into a set of clusters that have to be explored to avoid repeated visits of the same area, e.g., to explore particular rooms.

In this paper, we address the exploration task using a new algorithm based on dynamics and underlying principles of Reaction-Diffusion (RD) models. Although it is similar in many aspects with a regular frontier-grid-based approach, it provides a new way to generate the goal candidates. Moreover, we define the main decision logic as well as necessary supporting algorithms using principles arising from the spatial evolution of state variables described by the nonlinear RD model. Based on this effort, we can introduce computational building blocks that provide a groundwork for the definition of a computational model based on RD processes to address various robotic navigation problems. Such a computational model may provide a mechanism by which a hardware solution of the computation can be realized in a practical deployment within real robots.

II. Reaction-Diffusion properties of the computational model

The considered computational model is based on an RD process, where a diffusive process responsible for the spreading of the substances out in the space and a reactive process, in which the substances are transformed into each other [8], [9], [10]. In particular, herein the FitzHugh-Nagumo (FHN) [11] model is considered, which adopts the basic form:

$$\begin{array}{rcl} \dot{u} & = & \varepsilon\left(u - u^3 - v + \phi\right) + D_u \triangle u \\ \dot{v} & = & \left(u - \alpha v + \beta\right) + D_v \triangle u \end{array}, \qquad (1)$$

where α, β, ϵ, and ϕ are parameters of the model.

The so-called bistable configuration is used, where null-clines (for $\dot{u} = 0$ and $\dot{v} = 0$ in the absence of diffusion) represent the shape depicted in Fig. 1, where intersections of both curves define the *fixed points* of the system, classified in stable (in green, towards which the concentration levels of the state variables (u, v) evolve naturally) and unstable (in red). Asymmetric configurations that constitute a simple method for modulating the relative stability of both stable states are depicted in Fig. 1c and Fig. 1b, where SS^+ and SS^- represent more and less stable states, respectively.

An interesting feature is that a system in a default configuration SS^- has a natural tendency to evolve towards SS^+ (the most stable state) if a small perturbation is introduced to the system. In addition, the frontwave driving this shift

[1] The authors are with the Department of Computer Sciences and Automatic Control, UNED, 28040 Madrid, Spain. Alejandro.vazquez@ieee.org, {nduro, raquel}@dia.uned.es

[2] J. Faigl is with the dept. of Computer Science and Engineering, Czech Technical University in Prague, Czech Republic faiglj@fel.cvut.cz

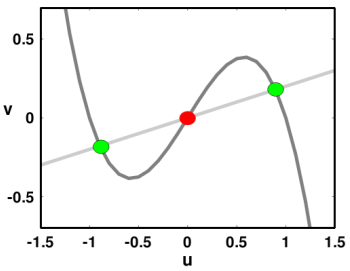

(a) General symmetric configuration for a bistable system. Both stable states are equally stable.

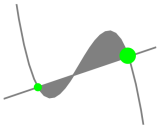

(b) propagation

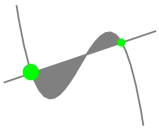

(c) contraction

Fig. 1. Nullcline configuration, the green disks represent stable states (SS) and the red disk represents unstable state.

exhibits different properties than standard waves, an attribute of the strong nonlinear character of the underlying model. Another remarkable feature is the possibility of regulating its behavior in such a way that can reproduced frontwaves that annihilates after a collision, or conversely frontwaves that do not interfere after a collision, and therefore, remain static at the collision point.

This behaviour is one of the fundamental principles used for the path planning algorithm introduced in [10] and in the proposed exploration algorithm described in the following section.

III. Exploration Strategy Based on Autowaves

The proposed exploration strategy is motivated by the idea to exhibit a similar behaviour as regular frontier-based approaches; however, our intention is to use different underlying principles based on features of the autowaves, which allows us to propose a new concept of utility function. Thus, the proposed approach follows standard exploration procedure with the main loop consisting of the steps:

1) Integrate new sensor measurements into a map;
2) Determine goal candidates;
3) Select the next goal;
4) Navigate the robot towards the goal.

In the first step, a common approach based on the occupancy grid is considered. The second step is solved in a new way by using the frontwave propagation. Also the next steps are based on principles of autowaves. In particular, the next goal is selected using the same principles of the frontwave propagation. Finally, the step four is solved using the autowaves-based path planning [10] to determine the path to the goal along which the robot is then navigated.

Prior a description of the proposed candidates' generation and goal selection methods, particularities of the exploring units and working environment in the proposed autowaves-based approach are exposed:

- The environment being explored is considered as a set of objects and boundaries represented by their edges, all treated as binary information.
- The exploring unit shapes the environment within its sensor range without any awareness about the correspondence between objects or boundaries.
- Since all is treated as binary information, the operational space is split into reachable and unreachable locations.

The goal candidates are determined as a border of the currently known space of the environment; hence the current map is used as a medium for exhibiting the RD model dynamics. A frontwave (triggered from a bistable configuration with annihilation) starts at the robot position and evolves as an ordinary fluid, covering all the available space, which provides the boundary of the reachable area for the stable state of the system. Then, superimposing obstacles detected by the sensor system (e.g., laser range scanner) results in the reachable border to the robot, as depicted in the red profile shown in Fig. 2, where a complete obstacle is drawn just for an illustration because only edges of obstacles are sensed by the scanner.

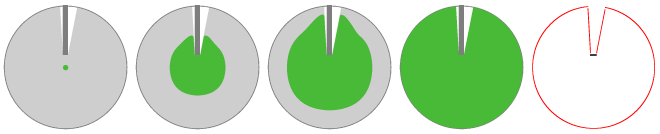

Fig. 2. A wavefront evolution in determination of the goal candidates. The light gray circular area corresponds to an omnidirectional sensor data (laser range scanner), whilst the dark gray rectangle in the top of the scene is an obstacle, which is completely drawn to improve clarity of the figure as only its edges can be sensed by the laser scanner. The green wavefront evolves from the robot position, covering all the discovered area till it reaches a static situation. The rightmost figure represents the final border reachable by the robot (depicted in red).

Once the border is determined, the next goal is selected using the autowaves-based path planning approach [10]. The border does not distinguish the unknown cells from the obstacles. An advantage of this planning is an ability to deal with noisy data (e.g., due to imperfect sensor measurements), see the referenced work for details.

A concept of utility functions for evaluating goal candidates aims to consider an expected benefit of the candidates to select the most suitable goal in order to improve performance of the exploration strategy according to the mission objective, e.g., to collect the map of the whole environment as quickly as possible. Such approaches usually combine the distance cost with expectations of exploring new areas [6], [3]. Contrary to these approaches, herein a different concept based on features of the frontwave propagation is proposed.

Fig. 3. Visualization of the utility introduction in the frontwave propagation for selecting the next goal. The gray circle represents a reachable area. The absence of obstacles allows the emerging frontwave to freely evolve from the robot position (slightly displaced downward relatively to the center of the circle) till the borders of the gray area, which in this particular case represents the boundary between explored and unexplored regions.

The dynamics of the underlying RD model allows to add an extra term representing additional information that is considered in the model evolution. Such an extra term is numerically represented as a matrix (an extra background with values from the range $bck \in \langle -2, 0 \rangle$) that selectively

introduces delays in the wavefront propagation, and therefore, it can prioritize (bck=0) some regions over others, $bck \in \langle -2, 0)$. Thus, a local modifications of nullclines for the particular cells of interest allow to adapt a configuration that inhibits the wavefront propagation.

Considering a general background that introduces a general delay in the propagation, its reduction around object (obstacle) cells turns out into an increase of the wavefront propagation velocity around those places, leading to a basic boundary-follower exploring unit, which significantly reduces the tendency to perform multiple-visit to the same regions. A demonstration of such modified evolution of the frontwave is shown in Fig. 3, where the growth of the frontwave in the vicinity of the wall is clearly faster than in any other direction.

IV. Results

The proposed autowaves-based exploration strategy has been employed in an exploration of a simple circular environment to verify the proposed concept. An example of the robot exploration path from which the whole environment is explored (covered) using an omnidirectional laser scanner with the sensing radius ρ=5 m is depicted in Fig. 4.

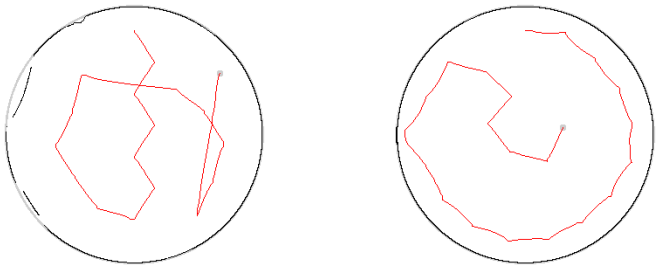

(a) open-space preference (b) wall-following preference

Fig. 4. An example of exploration strategies based on different settings of the computational model.

Based on these results, two additional environments are considered to verify feasibility of the proposed approach. In addition, the greedy exploration [1] approach (using all frontiers cells as goal candidates) and the TSP based approach [5] are used to provide a preliminary overview of the proposed strategy behaviour. In these strategies, the next goal is determined after performing 7 navigational primitives as it is recommended in [12].

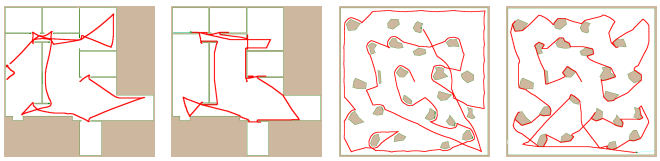

(a) *Autowaves*, ρ=7 m, L=110 m (b) *Greedy*, ρ=7 m, L=93 m (c) *Autowaves*, ρ=5 m, L=332 m (d) *TSP*, ρ=5 m, L=315 m

Fig. 5. An example of found solutions using different exploration approaches. The length of the final exploration path is denoted as L.

Selected exploration paths are shown in Fig. 5. Here, it should be mentioned that in these exploration scenarios, the proposed autowaves-based exploration approach has not been specifically tuned; hence, there is a possibility for an improvement of its performance. Regarding these preliminary results, it seems that the proposed exploration strategy provides competitive solutions to the standard approaches.

V. Conclusions and Future Work

In this paper, a novel exploration algorithm based on underlying principles of a reaction-diffusion model is presented. The proposed approach can be considered as a direct extension of our previous work, which introduced an autowaves-based path-planning method, and was found to exhibit interesting properties in comparison to standard approaches. Although the presented results can be considered as preliminary, they indicate feasibility of the proposed autowaves-based exploration and provide a premise for at least a competitive performance with the current state-of-the-art exploration methods. Moreover, the algorithm provides basic building blocks of a computational model for a mobile robot exploration solely based on an RD process, which is a subject of our future work.

Acknowledgments

This work has been funded by the National Plan Project DPI2011-27818-C02-02 of the Spanish Ministry of Economy and Competitiveness and FEDER funds.

The work of Jan Faigl has been supported by Czech Science Foundation GAČR under project No. 13-18316P.

The access to computing and storage facilities provided under the National Grid Infrastructure MetaCentrum, provided under project No. LM2010005 funded by Ministry of Education of Czech Republic is highly appreciated.

References

[1] B. Yamauchi, "A frontier-based approach for autonomous exploration," in *CIRA*, jul 1997, pp. 146–151.

[2] H. Moravec, "Sensor fusion in certainty grids for mobile robots," *AI Mag.*, vol. 9, no. 2, pp. 61–74, Jul. 1988.

[3] F. Amigoni and V. Caglioti, "An information-based exploration strategy for environment mapping with mobile robots," *Robotics and Autonomous Systems*, vol. 58, no. 5, pp. 684–699, 2010.

[4] D. Puig, M. Garcia, and L. Wu, "A new global optimization strategy for coordinated multi-robot exploration: Development and comparative evaluation," *Robotics and Autonomous Systems*, vol. 59, no. 9, pp. 635–653, 2011.

[5] M. Kulich, J. Faigl, and L. Přeučil, "On distance utility in the exploration task," in *ICRA*, 2011, pp. 4455–4460.

[6] H. Gonzalez-Banos and J.-C. Latombe, "Navigation Strategies for Exploring Indoor Environments," *International Journal of Robotics Research*, vol. 21, no. 10-11, pp. 829–848, 2002.

[7] D. Holz, N. Basilico, F. Amigoni, and S. Behnke, "Evaluating the efficiency of frontier-based exploration strategies," in *ISR/ROBOTIK*, 2010, pp. 1–8.

[8] A. Adamatzky, P. Arena, A. Basile, R. Carmona-Galan, B. Costello, L. Fortuna, M. Frasca, and A. Rodriguez-Vazquez, "Reaction-diffusion navigation robot control: from chemical to vlsi analogic processors," *IEEE Transactions on Circuits and Systems I: Regular Papers*, vol. 51, no. 5, pp. 926–938, may 2004.

[9] A. Vázquez-Otero and A. P. Muñuzuri, "Navigation algorithm for autonomous devices based on biological waves," in *CNNA*, 2010.

[10] A. Vázquez-Otero, J. Faigl, and A. P. Muñuzuri, "Path planning based on reaction-diffusion process," in *IROS*, 2012, pp. 896–901.

[11] R. FitzHugh, "Impulses and physiological states in theoretical models of nerve membrane," *Biophys. J.*, vol. 1, pp. 445–466, 1961.

[12] J. Faigl, M. Kulich, and L. Přeučil, "Goal assignment using distance cost in multi-robot exploration," in *IROS*, 2012, pp. 3741–3746.

Int. Journ. of Unconventional Computing, Vol. 10, pp. 295–316
Reprints available directly from the publisher
Photocopying permitted by license only

©2014 Old City Publishing, Inc.
Published by license under the OCP Science imprint,
a member of the Old City Publishing Group.

Reaction-Diffusion based Computational Model for Autonomous Mobile Robot Exploration of Unknown Environments

ALEJANDRO VÁZQUEZ-OTERO[1,3], JAN FAIGL[2], NATIVIDAD DURO[1] AND RAQUEL DORMIDO[1]

[1]*Department of Computer Sciences and Automatic Control, UNED, Madrid, Spain*
E-mail: Alejandro.vazquez@ieee.org, nduro@dia.uned.es, raquel@dia.uned.es
[2]*Department of Computer Science and Engineering, Faculty of Electrical Engineering, Czech Technical University in Prague, Czech Republic*
E-mail: faiglj@fel.cvut.cz
[3]*Institute of Physics, Academy of Science, Prague, Czech Republic*

Received: June 12, 2013. Accepted: November 4, 2013.

This paper introduces a computational model in which the main decision logic is based on principles arising from the dynamics of reaction-diffusion systems. The approach is an extension of our previous work where similar principles were used to develop a path planning algorithm. In this work, we select a mobile robot exploration task as a platform for exhibiting the core properties of the proposed computational framework. The functionalities represent particular building blocks that provide decision-logic capability of the exploration strategy. Beside a single mobile robot exploration, the proposed principles can also be generalized for multi-robot exploration, which is supported by the presented results.

Keywords: Reaction-diffusion equations, autowaves, exploration, mobile robots

1 INTRODUCTION

When surfing the rich tapestry of patterns arising when playing with nonlinear systems, a persistent idea comes to mind: there is a huge amount of decision-logic taking place in the background as the pattern develops [3]. By means of a simple Reaction-Diffusion (RD) system, a wide range of

behaviors can be reproduced: from simple excitations waves [19] to a more complex stable pattern formation through the so called Turing instability [23].

Beyond this, different instabilities or combinations of them [5, 24] have given rise to very intriguing static and dynamic structures. Moreover, the nuances found in the resulting concentration profiles reveal a mechanism that can be summarized in a single word: *self-organization*. A local transfer of information originates self-organize complex structures in a larger scale. Regarding this, it would be desirable to find out how to integrate this complex behavior into a conventional algorithm in order to take advantage of such implicit decision-logic as well as the nonlinear properties that RD systems exhibit.

Computationally, these concentration profiles are identified as simple geometric information, not surprisingly early works in this topic have already emphasized this point of view [11, 12, 14, 17, 19, 20, 26], subsequently extended by the motivation of introducing information into the system during the execution. This approach allows to codify such external information within the spatio-temporal dynamics, and constitutes the cornerstone of the present work. Here, it is used to solve the specific problems arising from a practical deployment of mobile robots.

In short, the approach relies in a computer algorithm based on a RD-core whose different configurations encapsulate the necessary logic to perform suitable decisions during the execution. The basis of the computation consists of a set of independent blocks each one holding a different model configuration designed to exhibit a particular decision-logic capability. Upon this, an algorithm can be built putting together several of these blocks in sequence, being the output information of each stage the input of the next one. The communication with the rest of the algorithm takes place through the exchange of 2D geometric information as a set of I/O operations. It can be understood in terms of "black box", where some inputs deliver some outputs and where the main benefit is the ability to deal with complexity in a natural way, constituting an RD-based computational approach to decision-solving algorithms.

There is a vast amount of properties that can be extracted from the general dynamics of an RD system, though those described below provides a satisfactory framework for designing algorithms focused on robotic applications:

- Natural parallelism of the model evolution.
- Natural resistance to isolated damaged cells, interpreted as noise resistance.
- The possibility of choosing annihilation or non-annihilation of front-waves upon a collision. Therefore the information can be mixed or not at any time during the execution.

- Absence of pattern formation during the frontwave evolution that is spread out like an ordinary fluid, which leads to a background recognition inside the algorithm, after covering all available space.
- Change of relative stability in a bistable configuration leading to a switch of the direction of the fronts propagation.

Each one of these properties encapsulates a different decision-logic capability. For instance, the non-annihilation provides information about frontwave collisions, where the particular location of that collision remains a part of the system evolution. Although the inclusion of additional properties can extend the scope of applicability, we restrict to the aforementioned ones, which have been successfully applied to the robotic exploration.

The mobile robot exploration refers to an algorithm to create a map of an unknown environment, *i.e.*, a problem, where a mobile robot is requested to autonomously cover all reachable regions by its sensory system. Although such an algorithm can be considered as tailored to accomplish a very specific mission, it provides a basis for decision-making principles throughout this work. Thus, it represents a special case of more general methods. Therefore herein is also used as a platform for introducing several capabilities of the proposed computational framework.

Beyond the basic feature of exploring an unknown area, a desired quality of the exploration algorithms relies upon the generation of a minimal-cost path by the exploring unit. This property can be specified by a distribution of the possible observation points, resulting in a set of points that minimizes the path length through the environment. In other words, this set of observation points guarantees an optimized route that a robot must follow to uncover with its sensory system the unknown environment, leading to an efficient exploration.

Therefore, measuring the performance of the exploration task is based on the strategy for determining the next goal. And consequently, the characterization of the exploration strategy is based on the optimizations used for the selection of such goals.

The basic exploration approach was introduced by Yamauchi in a seminal paper [28], along with the concept of frontier based exploration strategy. In Yamauchi's approach, the robot is navigated towards the closest location (the so-called frontier) in the limit between the known/unknown area. This approach provides a feasible solution of the exploration task and it forms a fundamental approach for more advanced exploration strategies [18], where additional improvements are in two streams. First stream focuses on determination of candidates from which next robot goal is selected. The second stream deals with the evaluation of navigation cost towards such goals. Thus,

not only the distance cost is used, but also additional aspects can be considered like localization issues [22] or expected utility of the next goal [1], *e.g.*, a combination of the distance cost with an expected information gain [8].

In this work, a new robot exploration algorithm fully based on RD processes is introduced and used for presenting a set of operations over the RD core. Although it is similar in many aspects to a regular frontier-grid-based approach, it provides a new way to generate goal candidates and to select the next goal. The approach is based on our previous work on computational autowaves applied to the path planning problem [25]. By considering the path planning method in the exploration task a new way to deal with multi-criteria cost function is provided.

The paper is organized as follows. A brief introduction to the underlying principles of the considered RD model and computational autowaves involved in the proposed approach are presented in Section 2 and Section 3. The proposed autowaves based exploration strategy is introduced in Section 4, evaluation of such strategy is presented in Section 5 together with a comparison with two standard exploration strategies. Besides, early results of the proposed computational principle applied to multi-robot exploration are presented. Concluding remarks are presented in Section 6.

2 BASIC AUTOWAVES BACKGROUND

The fundamental principles of the RD dynamics considered with the basic methods for triggering frontwaves in particular configurations are already published in our previous work [25, 26] together with introduction of the nullcline configurations that characterize the model dynamics. Nonetheless, we shall provide an overview of such RD-based computation principles to increase the overall readability of this paper. Therefore, this section is a roundup of pillars for RD based computation model, followed by a more detailed description of specific properties used in the exploration task.

2.1 Reaction-Diffusion Computational Core Properties

A reaction-diffusion system stands for an evolution of one or more substances, spatially distributed, by means of two processes. The diffusive process is responsible for spreading of the substances out in the space while in the reactive process the substances are transformed into each other. The considered mathematical model for describing the RD system is the FitzHugh-Nagumo (FHN) [7, 15] model, which adopts the basic form:

$$\begin{array}{rcl} \dot{u} & = & \varepsilon\left(u - u^3 - v + \phi\right) + D_u \triangle u \\ \dot{v} & = & (u - \alpha v + \beta) + D_v \triangle v \end{array} , \tag{1}$$

where α, β, ϵ, and ϕ are parameters of the model.

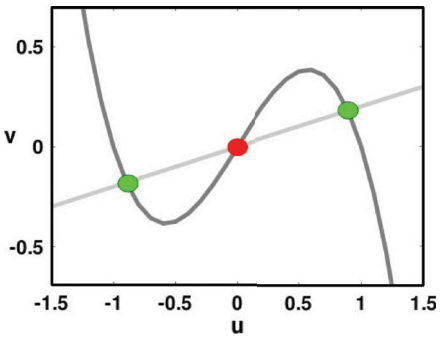

(a) General symmetric configuration for a bistable system. Both stable states are equally stable.

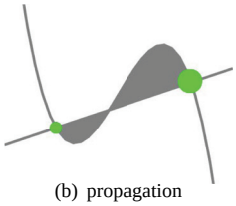

(b) propagation

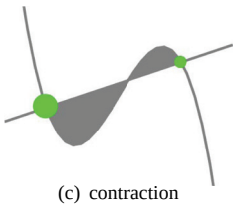

(c) contraction

FIGURE 1
Nullcline configurations, the green discs represent stable steady states (SS) and the red disc represents the unstable state.

The reactive process has a local character and it is responsible for the dynamics of the model, which can be characterized by the associated nullclines (the geometric shape for which $\dot{u} = 0$ and $\dot{v} = 0$ in the absence of diffusion). Thus, in the so-called bistable configuration, the nullclines represent the shape depicted in Figure 1, where intersections of both curves define the *fixed points* of the system. These fixed points can be classified in stable states (in green, states towards which the concentration levels of the state variables (u, v) evolve naturally) and an unstable state (in red).

Asymmetric configurations that constitute a simple method for modulating the relative stability of both stable states (the larger area under the curve defines a bigger stability) are depicted in Figure 1(c) and Figure 1(b). Therefore, it is possible to differentiate between SS^+ and SS^- for each asymmetric configuration. Which represent a particular case for a more stable state and less stable state, respectively.

As the natural tendency of the system is evolving towards the concentration level of SS^+. A default configuration in SS^- causes the system to move to SS^+ when a small perturbation is introduced. The frontwaves driving this shift are well known for exhibiting different properties from standard waves, which is an attribute of the strong nonlinear character of the underlying model. Its behavior can be regulated by means of the nullcline configuration, it is possible to reproduce either frontwaves that annihilates after a collision, or conversely frontwaves that do not interfere after a collision, remaining static at the collision point. This fact contains a fundamental result from the information processing point of view: as long as collisions turns out

in an active part of the model evolution, tracking of such collisions becomes unnecessary.

2.2 The Computational Model

The computation of the RD model itself takes place within a Cartesian grid in which the FHN model is discretized following the forward in time centered in space scheme (FTCS), *i.e.*, the model evolution is performed within the integration grid. The discretization is bounded by Dirichlet conditions aimed to stop any wavefront propagation in the limits of the integration grid. Therefore, all computations rely on the dynamics of the spatially coupled cells endowed with the FHN model, where the short cell connectivity provided by the Laplacian term (coming from the associated diffusion process and which is responsible for the frontwaves propagation) is also the key allowing a simple hardware implementation.

The output of the model calculations consists of the concentration profiles for both variables: u and v. The employed process for the proposed decision logic is based on the dynamics of u; however, v provides a similar behavior.

Finally, the model allows us to consider additional constraints to the dynamics, which stands for an extra (point dependent) term aimed to represent the environmental information. Thus, the final expression to be discretized becomes a sum of the FHN model and the map grid containing information about the environment.

Note about the Computational Model – The proposed approach aims to use the evolution of the underlying RD model as much as possible for avoiding explicit computation, *e.g.*, using computer graphics methods. The main interest of transferring as many operations as possible to the RD framework is because of possibility to use a hardware implementation for the underlying numerical models. This has been already discussed in [16] and some examples of practical realizations can be found in [2, 10, 27] providing a real time environment for the used operations. The particular techniques related to the exploration task are presented in Section 4.

3 PROPERTIES OF THE RD BASED COMPUTATIONAL MODEL

The underlying RD model provides the basic computational model exhibiting evolution of state variables u and v, which are used to build a decision-making logic for a particular problem. On top of this, we can exploit the model by considering its specific parameters and its behaviour after introducing additional information into the computational grid model. The following

sections are dedicated to the particular properties that are used in the RD based computational framework for mobile robot exploration.

3.1 RD based Path Planning with Binary Forcing

The path planning problem is the problem of finding a shortest collision free path starting from some initial location and ending at the desired location, while a robot navigated along the path will avoid a collision with obstacles. A path planning algorithm based on the discussed RD computational principles has been introduced in [25] and the key point of the method is a consideration of the obstacles in a form of grid map used for forcing the RD model. The concept of the RD based planning is visualized in Figure 2.

The planning algorithm consists of two phases: *propagation* and *contraction*. The dynamics of the *propagation* phase is ruled by the nullcline configuration depicted in Figure 1(b), whilst the *contraction* phase is governed by the configuration shown in Figure 1(c). The algorithm works as follows. First, the system is initially set in SS^- and a small perturbation is introduced at the robot location, which triggers a frontwave to move the system towards SS^+, see the upper-left picture in Figure 2. When the frontwave reaches the goal area (*i.e.*, changing the concentration values to SS^+), which can be

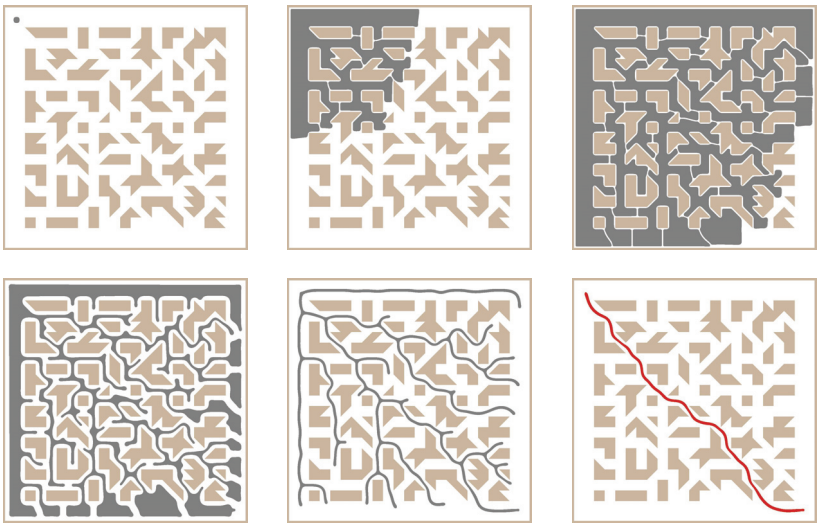

FIGURE 2
An example of the system evolution in the path planning problem; *upper*: propagation phase; *bottom*: contraction phase. The free space is in white and obstacles are in brown; values of the u state variable are in gray; the final solution is shown in red.

easily detected to constitute the termination condition for the propagation, the *contraction* phase is activated. During the contraction phase, the start and goal locations are simultaneously kept at the concentration levels of SS^- in opposition to the system tendency of evolving towards SS^+.

The result of combining the changing of phase together with forcing the start and goal locations in the *contraction* phase is shown in the bottom row in Figure 2. The contraction of the domain $\left(SS^-\right)_{contract}$ over itself in benefit of the more stable domain $\left(SS^+\right)_{contract}$ leads to a final single path linking the start and goal locations, which corresponds to the requested shortest path.

3.2 Gradient-like Forcing: Modifying the Frontwave Velocity

In the previous section, a binary grid in the form of the grid map of the environment has been introduced as external information into the integration grid through the local modification of the nullclines of the particular point of interest (the obstacles). It means that at each point of the grid representing an obstacle the nullcline configuration is replaced by other that inhibits the wavefront propagation. This inhibition is suitable for introducing binary information into the integration grid and thus any propagating will stop at reaching any of these locations. However, it is also possible to introduce gradient-like information by means of an extra matrix (point dependent) F that is added to the model. Considering this term, the final form of the computational model is:

$$\begin{aligned} \dot{u} &= \varepsilon\left(u - u^3 - v + \phi\right) + F + D_u \triangle u \\ \dot{v} &= (u - \alpha v + \beta) + D_v \triangle u \end{aligned} \quad . \tag{2}$$

Equation (2) is a common procedure for introducing different types of spatial or even temporal forcing in the model evolution. Based on this formulation, we can establish an effective range from zero to a specific value to gradually generate an increasing delay in the frontwave advance till the complete inhibition of the propagation. Therefore, environmental information can be introduced by means of the above described matrix, which slows down the frontwave propagation according to the predefined strength. An example of such a behavior is depicted in Figure 3, where a planar frontwave evolves according to a different values of F along the vertical axis: a maximum delay in the upper part of the front regarding the lower part where the value $F = 0$ means no forcing at all. Therefore, we can generate a profile that exhibits a gradient of velocities in the wavefront propagation along the vertical axis. This result is compatible with other RD properties used in the framework, like the annihilation upon a collision, and hence opens up a wide range of possibilities.

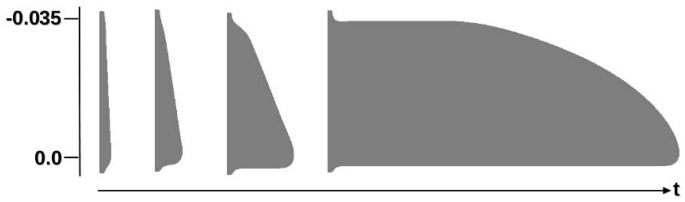

FIGURE 3
A profile of velocities in a wavefront propagation in 2D (300×700 grid size) under the influence of the F matrix, where the abscissa represents four states of the same evolving front at different times. The forcing matrix F is introduced along the vertical axis, with values in the range $\langle 0, -0.035 \rangle$.

4 EXPLORATION STRATEGY BASED ON AUTOWAVES

Although the proposed exploration strategy exhibits similar behaviour as regular frontier-based approaches, it is based on different underlying principles. That is why we split the description into a formal characterization of the algorithm, features of the autowaves applied in the exploration task, and proposed concept of utility consideration in the selection of the next goal for a mobile robot. The proposed approach follows standard exploration procedure in which the main loop can be defined by the following steps:

1. Integrate new sensor measurements into a map;
2. Determine goal candidates;
3. Select the next goal;
4. Navigate the robot towards the goal.

For the first step, we consider a common approach based on the occupancy grid [4]. However, the next three steps are based on principles of autowaves. In particular, instead of explicit Yamauchi's frontiers search, we use propagation of the frontwave to determine the possible goal candidates. The candidates correspond to frontiers; however, we can take advantages of the RD model dynamics and consider the determination of the candidates in a completely new way, see Section 4.1. The next goal is then selected by using the same principles used in the propagation of the frontwave. Finally, we employ the autowaves-based path planning [25] to determine the path to the goal along which the robot is then navigated. A detailed description of these three steps is presented in Section 4.1. Moreover, the new concept of dealing with utility of the goal candidates is proposed in Section 4.2.

The following assumptions need to be considered to expose the particularities of the exploring units and working environment in the proposed autowaves-based exploration approach:

- The map being explored consists of a series of objects and boundaries, all treated as binary information.
- Objects and boundaries are both represented by their edges.
- Each object or boundary within the sensor range is interpreted as an object–edge. Therefore, the exploring unit shapes the environment without any awareness about the correspondence between objects or boundaries.
- Since everything is treated as binary information, the discovered area is simply split into reachable and unreachable locations.

4.1 Determination of the Next Goal

The goal candidates are determined as a border of the currently known space of the environment. Here, the current map of the environment is used as a medium for exhibiting the RD model dynamics. The principle of the process is visualized in Figure 4. A frontwave (triggered from an excitable null-cline configuration) starts at the robot position and evolves as an ordinary

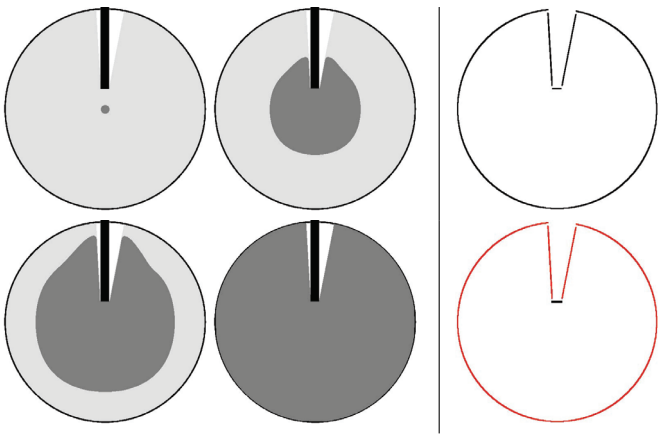

FIGURE 4
Calculation of the frontier using autowaves. Four left pictures represent a wavefront evolution. In particular, the light gray circular area corresponds to an omnidirectional sensor data (laser scanner), whilst the black rectangle in the top is an obstacle. The gray wavefront evolves from the robot position, covering all the discovered area till it reaches a static situation. The rightmost pictures represent the complete profile of the wavefront (top), and the final border reachable to the robot depicted in red (bottom).

fluid, covering all the available space (freespace in the integration grid) while adopting the shape of the space, and therefore, providing the boundary of the reachable area after reaching a static situation. Then, superimposing the obstacles (unreachable positions) results in the reachable border to the robot, as depicted in the red profile shown in Figure 4* .

The determined border corresponds to the frontier; however, the main difference is that we consider only reachable and unreachable parts of the space and all the logic of getting the contour is provided by the underlying dynamics of the RD system.

Once the border is determined, the next goal can be selected. Even though any path planning algorithm can be eventually used, we rather consider autowaves based approach [25]. The border does not distinguish the unknown cells from the obstacles. However, the frontwave propagation within the determined area given by the border takes advantage of the superimposing obstacles because autowaves preserved a distance (according to the wavelength of the frontwave) from the obstacles, see [25] for a more detailed discussion. An example of determining the next robot goal together with the determination of the path using the propagation and contraction phases is depicted in Figure 5. Another example of the goal determination is shown in Figure 9.

4.2 Utility Function

The aforementioned algorithm provides a basic approach for the exploration task and can be considered similar to the greedy frontier-based approach. The performance of the frontier-based exploration can be improved using the so-called utility function. It aims to consider an expected benefit of the frontiers to select the most suitable frontier in order to fulfill the mission objective, *e.g.*, to collect the map of the whole environment as quickly as possible. Such approaches usually combine the distance cost with expectations about new areas, *e.g.*, based on entropy [1]. Contrary to these approaches, we propose a different concept based on features of the frontwave propagation.

The dynamics of the underlying RD model allows to add an extra term representing additional information that is considered in the model evolution. This is numerically represented as a matrix (point dependent) term that can selectively introduce delays in the wavefront propagation, and therefore, it can prioritize some regions over others. This means that gradient-like information, rather than a binary map, can be used to represent the working environment. Consequently, the shortest-path technique for determination of the next goal can be switched into a more interesting lower-cost-path technique.

* Notice, the rectangular obstacle is drawn only for the visualization purpose as only its bottom edge is detected by the sensor system.

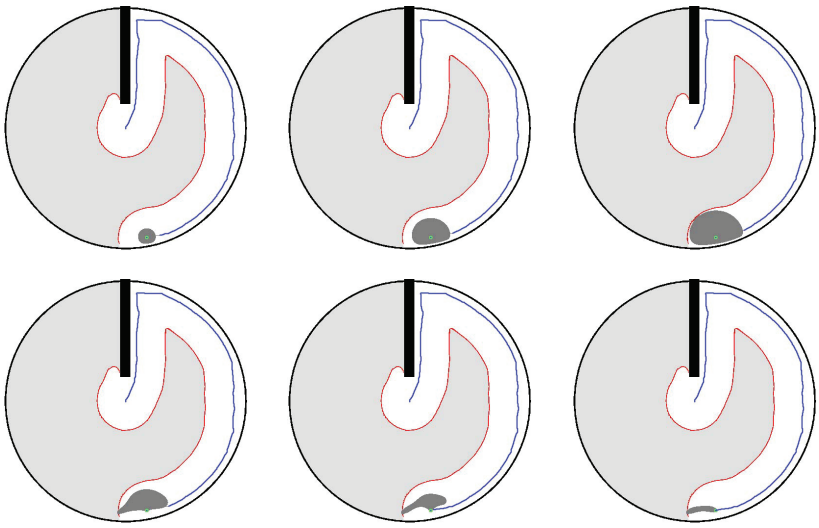

FIGURE 5
An example of determination of the next goal and the particular path towards the goal in a circular shaped environment. The already explored area is in white while the gray denotes not yet explored areas; the black color is the shape of the environment and the obstacles are superimposed only for a visualization purpose as they are not known during the exploration.

For example, we can establish a range $\langle -2, 0\rangle$ to the computational grid. Then, the range can discriminate states from the complete stop of the frontwave propagation (the value -2) over successively decreasing resistance till the effect vanishes (the value 0). In this sense, a very simple yet surprisingly useful utility function can be defined as follows:

1. Introduce an extra background (-0.35) within the explored area at every cell point, which in general slows down the wavefront evolution.
2. Remove the extra background from all cells representing objects as wells as their neighboring cells in the radius of 25 cells.
3. Change the value of the extra background from -0.35 to -0.25 for all cells at the border (frontiers-like cells) and their neighboring cells with the same radius 25 cells; thus, decreasing the resistance to the frontwave propagation.

Removing the extra background at the cells containing information about objects (obstacles) turns out into an increase of the wavefront propagation velocity around those places, and therefore, we get a basic boundary-follower

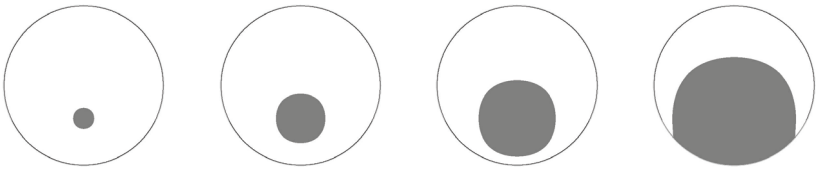

FIGURE 6
Demonstration of the utility introduction in the autowaves-based exploration approach. The circle represents a reachable area. The absence of obstacles allows the emerging frontwave to freely evolve from the robot position (slightly displaced downward relatively to the center of the circle) till the borders of the gray area, which in this particular case represents the boundary between explored and unexplored regions. Notice how the frontwave is not evolving to directly follow the circular shape since in the vicinity of the boundary, the forcing values have been deleted, which locally increases the speed of the frontwave.

exploring unit, which significantly reduces the tendency to perform multiple-visit to the same regions. A demonstration of such modified evolution of the frontwave is shown in Figure 6, where the growth of the frontwave in the vicinity of the wall is clearly faster than in any other direction.

5 RESULTS

The proposed building blocks of the RD core of the studied computational model have been verified in a series of exploration problems. The main intention of the presented results is to demonstrate feasibility of the proposed computational techniques and to provide an initial overview of the expected performance of the RD based exploration strategy. A natural performance metric for the exploration is the total time required to explore the environment, which can be estimated by the total traveled path. However, the real required time can be different according to the particular navigation strategy and low-level motion control. Thus, due to very high computational complexity of the underlying RD model implemented using a regular CPU the presented results focus on the travelled path[†] .

The section is divided into three subsections to show particular properties of the proposed RD based computational model. A demonstration of the alternative approach to the so-called utility based exploration is presented in Section 5.1, where the proposed concept of introducing preferences of areas to be explored by adding extra background is employed in a simple environment. In Section 5.2, the proposed computational principles of the selection

[†] The real-time factor is dedicated to our next work where a hardware parallelization will provide the required computational power.

of the next robot goal and the consecutive path planning (both based on the RD model) are employed in the exploration task by a single robot. In this case, the computational principles are integrated to the exploration framework introduced in [6]. The proposed computational model can be easily extended for multi-robot exploration, which is demonstrated in Section 5.3. A discussion of the achieved results is dedicated to Section 5.4.

5.1 Demonstration of Introducing Preferences of Areas to be Explored

The introduction of the extra background as the gradient like forcing allows to modify the velocity of the frontwave propagation; hence, it provides a mechanism to prefer exploration of specific parts of the environment, *i.e.*, a kind of the utility function (see Section 4.2). This proposed concept has been verified in an exploration of a simple circular environment. In this simulation, the robot is equipped with an omnidirectional laser scanner with the sensing radius 5 m.

Two basic implementations of the utility function are visualized in Figure 7, which leads to two different behaviors. In the left case, the function is designed to prefer unexplored areas, this is achieved by decreasing the extra background along regions of the frontier that do not represent obstacles, therefore these regions become candidates for the next goal. As a consequence, the robot prefers to explore the open-space first. Conversely, in the right sub-figure, the background is especially decreased along detected obstacles, which increases the frontwave velocity along these regions. Therefore,

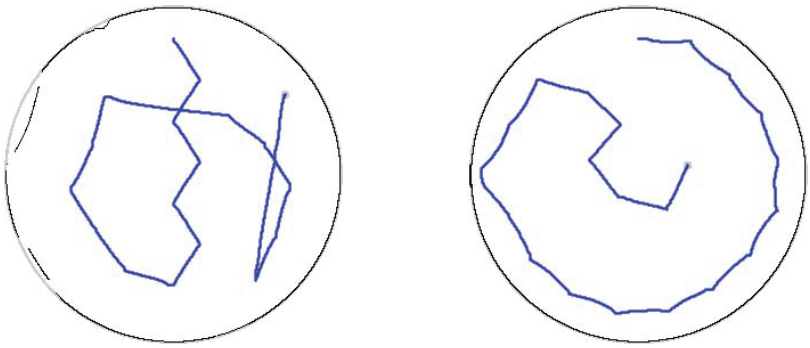

(a) open-space preference (b) wall-following preference

FIGURE 7
Visualization of the exploration behaviour for two different settings of the RD based computational model using extra background for modifying velocity of the frontwave propagation. The blue curve represents the traveled path of the robot to explore the whole environment.

once the robot discovers an obstacle, the next goal is naturally selected close to the already known obstacles, which provides a wall-following behaviour.

5.2 Performance of the RD based Exploration and Standard Approaches

The proposed principles of the selection of the next robot goal and planning a path to the goal by means of propagation of the frontwave in the known reachable environment have been integrated into the exploration framework [6]. The integration provides an initial overview of the performance of RD based exploration strategy in comparison to standard approaches. The considered performance indicator is the path length of the robot to explore the whole environment.

The proposed RD based exploration strategy does not explicitly consider information gain, and therefore, it can be considered as a pure distance cost strategy. Therefore, we select the greedy exploration [28] and the TSP based approach [13] with the TSP distance cost for the comparison presented. However, a direct comparison of the approaches is not an easy task. It is because the proposed approach is based on a different computational model, where some properties directly accessible in regular frontier-based approaches are not straightforwardly and easily tunable. For example, a filtration of small frontier groups, which can significantly improve performance [9], and especially the planning horizon [6], *i.e.*, a period of new goal determination. Thus, a direct comparison of the results would not be fair, and therefore, we include two variants of the greedy and TSP exploration strategies.

In the first variant, denoted by a subscript 1 (*i.e.*, $greedy_1$ and TSP_1), the next goal is determined after the robot reaches its current goal (like in the RD based exploration), while in the second variant ($greedy_2$ and TSP_2), the next goal is determined after performing 7 navigational primitives, as it is suggested in [6]. In all these approaches, selected representative of the frontiers are considered as goal candidates using K-means algorithm, which decreases the computational burden of the TSP solution and also improves the exploration performance. A further description of this selection can be found in [13].

The RD based and greedy strategies are deterministic while the TSP based strategy is a stochastic method (due to the used approximate solution of the TSP). Despite that, we consider a single trial for each problem in this feasibility study and thus the presented results have only an indicative importance.

Two environments denoted as *autolab* and *potholes* are considered for the evaluation. The *autolab* environment represents an office like environment with dimensions 35×30 meters, and the *potholes* environment is a large open space (40×40 meters) with several obstacles, see Figure 8.

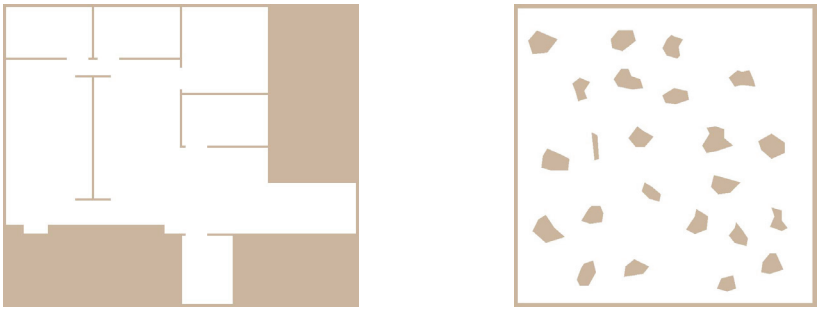

(a) *autolab* (b) *potholes*

FIGURE 8
Environments considered in the feasibility evaluation of the RD based exploration.

An example of the frontwave propagation during the selection of the next robot goal and the consecutive contraction phase of the used RD based path planning [25] is shown in Figure 9.

Indicative results are presented in Table 1, where the columns represent the length of the total traveled path (in meters) for the particular sensor range ρ. Notice, how a faster replanning period improves the exploration performance. On the other hand, for replanning after reaching the current goal,

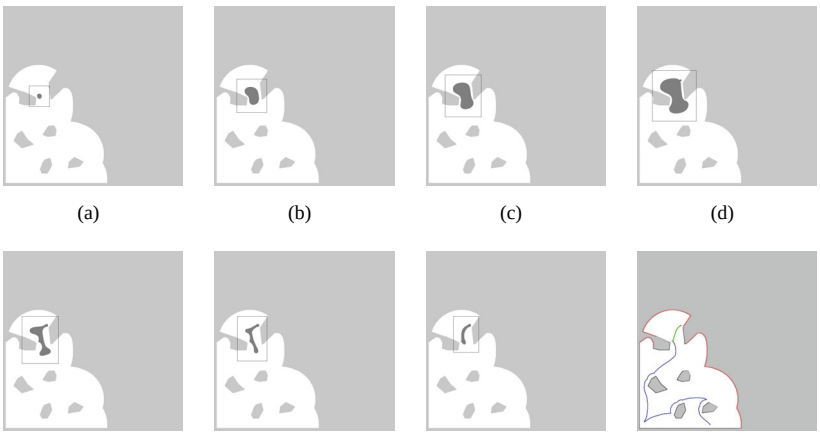

(a) (b) (c) (d)

(e) (f) (g) (h)

FIGURE 9
Propagation of the frontwave towards goal candidates, selection of the next goal (**a-d**), an evolution of the RD model for the determination of the path to the selected goal (**e-g**) and the final found path is shown in green in the bottom rightmost picture; (**h**) the current travelled path is in blue.

	autolab			*potholes*		
Algorithm	**ρ =3 m**	**ρ =5 m**	**ρ =7 m**	**ρ =3 m**	**ρ =5 m**	**ρ =7 m**
RD based	256.1	196.4	141.1	570.7	375.7	271.1
$Greedy_1$	262.5	232.5	182.9	545.8	398.8	320.4
TSP_1	263.0	222.8	174.9	543.9	342.5	283.0
$Greedy_2$	223.6	183.7	118.2	552.6	349.0	276.8
TSP_2	219.1	159.4	107.8	466.5	345.6	243.1

TABLE 1
Length of the Exploration Path

the RD based exploration provides competitive results to other approaches. Selected exploration paths for particular exploration strategies are depicted in Figure 10.

5.3 An Extension of the Proposed RD based Computational Model for Multi-Robot Exploration

The proposed computational model can be easily extended for exploration by a team of mobile robots. The extension can be considered as a

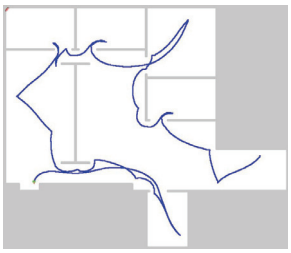

(a) *autolab*, *RD*, ρ=7 m

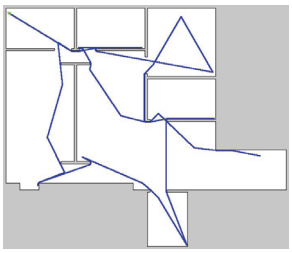

(b) *autolab*, $Greedy_1$, ρ=7 m

(c) *potholes*, *RD*, ρ=5 m

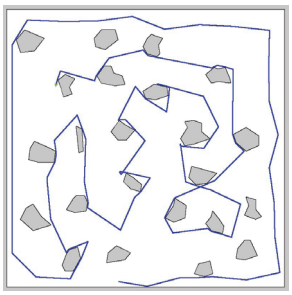

(d) *potholes*, TSP_1, ρ=5 m

FIGURE 10
Final exploration paths, the edges of the detected obstacles are in black while the unexplored areas (“inside the obstacles”) are in gray.

semi-centralized approach, where the robots are considered independently while they shared a common map of the environment being explored. The proposed demonstration of the multi-robot exploration works as follows:

- Prior the determination of the next robot goal, each robot makes a local copy of the common map.
- The position of the other robots is introduced to the local map as solid objects; thus, robot considers the remaining robots as simple obstacles.
- A single step of the exploration algorithm is performed and new information is gathered from the environment.
- The local maps are merged into the common map (*e.g.*, using the notion of occupancy grid and Bayes' rule like in [21]) and the process of determination of the robot goals is repeated.

The termination condition of the exploration is identical as in the single exploration algorithm, *i.e.*, the exploration is terminated if all goal candidates (frontiers) have been covered. Examples of selected steps of the multi-robot exploration are visualized in Figure 11.

5.4 Discussion

The presented results indicate the proposed RD computational model based on the underlying dynamics of the highly non-linear system can be employed in the mobile robot exploration problem and it also seems the RD based exploration provides competitive exploration paths to the standard approaches.

Regarding the computational requirements of the proposed computational model based on the evolution of the RD model, it should be noted that it can take an advantage of the implicit parallel propagation; hence, it can be computed in parallel, and therefore, pruning all the possible solutions to the most adequate ones in parallel as well. This makes us optimistic about future implementation using massive parallel computation and a practical deployment of the method in real exploration problems.

Based on the presented results, we shall split our future work in two different streams. The first stream is to elaborate a detailed stability analysis of the diverse nullcline configurations used along this work to provide theoretical foundations for building blocks of the proposed RD based computational core. The second stream is to develop the exploration algorithm in order to perform quantitative comparisons with other state-of-the-art methods. This also includes study of the proposed concept of the utility towards exhibition of the benefits arising from a different computational model used for the decision-logic in the exploration missions.

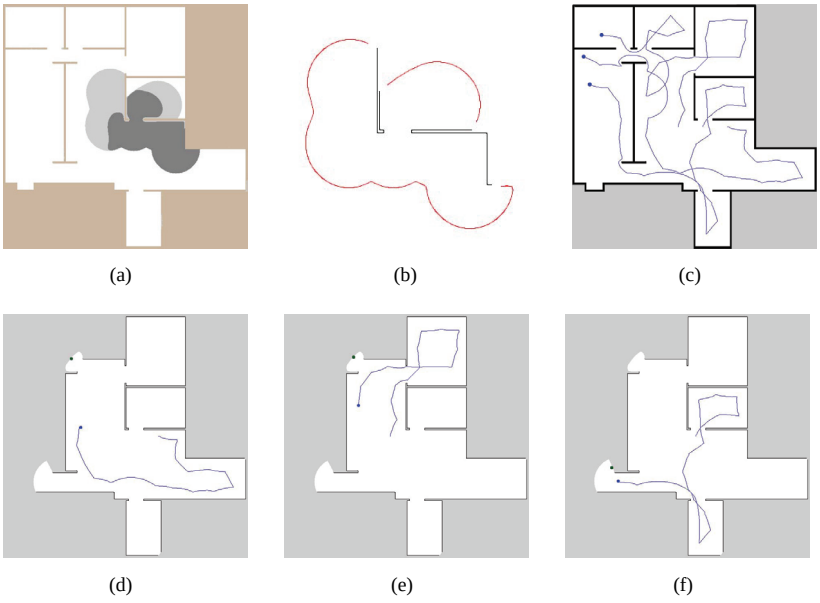

FIGURE 11
Examples of selected steps of the multi-robot exploration: (**a**) frontwave propagation during determination of the possible goal candidates (frontiers) superimposed to the map of the environment; (**b**) determined goal candidates (part of the map is enlarged for the sake of clarity); (**c**) final exploration paths for all robots; (**d**), (**e**), (**f**) same step of the exploration algorithm from the perspective of each robot (notice that all robots share the same map, corresponding to the whole discovered area in this particular step).

6 CONCLUSIONS

We present particular building blocks of a new computational model based on underlying principles of a reaction-diffusion model. The approach bears a huge potential for formalization due to its flexibility to be specialized and ease to incorporate new properties coming from the general dynamics of RD systems. In particular, herein, the approach has been successfully employed for solving the exploration task studied in mobile robotics. The approach constitutes a direct extension of our previous work where an autowaves-based path-planning was introduced, exhibiting interesting properties in comparison to standard approaches.

Although the presented results are preliminary, they indicate feasibility of the proposed RD based exploration and provide a premise for at least a competitive performance with the current state-of-the-art methods. The premise provides a ground for a further development towards a complete

computational model for robotic tasks solely based on RD principles; thus, an approach where the decision logic is transfered to the RD core, which consistently provides ability of hardware implementation for real-time operations.

ACKNOWLEDGMENTS

This work has been funded by the National Plan Project DPI2011-27818-C02-02 of the Spanish Ministry of Economy and Competitiveness and FEDER funds.

The work of Jan Faigl has been supported by Czech Science Foundation GAČR under project No. 13-18316P.

The access to computing and storage facilities provided under the National Grid Infrastructure MetaCentrum, provided under project No. LM2010005 funded by Ministry of Education of Czech Republic is highly appreciated.

REFERENCES

[1] Francesco Amigoni and Vincenzo Caglioti. (2010). An information-based exploration strategy for environment mapping with mobile robots. *Robotics and Autonomous Systems*, 58(5):684–699.

[2] Paolo Arena, Marco Branciforte, and Luigi Fortuna. (1998). A cnn-based experimental frame for patterns and autowaves. *International Journal of Circuit Theory and Applications*, 26(6):635–650.

[3] Miroslav M. Novak (Editor). (2006). *Complexus Mundi: Emergent Patterns in Nature*. World Scientific.

[4] Alberto Elfes. (1987). Sonar-based real-world mapping and navigation. *IEEE Journal of Robotics and Automation*, 3(3):249–265.

[5] Irving R Epstein, Igal B Berenstein, Milos Dolnik, Vladimir K Vanag, Lingfa Yang, and Anatol M Zhabotinsky. (2008). Coupled and forced patterns in reactiondiffusion systems. *Philosophical Transactions of the Royal Society A: Mathematical, Physical and Engineering Sciences*, 366(1864):397–408.

[6] Jan Faigl, Miroslav Kulich, and Libor Přeučil. (2012). Goal assignment using distance cost in multi-robot exploration. In *IEEE/RSJ Int. Conf. Intelligent Robots and Systems (IROS)*, pages 3741–3746.

[7] Richard Fitzhugh. (1961). Impulses and physiological states in theoretical models of nerve membrane. *Biophysical Journal*, 1(6):445–466.

[8] Hector H. Gonzalez-Banos and Jean-Claude Latombe. (2002). Navigation strategies for exploring indoor environments. *The International Journal of Robotics Research*, 21(10-11):829–848.

[9] Dirk Holz, Nicola Basilico, Francesco Amigoni, and Sven Behnke. (2010). Evaluating the efficiency of frontier-based exploration strategies. In *ISR/ROBOTIK*, pages 1–8.

[10] Koray Karahaliloglu and Sina Balkir. (2005). Bio-inspired compact cell circuit for reaction-diffusion systems. *IEEE Transactions on Circuits and Systems II: Express Briefs*, 52(9):558–562.

[11] V. I. Krinsky, V. N. Biktashev, and I. R. Efimov. (1991). Autowave principles for parallel image processing. *Phys. D*, 49(1-2):247–253.

[12] L. Kuhnert, K. I. Aglazde, and V. I. Krinsky. (1989). Image-processing using light-sensitive chemical waves. *Nature*, 337(6204):244–247.

[13] Miroslav Kulich, Jan Faigl, and Libor Přeučil. (2011). On distance utility in the exploration task. In *IEEE Int. Conf. on Robotics and Automation (ICRA)*, pages 4455–4460.

[14] A. S. Mikhailov. (1989). Engineering of dynamical systems for pattern recognition and information processing. In AndreiV. Gaponov-Grekhov, MikhailI. Rabinovich, and Jri Engelbrecht, editors, *Nonlinear Waves*, Research Reports in Physics, pages 104–115. Springer Berlin Heidelberg.

[15] J. Nagumo, S. Arimoto, and S. Yoshizawa. (1962). An active pulse transmission line simulating nerve axon. *Proceedings of the IRE*, 50(10):2061–2070.

[16] Alberto P. Mu nuzuri and Alejandro Vázquez-Otero. (2008). The cnn solution to the shortest-path-finder problem. In *11th International Workshop On Cellular Neural Networks and Their Applications*, pages 248–251.

[17] V. Perez-Munuzuri, V. Perez-Villar, and L. O. Chua. (mar 1993). Autowaves for image processing on a two-dimensional cnn array of excitable nonlinear circuits: flat and wrinkled labyrinths. *IEEE Transactions on Circuits and Systems I: Fundamental Theory and Applications*, 40(3):174–181.

[18] Domenec Puig, Miguel A. Garcia, and L. Wu. (2011). A new global optimization strategy for coordinated multi-robot exploration: Development and comparative evaluation. *Robotics and Autonomous Systems*, 59(9):635–653.

[19] Kenneth Showalter, Richard M. Noyes, and Harold Turner. (1979). Detailed studies of trigger wave initiation and detection. *Journal of the American Chemical Society*, 101(25):7463–7469.

[20] Oliver Steinbock, Agota Toth, and Kenneth Showalter. (1995). Navigating complex labyrinths: Optimal paths from chemical waves. *Science*, 267:868–871.

[21] Sebastian Thrun. (1998). Learning metric-topological maps for indoor mobile robot navigation. *Artificial Intelligence*, 99(1):21–71.

[22] Benjamín Tovar, Lourdes Muñoz-Gómez, Rafael Murrieta-Cid, Moisés Alencastre-Miranda, Raúl Monroy, and Seth Hutchinson. (2006). Planning exploration strategies for simultaneous localization and mapping. *Robotics and Autonomous Systems*, 54(4):314–331.

[23] Alan M. Turing. (1952). The chemical basis of morphogenesis. *Philosophical Transactions of the Royal Society of London. Series B, Biological Sciences*, 237(641):37–72.

[24] Vladimir K. Vanag and Irving R. Epstein. (2009). Pattern formation mechanisms in reaction-diffusion systems. *International Journal of Developmental Biology*, 53(5-6):673–683.c

[25] Alejandro Vázquez-Otero, Jan Faigl, and Alberto P. Muñuzuri. (2012). Path planning based on reaction-diffusion process. In *IEEE/RSJ Int. Conf. Intelligent Robots and Systems (IROS)*, pages 896–901.

[26] Alejandro Vázquez-Otero and Alberto P. Muñuzuri. (2010). Navigation algorithm for autonomous devices based on biological waves. In *12th International Workshop on Cellular Nanoscale Networks and Their Applications (CNNA)*, pages 1–5.

[27] Müstak E. Yalcin. (2008). A simple programmable autowave generator network for wave computing applications. *IEEE Transactions on Circuits and Systems II: Express Briefs*, 55(11):1173–1177.

[28] Brian Yamauchi. (1997). A frontier-based approach for autonomous exploration. In *IEEE International Symposium on Computational Intelligence in Robotics and Automation (CIRA)*, pages 146–151.

Sensors **2015**, *15*, 12736-12764; doi:10.3390/s150612736

OPEN ACCESS
sensors
ISSN 1424-8220
www.mdpi.com/journal/sensors

Article

Reaction Diffusion Voronoi Diagrams: From Sensors Data to Computing

Alejandro Vázquez-Otero [1,2,*], Jan Faigl [3], Raquel Dormido [1] and Natividad Duro [1]

[1] Department of Computer Sciences and Automatic Control, UNED, C/ Juan del Rosal, 16, Madrid 28040, Spain; E-Mails: raquel@dia.uned.es (R.D.); nduro@dia.uned.es (N.D.)
[2] Institute of Physics ASCR, Na Slovance 2, 18221 Prague 8, Czech Republic
[3] Department of Computer Science, Faculty of Electrical Engineering, Czech Technical University in Prague, Technicka 2, 16627 Prague 6, Czech Republic; E-Mail: faiglj@fel.cvut.cz

* Author to whom correspondence should be addressed;
E-Mail: alejandro.vazquez-otero@eli-beams.eu; Tel.: +420-266-051-266.

Academic Editor: Vittorio M.N. Passaro

Received: 17 January 2015 / Accepted: 25 May 2015 / Published: 29 May 2015

Abstract: In this paper, a new method to solve computational problems using reaction diffusion (RD) systems is presented. The novelty relies on the use of a model configuration that tailors its spatiotemporal dynamics to develop Voronoi diagrams (VD) as a part of the system's natural evolution. The proposed framework is deployed in a solution of related robotic problems, where the generalized VD are used to identify topological places in a grid map of the environment that is created from sensor measurements. The ability of the RD-based computation to integrate external information, like a grid map representing the environment in the model computational grid, permits a direct integration of sensor data into the model dynamics. The experimental results indicate that this method exhibits significantly less sensitivity to noisy data than the standard algorithms for determining VD in a grid. In addition, previous drawbacks of the computational algorithms based on RD models, like the generation of volatile solutions by means of excitable waves, are now overcome by final stable states.

Keywords: reaction diffusion; FitzHugh–Nagumo; path planning; navigation; exploration; Voronoi diagram; laser range sensor; sonar sensor; Turing instability

---

1. Introduction

Many systems in nature show organization. For example, think about the prenatal development of human embryos or the resource tracking in a population of insects. However, as this organization happens in a spontaneous, way we usually talk about self-organization. General rules under which such structures appear or predictions of their changes are some of the interests of the self-organization field. An approach to model these behaviors relies in the so-called reaction diffusion (RD) processes [1], the Turing instability [2] being a classical method for a stable pattern formation. The study of the complex phenomena modeled by such RD systems has been in the spotlight of the scientific community for a long time, becoming an endless source of attempts for finding out how to take advantage of their rich behavior [3–6]. Computationally, the apparent decision-logic exhibited by the model dynamics can be seen as an abstraction layer for problem solving, allowing one to embed the complexity of a real problem into the model spatiotemporal evolution. This analogy confers the RD model the status of a computational framework in which geometrical operations can be performed. In this paper, we introduce a model setup that exhibits a construction of the Voronoi diagram, considered as a fundamental geometrical structure that can be used to computationally reproduce many natural formations, like soap bubbles [7], bone cells [8] and pattern formation in some mammalian models [9].

Having a set of seeds, the Voronoi diagram can be imagined as partitioning of a plane into a set of cells, where each cell is originated from a particular seed, and the cell represents the region for which the seed of the cell is the closest seed [10]. In other words, the boundary of the regions is formed from points that are equidistant to the two closest seeds. In robotics, the generalized Voronoi graphs (GVG) are used to create a navigational roadmap and a topological representation of the environment [11]. Herein, the equidistant property of the boundary of the Voronoi regions is utilized to find a path that maximizes the clearance from the obstacles. Moreover, the junction places, *i.e.*, locations where the boundary of the cells are connected, represent topologically important places of the environment, like corridor intersections.

The problem being addressed in this paper is to determine the junction places in a grid map of the environment by generation of the Voronoi diagram in the grid map. The proposed RD-based computational model is employed in the generation of such Voronoi diagrams from which the junction places are extracted. We also compare the proposed approach with the state-of-the-art algorithm introduced by the authors of [12]. Based on the presented results, it can be observed that the proposed RD-based computational model is less sensitive to noise than the thinning approach [12]. This new feature also extends the applicability range of our previous works [13–15], where a modelization for tackling robotics problems, like path planning and the exploration task, has been developed.

The paper is organized as follows. The next section provides the theoretical basis of the RD systems and, more particularly, an explanation about how the external (*i.e.*, sensory) information can be introduced into the model dynamics. Section 3 introduces a standard Voronoi algorithm, intended to provide a suitable comparison method for the RD-based approach. Sections 4 and 5 present experimental results and the discussion about the insights found. This paper concludes in Section 7 with a summary of the contributions and conclusions, as well as our future directions.

2. Reaction Diffusion Computational Model

2.1. The Reaction Diffusion Model of FitzHugh–Nagumo

One of the first reaction diffusion (RD) models was introduced in a seminal work of Hodgkin and Huxley [16] in 1952, where the authors model the electric signaling of firing of individual neurons. Later on, a simplified model was introduced by FitzHugh and Nagumo (FHN) [17,18]. This model adopts the basic form of a coupled system described by:

$$\begin{aligned} \dot{u} &= g(u,v) + D_u \triangle u \\ \dot{v} &= f(u,v) + D_v \triangle v \end{aligned} \tag{1}$$

where $g(u,v) = \varepsilon\,(u - u^3 - v + \phi)$ and $f(u,v) = (u - \alpha v + \beta)$. Computationally, it describes the evolution of the states variables u and v for each point over an integration grid, the remaining parameters being constants of the model. The grid points (also called grid cells) are spatially coupled with their neighbors by means of the Laplacian component, which is also responsible for spreading out information along the integration domain. A standard method for analyzing the associated dynamics of Equation (1) involves plotting the nullclines (sometimes called zero-growth isoclines) that describe the dynamics of a zero-dimensional system or a single cell. Thus, for a system characterized by the FHN model, the dynamics of each cell is governed by its associated nullcline configuration, plus the spatial interactions with other cells due to the diffusive coupling. The possible nullcline combination regarding the FHN model is depicted in Figure 1. In particular, Figure 1a corresponds to the aforementioned excitable system in which the nullclines define one single point that is stable. Any initial configuration far from this point will decay to the stable state by means of an excitable wave. The next figure represents an oscillating system that leads to an oscillatory regime. For the purpose of this work, we are interested in the bistable regime depicted in Figure 1c showing a symmetric nullcline configuration. In this configuration, the nullclines define two stable points (drawn as green discs) that are equally stable. Consequently, the concentration levels of the state variables can be found along the integration domain in any of both stable states, where even a heterogeneous combination of both steady states is feasible. Conversely, asymmetric configurations as depicted in Figure 2a lead to one of the stable states possessing a higher stability than the other. In this case, as the natural tendency of the system is evolving towards the concentration level of the most stable state, any initial configuration that is far from this point will inevitably move the whole system to the more stable point. This change is driven by a wavefront, characterized by its strong nonlinear properties. Wavefronts with radically different behaviors can be reproduced in a bistable configuration while maintaining the global behavior of evolving towards the more stable state only by a slight change of the FHN model parameters.

Examples of such a behavior can be found in [13,14], where a non-annihilation behavior for wavefronts was introduced. This property of non-annihilation of the wavefronts allows an implementation of a path planning algorithm that is solely based on the RDmodel to perform the required computations. Later on, a fluid-like behavior was successfully applied in different stages of a robot exploration task [15]. In this paper, we present a behavior of the RD model that provides a computation of Voronoi diagrams.

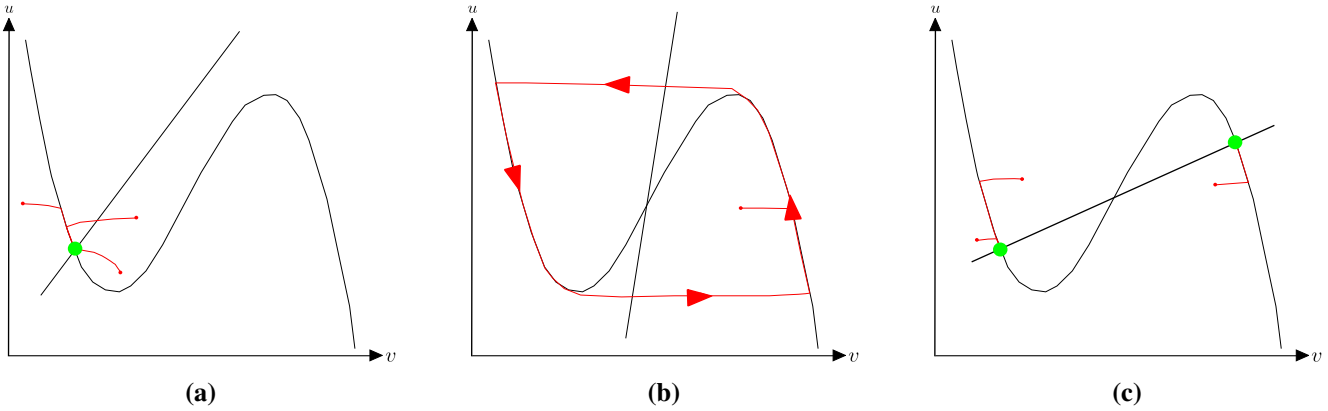

Figure 1. An overview of different nullcline configurations. The green discs represent stable states. Notice that the oscillatory configuration does not have any stable point. The red lines indicate the associated trajectories in the phases space for the particular initial condition. (**a**) Excitable system; (**b**) oscillatory system; (**c**) bistable system.

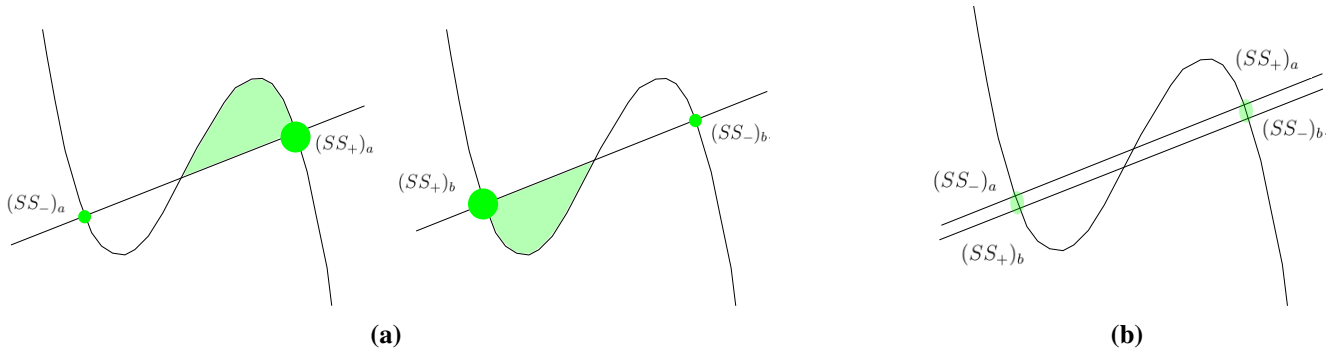

Figure 2. Asymmetric nullcline configurations for a bistable system. The green discs represent stable states. In a spatially extended system, the stable states drive the system to spatially distributed steady states. (**a**) Two possible asymmetric configurations for a bistable system; (**b**) Superposition of both asymmetric configurations.

2.2. The Switch-of-Phase Strategy

The nullcline configuration depicted in the left part of Figure 2a characterizes a system with a tendency to evolve towards the stable point $(SS_+)_a$, while for the right diagram in the same figure, the tendency is towards $(SS_+)_b$. From a superimposition of the both figures, as is shown in Figure 2b, it is evident that the stable points are relatively close in both nullclines, *i.e.*, $(SS_-)_a \approx (SS_+)_b$ and $(SS_+)_a \approx (SS_-)_b$. The fact that their concentration levels are so close enables a smooth transition from the nullcline configuration depicted in the left part of Figure 2a to the configuration depicted in the right part of the figure, and *vice versa*. Therefore, if the parameters of the model are slightly modified, after a short period of conditioning in which $(SS_-)_a$ becomes $(SS_+)_b$ and $(SS_+)_a$ becomes $(SS_-)_b$, the model evolves according to the new nullcline configuration. It is because the system dynamics can be tailored to reproduce different behaviors using diverse nullcline configurations that geometric operations like the Voronoi reconstruction can be encapsulated in the model spatiotemporal evolution using this

switch-of-phase mechanism. Hence, the problem boils down to finding proper nullcline configurations capable of reproducing the desired behaviors. In the present study, such a behavior is the computation of the Voronoi diagram.

2.3. Sensory Information and the External Forcing

It has been shown in the literature that some natural phenomena can be explained in terms of the RD systems, e.g., a pattern formation where self-organization plays a key role. An intriguing characteristic of such natural processes is how their development becomes fairly robust against the unavoidable imbalances that arise in every living system. This behavior is consistently reproduced by the RD dynamics, which exhibits a strong capacity to deal with external perturbations, either overcoming them or adapting its internal behavior to accommodate them. The so-called external forcing has been systematically studied as a mechanism for interacting with RD systems. It comprises both the spatial [19,20] and the spatiotemporal [21] domains, and it can consist of a weak influence that barely affects the dynamics or a strong perturbation that determines its behavior. For perturbing the FHN model as it is defined in Equation (1), the main technique consists of the local modification of the nullcline configuration for a few cells of interest. The effect of this modification on the dynamics is an inhibition of the wavefront propagation at these points; hence, it is equivalent to the introduction of binary information into the system, which can be used to represent obstacles in robot path planning, as was shown in [14]. Besides, the model allows one to consider an additional constraint in the form of an extra (point dependent) term, the final expression to be discretized being:

$$\begin{aligned} \dot{u} &= g(u,v) + D_u \triangle u \\ \dot{v} &= f(u,v) + F + D_v \triangle v \end{aligned} \tag{2}$$

For our interest, the F term (F_{ij} for a cell at the coordinates ij in the computational grid) represents the environmental information coming from sensors, and the main difference with regards to the previous method (the local nullcline modification) is that it allows one to introduce gradient-like information. In other words, the FHN dynamics is determined by a combination of the nullcline configuration plus the diffusive term, and such a behavior is somehow resistant to a set of values that can be introduced through F_{ji} at each cell. For example, it can establish an effective range $F_{ji} \subset [0, max)$, which introduces a gradual delay in the wavefront propagation, reaching complete inhibition. An intensive use of this feature is shown in [15], where the RD model is employed for planning a path in the robotic exploration task.

An example of an environment representation created from raw sensor measurements is shown in Figure 3a. The map shown is created by integration of the sensors' measurements into an occupancy grid, where each cell denotes a probability that the cell is occupied by an obstacle. New sensor measurements, in this case, a scan from a laser ranger finder, are integrated into the occupancy grid using Bayes' rule [22]. Then, a grid map of the environment is created from the occupancy grid by thresholding the probability value of each cell into one of three states: occupied, free and unknown.

A wavefront evolution in a grid map is shown in Figure 3b,c, where it can be noticed how the wavefront covers the available space during its evolution, while stopping at the edges of the grid map, which represent obstacles. This feature allows one to integrate the external (environmental) information into the RD computational grid in a straightforward way.

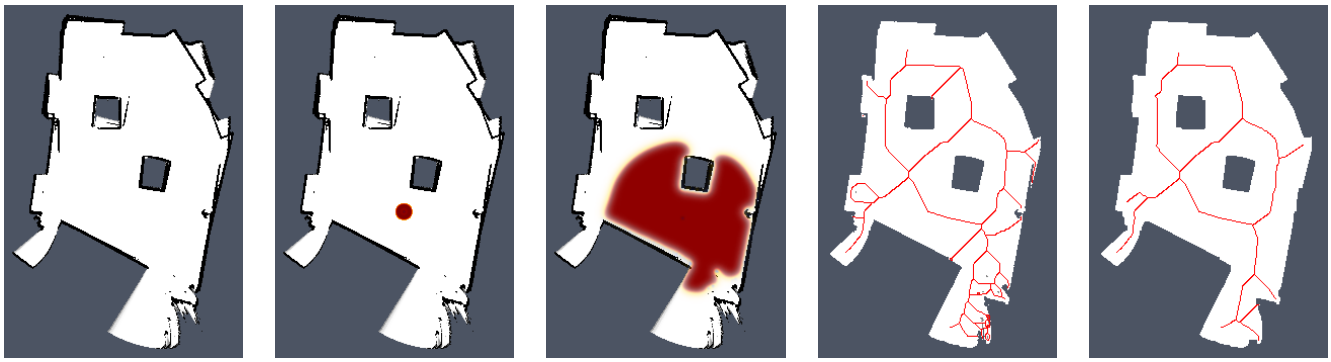

(a) **(b)** **(c)** **(d)** **(e)**

Figure 3. A visualization of sensor measurements transferred to the integration grid of the FHN model for the environment called *cube* and examples of conventional Voronoi diagrams: (**a**) occupancy grid with integrated sensor measurements where detected obstacles are in black, identified freespace is in white, and unknown parts of the environment are in gray; (**b**,**c**) the occupancy grid that represents the map of the environment is transferred (merged) to the integration grid of the model, where a wavefront is triggered; (**d**) conventional Voronoi diagram in the rough map; (**e**) conventional Voronoi diagram in the map after removing noisy measurements by application of dilation and erosion operations of the mathematical morphology.

3. Voronoi Diagram

3.1. Conventional Computation of Voronoi Diagrams

A computation of a Voronoi diagram (VD) is a basic problem studied in computational geometry. One of the simplest cases of a Voronoi diagram is a division of a plane with n points (called generating points) into a set of convex cells, where each cell contains exactly one generating point. For all points inside a cell, the distance to its generating point is smaller than to any other [10]. An example of this ordinary Voronoi diagram is shown in Figure 4a,b.

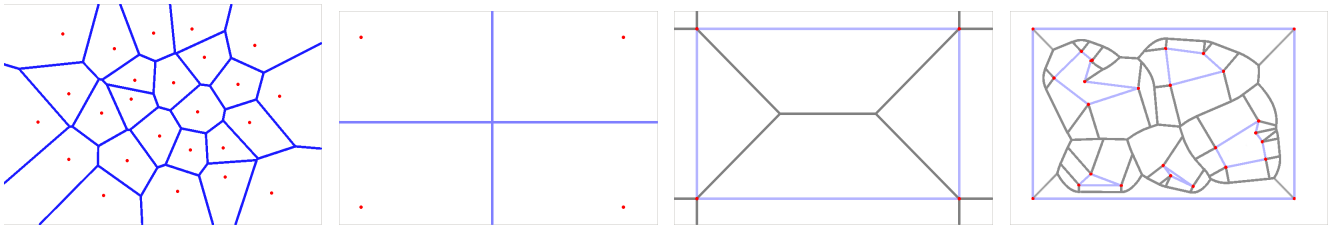

(a) **(b)** **(c)** **(d)**

Figure 4. Examples of the ordinary Voronoi diagram for k generating points in a plane and generalized Voronoi graph in walled environment: (**a**) random points, $k = 25$; (**b**) four points forming a rectangle, $k = 4$; (**c**) four walls forming a rectangular environment; (**d**) rectangular environment with fives polygonal obstacles with pruned parts of the Voronoi diagram outside the freespace of the polygonal environment.

Many applications of the Voronoi diagram can be found. We are interested in an identification of the topology of the environment to improve the navigation of a mobile robot that is not solely based on metric information, but rather on identification of important places, e.g., crossings and rooms. In our case, the environment is represented by a discrete cell lattice called a grid map. The map can be created from the occupancy grid in which new sensor measurements of the robot's surroundings taken by sonar or laser-based ranger finder are integrated using Bayes' rule [22]. A cell in the occupancy grid has associated probability that the cell is occupied, and thus, a grid map is created from the occupancy grid by thresholding the value of the probability, e.g., all cells with the probability of being occupied higher than 0.5 are considered as obstacles.

Regarding the navigation, a generalized Voronoi graph (GVG) has been introduced in [11] to identify topological places and also to determine paths between the places. A formal definition of the GVG can be found in [23], but basically, the GVG is a one-dimensional set of points that are equidistant to the n closest obstacles in n dimensions. For a walled environment [12], for example as visualized in Figure 4c,d, the GVG results in a set of points equidistant from two or more obstacles. It is known that Voronoi diagrams are sensitive to noise, which can be seen in Figure 3d,e. That is why Beeson *et al.* introduced an additional pruning technique to remove poor junction places [12]. In this paper, we consider RD-based computation of the Voronoi diagram to determine a skeleton of the grid map that represents the topology of the robot environment. The method is described in the next section.

3.2. RD-Based Computation of Voronoi Diagrams

The pioneering work of developing algorithms for computing planar Voronoi diagrams (PVD) using RD models (to the best of our knowledge) deals with the cellular automaton (CA) modelizations of RD systems [24,25] in which some of the well-known RD behaviors were successfully reproduced. In particular, a type of excitable wave that travels and interacts with others, annihilating after a collision, constituted the early pillars for developing RD-based computation. These waves in a cellular automaton lattice spread with a constant velocity, whereby two wavefronts starting from two different sources meet at equidistant points at the same time. The result of the mutual wavefront annihilation at those points is a series of bisectors that separate the wavefront sources. Therefore, it provides a generation of the Voronoi diagram of the sources.

On the experimental side, the so-called RD computers are implemented in a spatially-extended chemical medium, where diffusive or excitation waves propagate and interact. In this way, the results of the computations are represented by spatial distributions of reagent concentrations. Some interesting, yet computationally-limited experimental realizations can be found in [26,27]. These are based on the palladium processor and on a supersaturated solution of sodium acetate, commonly called hot ice. Systematic studies have highlighted the drawbacks of such implementations, like the impossibility of inverting a VD using an RD chemical processor. This characteristic has been shared by all subsequent implementations of experimental RD processors. For instance, VD irreversibility is found in [28].

Although the RD computation is the common substrate for most of these prototypes of processors, they are better contextualized as unconventional computing approaches. These approaches do not only cover RD systems, but they also include a wider scope, like the true slime mold *Physarum*

polycephalum [29], a single-celled organism visible to the naked eye that in the plasmodium stage grows up to the square meter scale in size. A comprehensive description of such unconventional methods, including gas discharge, can be found in [30].

3.3. FHN-Based Voronoi Diagrams

The technique for generating VD by means of the FHN model uses the switch-of-phase mechanism described in Section 2.2, in addition to the way of introducing information in the integration grid as described in Section 2.3. Firstly, an expansion phase that uses the fluid-like behavior (a comprehensive description of this behavior can be found in [15]) triggers a wavefront that evolves till it covers the whole domain. This mechanism is exemplified in the first row of pictures depicted in Figure 5. Then, the second stage based on a contraction phase recovers the wavefront over itself, as is shown in the second row of pictures in Figure 5. The resulting concentration profile coincides with a planar Voronoi diagram. Therefore, all of the logic required for a computation of the diagram is transferred to the spatiotemporal dynamics of the FHN model. The set of required values for the used FHN model are presented in Table 1. Notice that the termination condition for both stages is trivially implemented by measuring the total amount of u (or v) summing over all grid points. A constant value within two different iterations means the system has reached a static situation; hence, the next phase can be triggered.

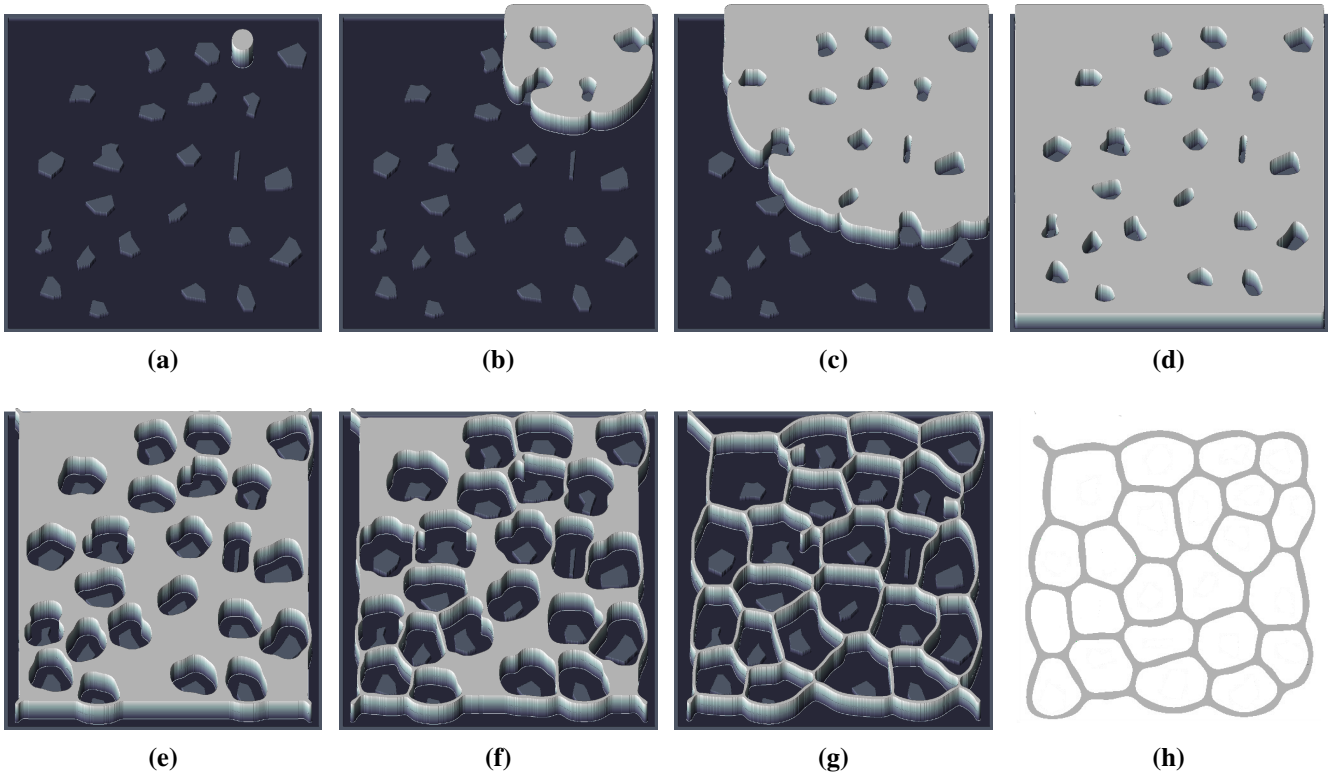

Figure 5. Steps of the RD-based Voronoi algorithm applied to the *potholes* environment: (**a**–**d**) expansion phase, a wavefront using the *fluid-like* behaviour evolves over the integration domain; (**e**–**h**) contraction phases, the resulting concentration profile of the previous stage evolves till generating a VD of the environment.

Table 1. Set of values for the FHN model to reproduce the desired behavior in both phases: expansion and contraction.

		FHN Parameters				
		α	β	ϵ	D_u	D_v
Phase	*expansion*	4	−0.5	40	0.45	2
	contraction	3.8	0.1	10	0.1	1.5

4. Experimental Results

4.1. Comparison Method

One of the expected advantages of the proposed RD-based computational model is that it has less sensitivity to spatially noisy data. This is particularly interesting in the application of the Voronoi diagram to compute a skeleton of the grid map of the robot's operational environment that can be used to create a topological representation of the environment. A map of the environment created from the sensor measurements can be noisy, e.g., because of a poor localization, which can lead to a misalignment of the range measurements and a noisy grid map. Regarding the topology, the Voronoi diagram is a graph (skeleton) describing the topology of the environment, where the nodes of the graph represent topologically important places in the environment. The nodes with a degree higher than three are junction places that represent crossings in the environment, while the nodes with a degree of one are the leaves of the skeleton and represent particular areas in the environment, like rooms. A skeleton of a walled environment computed as the Voronoi diagram (by means of the thinning alrotithm [12]) in the grid map of the environment called *jh* is shown in Figure 6, together with the highlighted junction places and leaves that represent rooms.

If we consider a static environment, its topology is fixed, and thus, the number of junction places and leaves should be the same even for an imperfect reconstruction of the map using noisy sensor measurements. Based on this observation, we propose the following methodology to study the sensitivity of the computational model to the noisy sensor data and compare the proposed RD-based Voronoi diagram computation with the thinning algorithm for finding a skeleton of the grid map [12].

The evaluation of the sensitivity is based on adding a noise to the map, where the noise is added as small discs with the radius r at all boundary cells (*i.e.*, obstacle cells that are incident with at least one free space cell). The radius r is drawn from a normal distribution with zero mean and variance $\sigma_r \leq 10$. For each map, we considered 10 values of σ_r, and because the determination of the map skeleton (using the thinning algorithm [12], as well as the proposed RD-based computational model) is deterministic, we create 20 noisy maps with added noise for each original map and a particular value of σ_r. Then, the studied parameters of the skeleton according to the level of noise σ_r are considered as average values and standard deviations computed from 20 trials of each algorithm run on these 20 noisy maps. Having four environments, called *autolab*, *jh*, *cube*, and *potholes*, the number of performed trials for two algorithms in this evaluation is 1600. An example of the maps with added noise is shown in Figure 7. Moreover, we also performed additional evaluation for scaled maps for the *jh*, *cube* and *potholes* environments

enlarged by four different scale, which gives 4800 additional trials, which gives 6400 performed trials in total.

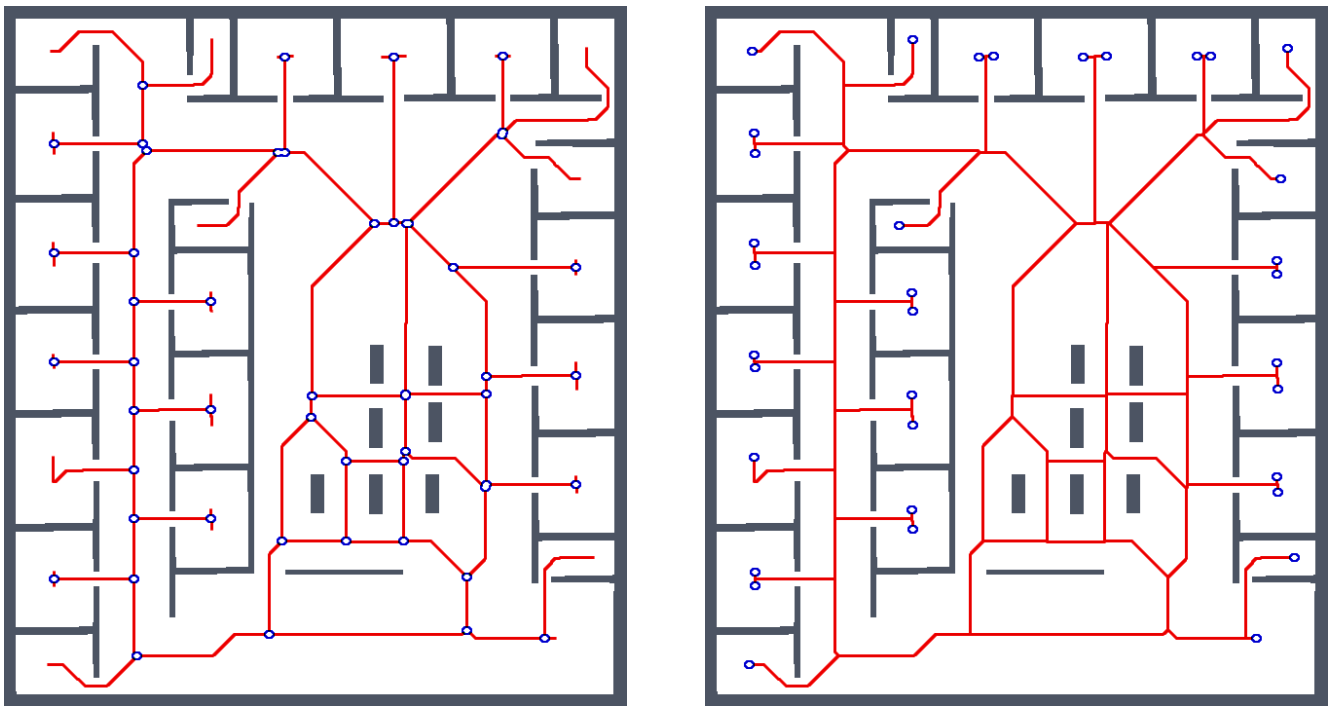

(a) **(b)**

Figure 6. Example of the topology representation of the walled environment *jh* computed as the GVG of the grid map. The computed Voronoi diagram is transformed into a graph, where nodes with the degree (number of incident edges) higher than 2 represent junction places and nodes with the degree 1 are the leaves representing particular rooms. (**a**) junction places; (**b**) leaves.

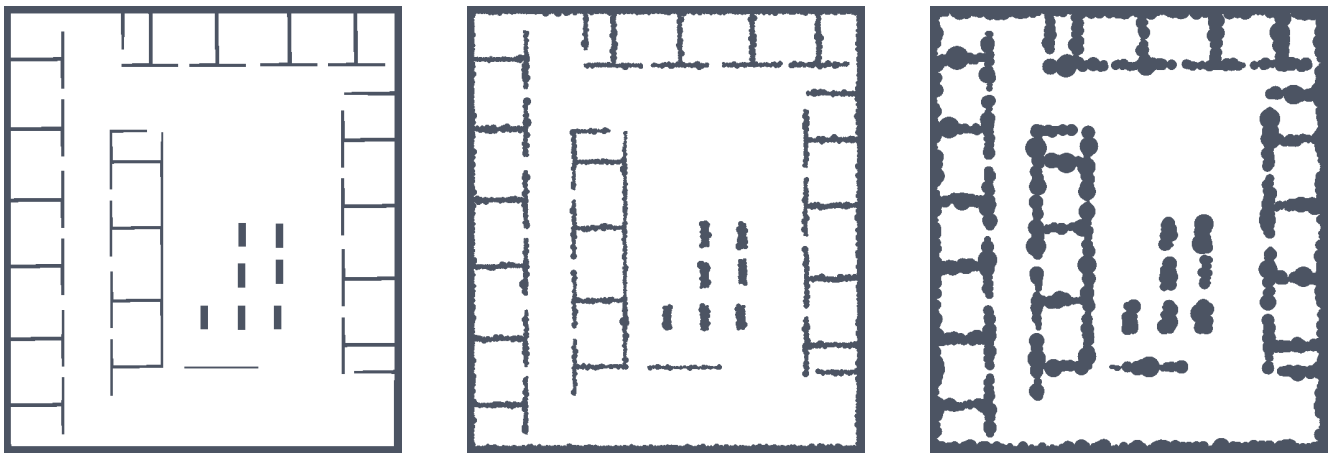

(a) **(b)** **(c)**

Figure 7. Environment *jh*: (**a**) without added noise; and with added noise for (**b**) $\sigma_r = 2$; and (**c**) $\sigma_r = 5$.

The influence of the added noise is studied as the change of the number of detected junction places and the number of leaves according to the reference numbers computed from the noise-less map. The change in the number of junction places is measured as the percentage deviation from the reference value denoted as JPDM. Let J_0 be the number of junction places detected in the noise-less map and J_σ be the number of detected junction places in the map with added noise according to σ. Then, the JPDM is computed as:

$$JPDM = \frac{\overline{J_\sigma} - J_0}{J_0} \cdot 100\% \tag{3}$$

where $\overline{J_\sigma}$ is the average number of the detected junction places over all trials for the particular value σ and map. The number of leaves is computed as the average number of the detected leaves in the topology graph of the Voronoi diagram that is accompanied by the standard deviation.

A value of the JPDM around zero indicates that the particular method is not sensitive to noise. A negative value indicates that the number of junction places in the noisy map is lower than the reference value J_0. Notice that this does not necessarily mean a worse result. A lower number of junction places is usually related to a lower number of leaves (e.g., detected rooms), and with increasing level of noise, an entrance to a particular room can be more and more narrow. Hence, a robot cannot safely navigate to such a location, and therefore, the room is unreachable; the corresponding leaf is not part of the skeleton, and also, the number of junction places is lower. On the other hand, if the method of the determination of the Voronoi diagram is sensitive to noise, many small branches can be part of the skeleton, and thus, also, the number of junction places is increased.

4.1.1. Determine Topology Graph for the RD-Based Voronoi Diagram

In Figure 5, it can be seen that the skeleton of the map determined by the proposed RD-based computational model is not a set of single pixel width paths, and therefore, there can be various ways to determine the studied indicators.

For simplicity and also with regard to the used thinning algorithm [12], we considered the RD-based skeleton as a simple polygon (or a set of simple polygons) and determine a single-pixel width skeleton in this polygon using the thinning algorithm. This allows us to consider the identical procedure to compute the indicators for determination of the skeleton based solely on the thinning algorithm and on the RD-based computational model. Such a skeleton of the determined RD-based Voronoi diagram is shown in Figure 8. An example of superimposed Voronoi diagrams determined in the map with and without the added noise in the environment *autolab* is shown in Figure 9.

It can be noticed that the thinning algorithm prunes branches of the skeleton that would go to the corners of the particular rooms. On the other hand, this is not exactly the case of the RD-based computation of the skeleton, which splits the skeleton according to the space around the propagated wavefront. Therefore, instead of direct comparison of the RD-based skeleton with the thinning algorithm accompanied by advanced pruning of branches, we study how the determined skeletons differ with increasing σ_r for each particular method, and thus, we study the algorithms' sensitivity to the level of noise.

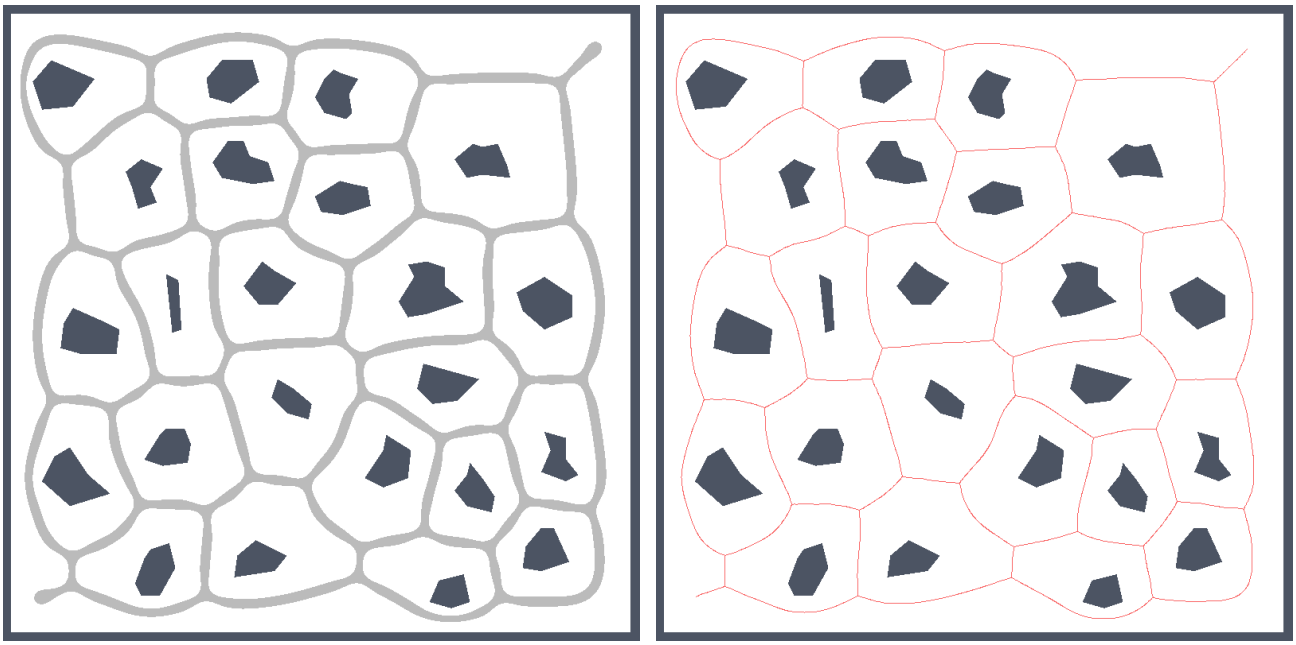

(a) **(b)**

Figure 8. Example of found skeleton (Voronoi diagram) by the RD-based computational model for the pothole environment: (**a**) light gray structure; (**b**) and its one pixel width skeleton shown in red.

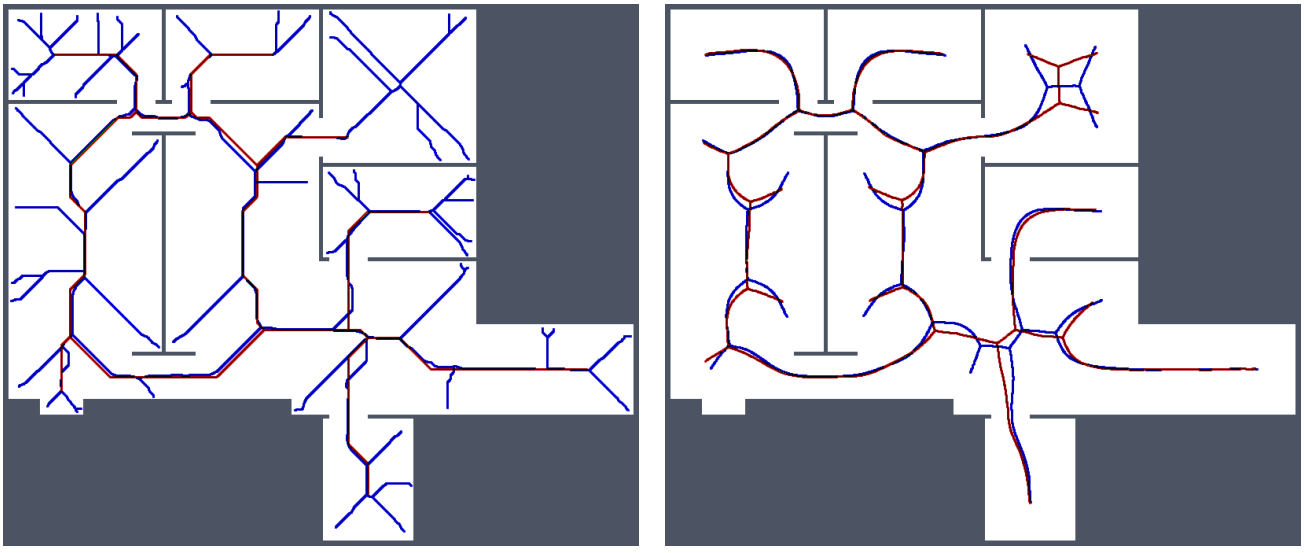

(a) **(b)**

Figure 9. *Cont.*

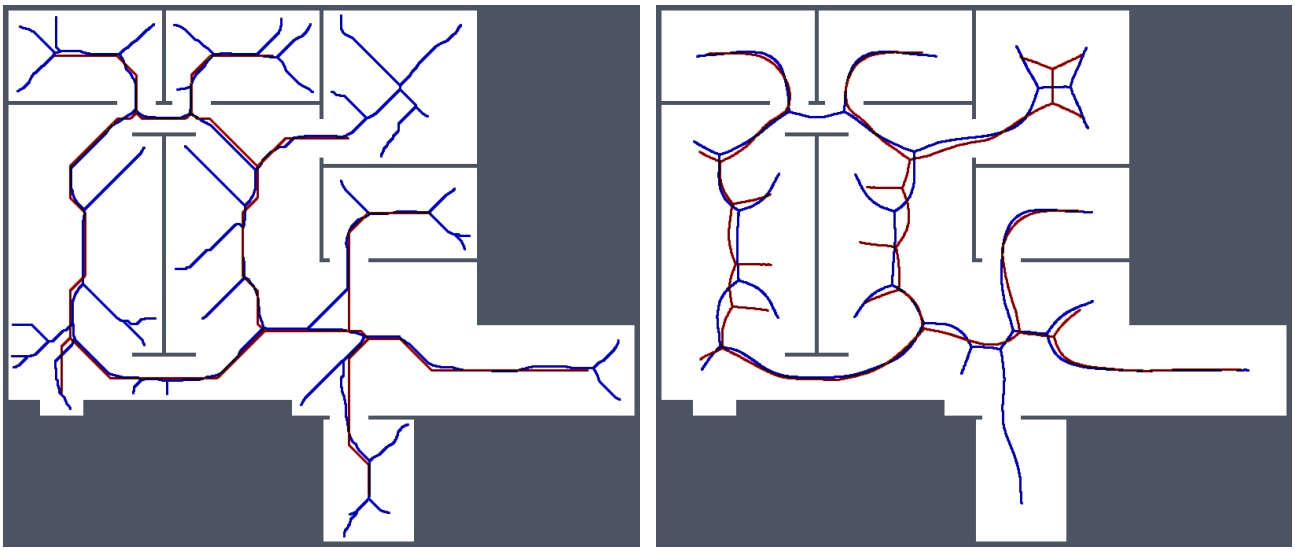

(c) **(d)**

Figure 9. Determined Voronoi diagrams by the thinning and RD-based algorithms in a map of the *autolab* environment for $\sigma_r = 4$ and $\sigma_r = 7$. The skeleton determined in noise-less map is in red while the skeleton found in the noisy map is in blue. (**a**) Thinning algorithm, $\sigma_r = 4$; (**b**) RD-based algorithm, $\sigma_r = 4$; (**c**) Thinning algorithm, $\sigma_r = 7$; (**d**) RD-based algorithm, $\sigma_r = 7$.

4.1.2. Results

The proposed statistical indicators of the noise sensitivity, *i.e.*, JPDM Equation (3), and the average number of the detected leaves are depicted in Figures 10 and 11, respectively. The results show that the proposed RD-based computation of the Voronoi diagram is less sensitive to the added noise, as the number of junction places is usually lower than the number of junction places for the map without the noise. The lowest value of the JPDM is -100% for the *cube* environment, where none of the junction places have been detected in the environment, see Figures 12 and 13. On the other hand, the thinning algorithm is a more sensitive to the noise as the number junction places is quickly increasing, and for the *autolab*, *jh* and *potholes* environments, the maximal number of the junction places is for the noise level $\sigma = 4$; see the example in Figure 14.

The number of leaves significantly changes with the noise level for the thinning algorithm, while for the proposed RD-based computation of the skeleton, it changes only slightly and typically decreases with a higher level of the noise σ, as can be seen in Figure 11. The only exception is the environment *potholes*, where the initial skeleton for $\sigma = 0$ does not contain any leaves; see Figure 15, while with increasing σ, some parts become unreachable for the robot (wavefront propagation), which is visualized in Figure 16.

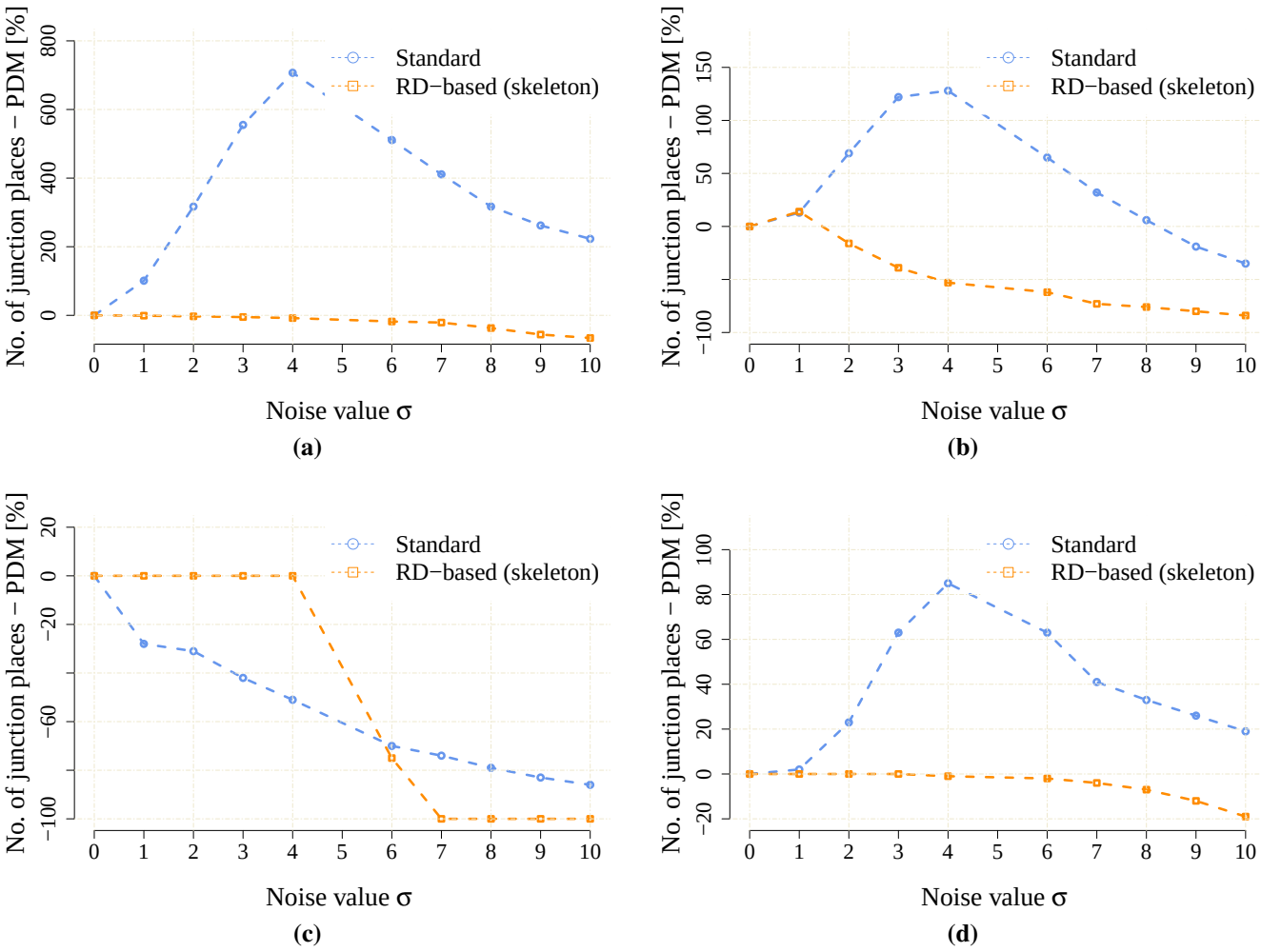

Figure 10. The noise sensitivity indicator JPDM Equation (3) in the noisy maps created for the particular value of the noise level σ. (**a**) environment *autolab*; (**b**) environment *jh*; (**c**) environment *cube*; (**d**) environment *potholes*.

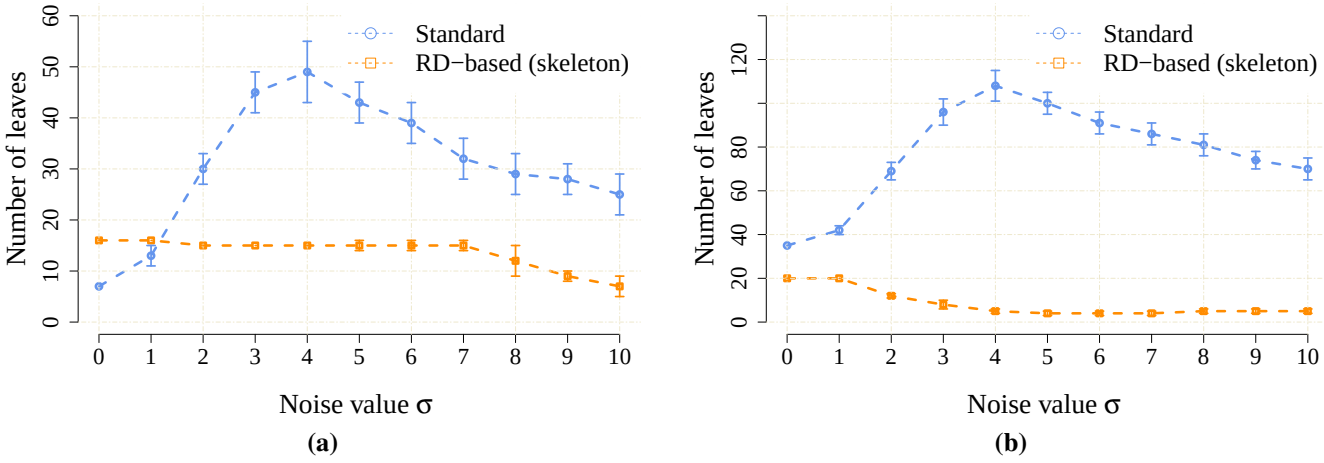

Figure 11. *Cont.*

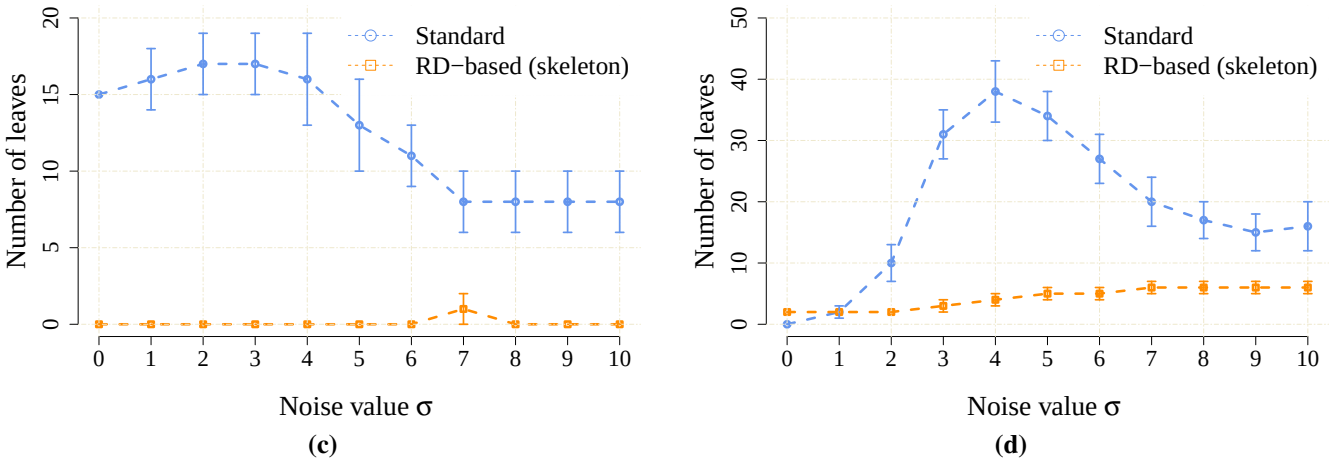

Figure 11. Average numbers of the leaves detected in the noisy maps created for the particular value of the noise level σ. (**a**) environment *autolab*; (**b**) environment *jh*; (**c**) environment *cube*; (**d**) environment *potholes*.

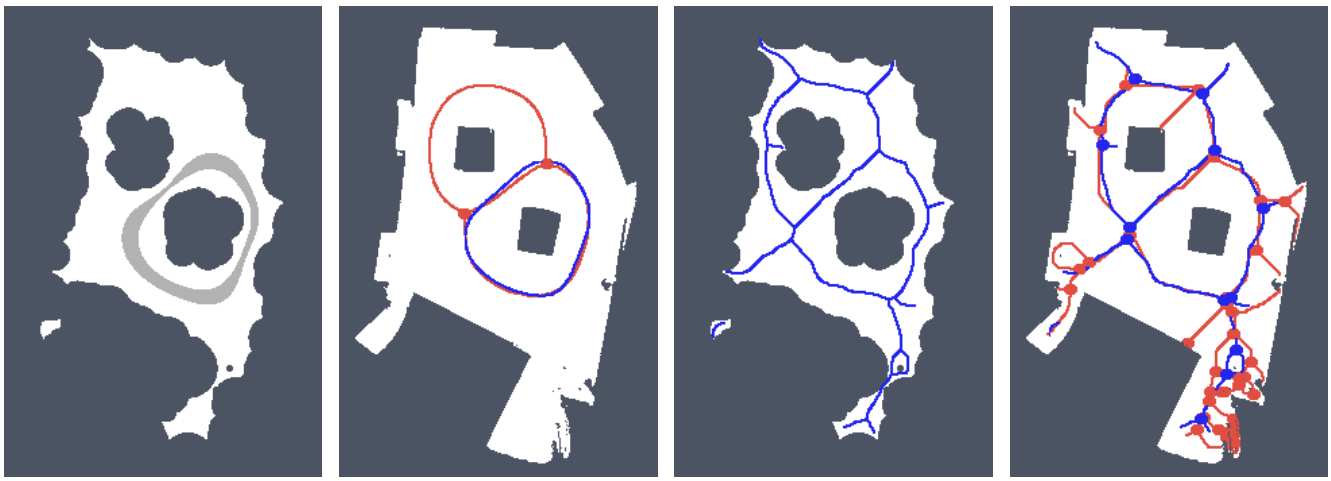

(a) RD-based **(b)** RD-based **(c)** Thinning **(d)** Thinning

Figure 12. Skeletons and the determined topological maps with highlighted junction places and leaves in the map *cube* with the noise level $\sigma = 7$: (**a**) RD-based Voronoi diagram; (**b**) and its corresponding skeleton (shown in green) that is superimposed on the skeleton determined in the noise-less map (in red); (**c**) Pruned GVG representing skeleton of the map determined by the thinning algorithm [12]; (**d**) and the corresponding skeleton superimposed on the skeleton determined in the noise-less map.

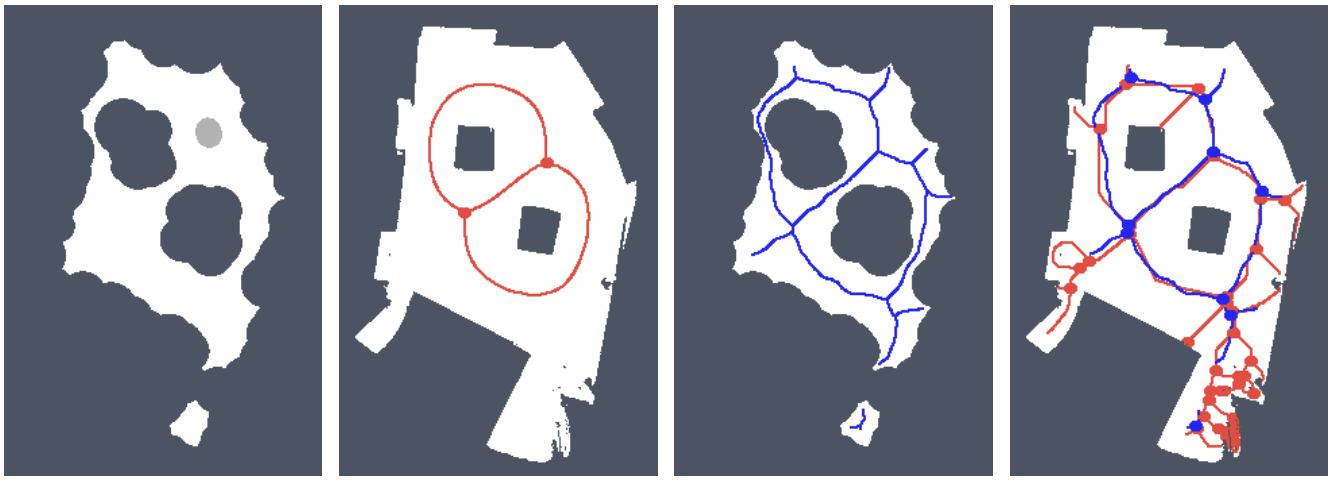

(a) RD-based **(b)** RD-based **(c)** Thinning **(d)** Thinning

Figure 13. Determined skeletons and topological maps with highlighted junction places and leaves in the map *cube* with the noise level $\sigma = 8$: (**a**) RD-based Voronoi diagram; (**b**) and its corresponding skeleton (shown in green) that is superimposed on the skeleton determined in the noise-less map (in red); (**c**) Pruned GVG representing skeleton of the map determined by the thinning algorithm [12]; (**d**) and the corresponding skeleton superimposed on the skeleton determined in the noise-less map.

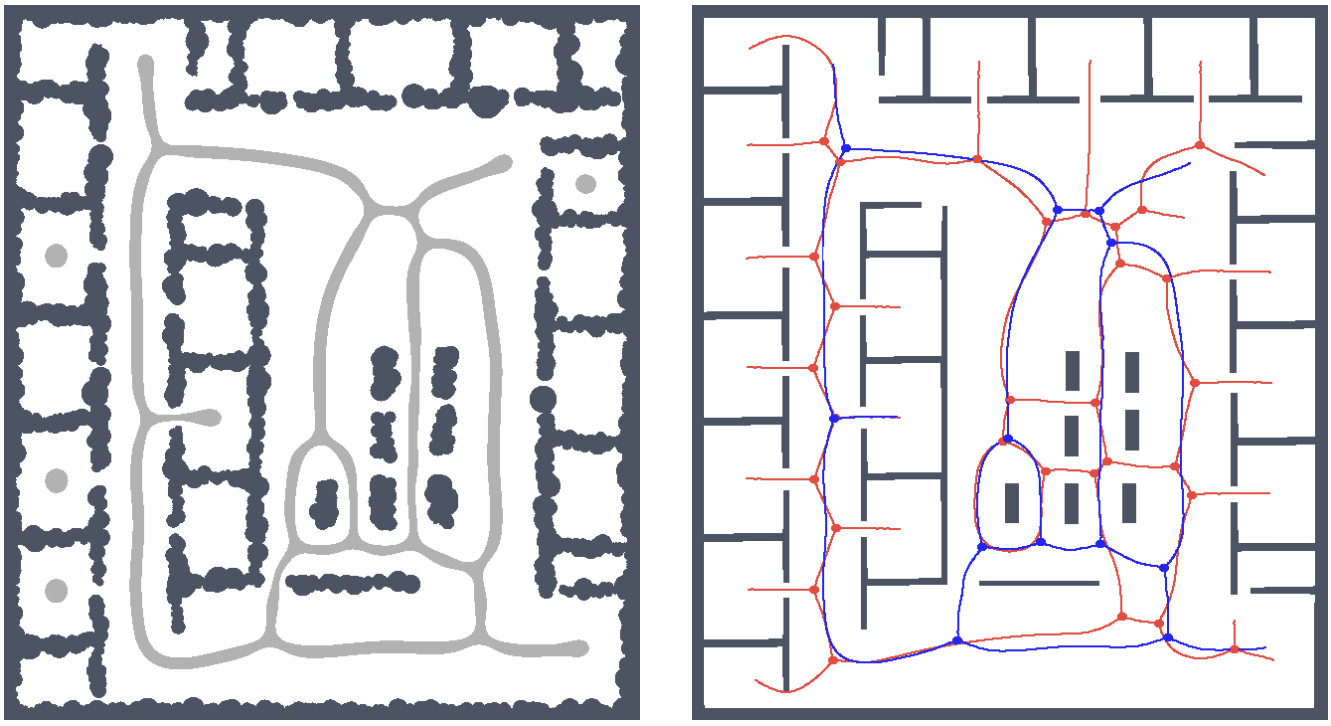

(a) RD-based **(b)** RD-based

Figure 14. *Cont.*

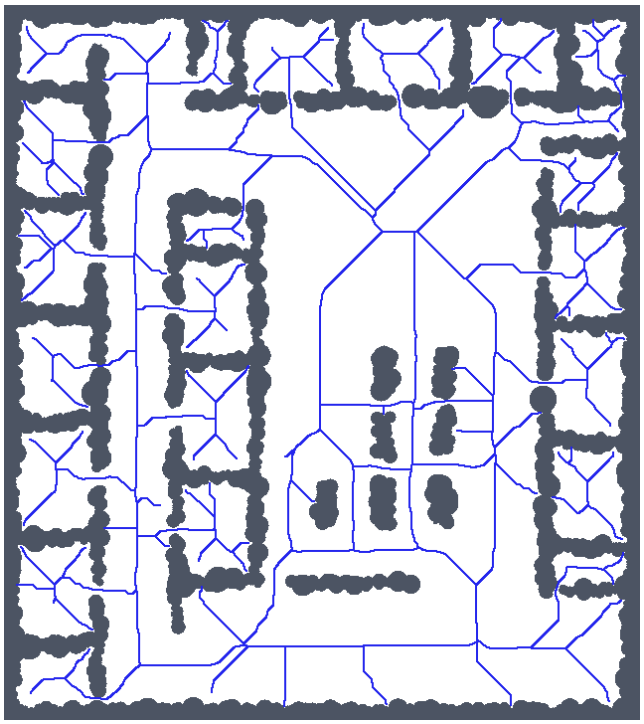

(c) Thinning

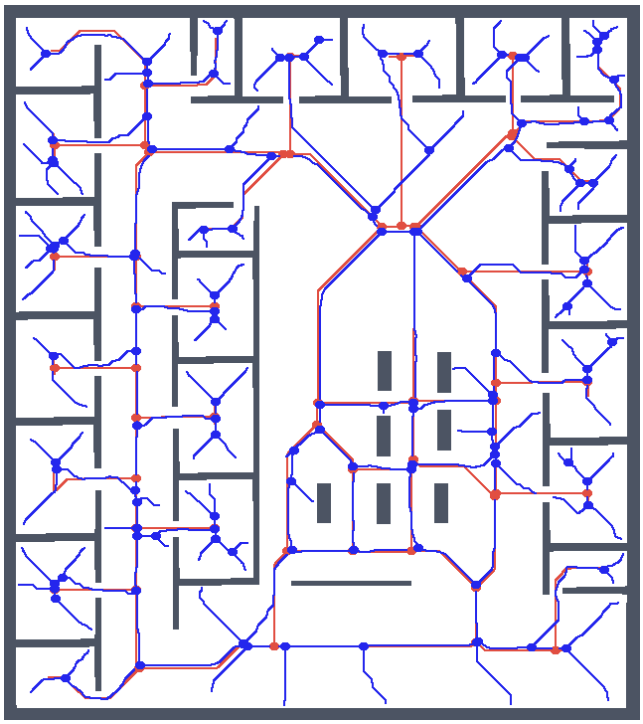

(d) Thinning

Figure 14. Determined skeletons and topological maps with highlighted junction places and leaves in the map *jh* with the noise level $\sigma = 4$: (**a**) RD-based Voronoi diagram; (**b**) and its corresponding skeleton superimposed on the skeleton determined in the noise-less map (in red); (**c**) Pruned GVG representing skeleton of the map determined by the thinning algorithm [12]; (**d**) and the corresponding skeleton superimposed on the skeleton determined in the noise-less map.

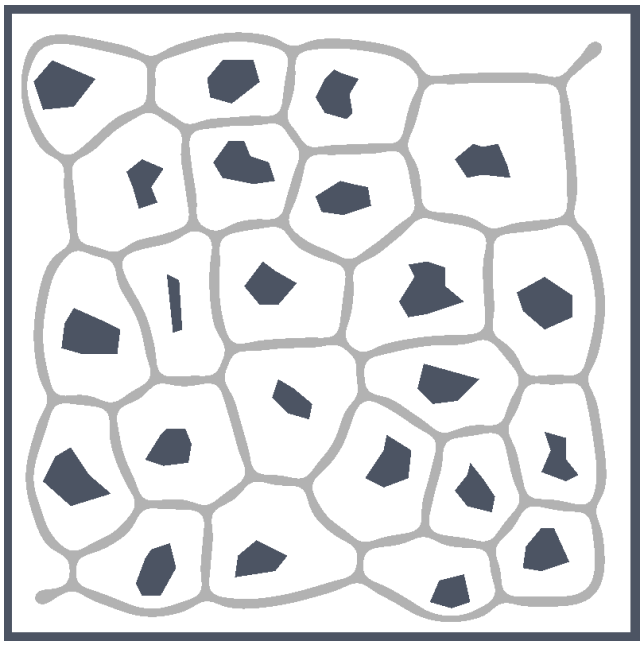

(a) RD-based

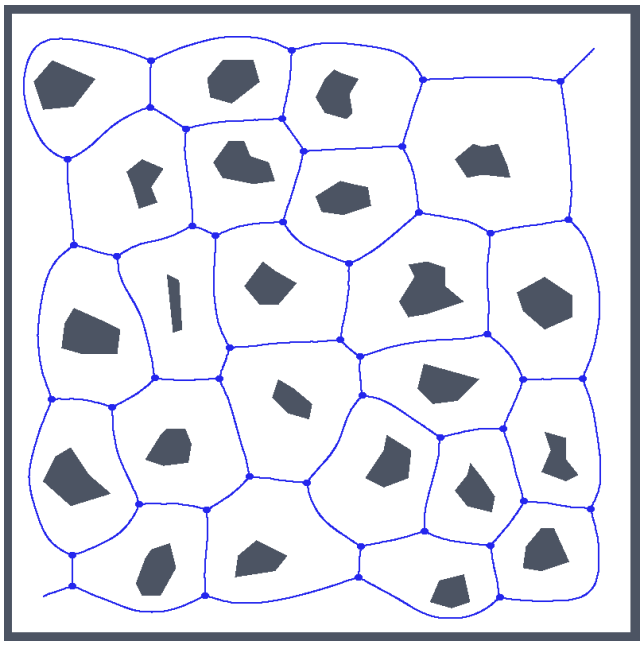

(b) RD-based

Figure 15. *Cont.*

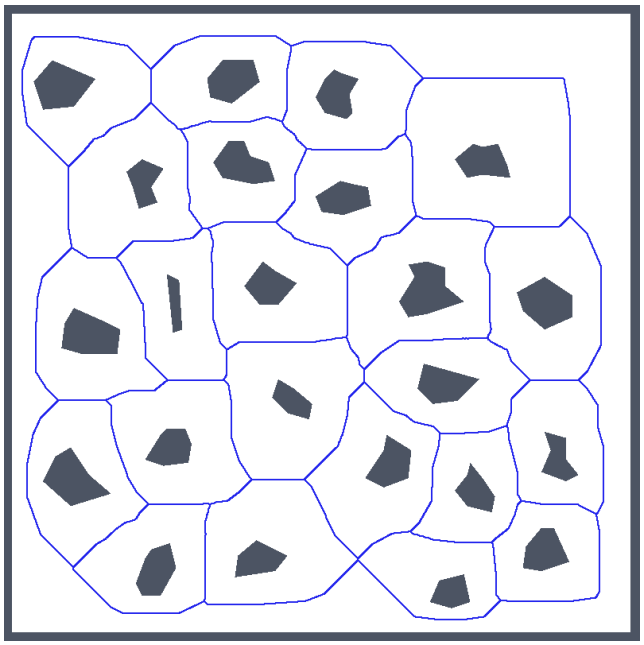

(c) Thinning

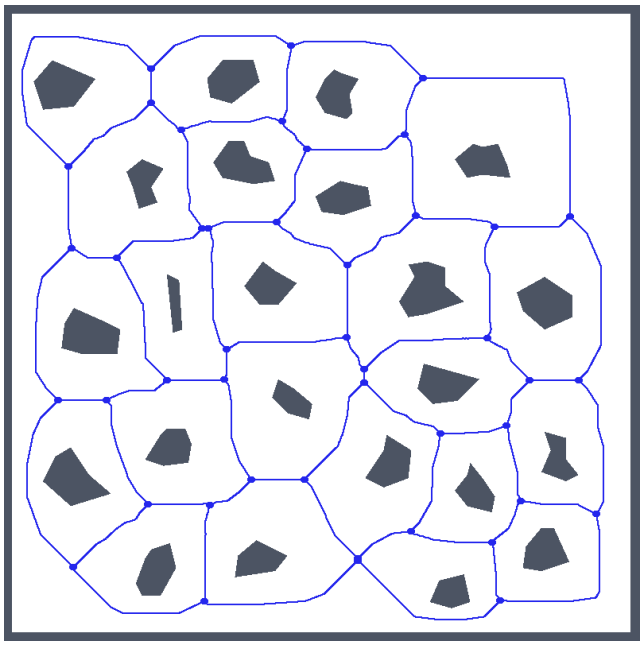

(d) Thinning

Figure 15. Determined skeletons and topological maps with highlighted junction places and leaves in the map *potholes* with the noise level $\sigma = 0$: (**a**) RD-based Voronoi diagram; (**b**) and its corresponding skeleton superimposed on the skeleton determined in the noise-less map (in red); (**c**) Pruned GVG representing skeleton of the map determined by the thinning algorithm [12]; (**d**) and the corresponding skeleton superimposed on the skeleton determined in the noise-less map.

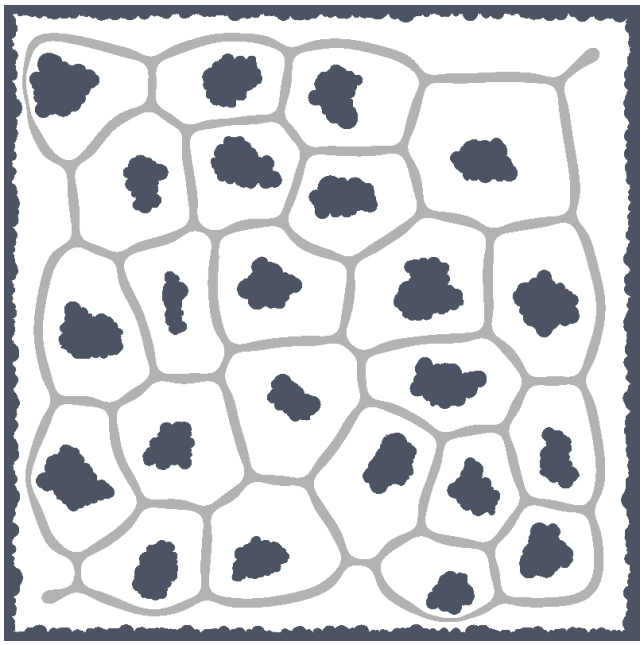

(a) RD-based

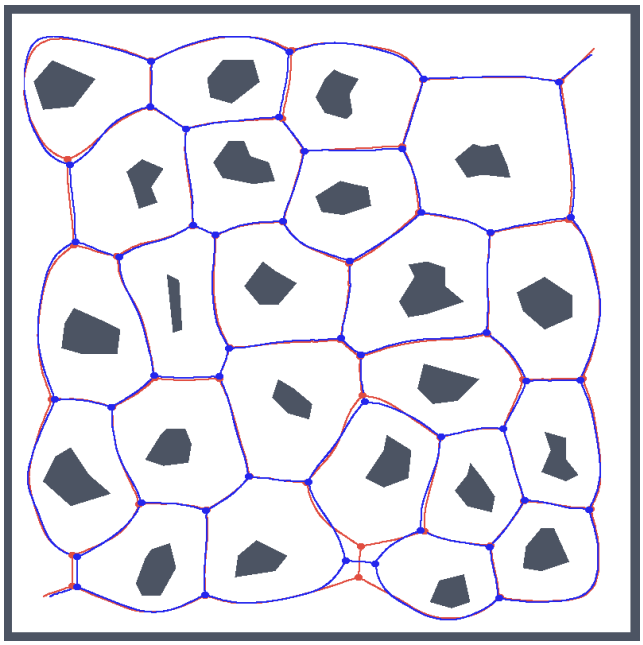

(b) RD-based

Figure 16. *Cont.*

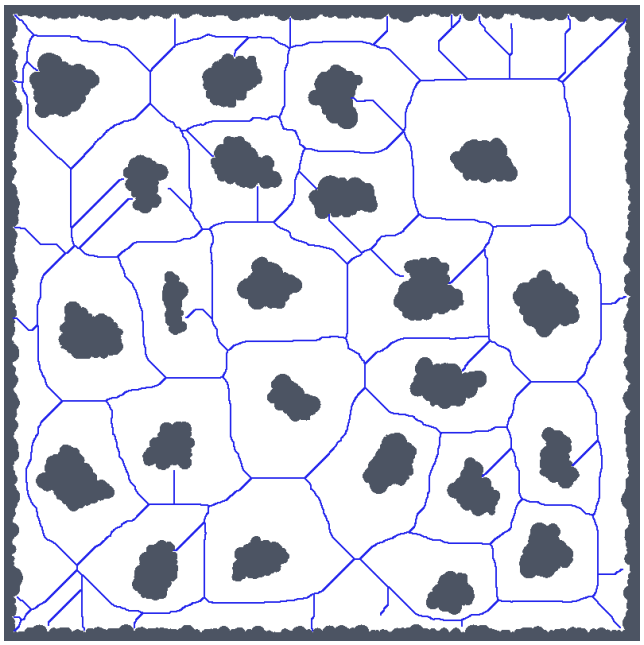

(c) Thinning

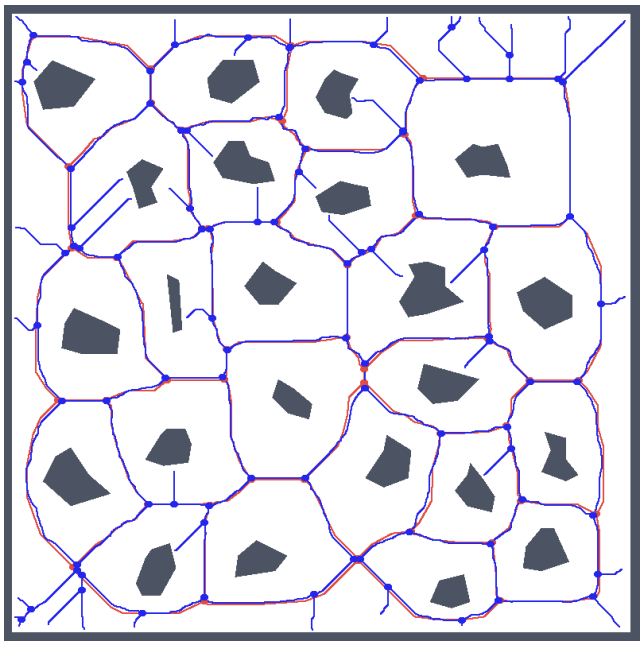

(d) Thinning

Figure 16. Determined skeletons and topological maps with highlighted junction places and leaves in the map *potholes* with the noise level $\sigma = 4$: (**a**) RD-based Voronoi diagram; (**b**) and its corresponding skeleton superimposed on the skeleton determined in the noise-less map (in red); (**c**) Pruned GVG representing skeleton of the map determined by the thinning algorithm [12]; (**d**) and the corresponding skeleton superimposed on the skeleton determined in the noise-less map.

4.1.3. Influence of the Map Resolution

The resolution of the grid map may influence both computational techniques to determine the Voronoi diagram, and therefore, its influence has been studied for the *potholes*, *cube* and *jh* environments for which all the maps have been scaled 1.2, 1.5, 1.7 and 2 times. Particular results of the JPDM indicator are shown in Figures 17–19. Examples of the determined skeletons for both algorithms using different map resolutions are shown in Figures 20–22. Although a higher resolution increases the computational burden of both techniques, it can be noticed that the proposed RD-based computation is significantly less sensitive to the change of the resolution, and the number of junction places and leaves remains almost the same according to the change in the thinning algorithm.

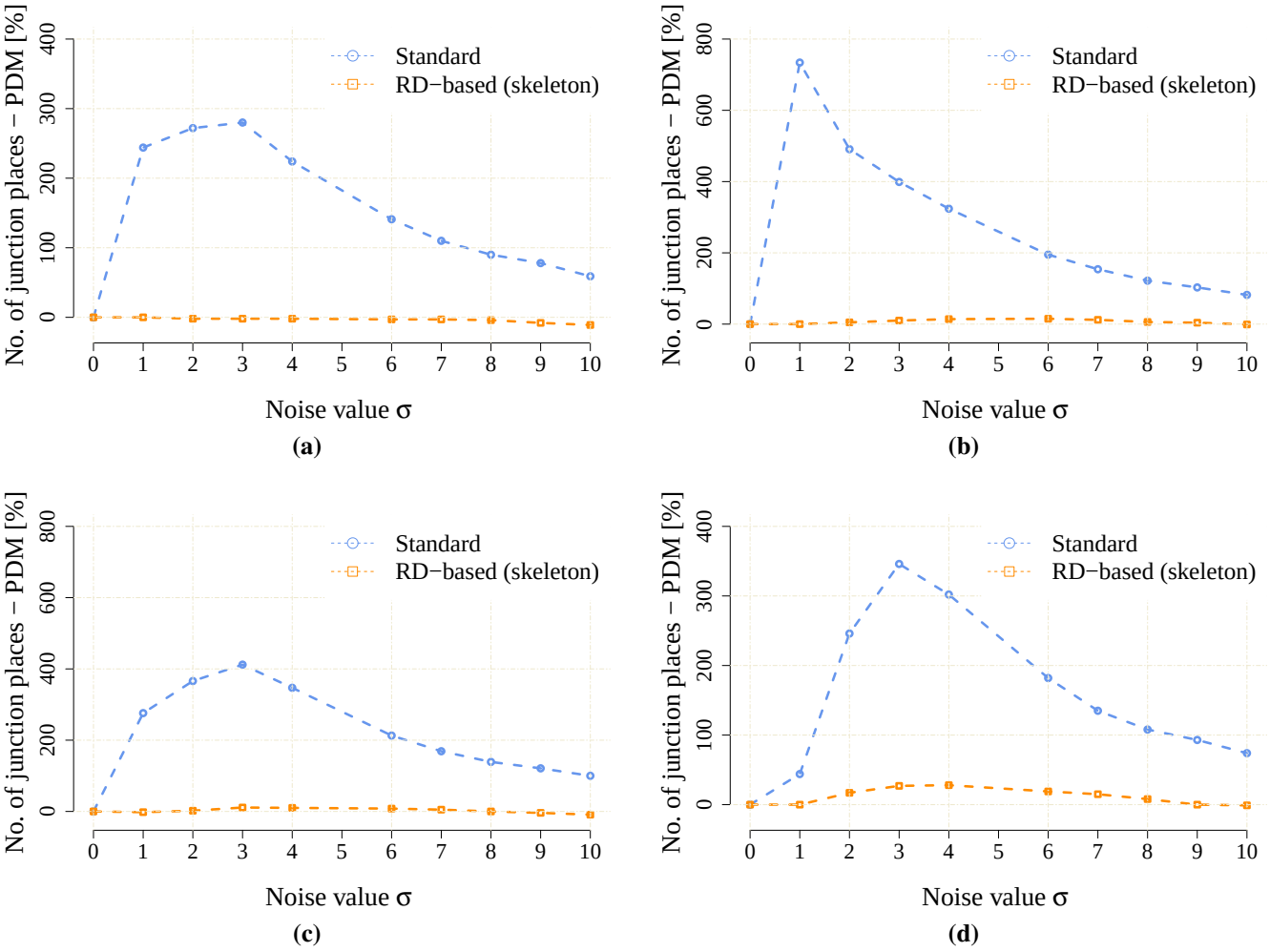

Figure 17. The noise sensitivity indicator JPDM Equation (3) in the scaled noisy maps of the *potholes* environment. (**a**) *potholes*, 960 × 960; (**b**) *potholes*, 1200 × 1200; (**c**) *potholes*, 1360 × 1360; (**d**) *potholes*, 1600 × 1600.

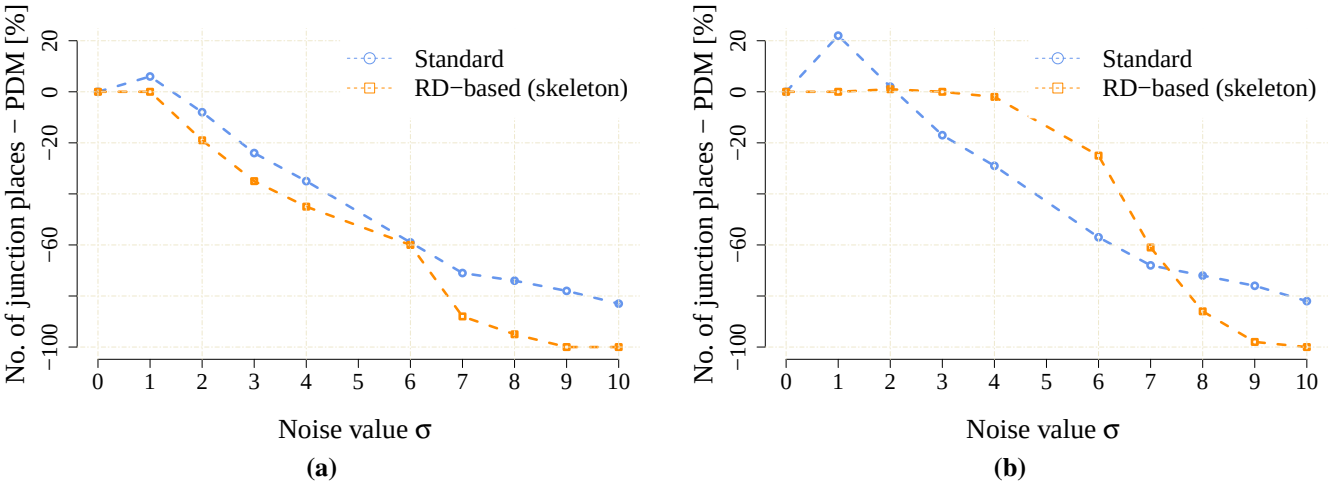

Figure 18. *Cont.*

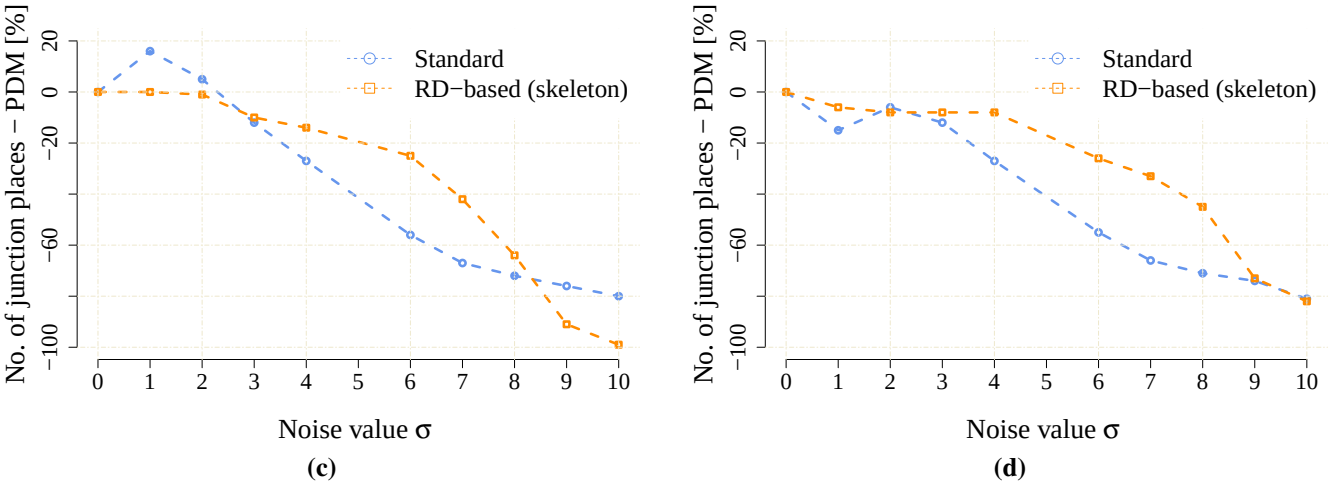

Figure 18. The noise sensitivity indicator JPDM Equation (3) in the scaled noisy maps of the *cube* environment. (**a**) *cube* 283 × 419; (**b**) *cube*, 354 × 524; (**c**) *cube*, 401 × 593; (**d**) *cube*, 472 × 698.

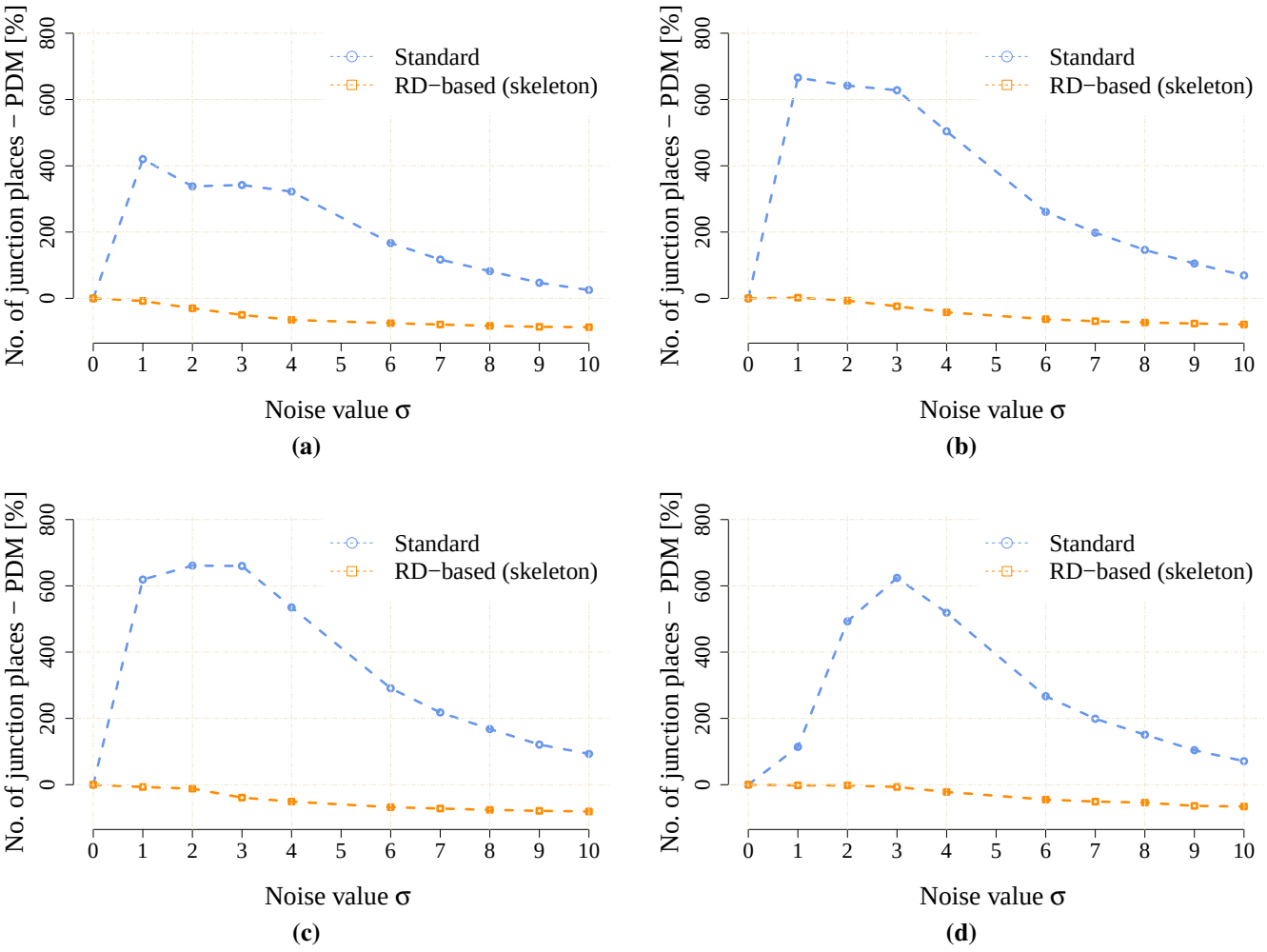

Figure 19. The noise sensitivity indicator JPDM Equation (3) in the scaled noisy maps of the *jh* environment. (**a**) *jh*, 768 × 863; (**b**) *jh*, 960 × 1079; (**c**) *jh*, 1088 × 1222; (**d**) *jh*, 1280 × 1438.

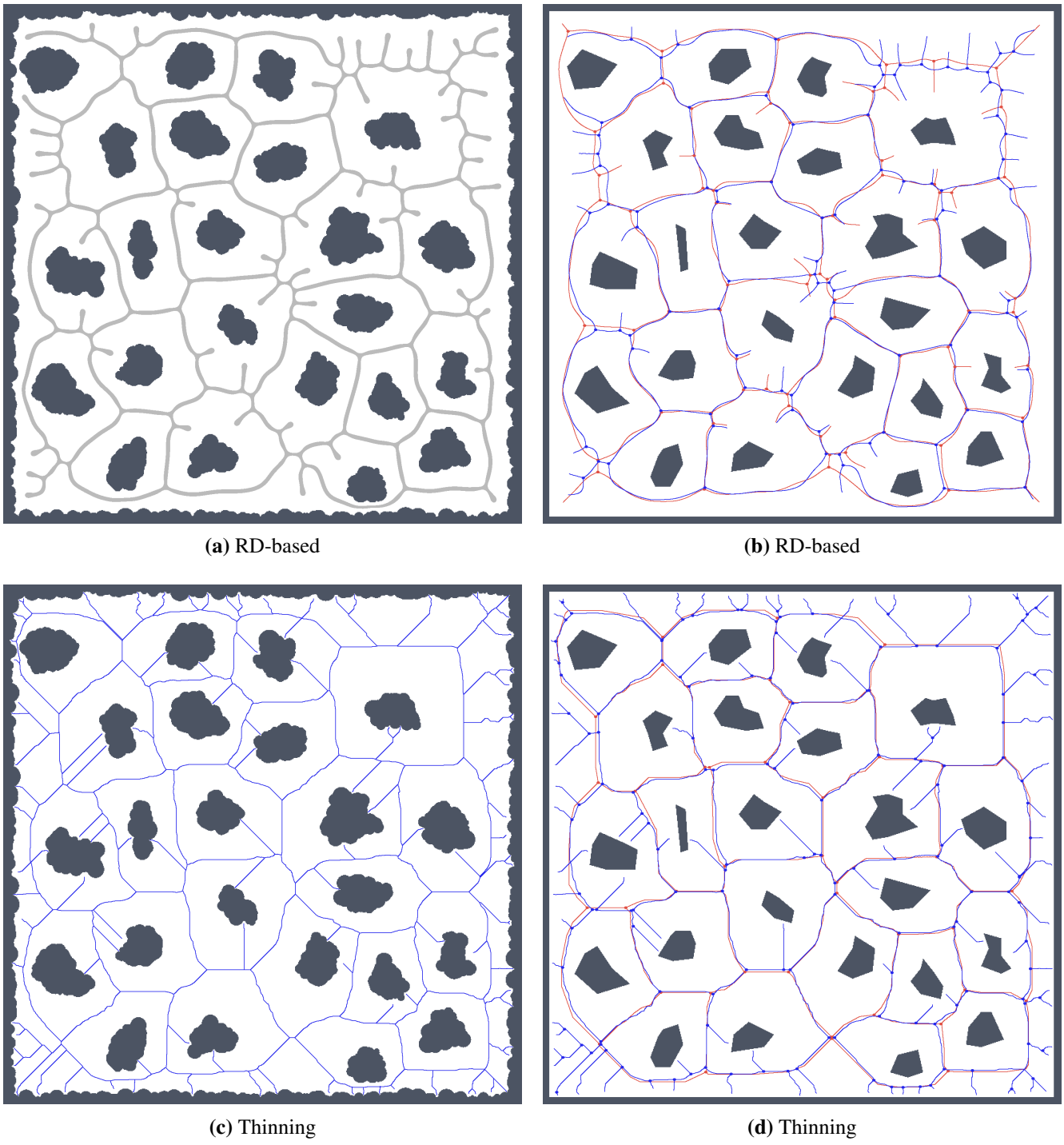

(a) RD-based

(b) RD-based

(c) Thinning

(d) Thinning

Figure 20. Determined skeletons and topological maps with highlighted junction places and leaves in the map *potholes* with the noise level $\sigma = 5$ for the scaled map with 1600 $\times$ 1600 grid points: (**a**) RD-based Voronoi diagram; (**b**) and its corresponding skeleton superimposed on the skeleton determined in the noise-less map (in red); (**c**) Pruned GVG representing skeleton of the map determined by the thinning algorithm [12]; (**d**) and the corresponding skeleton superimposed on the skeleton determined in the noise-less map.

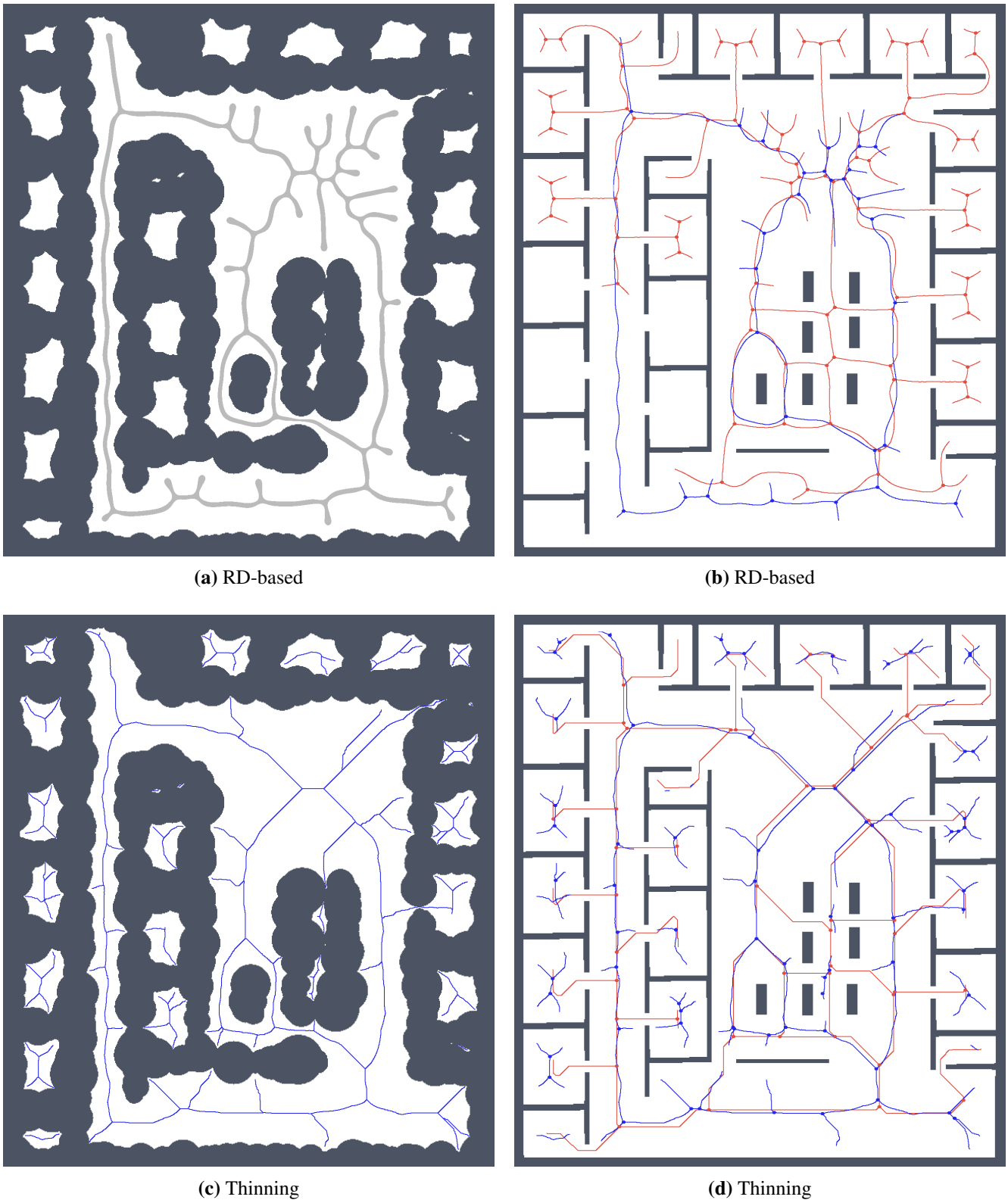

(a) RD-based

(b) RD-based

(c) Thinning

(d) Thinning

Figure 21. Determined skeletons and topological maps with highlighted junction places and leaves in the map *jh* with the noise level $\sigma = 10$ for the scaled map with 1280×1438 grid points: (**a**) RD-based Voronoi diagram; (**b**) and its corresponding skeleton superimposed on the skeleton determined in the noise-less map (in red); (**c**) Pruned GVG representing skeleton of the map determined by the thinning algorithm [12]; (**d**) and the corresponding skeleton superimposed on the skeleton determined in the noise-less map.

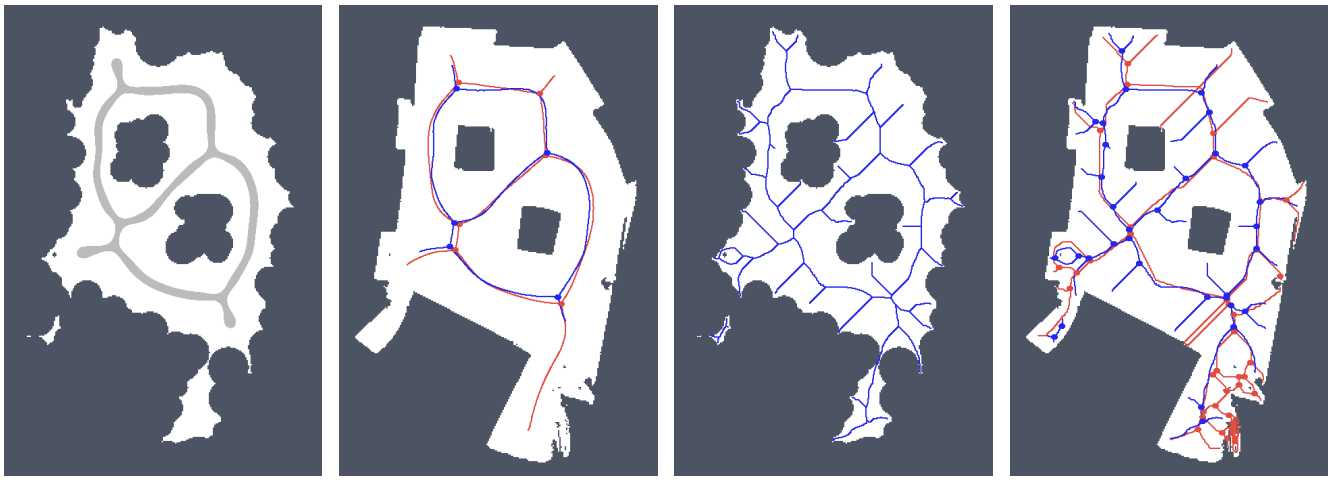

(a) RD-based **(b)** RD-based **(c)** Thinning **(d)** Thinning

Figure 22. Determined skeletons and topological maps with highlighted junction places and leaves in the map *cube* with the noise level $\sigma = 5$ for the scaled map with 478 $\times$ 698 grid points: (**a**) RD-based Voronoi diagram; (**b**) and its corresponding skeleton superimposed on the skeleton determined in the noise-less map (in red); (**c**) Pruned GVG representing skeleton of the map determined by the thinning algorithm [12]; (**d**) and the corresponding skeleton superimposed on the skeleton determined in the noise-less map.

5. Discussion

The presented evaluation of the Voronoi diagram generation for the maps with added noise demonstrates that one of the main advantages of the RD-based computation is a lower sensitivity to the noise level in comparison to the thinning algorithm. This advantage comes from the stability, in the Lyapunov sense, of the FHN system. The dynamics of the system drive it to the stable state, so that the spatiotemporal evolution is resistant to the inclusion of external information, which in the present case is interpreted as noise. This is mainly visible in the skeleton of the environment, where the RD-based skeleton does not include new branches for small "pockets" created as a result of the added noise. As a consequence, the number of junction places slowly decreases with the increasing noise level, which means that some parts of the environment become unreachable for the robot. On the other hand, the thinning algorithm is sensitive to the added noise, and additional pruning techniques are necessary.

Regarding these observations, the proposed RD-based computational model seems to be a suitable technique to process real sensor data and provides more robust solutions than purely geometrical-based approaches. The RD-based computational model works on a computational grid, where the underlying non-linear dynamics model exhibits its behavior based on the particular system properties. One of the important properties is the resolution of the computational grid itself, which is related to the ability of the wavefront propagation into a narrow passage in the environment. Thus, it is related to the dimension of the robot, and it guarantees finding a safe path. Although an additional pruning of the determined skeleton can be used to guarantee the required clearance of the topological roadmap (*i.e.*, generated skeleton of the environment), the relation is an indivisible part of the RD-based model.

It is noteworthy that this approach takes advantage of the common and well-known properties inherent to RD systems, like the natural parallelism of the computation and fault tolerance to damaged cells, interpreted as noise resistance. Besides, it is possible to physically implement this model by means of already existing technologies, such as CNN [31] via a VLSIchip, a feature that enables real-time computations.

6. Comments on the Stability of the RD System and Reduction of Computational Requirements

A computation of the RD-based model evolution can be significantly sped up based on the observation of the system stability in the sense of Lyapunov. The wavefronts whose propagation leads to the shift from one stable state to the other define the only regions in the environment that are actually evolving. In the computational grid, this means that as the evolution of the grid cells reaches the new stable state, these nodes remain in this state unchanged. Hence, this observation can be utilized to decrease the computational burden of the spatial integration of the model by performing computations only for these grid cells. Notice that although this approach can restrict the propagation of the wavefronts in the boundaries of evolving areas, the values of u and v tend to a stable level, and therefore, the restrictions only limit the velocity of the propagation. Moreover, the velocity of the underlying physical model is also limited and constant, and therefore, using the knowledge of the propagation behavior, one can set suitable parameters without affecting the propagation. These parameters have been experimentally set for the particular developed approach.

The proposed routine can be exemplified as follows: after several computational steps, cells are examined to see if their value of the concentration level u has changed after the selected period T_{active}, *i.e.*, testing the value $u_{activation} = |u(k) - u(k+T_{active})|$ of the computational steps k and $k+T_{active}$. Then, the cells for which the difference $u_{activation}$ is above a certain limit (e.g., $> 10^{-3}$) are denoted as active for the next batch of the computational steps. Besides, a small neighborhood of each such active cell is also marked as active to further support a propagation of the wavefronts. The herein used discretization of the FHN model is a simple finite difference method on a Cartesian grid: a simple forward in time centered in space (FTCS) scheme that facilitates the manipulation of the integration loop for including the described optimization.

Although a detailed comparison is out of the scope of the present work, a basic comparison for the two environments *potholes* and *jh* is shown in Table 2. Using a grid resolution of 800 $\times$ 800 points as a baseline for the *potholes* environment and 840 $\times$ 960 for the *jh* environment, four additional resolutions have been computed for the propagation phase of the Voronoi problem. The results show that the proposed optimization technique scales well with the increasing grid resolution. Moreover, since this optimization is hardware-agnostic, it can be ported to specialized platforms.

Table 2. Computational time (in minutes) spent in the expansion phase of the Voronoi computation for the environments *potholes* and *jh*. For both variants of the RD-based algorithm: the original, named naive, and the optimized version according to Section 6, named optimized. The size of the baseline is 800 × 800 grid points for the *potholes* and 840 × 960 grid points for the *jh*. The computational times have been collected using a workstation with an Intel iCore7 3770 processor, Debian jessie (64-bit), 16 GB RAM and C++ implementation compiled by the GCC 4.9.2 with the O3 enabled.

		Resolution Factor				
		1	***1.2***	***1.5***	***1.7***	***2***
potholes	*naive*	8.49	15.3	27.4	44.4	69.3
	optimized	1.3	2.1	2.5	3.3	5.2
jh	*naive*	12.5	20.7	44.5	65.8	103.4
	optimized	1.4	2.2	4.1	5.2	7.2

7. Conclusions and Future Work

Computational geometry is concerned with the study of algorithms for solving geometrical problems, and the Voronoi diagram arises as a data structure that underlies the geometry of seemingly different ones. An example of this, in a discrete cell lattice, is the generalized Voronoi graph, which identifies topological places and also determines paths between the places. In that context, the Voronoi diagram can be used for addressing the robot navigation problem.

In this paper, we consider RD-based computation of the Voronoi diagram to determine a skeleton of the grid map that represents a topology of the robot's operational environment. The herein presented approach binds robotics and the Voronoi diagram under a computational umbrella of RD systems, which allows a direct integration of raw sensor data into the computational grid.

The discovered findings are clearly split into two distinctive features: first is the exploitation of the newly-found behavior that leads to Voronoi-like concentration patterns as the final stable states of the model's spatiotemporal evolution, also allowing one to recover the system to its original state by means of the Voronoi diagram inversion; the second feature is the lack of sensitivity to the added noise that makes any pruning technique unnecessary for removing poor junction places, as is required in the case of the considered thinning algorithm.

Furthermore, the presented results are an extension of our previous studies, where different behaviors were successively included in the RD-based computational core and successfully applied to decision-planning and motion-planning in robotics. Therefore, the addition of the Voronoi diagram pattern sets the foundation of a reaction diffusion-based computational framework suitable for addressing geometrical problems, up to now particularly tailored to face the challenges associated with navigational problems in robotics.

Acknowledgments

This work has been funded by the National Plan Projects DPI2011-27818-C02-02 and DPI2012-31303 of the Spanish Ministry of Economy and Competitiveness and FEDER funds. The presented work is supported by the Czech Science Foundation (GAČR) under Research Project No. 13-18316P.

Computational resources were provided by the MetaCentrum under the program LM2010005and the CERIT-SCunder the program Centre CERIT Scientific Cloud, part of the Operational Program Research and Development for Innovations, Reg. No. CZ.1.05/3.2.00/08.0144.

Author Contributions

Alejandro Vázquez-Otero and Jan Faigl conceived and designed the experiments, performed the experiments and analyzed the data. Alejandro Vázquez-Otero and Jan Faigl wrote the paper. Natividad Duro and Raquel Dormido contributed analyzing the data and writing the paper.

Conflicts of Interest

The authors declare no conflict of interest.

References

1. Walgraef, D. *Spatio-Temporal Pattern Formation, with Examples in Physics, Chemistry and Materials Science.* Springer-Verlag: New York, NY, USA, 1997.
2. Turing, A.M. The Chemical Basis of Morphogenesis. *Philos. Trans. R. Soc. Lond. Ser. B Biol. Sci.* **1952**, *237*, 37–72.
3. Kuhnert, L.; Aglazde, K.I.; Krinsky, V.I. Image-Processing Using Light-Sensitive Chemical Waves. *Nature* **1989**, *337*, 244–247.
4. Krinsky, V.I.; Biktashev, V.N.; Efimov, I.R. Autowave principles for parallel image processing. *Phys. D Nonlinear Phenom.* **1991**, *49*, 247–253.
5. Steinbock, O.; Showalter, K.; Kettunen, P. Navigating complex labyrinths—Optimal paths from chemical waves. *Science* **1994**, *100*, 868–871.
6. Zhong, Y.; Shirinzadeh, B.; Alici, G.; Smith, J. An autowave based methodology for deformable object simulation. *Comput.-Aided Des.* **2006**, *38*, 740–754.
7. Busaryev, O.; Dey, T.K.; Wang, H.; Ren, Z. Animating Bubble Interactions in a Liquid Foam. *ACM Trans. Graph.* **2012**, *31*, 63:1–63:8.
8. Li, H.; Li, K.; Kim, T.; Zhang, A.; Ramanathan, M. Spatial modeling of bone microarchitecture. *Proc. SPIE* **2012**, *8290*, 82900P:1–82900P:9.
9. Walter, M.; Fournier, A.; Menevaux, D. Integrating Shape and Pattern in Mammalian Models. In Proceedings of the 28th Annual Conference on Computer Graphics and Interactive Techniques (SIGGRAPH '01), Los Angeles, CA, USA, 12–17 August 2001; pp. 317–326.
10. De Berg, M.; van Kreveld, M.; Overmars, M.; Swarzkopf, O. *Computational Geometry: Algorithms and Applications*; Springer: Berlin, Germany, 2000.

11. Choset, H.; Keiji, N. Topological simultaneous localization and mapping (SLAM): Toward exact localization without explicit localization. *IEEE Trans. Robot. Autom.* **2001**, *17*, 125–137.
12. Beeson, P.; Jong, N.; Kuipers, B. Towards Autonomous Topological Place Detection Using the Extended Voronoi Graph. In Proceedings of the IEEE International Conference on Robotics and Automation (ICRA), Barcelona, Spain, 18–22 April 2005; pp. 4373–4379.
13. Vázquez-Otero, A.; Muñuzuri, A.P. Navigation algorithm for autonomous devices based on biological waves. In Proceedings of the 2010 12th International Workshop on Cellular Nanoscale Networks and Their Applications (CNNA), Berkeley, CA, USA, 3–5 February 2010; pp. 1–5.
14. Vázquez-Otero, A.; Faigl, J.; Munuzuri, A.P. Path planning based on reaction-diffusion process. In Proceedings of the 2012 IEEE/RSJ International Conference on Intelligent Robots and Systems (IROS), Algarve, Portugal, 7–11 October 2012; pp. 896–901.
15. Vázquez-Otero, A.; Faigl, J.; Duro, N.; Dormido, R. Reaction-Diffusion based Computational Model for Autonomous Mobile Robot Exploration of Unknown Environments. *Int. J. Unconv. Comput.* **2014**, *4*, 295–316.
16. Hodgkin, A.; Huxley, A. A quantitative description of membrane current and its application to conduction and excitation in nerve. *J. Physiol.* **1952**, *117*, 500–544.
17. FitzHugh, R. Impulses and Physiological States in Theoretical Models of Nerve Membrane. *Biophys. J.* **1961**, *1*, 445–466.
18. Nagumo, J.; Arimoto, S.; Yoshizawa, S. An Active Pulse Transmission Line Simulating Nerve Axon. *Proc. IRE* **1962**, *50*, 2061–2070.
19. Preska Steinberg, A.; Epstein, I.R.; Dolnik, M. Target Turing Patterns and Growth Dynamics in the Chlorine Dioxide-Iodine-Malonic Acid Reaction. *J. Phys. Chem. A* **2014**, *118*, 2393–2400.
20. Mau, Y.; Haim, L.; Hagberg, A.; Meron, E. Competing resonances in spatially forced pattern-forming systems. *Phys. Rev. E* **2013**, *88*, doi:10.1103/PhysRevE.88.032917.
21. Rudiger, S.; Nicola, E.M.; Casademunt, J.; Kramer, L. Theory of pattern forming systems under traveling-wave forcing. *Physics Reports* **2007**, *447*, 73–111.
22. Moravec, H. Sensor Fusion in Certainty Grids for Mobile Robots. *AI Mag.* **1988**, *9*, 61–74.
23. Choset, H.; Burdick, J.W. Sensor-Based Exploration: The Hierarchical Generalized Voronoi Graph. *Int. J. Robot. Res.* **2000**, *19*, 96–125.
24. Adamatzky, A. Voronoi-like partition of lattice in cellular automata. *Math. Comput. Model.* **1996**, *23*, 51–66.
25. Adamatzky, A.; Holland, O. Voronoi-like Nondeterministic Partition of a Lattice by Collectives of Finite Automata. *Math. Comput. Model.* **1998**, *28*, 73–93.
26. Tolmachiev, D.; Adamatzky, A. Chemical processor for computation of Voronoi diagram. *Adv. Mater. Opt. Electron.* **1996**, *6*, 191–196.
27. Adamatzky, A. Hot ice computer. *Phys. Lett. A* **2009**, *374*, 264–271.
28. Adamatzky, A.; de Lacy Costello, B. On some limitations of reaction diffusion chemical computers in relation to Voronoi diagram and its inversion. *Phys. Lett. A* **2003**, *309*, 397–406.
29. Jones, J.; Adamatzky, A. Slime mold inspired generalised Voronoi diagrams with repulsive fields. *Int. J. Bifurc. Chaos* **2015**, in press.

30. De Lacy Costello, B.; Ratcliffe, N.; Adamatzky, A.; Zanin, A.L.; Liehr, A.W.; Purwins, H.G. The Formation of Voronoi Diagrams in Chemical and Physical Systems: Experimental findings and theoretical models. *Int. J. Bifurc. Chaos* **2004**, *14*, 2187–2210.
31. Muñuzuri, A.P.; Vázquez-Otero, A. The CNN solution to the shortest-path-finder problem. In Proceedings of the 11th International Workshop On Cellular Neural Networks and Their Applications, Santiago de Composteia, Spain, 14–16 July 2008; pp. 248–251.

© 2015 by the authors; licensee MDPI, Basel, Switzerland. This article is an open access article distributed under the terms and conditions of the Creative Commons Attribution license (http://creativecommons.org/licenses/by/4.0/).